

Zinc Precursor Synthesis and the Aerosol Assisted Chemical Vapour Deposition of Zinc Oxide Thin Films

**This thesis is submitted in partial fulfilment of the requirements for the Degree
of Doctor of Engineering (Chemistry).**

Joe Anthony Manzi

Supervised by Professor Ivan P. Parkin and Professor Claire J. Carmalt

Department of Chemistry
University College London
Christopher Ingold Laboratories
20 Gordon Street
London
WC1H 0AJ

2016

I, Joe Anthony Manzi confirm that the work presented in this thesis is my own. Where information has been derived from other sources, I confirm that this has been indicated in the thesis.

Abstract

This thesis describes the synthesis of novel zinc complexes formed from the reaction of diethylzinc (ZnEt_2) and a range of dicarbonyl and β -iminoester ligands. These complexes, as well as zinc triflate, $[\text{Zn}(\text{OTf})_2]$ were successfully employed as precursors in the aerosol assisted chemical vapour deposition (AACVD) of zinc oxide (ZnO) and aluminium doped ZnO (AZO) thin films. Films of this type are of significant interest for a number of applications, including as transparent conducting oxide (TCO) materials.

Investigations into the reactions between ZnEt_2 and dicarbonyl compounds led to the successful synthesis, isolation and characterisation of trimeric zinc oxane complexes $[(\text{Zn}(\text{Et})(\text{OC}(\text{R})\text{CHC}(\text{Me})\text{O}))_3]$ with a central six membered Zn_3O_3 ring, where $\text{R} = \text{OMe}$ (**1**), Me (**2**), OEt (**3**) and O^tBu (**4**). Controlled oxygenation reactions of solutions of (**1**) – (**4**) also lead to the successful synthesis of zinc oxane clusters $[(\text{Zn}(\text{OC}(\text{R})\text{CHC}(\text{Me})\text{O})_2\text{Zn}(\text{Et})\text{OEt})_2]$, where $\text{R} = \text{OMe}$ (**5**), Me (**6**), OEt (**7**) and O^tBu (**8**).

Zinc β -iminoesterate complexes with increased functionality have also been synthesised in reactions between ZnEt_2 and the synthesised β -iminoester ligands $\text{MeC}(\text{NHR})\text{CHC}(\text{O})\text{OEt}$, where R is ^iPr (**L1**), Me (**L2**), ^iBu (**L3**) and $(\text{CH}_2)_2^i\text{Pr}$ (**L4**). Homoleptic zinc β -iminoesterates $[\text{Zn}(\text{OC}(\text{OEt})\text{CHC}(\text{Me})\text{NR})_2]$ (**9**) – (**12**) were synthesised in 1:2 equivalence reactions between ZnEt_2 and (**L1**) – (**L4**) respectively. Heteroleptic dimeric complexes $[(\text{Zn}(\text{OC}(\text{OEt})\text{CHC}(\text{Me})\text{N}^i\text{Pr})(\text{Et}))_2]$ (**13**) and $[(\text{Zn}(\text{OC}(\text{OEt})\text{CHC}(\text{Me})\text{N}(\text{CH}_2)_2^i\text{Pr})(\text{Et}))_2]$ (**14**) were synthesised in 1:1 reactions of ZnEt_2 and (**L1**) and (**L4**) respectively.

Thermal decomposition and AACVD studies were performed using $[\text{Zn}(\text{OTf})_2]$ and zinc complexes (**6**), (**9**) and (**10**) leading to the successful deposition of ZnO and AZO thin films. Films deposited from (**6**) and (**10**) required annealing to remove significant carbon content but the change in identity of the organic substituent between (**10**) and (**9**) in the β -iminoesterate system was found to greatly reduce the carbon in the films. $[\text{Zn}(\text{OTf})_2]$ and complex (**9**) were both determined to be highly suitable AACVD precursors for the deposition of doped and undoped ZnO thin films.

Acknowledgements

I would like to start by thanking my two supervisors, Professor Ivan P. Parkin and Professor Claire J. Carmalt for their unwavering support and encouragement over these last few years. I would also like to give particular thanks to my colleague and dear friend Dr. Caroline E. Knapp. Thank you for running and solving all the single crystal X-ray diffraction structures presented in this thesis and for your guidance and friendship along the way.

I would like to thank Dr. Deborah Raisbeck and the Online Coatings Group at NSG Group for all the discussions and for making me feel so welcome in the north. Thanks also to the NSG analysis team for running XPS and SEM analysis on my samples, the results of which are presented in this thesis.

UCL has also allowed me the pleasure of working with some great colleagues. I would like to thank Dr. Kersti Karu and Dr. Vincent Gray for performing mass spectroscopy on my samples, Jill Maxwell for the elemental analysis and Dr. Abil Aliev for his assistance in NMR. I would also like to thank my friends and colleagues at UCL Chemistry as well as all the administrators, support staff, technicians and academics who keep the department running. I would especially like to thank Hazel Kitching and Ben Robinson for their special friendship.

My thanks wouldn't be complete without a few acknowledgements outside of chemistry. I would like to thank my Mum for being such a wonderful woman and teaching me well and to the rest of my family for their support and for inspiring me to be the best person I can be. Also to my brilliant friends, I am incredibly grateful to have you all.

Finally, I would like to thank UCL, the EPSRC and NSG Group for funding this project.

Table of Contents

Title Page	1	
Declaration	2	
Abstract	3	
Acknowledgments	4	
Table of Contents	5	
List of Figures	11	
List of Schemes	14	
List of Tables	16	
List of Abbreviations	17	
1	Introduction	19
1.1	Zinc Oxide	20
1.1.1	Semiconductor Properties	21
1.1.2	Doped Zinc Oxide	22
1.2	Transparent Conducting Oxide (TCO)	23
1.3	Applications	25
1.4	Deposition of ZnO Thin Films	26
1.4.1	Physical Vapour Deposition	26
1.4.2	Solution Based Deposition	27
1.4.3	Chemical Vapour Deposition	27
1.4.3.1	Aerosol Assisted Chemical Vapour Deposition	30
1.5	CVD Precursors	31
1.5.1	Desired Precursor Properties	31
1.5.2	Dual – Source Precursors	33
1.5.3	Single – Source Precursors	34
1.5.4	Zinc Precursors	35
1.6	Overview of Thesis	35
1.7	Conclusion	36
1.8	References	37

2	Experimental Procedures	41
2.1	Introduction	42
2.2	Synthesis	42
2.2.1	General Procedures	42
2.2.2	Characterisation Measurements	43
2.2.3	Zinc Oxane Complexes	43
2.2.3.1	Synthesis of Zinc Oxane Trimer Complexes	43
2.2.3.1.1	Synthesis of [(Zn(Et)(OC(OMe)CHC(Me)O)) ₃] (1)	43
2.2.3.1.2	Synthesis of [(Zn(Et)(OC(Me)CHC(Me)O)) ₃] (2)	44
2.2.3.1.3	Synthesis of [(Zn(Et)(OC(OEt)CHC(Me)O)) ₃] (3)	44
2.2.3.1.4	Synthesis of [(Zn(Et)(OC(O ⁱ Bu)CHC(Me)O)) ₃] (4)	44
2.2.3.2	Synthesis of Zinc Oxane Cluster Complexes	45
2.2.3.2.1	Synthesis of [(Zn(OC(OMe)CHC(Me)O) ₂ Zn(Et)OEt) ₂] (5)	45
2.2.3.2.2	Synthesis of [(Zn(OC(Me)CHC(Me)O) ₂ Zn(Et)OEt) ₂] (6)	45
2.2.3.2.3	Synthesis of [(Zn(OC(OEt)CHC(Me)O) ₂ Zn(Et)OEt) ₂] (7)	46
2.2.3.2.4	Synthesis of [(Zn(OC(O ⁱ Bu)CHC(Me)O) ₂ Zn(Et)OEt) ₂] (8)	47
2.2.4	Synthesis of Zinc β -Iminoesterate Complexes	47
2.2.4.1	Synthesis of β -Iminoester Ligands	47
2.2.4.1.1	Synthesis of MeC(NH ⁱ Pr)CHC(O)OEt (L ₁)	47
2.2.4.1.2	Synthesis of MeC(NHMe)CHC(O)OEt (L ₂)	48
2.2.4.1.3	Synthesis of MeC(NH ⁱ Bu)CHC(O)OEt (L ₃)	48
2.2.4.1.4	Synthesis of MeC(NH(CH ₂) ₂ ⁱ Pr)CHC(O)OEt (L ₄)	49
2.2.4.2	Synthesis of Homoleptic Zinc β -Iminoesterate Complexes	49
2.2.4.2.1	Synthesis of [Zn(OC(OEt)CHC(Me)N ⁱ Pr) ₂] (9)	49
2.2.4.2.2	Synthesis of [Zn(OC(OEt)CHC(Me)NMe) ₂] (10)	50
2.2.4.2.3	Synthesis of [Zn(OC(OEt)CHC(Me)N ⁱ Bu) ₂] (11)	50
2.2.4.2.4	Synthesis of [Zn(OC(OEt)CHC(Me)N(CH ₂) ₂ ⁱ Pr) ₂] (12)	50
2.2.4.3	Synthesis of Heteroleptic Zinc β -Iminoesterate Complexes	51
2.2.4.3.1	Synthesis of [(Zn(OC(OEt)CHC(Me)N ⁱ Pr)(Et)) ₂] (13)	51
2.2.4.3.2	Synthesis of [(Zn(OC(OEt)CHC(Me)N(CH ₂) ₂ ⁱ Pr)(Et)) ₂] (14)	51
2.3	Chemical Vapour Deposition	52
2.3.1	Analysis Methods	52
2.3.1.1	Precursor Thermal Decomposition Analysis	52

2.3.1.2	Film Analysis Methods	52
2.3.2	Thin Film Deposition	53
2.3.2.1	Chemical Vapour Deposition Rig	53
2.3.2.2	Aerosol Assisted Chemical Vapour Deposition Delivery	54
2.3.2.3	General Procedures	55
2.3.2.4	AACVD from $[\text{Zn}(\text{OTf})_2]$	55
2.3.2.5	AACVD from Zinc Complex (6)	55
2.3.2.6	AACVD from (9) and (10)	56
2.4	Conclusion	56
3	AACVD of Zinc Oxide and Aluminium Doped Zinc Oxide	
	Thin Films from Zinc Triflate	57
3.1	Introduction	58
3.1.1	Zinc Complexes as ZnO CVD Precursors	59
3.1.1.1	Alkyl Zinc Compounds	59
3.1.1.2	Zinc Acetate	62
3.1.1.3	Zinc Acetylacetonate	63
3.1.1.4	Zinc 2-Ethylhexanoate	64
3.1.1.5	Zinc Triflate	65
3.2	Results and Discussion	67
3.2.1	Precursor Properties	67
3.2.1.1	Solubility and Solvent Choice	67
3.2.1.2	Thermal Gravimetric Analysis	68
3.2.2	AACVD of ZnO and AZO Thin Films	69
3.2.3	Aside: Alternative Deposition Methods	71
3.2.4	Film Characterisation	71
3.2.4.1	X-ray Diffraction	72
3.2.4.2	X-ray Photoelectron Spectroscopy	73
3.2.4.2.1	Depth Profiling	74
3.2.4.3	Scanning Electron Microscopy	76
3.2.4.4	Functional Properties	77
3.2.4.4.1	Optical Properties	77
3.2.4.4.1.1	Band Gap	77

3.2.4.4.2	Electrical Properties	79
3.3	Potential of Triflate Precursors	79
3.4	Conclusion	81
3.5	References	82
4	Synthesis of Zinc Oxane Complexes and the AACVD of Zinc Oxide Thin Films	85
4.1	Introduction	86
4.1.1	Zinc Oxane Structures	86
4.1.1.1	Cyclic Structures	88
4.1.1.1.1	Cyclic Structures with Chelating Ligands	89
4.1.1.2	Cubane Structures	92
4.1.1.2.1	Defective Cubane Structures	94
4.2	Results and Discussion	96
4.2.1	Synthesis of Zinc Oxane Complexes	96
4.2.1.1	Synthesis of Zinc Oxane Trimer Complexes	96
4.2.1.1.1	Synthesis of $[(\text{Zn}(\text{Et})(\text{OC}(\text{OMe})\text{CHC}(\text{Me})\text{O}))_3]$ (1)	97
4.2.1.1.2	Synthesis of $[(\text{Zn}(\text{Et})(\text{OC}(\text{Me})\text{CHC}(\text{Me})\text{O}))_3]$ (2)	104
4.2.1.1.3	Synthesis of $[(\text{Zn}(\text{Et})(\text{OC}(\text{OEt})\text{CHC}(\text{Me})\text{O}))_3]$ (3)	105
4.2.1.1.4	Synthesis of $[(\text{Zn}(\text{Et})(\text{OC}(\text{O}^t\text{Bu})\text{CHC}(\text{Me})\text{O}))_3]$ (4)	106
4.2.1.2	Synthesis of Zinc Oxane Cluster Complexes	106
4.2.1.2.1	Synthesis of $[(\text{Zn}(\text{OC}(\text{OMe})\text{CHC}(\text{Me})\text{O})_2\text{Zn}(\text{Et})\text{OEt})_2]$ (5)	108
4.2.1.2.2	Synthesis of $[(\text{Zn}(\text{OC}(\text{Me})\text{CHC}(\text{Me})\text{O})_2\text{Zn}(\text{Et})\text{OEt})_2]$ (6)	110
4.2.1.2.3	Synthesis of $[(\text{Zn}(\text{OC}(\text{OEt})\text{CHC}(\text{Me})\text{O})_2\text{Zn}(\text{Et})\text{OEt})_2]$ (7)	116
4.2.1.2.4	Synthesis of $[(\text{Zn}(\text{OC}(\text{O}^t\text{Bu})\text{CHC}(\text{Me})\text{O})_2\text{Zn}(\text{Et})\text{OEt})_2]$ (8)	118
4.2.1.3	Crystal Structure Comparison of (6) and (8)	124
4.2.2	AACVD Precursors Study	125
4.2.2.1	Thermal Gravimetric Analysis	125
4.2.3	AACVD of ZnO Thin Films	127
4.2.3.1	X-ray Photoelectron Spectroscopy	128
4.2.3.2	X-ray Diffraction	129
4.2.3.3	Scanning Electron Microscopy	130
4.2.3.4	Functional Properties	131

4.2.3.4.1	Electrical Properties	131
4.2.3.4.2	Optical Properties	132
4.2.3.4.2.1	Band Gap	133
4.3	Conclusion	133
4.4	References	135
5	Synthesis of Zinc β-Iminoesterates and the AACVD of Zinc Oxide Thin Films	137
5.1	Introduction	138
5.1.1	β -Ketoimine and β -Iminoester Ligands	139
5.1.2	β -Ketoiminates and β -Iminoesterates Metal Complexes	142
5.1.2.1	Commercial Importance	142
5.1.2.2	Alkaline Earth β -Ketoiminates	143
5.1.2.3	Group 13 β -Ketoiminates	144
5.1.2.3.1	Aluminium β -Ketoiminate Complexes	144
5.1.2.3.2	β -Ketoiminate Stabilised Gallium Complexes	145
5.1.2.4	Transition Metal β -Ketoiminate Complexes	147
5.1.2.4.1	Group 4 Transition Metal β -Ketoiminate Complexes	147
5.1.2.4.2	Zinc β -Ketoiminate/Iminoesterate Complexes	149
5.2	Results and Discussion	152
5.2.1	Synthesis of β -Iminoester Ligands	152
5.2.2	Synthesis of Zinc β -Iminoesterate Complexes	154
5.2.2.1	Homoleptic Zinc β -Iminoesterate Complexes Synthesis	155
5.2.2.1.1	Synthesis of $[\text{Zn}(\text{MeCN}(^i\text{Pr})\text{CHC}(\text{OEt})\text{O})_2]$ (9)	155
5.2.2.1.2	Synthesis of $[\text{Zn}(\text{MeCN}(\text{Me})\text{CHC}(\text{OEt})\text{O})_2]$ (10)	161
5.2.2.1.3	Crystal Structure Comparison of (9) and (10)	164
5.2.2.1.4	Synthesis of $[\text{Zn}(\text{MeCN}(^i\text{Bu})\text{CHC}(\text{OEt})\text{O})_2]$ (11)	165
5.2.2.1.5	Synthesis of $[\text{Zn}(\text{MeCN}((\text{CH}_2)_2^i\text{Pr})\text{CHC}(\text{OEt})\text{O})_2]$ (12)	165
5.2.2.2	Synthesis of Zinc β -Iminoesterate Dimer Complexes	166
5.2.2.2.1	Synthesis of $[(\text{Zn}(\text{MeCN}(^i\text{Pr})\text{CHC}(\text{OEt})\text{O})(\text{Et}))_2]$ (13)	167
5.2.2.2.2	Synthesis of $[(\text{Zn}(\text{MeCN}((\text{CH}_2)_2^i\text{Pr})\text{CHC}(\text{OEt})\text{O})(\text{Et}))_2]$ (14)	171
5.2.2.2.3	Crystal Structure Comparison of (13) and (14)	175
5.2.2.2.4	Crystal Structure Comparison of (9) and (13)	176

5.2.3	AACVD Precursors Study	177
5.2.3.1	Thermal Gravimetric Analysis	177
5.2.4	AACVD of ZnO Thin Films	179
5.2.4.1	Film Thickness	180
5.2.4.2	X-ray Photoelectron Spectroscopy	180
5.2.4.3	X-ray Diffraction	183
5.2.4.4	Scanning Electron Microscopy	184
5.2.4.5	Functional Properties	186
5.2.4.5.1	Electrical Properties	186
5.2.4.5.2	Optical Properties	186
5.2.4.5.2.1	Band Gap	187
5.3	Conclusion	187
5.4	References	189
6	Conclusions and Future Work	191
7	Appendix	195

List of Figures

Figure 1.1:	Stick and ball diagram of hexagonal wurtzite ZnO	20
Figure 1.2:	Band structures for a conductor, insulator and semiconductor	21
Figure 1.3:	Band structures for extrinsic <i>n</i> -type and <i>p</i> -type doping	22
Figure 1.4:	Steps of the CVD process	28
Figure 1.5:	Single-source Zn β -ketoiminate and β -iminoesterate complex	34
Figure 2.1:	Horizontal cold-walled CVD reactor	53
Figure 2.2:	AACVD bubbler set-up	54
Figure 3.1:	Commercially available Zn complexes used as CVD precursors	58
Figure 3.2:	Synthesis of mono and bis(heterocubanes)	61
Figure 3.3:	Structure of $[\text{Zn}_4\text{O}(\text{OOCMe})_6]$	63
Figure 3.4:	Deposition matrix of ZnO from $[\text{Zn}(\text{OOCCH}(\text{C}_2\text{H}_5)\text{C}_4\text{H}_9)_2]$	65
Figure 3.5:	Structure of $[\text{Zn}(\text{OTf})_2]$	66
Figure 3.6:	TGA and DCS of $[\text{Zn}(\text{OTf})_2]$	68
Figure 3.7:	XRD of ZnO and AZO from $[\text{Zn}(\text{OTf})_2]$	72
Figure 3.8:	XPS of Zn 2p from AZO film from $[\text{Zn}(\text{OTf})_2]$ and $[\text{Al}(\text{acac})_3]$	73
Figure 3.9:	XPS of Al 2p from AZO from $[\text{Zn}(\text{OTf})_2]$ and $[\text{Al}(\text{acac})_3]$	74
Figure 3.10:	XPS depth profile for ZnO from $[\text{Zn}(\text{OTf})_2]$	75
Figure 3.11:	XPS depth profile for AZO from $[\text{Zn}(\text{OTf})_2]$ and $[\text{Al}(\text{acac})_3]$	75
Figure 3.12:	Plane view and cross section SEM of ZnO and AZO	76
Figure 3.13:	Transmission spectra and Tauc plots for ZnO and AZO	78
Figure 3.14:	TGA and DCS for $[\text{Mg}(\text{OTf})_2]$	80
Figure 4.1:	Common zinc oxane rings and cubane central structures	87
Figure 4.2:	Structure of $[(\text{Zn}'\text{BuO}'\text{Bu})_3]$	89
Figure 4.3:	Structure of an eight membered Zn_4O_4 ring	91
Figure 4.4:	Structure of $[(\text{Zn}(\text{Et})(\text{O}'\text{Bu}))_4]$	92
Figure 4.5:	Structure of $[(\text{ZnEt})_6\text{Zn}(\text{OMe})_8]$	93
Figure 4.6:	Structure of $[(\text{EtOOZn}(\text{azol}))_2(\text{EtZn}(\text{azol}))_2]$	94
Figure 4.7:	Structure of $[\text{Zn}_4(\text{Et})_2(\text{OEt})_2(\text{OMal})_4]$	95
Figure 4.8:	Structure of $[\text{Zn}_4(\text{OMe})_2(\text{acac})_6]$	95
Figure 4.9:	^1H NMR spectrum of $[(\text{Zn}(\text{Et})(\text{OC}(\text{OMe})\text{CHC}(\text{Me})\text{O}))_3]$ (1)	98

Figure 4.10:	X-ray crystal structure of $[(\text{Zn}(\text{Et})(\text{OC}(\text{OMe})\text{CHC}(\text{Me}))_3]$ (1)	100
Figure 4.11:	Highly distorted representation of (1) for comparison of bond angles to $[(\text{Zn}^t\text{BuO}^t\text{Bu})_3]$	103
Figure 4.12:	^1H NMR spectrum of $[(\text{Zn}(\text{OC}(\text{OMe})\text{CHC}(\text{Me})\text{O})_2\text{Zn}(\text{Et})\text{OEt})_2]$ (5)	109
Figure 4.13:	^1H NMR spectrum recorded at 75 °C of $[(\text{Zn}(\text{OC}(\text{OMe})\text{CHC}(\text{Me})\text{O})_2\text{Zn}(\text{Et})\text{OEt})_2]$ (5)	110
Figure 4.14:	X-ray crystal structure of $[(\text{Zn}(\text{OC}(\text{Me})\text{CHC}(\text{Me})\text{O})_2\text{Zn}(\text{Et})\text{OEt})_2]$ (6)	112
Figure 4.15:	^1H NMR spectrum of $[(\text{Zn}(\text{OC}(\text{OEt})\text{CHC}(\text{Me})\text{O})_2\text{Zn}(\text{Et})\text{OEt})_2]$ (7)	117
Figure 4.16:	X-ray crystal structure of $[(\text{Zn}(\text{OC}(\text{O}^t\text{Bu})\text{CHC}(\text{Me})\text{O})_2\text{Zn}(\text{Et})\text{OEt})_2]$ (8)	120
Figure 4.17:	TGA and DSC of $[(\text{Zn}(\text{OC}(\text{Me})\text{CHC}(\text{Me})\text{O})_2\text{Zn}(\text{Et})\text{OEt})_2]$ (6)	126
Figure 4.18:	XPS of Zn 2p from ZnO from $[(\text{Zn}(\text{OC}(\text{Me})\text{CHC}(\text{Me})\text{O})_2\text{Zn}(\text{Et})\text{OEt})_2]$ (6)	128
Figure 4.19:	XPS depth profile for films from $[(\text{Zn}(\text{OC}(\text{Me})\text{CHC}(\text{Me})\text{O})_2\text{Zn}(\text{Et})\text{OEt})_2]$ (6)	129
Figure 4.20:	XRD patterns of films from $[(\text{Zn}(\text{OC}(\text{Me})\text{CHC}(\text{Me})\text{O})_2\text{Zn}(\text{Et})\text{OEt})_2]$ (6)	130
Figure 4.21:	Plane view and cross section SEM images of films from $[(\text{Zn}(\text{OC}(\text{Me})\text{CHC}(\text{Me})\text{O})_2\text{Zn}(\text{Et})\text{OEt})_2]$ (6)	131
Figure 4.22:	Transmission spectra and Tauc plot observed for films deposited from $[(\text{Zn}(\text{OC}(\text{Me})\text{CHC}(\text{Me})\text{O})_2\text{Zn}(\text{Et})\text{OEt})_2]$ (6)	132
Figure 5.1:	Structure of the β -ketoimine ligand	138
Figure 5.2:	Structure of a range of β -ketoimine and β -iminoester ligands	139
Figure 5.3:	Tautomeric structures of a β -ketoimine and β -iminoester ligand	140
Figure 5.4:	Patented metal β -ketoiminate complexes	142
Figure 5.5:	Zinc β -ketoiminate MOCVD precursor	150
Figure 5.6:	Tautomer forms of the β -iminoester ligand	154
Figure 5.7:	^1H NMR spectrum of $[\text{Zn}(\text{OC}(\text{OEt})\text{CHC}(\text{Me})\text{N}^i\text{Pr})_2]$ (9)	156
Figure 5.8:	Mass spectroscopy analysis of $[\text{Zn}(\text{OC}(\text{OEt})\text{CHC}(\text{Me})\text{N}^i\text{Pr})_2]$ (9)	157

Figure 5.9:	Molecular ion peak observed in the mass spectrum for [Zn(OC(OEt)CHC(Me)N ⁱ Pr) ₂] (9)	158
Figure 5.10:	X-ray crystal structure of [Zn(OC(OEt)CHC(Me)N ⁱ Pr) ₂] (9)	159
Figure 5.11:	X-ray crystal structure of [Zn(OC(OEt)CHC(Me)NMe) ₂] (10)	162
Figure 5.12:	X-ray crystal structure of [(Zn(OC(OEt)CHC(Me)N ⁱ Pr)(Et)) ₂] (13)	168
Figure 5.13:	X-ray crystal structure of [(Zn(OC(OEt)CHC(Me)N(CH ₂) ₂ ⁱ Pr)(Et)) ₂] (14)	172
Figure 5.14:	TGA and DSC of [Zn(OC(OEt)CHC(Me)N ⁱ Pr) ₂] (9) and [Zn(OC(OEt)CHC(Me)NMe) ₂] (10)	178
Figure 5.15:	XPS of Zn 2p peaks for ZnO films deposited from [Zn(OC(OEt)CHC(Me)N ⁱ Pr) ₂] (9)	181
Figure 5.16:	XPS depth profile for ZnO films from [Zn(OC(OEt)CHC(Me)N ⁱ Pr) ₂] (9)	181
Figure 5.17:	XPS depth profile for ZnO films from [Zn(OC(OEt)CHC(Me)NMe) ₂] (10)	182
Figure 5.18:	XRD patterns of ZnO films from [Zn(OC(OEt)CHC(Me)N ⁱ Pr) ₂] (9) and [Zn(OC(OEt)CHC(Me)NMe) ₂] (10)	184
Figure 5.19:	Plane view SEM images of ZnO films deposited from [Zn(OC(OEt)CHC(Me)N ⁱ Pr) ₂] (9) and [Zn(OC(OEt)CHC(Me)NMe) ₂] (10)	185
Figure 5.20:	Transmission spectra and Tauc plot observed for ZnO films deposited from [Zn(OC(OEt)CHC(Me)N ⁱ Pr) ₂] (9) and [Zn(OC(OEt)CHC(Me)NMe) ₂] (10)	186

List of Schemes

Scheme 1.1:	Dual-source reaction to form a ZnO thin film	33
Scheme 3.1:	Formation of ZnO from ZnEt ₂ and an alcohol	60
Scheme 3.2:	Decomposition mechanism of [MeZn(O ⁱ Bu)]	60
Scheme 3.3:	Deposition of ZnO from [Zn(OOCMe) ₂] · 2H ₂ O	62
Scheme 3.4:	Deposition of ZnO from [Zn(OOCCH(C ₂ H ₅)C ₄ H ₉) ₂]	64
Scheme 3.5:	Synthesis of [Zn(OTf) ₂] from Zn metal	66
Scheme 3.6:	Synthesis of [Zn(OTf) ₂] from [ZnCO ₃]	66
Scheme 3.7:	Ultrasonic activated synthesis of [Zn(OTf) ₂]	67
Scheme 3.8:	AACVD of ZnO from [Zn(OTf) ₂]	69
Scheme 3.9:	AACVD of AZO from [Zn(OTf) ₂] and [Al(acac) ₃]	70
Scheme 4.1:	Proposed reaction pathway for O ₂ insertion into a Zn-C bond	87
Scheme 4.2:	Synthesis of [(Zn(^t Bu)O ^t Bu(thf)) ₂] and [(Zn(^t Bu)OO ^t Bu(py-Me)) ₂]	88
Scheme 4.3:	Synthesis of [(LxZn(DMSO)) ₂]	89
Scheme 4.4:	Synthesis of [(MeZn(bdmap)ZnMe ₂) ₂], [(MeZn(bdmap)) ₂ MeZnOOMe] and [(MeZn(bdmap)) ₃ ZnMe ₂]	90
Scheme 4.5:	Synthesis of [(EtZn) ₂ Zn(OAr) ₄]	91
Scheme 4.6:	Suggested decomposition of [(Zn(Me)(O ⁱ Pr)) ₄]	93
Scheme 4.7:	Synthesis of [(EtOOZn(azol)) ₂ (EtZn(azol)) ₂]	94
Scheme 4.8:	Synthesis of [(Zn(Et)(OC(R)CHC(Me)O)) ₃] (1) – (4)	97
Scheme 4.9:	Synthesis of [(Zn(OC(R)CHC(Me)O) ₂ Zn(Et)OEt) ₂] (5) – (8)	107
Scheme 4.10:	AACVD of [(Zn(OC(Me)CHC(Me)O) ₂ Zn(Et)O(Et)) ₂] (6)	127
Scheme 5.1:	Microwave assisted preparation of β-ketoimine ligands	140
Scheme 5.2:	Preparation of β-ketoimine and β-iminoester ligands employing K-10 montmorillonite	141
Scheme 5.3:	Synthesis of Mg β-ketoiminate complexes	143
Scheme 5.4:	Synthesis of Sr, Cd and Ba β-ketoiminate complexes	144
Scheme 5.5:	Synthesis of Al β-ketoiminate complexes	144
Scheme 5.6:	Synthesis of Al β-ketoiminate complex	145
Scheme 5.7:	Synthesis of Ga β-ketoiminate complexes	146
Scheme 5.8:	Synthesis of Ga β-ketoiminate complexes	146

Scheme 5.9: Synthesis of Ti β -ketoiminate complexes	147
Scheme 5.10: Synthesis of Zr β -ketoiminate complexes	147
Scheme 5.11: Synthesis of Hf β -ketoiminates for potential CVD application	148
Scheme 5.12: Synthesis of a novel Zn β -ketoiminate and β -iminoesterate complex	149
Scheme 5.13: Synthesis of Zn β -ketoiminates with additional O atoms	150
Scheme 5.14: Synthesis of Zn β -ketoiminates with functionalised pendant arms	151
Scheme 5.15: Synthesis of β -iminoester ligands MeC(NHR)CHC(O)OEt (L ₁) – (L ₄)	152
Scheme 5.16: Synthesis of Zn β -iminoesterate complexes [Zn(OC(OEt)CHC(Me)NR) ₂] (9) – (12)	155
Scheme 5.17: Synthesis of Zn β -iminoesterates [(Zn(OC(OEt)CHC(Me)N ^{<i>i</i>} Pr)(Et)) ₂] (13) and [(Zn(OC(OEt)CHC(Me)N(CH ₂) ₂ ^{<i>i</i>} Pr)(Et)) ₂] (14)	166
Scheme 5.18: AACVD of ZnO thin films from [Zn(OC(OEt)CHC(Me)N ^{<i>i</i>} Pr) ₂] (9) and [Zn(OC(OEt)CHC(Me)NMe) ₂] (10)	179

List of Tables

Table 4.1:	Crystallographic data for $[(\text{Zn}(\text{Et})(\text{OC}(\text{OMe})\text{CHC}(\text{Me}))_3] \text{ (1)}$	100
Table 4.2:	Selected bond lengths (Å) and angles (°) for $[(\text{Zn}(\text{Et})(\text{OC}(\text{OMe})\text{CHC}(\text{Me}))_3] \text{ (1)}$	101
Table 4.3:	Crystallographic data for $[(\text{Zn}(\text{OC}(\text{Me})\text{CHC}(\text{Me})\text{O})_2\text{Zn}(\text{Et})\text{OEt})_2] \text{ (6)}$	113
Table 4.4:	Selected bond lengths (Å) and angles (°) for $[(\text{Zn}(\text{OC}(\text{Me})\text{CHC}(\text{Me})\text{O})_2\text{Zn}(\text{Et})\text{OEt})_2] \text{ (6)}$	114
Table 4.5:	Crystallographic data for $[(\text{Zn}(\text{OC}(\text{OC}(\text{Me})_3)\text{CHC}(\text{Me})\text{O})_2\text{Zn}(\text{Et})\text{OEt})_2] \text{ (8)}$	121
Table 4.6:	Selected bond lengths (Å) and angles (°) for $[(\text{Zn}(\text{OC}(\text{O}^t\text{Bu})\text{CHC}(\text{Me})\text{O})_2\text{Zn}(\text{Et})\text{OEt})_2] \text{ (8)}$	122
Table 5.1:	Stirring time and yield of synthesised β -iminoester ligands	153
Table 5.2:	Crystallographic data for $[\text{Zn}(\text{OC}(\text{OEt})\text{CHC}(\text{Me})\text{N}^i\text{Pr})_2] \text{ (9)}$	160
Table 5.3:	Selected bond lengths (Å) and angles (°) for $[\text{Zn}(\text{OC}(\text{OEt})\text{CHC}(\text{Me})\text{N}^i\text{Pr})_2] \text{ (9)}$	160
Table 5.4:	Crystallographic data for $[\text{Zn}(\text{OC}(\text{OEt})\text{CHC}(\text{Me})\text{NMe})_2] \text{ (10)}$	162
Table 5.5:	Selected bond lengths (Å) and bond angles (°) for $[\text{Zn}(\text{OC}(\text{OEt})\text{CHC}(\text{Me})\text{NMe})_2] \text{ (10)}$	163
Table 5.6:	Crystallographic data for $[(\text{Zn}(\text{OC}(\text{OEt})\text{CHC}(\text{Me})\text{N}^i\text{Pr})(\text{Et}))_2] \text{ (13)}$	169
Table 5.7:	Selected bond lengths (Å) and angles (°) for $[(\text{Zn}(\text{OC}(\text{OEt})\text{CHC}(\text{Me})\text{N}^i\text{Pr})(\text{Et}))_2] \text{ (13)}$	170
Table 5.8:	Crystallographic data for $[(\text{Zn}(\text{OC}(\text{OEt})\text{CHC}(\text{Me})\text{N}(\text{CH}_2)_2^i\text{Pr})(\text{Et}))_2] \text{ (14)}$	172
Table 5.9:	Selected bond lengths (Å) and angles (°) for $[(\text{Zn}(\text{OC}(\text{OEt})\text{CHC}(\text{Me})\text{N}(\text{CH}_2)_2^i\text{Pr})(\text{Et}))_2] \text{ (14)}$	173

List of Abbreviations

Å	Angstrom
AACVD	Aerosol Assisted Chemical Vapour Deposition
acac	Acetylacetonate
Anal.	Analysis
APCVD	Atmospheric Pressure Chemical Vapour Deposition
AZO	Aluminium Doped Zinc Oxide
br	Broad
Calcd.	Calculated
CI	Chemical Ionisation
cm	Centimetre
CVD	Chemical Vapour Deposition
δ	Chemical Shift
DCM	Dichloromethane
DMSO	Dimethyl Sulfoxide
DSC	Differential Scanning Calorimetry
EA	Elemental Analysis
EI	Electron Ionisation
Et	Ethyl
eV	Electron Volts
g	Grams
h	Hour
HSQC	Heteronuclear Single Quantum Correlation
i Pr	Isopropyl
i Bu	Isobutyl
J	Coupling Constant
L _x	Ligand of X
m	Multiplet
Me	Methyl
mL	Millilitre
mmol	Millimole

MOCVD	Metal Organic Chemical Vapour Deposition
mol	Mole
MS	Mass Spectrometry
NIR	Near Infrared
NMR	Nuclear Magnetic Spectroscopy
OEt	Ethoxide
OTf	Trifluoromethanesulfonate
PCT	Patent Cooperation Treaty
ppm	Parts Per Million
q	Quartet
R	Substituent
SEM	Scanning Electron Microscopy
s	Singlet
□	Square
t	Triplet
^t Bu	Tertbutyl
TCO	Transparent Conducting Oxide
TGA	Thermogravimetric Analysis
THF	Tetrahydrofuran
UV	Ultraviolet
Vis	Visible
XPS	X-ray Photoelectron Spectroscopy
XRD	X-ray Diffraction
xs	Excess

Chapter 1

Introduction

In this introduction chapter, the key themes, motivation and background to the work presented in this thesis are given. The properties of zinc oxide (ZnO) are presented with particular attention on how and why the material is of such interest for application. The methods employed for the deposition of ZnO are reviewed with particular focus paid to chemical vapour deposition (CVD), more specifically to aerosol assisted CVD (AACVD), the technique used in this work. The importance of precursor identity in CVD methods is discussed including the key factors and properties that determine the suitability of materials. This chapter concludes with an overview of the work contained in this thesis.

1.1 Zinc Oxide

The material properties of zinc oxide (ZnO) have been studied quite extensively since 1935,¹ although the interest has been quite fluxional over the time period. A recent revival results from renewed interest in the use of ZnO in a number of technologically important areas.² Zinc oxide can exist in three crystal structures: cubic zinc blende; rocksalt and hexagonal wurtzite. At ambient conditions it is the thermodynamically stable hexagonal wurtzite structure with a density of 5.606 g.cm^{-1} belonging to the $P6_3mc$ space group that crystallises,^{3,4} where $a = 3.250 \text{ \AA}$ and $c = 5.206 \text{ \AA}$.⁵ In this hexagonal lattice structure each Zn^{2+} cation and O^{2-} anion have four closest neighbours of O^{2-} anions and Zn^{2+} cations respectively and the structure can be thought of as two interpenetrating hexagonal closed-packed lattices of Zn and O ions,⁵ as shown in Figure 1.1. The c/a ratio is approximately 1.60, deviating slightly from the ideal c/a value of 1.63.⁶ The ionicity of the bonds between the Zn^{2+} and O^{2-} ions is borderline between ionic and covalent character.⁷

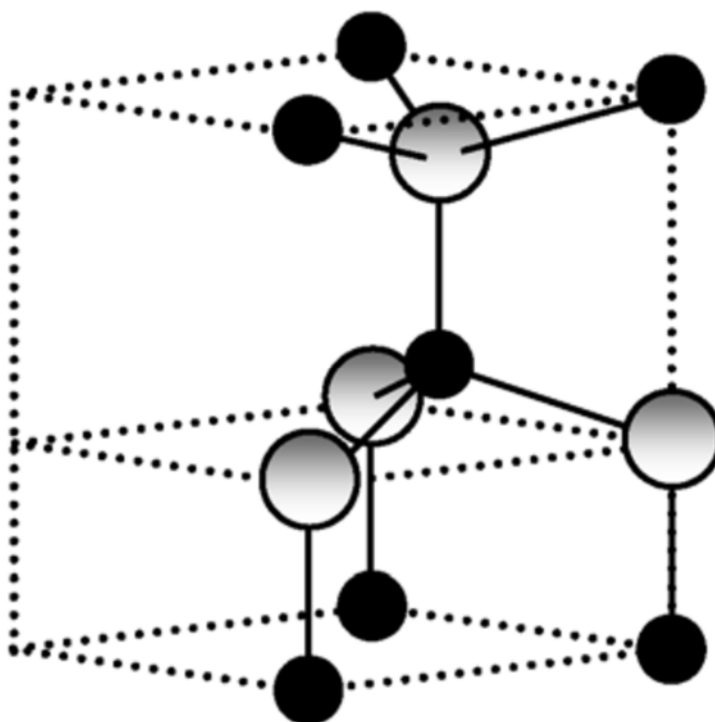


Figure 1.1: Stick and ball diagram of hexagonal wurtzite ZnO.⁸

It is the combination of the semiconducting and optical properties of ZnO that make the material of such interest to many in the research area of modern technology materials.⁹

1.1.1 Semiconductor Properties

Zinc oxide is an intrinsic *n*-type II-VI semiconductor material¹⁰ with a direct wide bandgap of 3.37 eV and a large exciton binding energy of 60 meV at room temperature.¹¹ The semiconductor properties of ZnO result from its electronic band structure which can be described using band theory. The vast number of bonding and antibonding molecular orbitals of the valence electrons (as core electrons are assumed non-interacting) combine to form bands of similar energy molecular orbitals, namely valence and conduction bands. The energy of the highest molecular orbital occupied by electrons at absolute zero (0 K) is called the Fermi Energy (E_f). The filling of the bands and their energy difference determines the electronic properties of the material. Figure 1.2 illustrates the band structure of a conductor, insulator and a semiconductor material.

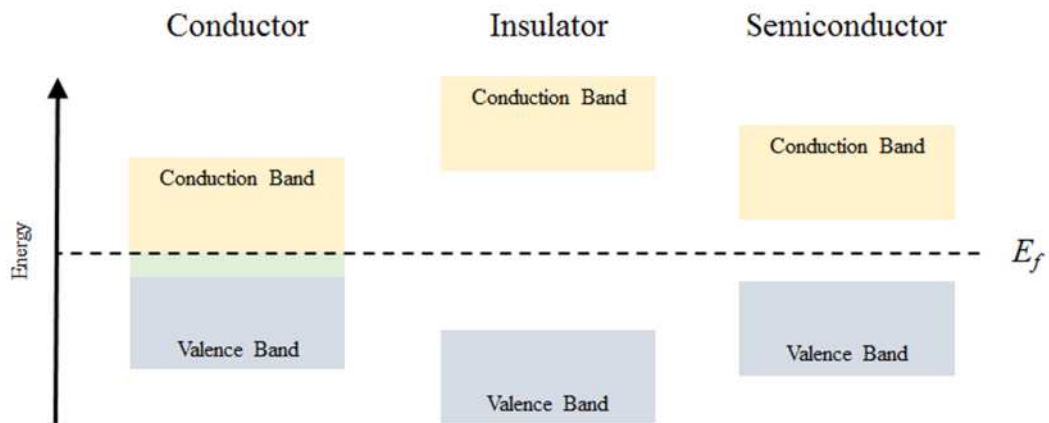


Figure 1.2: Band structures for a conductor, insulator and semiconductor.

In a conductor material, the conduction and valence band either overlap as shown in Figure 1.2 or the material has a partially full band. This means that the E_f is located within a band with the presence of energy levels close to E_f to which electrons can easily be promoted, ensuring conductance. In the case of insulating and semiconductor

materials, the valance band in both are full. Conductance can be achieved with the promotion of electrons from the full valence band to the empty conduction band. It is the magnitude of the energy gap (E_g) which determines into which category the material falls into. The E_g of an insulator is sufficiently large that promotion is not possible, as shown in Figure 1.2. A semiconductor such as ZnO has a small E_g , as shown in Figure 1.2 in which temperature dependant promotion of electrons is possible, leading to conductance. The conductivity of undoped ZnO is highly debated and often attributed to native point defects such as zinc interstitials or oxygen vacancies but computational studies also suggest the unintentional incorporation of hydrogen contributes significantly to the observed conductivity.^{12,13,14,15,16} The conductivity of the ZnO thin films can be increased by intentional doping with an extrinsic dopant source.

1.1.2 Doped Zinc Oxide

Since ZnO is only nominally conductive, an aliovalent extrinsic dopant source is required to increase the conductivity. The dopants can either be substitutional in which they replace atoms of the host material or interstitial, in which case they are located in the space between atoms of the host matrix. These dopants are added in small amounts and since they have different molecular orbitals, they introduce additional bands into the band structure of the material, as shown in Figure 1.3.

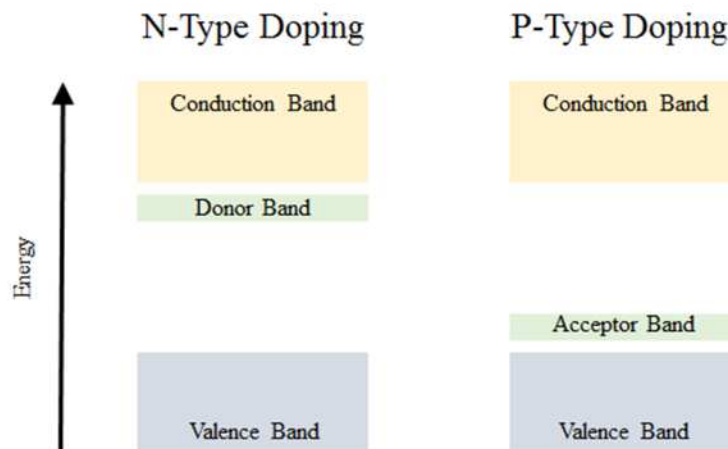


Figure 1.3: Band structures for extrinsic *n*-type and *p*-type doping in semiconductors.

If the dopants have one or more electrons than the host material they are electron donors. These electrons occupy a donor band close to the conduction band and since the charge of the carriers is negative, the material is known as an *n*-type semiconductor. Dopants which are electron deficient compared to the host material are electron acceptors and lead to the presence of positively charged holes. These holes act as positive charge carriers and the material is known as a *p*-type semiconductor. An acceptor band is established close to the valence band which the positive holes will occupy. Other impurities or defects, known as deep level defects can act as traps for carriers in the material and reduce the electronic properties of the films.

ZnO is typically doped with either aluminium or gallium to form aluminium-doped ZnO (AZO) or gallium-doped ZnO (GZO) respectively. Gallium and aluminium both have three valence electrons compared to the two valence electrons of zinc. This leads to *n*-type conductivity with the additional electrons occupying the shallow donor states close to the conduction band of ZnO since the valence band is full. ZnO is one of a small number of materials that can combine high conductivity with high optical transparency in the visible light region, known as a transparent conducting oxide (TCO) material.

1.2 Transparent Conducting Oxide (TCO)

The properties of high transparency in the visible light region and low electrical resistivity are seemingly counterintuitive. However, this is not the case for TCO materials, which are simultaneously highly conductive and highly transparent in the visible light region. ZnO is one such material and in thin film form is the focus of much commercial and academic attention. The zinc oxide film is doped as described above in Section 1.1.2 to improve electrical conductivity. For an *n*-type TCO material, such as ZnO, the conductivity (σ) of the film is related to the electron concentration (N) and electron mobility (μ) according to Equation 1.1, where e is the charge of an electron.

$$\sigma = Ne\mu$$

Equation 1.1

However, the level must be appropriate to maintain the high level of transparency required. TCO materials such ZnO have an $E_g > \sim 3.0 \text{ eV}$ ¹⁷ which allows the material to be transparent to visible light photons. Typically the metal cations in TCO materials are required to have filled d-shells, such as Zn^{2+} , Sn^{4+} , In^{3+} and Ga^{3+} to prevent d-d transitions in the visible light region.¹⁸

The first TCO was reported in 1907 when a sputtered film of cadmium underwent oxidation to form a thin film of CdO.^{19,20} Since then, TCO materials have been extensively researched and employed in many commercial applications. The first TCO material to be commercialised to any significant extent was tin oxide and tin(IV) oxide (SnO_2).²¹ The most commonly used TCO material at present is indium tin oxide (ITO) which is a solid-state mixture of indium(III) oxide (In_2O_3) and SnO_2 in a typical ratio of 90%:10% by oxide mass. However, the use of ITO has become unfavourable and there is an increasing need to replace ITO as the most widely used TCO material.

Firstly, there has been a huge surge in demand for devices such as LCDs, touch panels and solar cells all of which use TCO materials, as described in Section 1.3. Forecasts also suggest the likelihood that this demand is set to continue.²² This raises issues for the continued use of ITO since indium is relatively scarce in the earth's crust, although the degree to which is subject to debate.²³ The instability in the supply of indium is also problematic²⁴ since it is dominated by just two countries, China and Canada and is often procured as a byproduct of zinc mining.²² These factors are reflected in not only a high cost for ITO thin films²⁵ but also significant volatility in their price,²² both of which are commercially highly undesirable.

Alongside these commercial pressures, ITO is also thought to have reached its full potential and with the commercial demands for ever enhanced performance,²⁶ alternative materials are sought. The other physical properties of ITO films such as how the film changes when exposed to environmental or processing elements such as heat²⁷ may also be better with alternative materials. For emerging technologies such as flexible electronics, alternatives to TCO materials such as graphene,²⁸ conductive polymers²⁹ and polymer composites³⁰ are finding their place in the market. However, the potential systems to replace ITO in current applications are other binary doped oxides based on CdO, SnO_2 and ZnO.

The ZnO system offers a number of advantages over both the CdO and SnO₂ systems including higher levels of chemical and mechanical stability such as greater durability to heat and plasma.²⁷ The CdO system is also often deemed unfavourable given that cadmium is toxic,³¹ which is not the case for ZnO or SnO₂. However, the toxicity of many of the precursors for SnO₂ is also a limiting factor which is not as present for the ZnO system.³² Zinc is also abundant, around 1000 times more abundant than indium³³ and as such is inexpensive,³⁴ allowing for significantly lower cost TCO film fabrication. Zinc oxide based TCO films are strongly favoured as having the potential to replace the use of ITO in many of its current applications. Specifically, it is GZO and AZO which exhibit the promising optical, electronic and functional properties and the potential to meet the demands for ever improved film properties from the commercial technology sector.^{35,36,37}

1.3 Applications

The properties of ZnO make it the subject of both commercial and academic attention for use as an essential component in a number of devices of significant technological importance. In addition to the properties described above, when compared to other wide band gap semiconductors, ZnO offers higher thermal and chemical stability as well as high radiation stability^{38,39} Zinc oxide is also more stable in atmospheres with high levels of hydrogen, which often result when thin film solar cells are fabricated.³³

Much of the research on ZnO thin films focuses on optoelectronic applications which result from the nature of the ZnO band gap.⁴⁰ ZnO based thin films have received much attention for their use as transparent front contact electrodes in flat panel displays^{41,42} and thin film solar cells^{7,9,43,44} where they also eliminate shadow effects caused with metal-finger contacts.⁴⁵ For applications such as display panels and photovoltaics, the ZnO based TCO layer acts to transmit the current and signals to the device, transmit the light emitted without resistance and protect the internal device from external environmental factors.²⁷ It has also found use as the anode material in organic light emitting diodes,⁴⁶ and low cost thin film transistor in flexible and invisible electronics⁴⁷ where through the use of ZnO, the coverings preventing light exposure have been made redundant since ZnO is unaffected by light.⁷ ZnO based thin films have also been employed in smart windows in which visible light is transmitted

but the IR radiation is reflected.⁴⁵ The films have also found an important use as a material for blue and UV light emitting and detecting optical devices.¹ This includes low threshold laser development^{38,3} where the large excitation energy of ZnO allows use in simulated emission for lasing applications^{40,48} which has use in advanced data storage systems.³⁸

There is also significant application of ZnO based thin films outside of the optoelectronic area. One of the largest areas is sensing, where ZnO based thin films are used for gas sensing,⁴⁹ biosensors,⁵⁰ surface acoustic wave sensors⁵¹ and piezoelectric transducer sensors.⁵² The application and properties required in the deposited ZnO film are important factors when selecting the deposition method.

1.4 Deposition of ZnO Thin Films

The technique used for the deposition of thin films can greatly affect the structural properties such as grain size and orientation as well as the resulting functional properties of the films such as transparency and carrier mobility.⁵³ All deposition methods have their advantages and their limitations. The method chosen will likely be determined by the processing factors such as cost, size of area required coating and growth rates, as well as the desired film properties including morphology, crystallinity and functional properties. In broad terms, there are three main categories of deposition techniques for ZnO thin films: physical vapour deposition (PVD); solution based methods and chemical vapour deposition (CVD).

1.4.1 Physical Vapour Deposition

A wide variety of physical vapour deposition (PVD) techniques such as electron beam,⁵⁴ reactive,⁵⁵ and thermal evaporation⁵⁶ have been used to deposit ZnO thin films. In PVD techniques, deposition is purely physical involving the transfer of ZnO from a target source onto a substrate. These methods are generally capable of depositing high calibre ZnO based thin films with very respectable physical and TCO properties.⁵⁷ However, PVD methods are expensive and can often only deposit onto limited surface areas. They also require deposition to be carried out under high vacuum in sophisticated reactors which often limits their potential for large-scale practical application. Other factors which can limit their commercial use include the expense of

the ceramic starting targets,⁵⁸ for example those used for pulsed laser deposition, or relatively slow deposition rates, such as those of radio frequency magnetron sputtering.⁵⁹

1.4.2 Solution Based Deposition

Doped thin films of ZnO with promising TCO properties have also been obtained by sol-gel processing, a widely used solution based technique.⁶⁰ Sol-gel is a multi-step process requiring solution mixing/aging before deposition and temperature heating treatment after deposition.⁶¹ The deposition process itself consists of a spin or dip coating followed by drying which is repeated multiple times. As such, the overall process is quite timely. Single step sol-gel prepared ZnO films have been reported but these reports are very limited.⁶² Sol-gel offers the advantages of being low cost, simple and easily controlled.⁶³ Crackability of films deposited by sol-gel can also be an issue⁶⁴ as the drying process causes significant internal stress and volume contraction which, if drying conditions are not highly controlled will allow cracks to easily form.⁶⁵ The technique is also relatively limited for the deposition of TCO thin films as it is not compatible with the industrial float glass process. Zinc precursors for the sol-gel process are metal salts, most typically zinc acetate dehydrate.⁶³

Spray pyrolysis is an alternative solution based method which employs similar solutions to sol-gel which are transformed into droplets and sprayed onto a heated substrate to form a thin film. As with sol-gel, zinc acetate dihydrate is the most widely used precursor⁶⁶ and although other salts such as zinc nitrate⁶⁷ have been used, there have been very limited investigation into the nature of the precursor for this process.⁶⁸ Another major technique with a number of advantages for the deposition of ZnO thin films is chemical vapour deposition (CVD).

1.4.3 Chemical Vapour Deposition

CVD is a thin film deposition technique in which all the reactant species required arrive in the reaction chamber in the vapour phase. The precursors undergo chemical reaction leading to the deposition of a thin film of desired material according to Figure 1.4. The process initiates upon delivery of the precursors in a carrier gas, which may

first undergo a reaction to form intermediate gas-phase species. These reactant species reach the heated substrate and upon physisorption to the substrate surface, undergo heterogeneous chemical reactions to form molecules of the desired material. The molecules are weakly bound to the surface and can move to sites of lower energy before chemisorption occurs, leading to nucleation and growth of a thin film. Any unreacted precursor and the by-products of the reaction are removed in the gas phase and carried *via* the carrier gas to the chamber exhaust.

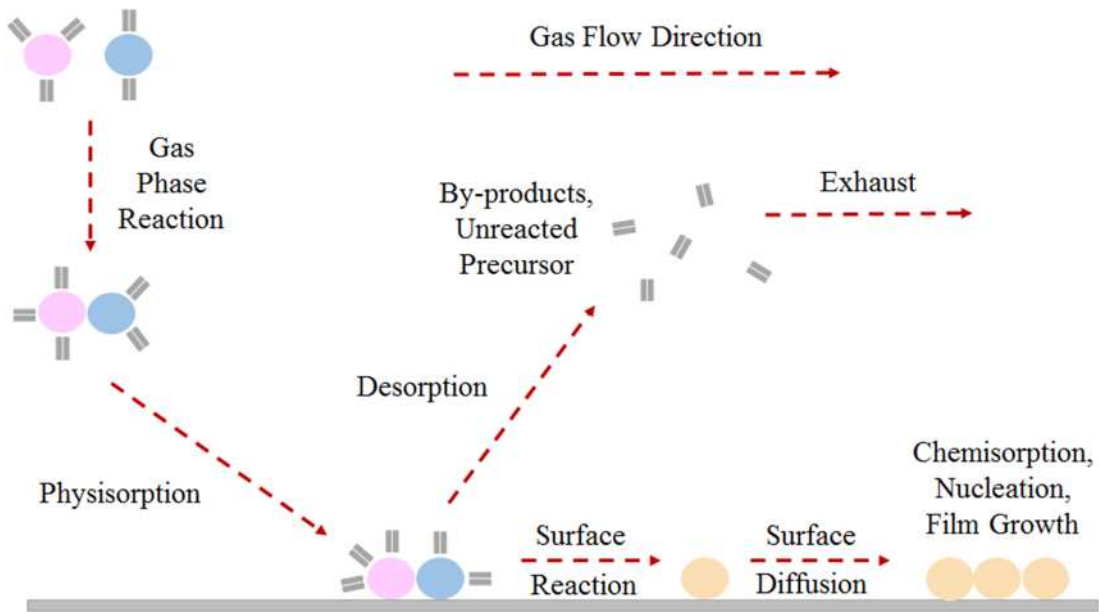


Figure 1.4: Steps of the CVD process.

The rate limiting step of film growth in CVD is dependent on the temperature of the system. When the substrate temperature is low, it is the chemical kinetics that determine film growth. The rate of growth increases exponentially according to the Arrhenius expression given as Equation 1.2, where A is a pre-exponential factor, E_A is the activation energy, R is the gas constant and T is substrate temperature.⁶⁹

$$\text{Growth Rate} = A \exp(E_A/RT)$$

Equation 1.2

As the substrate temperature increases, the growth rate becomes mass transport (diffusion) limited. In this region, the growth rate is independent of the substrate

temperature but is instead dependant on the delivery of the precursor to the substrate surface. This requires diffusion through a reactant concentration boundary layer which forms above the surface of the substrate. This growth region is ideal for CVD in a cold-walled system since substrate temperature can vary at different points in the reactor. At higher deposition temperatures, above the mass transport limited growth region, the growth rate is observed to decrease as a result of reactant desorption and depletion of reactant.

The reactions which occur in the CVD process are involved and intricate, requiring careful observation and regulation of the system parameters, including substrate temperature, gas-flow and reactant gas concentration.⁷⁰ The gas flow in the CVD system should be laminar, as turbulent flow can lead to the homogenous gas phase reactions and the formation of fine particles as opposed to thin films.⁷¹ The Reynolds number, Re , given in Equation 1.3, where ρ is the density, v is the velocity, L is the flow length inside the reactor and μ is the viscosity, is used to describe the flow through the CVD reactor.

$$Re = \rho v L / \mu \quad \text{Equation 1.3}$$

A low Reynolds number (< 100) indicates laminar flow whilst a high Reynolds number (> 2100) indicates a system with turbulent flow.⁷⁰ The flow will have an effect on the efficiency of the system as well as the uniformity and defect concentration in the deposited film.

CVD is an industrially favourable technique in that films tend to be conformal, reproducible, adherent and inexpensive.⁷² The technique offers the advantages of scalability in being able to cover large surface areas with good control of the film thickness and high growth rates. An additional crucial advantage is also the ease in which a dopant can be incorporated into the film.⁷³ Deposition costs are also middling compared to other systems since unlike PVD methods, the use of a vacuum is not required but the use of a sophisticated reactor is. These reactors can take a number of forms which introduces some additional flexibility into the system. For example the walls of the CVD chamber can be heated or cold and the substrate can be vertical or

horizontal and dynamic or still. Depositions discussed in this thesis were deposited using a horizontal, cold-walled reactor system, which is described in Chapter 2.3.2.1. It is for these reasons that CVD has become a widely used film deposition technique in industry, including at NSG Pilkington, in areas such as float-glass coatings.

However, the use of CVD in its conventional form at atmospheric pressure (APCVD) is somewhat hindered by the lack of suitable precursor material. APCVD relies on the thermal evaporation of the precursor to enable it to enter the gas phase. To allow for this and to avoid incomplete decomposition and problematic delivery, a precursor must have a high vapour pressure and low decomposition temperature.⁷⁴ This is quite often not the case and in order to overcome these requirements the CVD process has been adapted in a number of ways. These changes include, reducing the pressure of the system, providing external energy such as a plasma or flame to aid precursor decomposition or adapting the way the precursor is delivered. Examples of adapted systems include: low pressure LP(CVD),⁷⁵ plasma enhanced (PE)CVD,⁷⁶ combustion (C)CVD⁷⁷ and aerosol assisted (AA)CVD.⁷⁸ AACVD is the technique which has been used for all depositions described in this thesis.

1.4.3.1 Aerosol Assisted Chemical Vapour Deposition

The fundamental difference in AACVD compared to other CVD systems is how the precursor is delivered to the CVD chamber. The precursor is dissolved in an appropriate solvent which eliminates the restrictions that a precursor must be volatile and thermally stable.⁷⁹ Ultrasonic waves from a piezoelectric transducer are used to form waves in the precursor solution which cause fine droplets of precursor solution to be released which in such high numbers allow for the formation of an aerosol. The aerosol is then carried into the reaction chamber in a carrier gas where the heat causes the solvent to evaporate leaving the reactant molecules in the gas phase to undergo a reaction as per the system described in Section 1.4.3. With solubility in a suitable solvent replacing the volatility requirement,⁸⁰ the range of potentially applicable precursors⁸¹ increases significantly.

AACVD also offers a low cost route to thin films with a high deposition rate, increased flexibility of the deposition conditions,⁸² ability to operate under a range of pressures⁷¹ and allows for ease of doping of the deposited thin films.⁸³ The set-up is also simplified

as the lines to the CVD chamber in thermal CVD routes need heating in order to ensure the precursor does not deposit early, however, this is not required with AACVD.

The use of solvent in AACVD can also open up additional challenges such as the possible incorporation of solvent fragments into a film.⁸⁴ However, some investigators have found this route can offer significant potential for altering the quality and performance of deposited materials.²⁶ For example, identity of the solvent has been found to result in the deposition of films of differing morphologies.⁸⁵ Solvent identity has also been shown to change the crystallographic phase of deposited thin films deposited. Edusi *et al.*⁸⁶ found that that TiO₂ films on steel from titanium isopropoxide in methanol resulted in rutile TiO₂ films but when in alternative solvents such as hexane and ethanol, anatase TiO₂ films were deposited.

Unlike other variations of CVD such as APCVD, AACVD has not be scaled up for industrial use and remains quite a niche route towards ZnO thin films. However, this method is of industrial interest and Carmalt *et al.*⁸⁷ are investigating taking the technique to a large pilot reactor scale. The increasing use and interest in employing CVD routes to thin films has also driven interest in the use of different precursors and how they can be designed and their properties tailored.⁸⁴

1.5 CVD Precursors

The adaption and evolution of the CVD method illustrates the versatility of this technique and has greatly contributed to the production of films with desired properties at a reasonable cost and with relative simplicity. The chemistry of the precursor also has a major role in achieving this aim. As has been shown above, PVD methods tend to rely on ZnO targets and solution based methods on a number of relatively limited and simple solutions. In CVD however, the precursor has a more sophisticated role and as such, requires greater consideration.

1.5.1 Desired Precursor Properties

As discussed in Section 1.4.3.1, precursors used in thermal CVD routes must be thermally stable and volatile. The volatility of a precursor can be established accurately by determining its vapour pressure. However, the thermal gravimetric

analysis (TGA) technique which measures the mass loss of a sample upon heating is also widely used to indicate the potential volatility of a precursor. The precursor should not decompose before evaporation and there should be a sufficiently large separation between the temperature of evaporation and the temperature of decomposition.⁶⁹ The thermal stability of compounds can be determined using differential scanning calorimetry (DSC) in which the changes in heat flow are measured as a sample is heated. The CVD process has been adapted into many variations since many liquid and solid precursors do not exhibit these properties. In AACVD, precursors do not have to exhibit these properties. If they are soluble in an appropriate solvent then they do not need to be volatile or conform to the thermal properties described since they are delivered to the reaction chamber in their carrier solvent. However, there are also a number of other characteristics that a precursor would ideally exhibit and these have been set out by Jones and Hitchman⁶⁹ who state the ideal CVD precursor would:

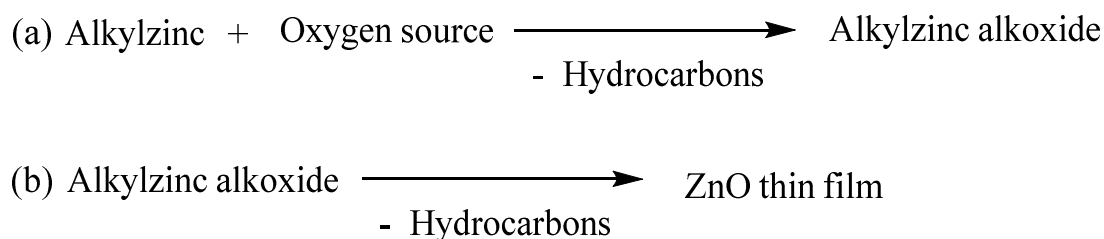
- I. Have a high chemical purity – Precursors which are not chemically pure run the risk of their impurities becoming incorporated in the deposited film resulting in a change to their properties. This is especially true for TCO films where even very small levels of impurity can dramatically affect the functional properties of the deposited film.
- II. Undergo clean decomposition without the incorporation of residual impurities – The ligand system will play an important role in the availability of clean decomposition such as the availability for β -hydride elimination. Impurities will be incorporated when a precursor does not undergo a clean decomposition and where organometallic complexes are used, this will quite often lead to high levels of carbon contamination.
- III. Be of good compatibility with co-precursors – The precursor must not only be suitable for the deposition method but also be suitable for use alongside the other reactants in the system. For example, it might be difficult to use two precursors together if their thermal properties vary wildly.
- IV. Have a long shelf life with indefinite stability under ambient conditions – The additional requirement for precursors which are not stable in air or degrade over time may prohibit their use.

- V. Be readily manufactured in high yield at low cost – It is important for commercialisation and manufacturing purposes that the synthesis of a precursor is a simple and low cost procedure.
- VI. Have a low or non-existent hazard risk – The use of toxic or pyrophoric precursors is less than ideal due to the risks involved and the issues around safety and precursor handling that will arise.

The properties are often interconnected and can also be dependent on deposition conditions. Jones⁸⁸ has previously noted that it is highly unlikely that a single precursor will demonstrate all of these properties and that the choice of precursor system will often be a compromise. This is certainly the case for ZnO precursors. The precursor routes towards ZnO films can be divided into two categories: dual-source or single-source.

1.5.2 Dual – Source Precursors

The most widely used precursor for ZnO thin films are alkylzinc compounds, typically diethylzinc, $[\text{Zn}(\text{Et})_2]$.^{89,90,91} Since alkylzinc compounds contains only zinc, carbon and hydrogen atoms an additional precursor acting as an oxygen source is also required. The reaction is termed dual-source since the constituents of the desired ZnO material come from two different precursors. The general reaction of an alkylzinc compound and an oxygen source is shown in Scheme 1.1.



Scheme 1.1: Dual-source reaction to form a ZnO thin film.

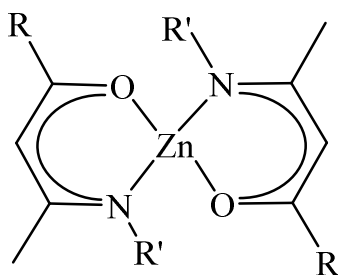
The reaction proceeds *via* the *in situ* formation of alkylzinc alkoxides which decompose to form ZnO thin films. This reaction, including the variety of oxygen sources is discussed in greater detail in Chapter 3. Before decomposition to ZnO, the

reactions of diethylzinc and organic ligands often leads to intermediate products which have highly interesting structures. These reactions form the basis of investigations covered in Chapter 4.

The zinc source for dual-source systems is often readily available commercially and these commercially available zinc complexes have been discussed and reviewed in Chapter 3.1. However, the dual-source precursor approach can complicate the overall deposition process. For example, the required mixing of precursors before reactions gives rise to the opportunity for undesired pre-reactions. It also serves to complicate the delivery system which has to accommodate for the delivery of multiple precursors as opposed to just one. As such, in recent years there has been a move towards the use of single-source precursors for the advantages that they offer.

1.5.3 Single – Source Precursors

Precursors which contain all the required elements of the desired end material in one molecule are termed single-source. These precursors contain the preformed M-O bond, for example single-source precursors for ZnO will contain Zn-O bonds. The β -ketoiminate and β -iminoesterate complexes⁹² shown in Figure 1.5 are an example of such compounds and are discussed in detail in Chapter 5.



(a) R = Me, R' = ⁿBu, (b) R = OEt, R' = ⁱPr

Figure 1.5: Single-source zinc β -ketoiminate and β -iminoesterate complex.⁹²

However, some commercial and synthesised precursors such as zinc acetate which do contain preformed Zn-O bonds are often used with an additional oxygen source in order to increase the oxygen available for reaction.⁹³ Single-source precursors offer a

number of advantages including often improved stability to air and moisture, lower toxicity and greater control over the stoichiometry with fewer defects in the resulting films.^{94,95} Single-source precursors also offer a simpler route to thin films and eliminate the need for precursor mixing, affording fewer opportunities for pre-reactions.⁹⁶ Depositions are also often carried out at a lower temperature as a result of the desired Zn-O bond already being present in the precursor molecule.⁹⁷ Single-source precursors are also often simple and their properties can be ‘tailored’ by altering the ligands on relevant moieties in the system. However, single-source precursors are often not available commercially and require synthesis.

1.5.4 Zinc Precursors

The use of specific zinc precursors has not been presented in this general introduction but are instead discussed in the relevant chapters throughout this thesis. The widely used and commercially available precursors including diethylzinc and zinc acetylacetonate have been reviewed in Chapter 3 as part of the introduction to the use of zinc triflate [Zn(OTf)₂] as a commercially available precursor for ZnO thin films. Zinc precursors are also regularly synthesised either *in situ* or isolated using a range of solution based techniques. An emerging alternative is mechanochemistry, a review of which is provided by James *et al.*⁹⁸ but is beyond the scope of this thesis. An overview of zinc oxane complexes as potential ZnO precursors is given in Chapter 4 whilst zinc β -ketoiminates and β -iminoesterates which exhibit significant promise for use as single-source precursors are discussed in detail in Chapter 5.

1.6 Overview of Thesis

This chapter serves as an introduction to ZnO, its properties and the motivation and context for the work presented in this thesis. Since there is common experimental content in terms of the synthesis, deposition and characterisation of precursors and thin films in the results chapters, all experimental details have been presented in Chapter 2. The results are presented in three chapters, each of which focuses on a precursor of a different nature:

- Chapter 3 reports the novel use of $[\text{Zn}(\text{OTf})_2]$ as a commercially available precursor for the AACVD of ZnO and aluminium-doped ZnO thin films.
- Chapter 4 presents the synthesis of zinc oxane trimers from the reaction of diethylzinc and dicarbonyl compounds. Selective oxidations of these complexes to zinc oxane clusters is presented, one of which was employed as a precursor in the AACVD of ZnO thin films.
- Chapter 5 reports the successful synthesis of zinc β -iminoesterate complexes of two structural types. Monomeric zinc β -iminoesterates were found to be air-stable and a comparative AACVD study of two of these complexes is presented in which ZnO thin films were successfully deposited.

A conclusion of this work is given in Chapter 6 which draws together the results presented in this thesis and summarises the future prospects.

1.7 Conclusion

This chapter has presented the properties of ZnO and described its technological importance in a range of applications. The techniques used to deposit ZnO have been introduced with particular emphasis on CVD and more specifically AACVD, the technique used throughout this thesis. The identity of a precursor is a highly important factor in CVD and one this thesis is heavily focused on. The properties of an ideal precursor have been described alongside other important factors and considerations such as the opportunities and benefit single-source precursors might offer. The chapter concludes with an overview of the work presented in this thesis.

1.8 References

1. V. A. Coleman and C. Jagadish, in *Zinc Oxide Bulk, Thin Films and Nanostructures*, ed. C. Jagadish and S. Pearton, Elsevier, 2006, pp. 1 – 20.
2. A. B. Djurišić, X. Chen, Y. H. Leung and A. Man Ching Ng, *J. Mater. Chem.*, 2012, **22**, 6526 – 6535.
3. S. J. Pearton, D. P. Norton, K. Ip, Y. W. Heo and T. Steiner, *Superlattices Microstruct.*, 2003, **34**, 3 – 32.
4. A. Gurlo, *Nanoscale*, 2011, **3**, 154 – 165.
5. G. Walters, and I. P. Parkin, *I. P. Appl. Surf. Sci.*, 2009, **255**, 6555 – 6560.
6. C. Klingshirn, *Phys. Status Solidi B*, 2007, **244**, 3027 – 3073.
7. Ü. Özgür, Y. I. Alivov, C. Liu, A. Teke, M. A. Reshchikov, S. Doğan, V. Avrutin, S.-J. Cho and H. Morkoç, *J. Appl. Phys.*, 2005, **98**, 041301(1) – 041301(103).
8. H. Morkoç and Ü. Özgür, in *Zinc Oxide: Fundamentals, Materials and Device Technology*, ed. H. Morkoç and Ü. Özgür, Wiley-VCH, 2009, pp. 1 – 76.
9. C. Woll, *Prog. Surf. Sci.*, 2007, **82**, 55 – 120.
10. N. R. Aghamalyan, I. A. Gambaryan, E. K. Goulanian, R. K. Hovsepyan, R. B. Kostanyan, S. I. Petrosyan, E. S. Vardanyan, and A. F. Zerrouk, *Semicond. Sci. Technol.*, 2003, **18**, 525 – 529.
11. S. T. Tan, B. J. Chen, X. W. Sun, W. J. Fan, H. S. Kwok, X. H. Zhang and S. J. Chua, *J. Appl. Phys.*, 2005, **98**, 013505(1) – 013505(5).
12. F. Oba, S. R. Nishitani, S. Isotani, H. Adachi and I. Tanaka, *J. Appl. Phys.*, 2001, **90**, 824 – 828.
13. G. D. Mahan, *J. Appl. Phys.*, 1983, **54**, 3825 – 3832.
14. A. B. Usseinov, E. A. Kotomin, A. T. Akilbekov, Y. F. Zhukovskii and J. Purans, *Phys. Scr.*, 2014, **89**, 045801(1) – 045801(7).
15. C. G. Van de Walle, *Phys. Rev. Lett.*, 2000, **85**, 1012 – 1015.
16. A. Janotti and C. G. Van de Walle, *Rep. Prog. Phys.*, 2009, **72**, 126501(1) – 126501(29).
17. A. Klein, C. Korber, A. Wachau, F. Sauberlich, Y. Gassenbauer, S. P. Harvey, D. E. Proffit and T. O. Mason, *Materials*, 2010, **3**, 4892 – 4914.
18. C. A. Hoel, T. O. Mason, J.-F. Gaillard and K. R. Poeppelmeier, *Chem. Mater.*, 2010, **22**, 3569 – 3579.
19. K. Bädcker, *Ann. Phys.*, 1907, **327**, 749 – 766.
20. Z. Zhao, D. L. Morel and C. S. Ferekides, *Thin Solid Films*, 2002, **413**, 203 – 211.
21. K. L. Chopra, S. Major and D. K. Pandya, *Thin Solid Films*, 1983, **102**, 1 – 46.
22. D. S. Hecht, L. Hu, L. and G. Irvin, *Adv. Mater.*, 2011, **23**, 1482 – 1513.
23. X. Chen, W. Guan, G. Fang and X. Z. Zhao, *Appl. Surf. Sci.*, 2005, **252**, 1561 – 1567.
24. T. Minami, *Thin Solid Films*, 2008, **516**, 5822 – 5828.
25. Y. Liu and J. Lian, *Appl. Surf. Sci.*, 2007, **253**, 3727 – 3730.
26. N. Noor and I. P. Parkin, *J. Mater. Chem. C*, 2013, **1**, 984 – 996.
27. S. Park, J. Park, Y. Z. Yoo, J. Y. Lee, S. H. Kim, G. S. Yoon, M. W. Kim, H. S. Shin, S. H. Yoo, S. D. Lee, S. I. Lee and S. J. Yim, 2014, Patent EP2719795A1, CN103710680A and US2014009443.
28. S. Bae, H. Kim, Y. Lee, X. Xu, J.-S. Park, Y. Zheng, J. Balakrishnan, T. Lei, H. R. Kim, Y. I. Song, Y.-J. Kim, K. S. Kim, B. Özyilmaz, J.-H. Ahn, B. H. Hong and S. Iijima, *Nat. Nanotechnol.*, 2010, **5**, 574 – 578.

29. H. Yan, T. Jo and H. Okuzaki, *Polym. J.*, 2009, **41**, 1028 – 1029.
30. J. Park, A. Lee, Y. Yim and E. Han, *Synth. Met.*, 2011, **161**, 523 – 527.
31. T. J. Coutts, D. L. Young, X. Li, W. P. Mulligan and X. Wu, *J. Vac. Sci. Technol. A*, 2000, **18**, 2646 – 2660.
32. H. Liang and R. G. Gordon, *J. Mater. Sci.*, 2007, **42**, 6388 – 6399.
33. K. Ellmer, *J. Phys. Appl. Phys.*, 2001, **34**, 3097 – 3108.
34. H. Kim, J. S. Horwitz, S. B. Qadri and D. B. Chrisey, *Thin Solid Films*, 2002, **420 – 421**, 107 – 111.
35. M. Chen, Z. L. Pei, X. Wang, C. Sun and L. S. Wen, *J. Vac. Sci. Technol. A*, 2001, **19**, 963 – 970.
36. J. L. Zhao, X. W. Sun, H. Ryu and Y. B. Moon, *Opt. Mater.*, 2011, **33**, 768 – 772.
37. T. Minami and T. Miyata, *Thin Solid Films*, 2008, **517**, 1474 – 1477.
38. A. Mahmood, N. Ahmed, Q. Raza, T. M. Khan, M. Mehmood, M. M. Hassan and N. Mahmood, *Phys. Scr.*, 2010, **82**, 065801(1) – 065801(8).
39. D. Bekermann, D. Rogalla, H.-W. Becker, M. Winter, R. A. Fischer and A. Devi, *Eur. J. Inorg. Chem.*, 2010, **9**, 1366 – 1372.
40. S. K. Arya, S. Saha, J. E. Ramirez-Vick, V. Gupta, S. Bhansali and S. P. Singh, *Anal. Chim. Acta*, 2012, **737**, 1 – 21.
41. L. Hadjeris, L. Herissi, M. B. Assouar, T. Easwarakhanthan, J. Bougdira, N. Attaf and M. S. Aida, *Semicond. Sci. Technol.*, 2009, **24**, 035006(1) – 035006(6).
42. M. Chen, Z. L. Pei, C. Sun, J. Gong, R. F. Huang, L. S. Wen, *Mater. Sci. Eng. B*, 2001, **85**, 212 – 217.
43. J. Hüpkens, B. Rech, S. Calnan, O. Kluth, U. Zastrow, H. Siekmann and M. Wuttig, *Thin Solid Films*, 2006, **502**, 286 – 291.
44. S. Venkatachalam, Y. Iida and Y. Kanno, *Superlattices Microstruct.*, 2008, **44**, 127 – 135.
45. C. Klingshirn, *ChemPhysChem*, 2007, **8**, 782 – 803.
46. H. Kim, J. S. Horwitz, W. H. Kim, A. J. Mäkinen, Z. H. Kafafi and D. B. Chrisey, *Thin Solid Films*, 2002, **420 – 421**, 539 – 543.
47. E. M. C. Fortunato, P. M. C. Barquinha, A. C. M. B. G. Pimentel, A. M. F. Gonçalves, A. J. S. Marques, L. M. N. Pereira and R. F. P. Martins, *Adv. Mater.*, 2005, **17**, 590 – 594.
48. S. Cho, J. Ma, Y. Kim, Y. Sun, G. K. L. Wong, J. B. Ketterson, *Appl. Phys. Lett.*, 1999, **75**, 2761 – 2763.
49. M. A. Chougule, S. Sen and V. B. Patil, *Ceram. Int.*, 2012, **38**, 2685 – 2692.
50. K. Jindal, M. Tomar and V. Gupta, *Analyst*, 2013, **138**, 4353 – 4362.
51. Y. Wang, X. Chen, L. Wang, S. Yang and Z. Feng, *Phys. Procedia*, 2011, **18**, 85 – 90.
52. A. Kuoni, R. I. Holzherr, M. Boillat and N. F. de Rooij, *J. Micromech. Microeng.*, 2003, **13**, S103 – S107.
53. M. Purica, E. Budianu, E. Rusu, M. Danila and R. Gavrilă, *Thin Solid Films*, 2002, **403 – 404**, 485 – 488.
54. D. C. Agarwal, R. S. Chauhan, A. Kumar, D. Kabiraj, F. Singh, S. A. Khan, D. K. Avasthi, J. C. Pivin, M. Kumar, J. Ghatak and P. V. Satyam, *J. Appl. Phys.*, 2006, **99**, 123105(1) – 123105(7).
55. J. S. Oyola, J. M. Castro and G. Gordillo, *Sol. Energ. Mat. Sol. C.*, 2012, **102**, 137 – 141.

56. O. Fouad, A. Ismail, Z. Zaki and R. Mohamed, *Appl. Catal. B*, 2006, **62**, 144 – 149.
57. X. Jiang, F. L. Wong, M. K. Fung and S. T. Lee, *Appl. Phys. Lett.*, 2003, **83**, 1875 – 1877.
58. Y. Liu and J. Lian, *Appl. Surf. Sci.*, 2007, **253**, 3727 – 3730.
59. J. Tsujino, N. Homma, T. Sugawara, I. Shimono and Y. Abe, *Thin Solid Films*, 2002, **407**, 86 – 91.
60. Z. Pan, P. Zhang, X. Tian, G. Cheng, Y. Xie, H. Zhang, X. Zeng, C. Xiao, G. Hu, Z. Wei, *J. Alloys Compd.*, 2013, **576**, 31 – 37.
61. S. Salam, M. Islam and A. Akram, *Thin Solid Films*, 2013, **529**, 242 – 247.
62. S. O'Brien, L. H. K. Koh and G. M. Crean, *Thin Solid Films*, 2008, **516**, 1391 – 1395.
63. L. Znaidi, *Mater. Sci. Eng. B*, 2010, **174**, 18 – 30.
64. M. Guglielmi, *J. Sol-Gel Sci. Technol.*, 1997, **8**, 443 – 449.
65. D. Wang and G. P. Bierwagen, *Prog. Org. Coat.*, 2009, **64**, 327 – 338.
66. F. Zahedi, R. S. Dariani and S. M. Rozati, *Mater. Sci. Semicond. Process.*, 2013, **16**, 245 – 249.
67. S. A. Studenikin, N. Golego and M. Cocivera, *J. Appl. Phys.*, 1998, **83**, 2104 – 2111.
68. E. Bacaksiz, M. Parlak, M. Tomakin, A. Özçelik, M. Karakzi and M. Altunbaş, *J. Alloys Compd.*, 2008, **466**, 447 – 450.
69. A. C. Jones and M. L. Hitchman, in *Chemical Vapour Deposition: Precursors, Processes and Applications*, ed. A. C. Jones and M. L. Hitchman, Royal Society of Chemistry, 2009, pp. 1 – 36.
70. K. L. Choy, *Prog. Mater. Sci.*, 2003, **48**, 57 – 170.
71. X. Hou and K. L. Choy, *Chem. Vap. Depos.*, 2006, **12**, 583 – 596.
72. S. Basharat, C. J. Carmalt, R. Palgrave, S. A. Barnett, D. A. Tocher and H. O. Davies, *J. Organomet. Chem.*, 2008, **693**, 1787 – 1796.
73. T. A. Polley, W. B. Carter and D. B. Poker, *Thin Solid Films*, 1999, **357**, 132 – 136.
74. L. G. Bloor, J. A. Manzi, R. Binions, I. P. Parkin, D. Pugh, A. Afonia, C. S. Blackman, S. Sathasivam and C. J. Carmalt, *Chem. Mater.*, 2012, **24**, 2864 – 2871.
75. S. Faÿ, U. Kroll, C. Bucher, E. Vallat-Sauvain and A. Shah, *Sol. Energ. Mat. Sol. C.*, 2005, **86**, 385 – 397.
76. Y. Ito, O. Sakai and K. Tachibana, *Thin Solid Films*, 2010, **518**, 3513 – 3516.
77. T. A. Polley and W. B. Carter, *Thin Solid Films*, 2001, **384**, 177 – 184.
78. M. R. Waugh, G. Hyett and I. P. Parkin, *Chem. Vap. Depos.*, 2008, **14**, 366 – 372.
79. C. E. Knapp, A. Kafizas, I. P. Parkin and C. J. Carmalt, *J. Mater. Chem.*, 2011, **21**, 12644 – 12649.
80. R. G. Palgrave and I. P. Parkin, *J. Am. Chem. Soc.*, 2006, **128**, 1587 – 1597.
81. P. Marchand, I. A. Hassan, I. P. Parkin and C. J. Carmalt, *Dalton Trans.*, 2013, **42**, 9406 – 9422.
82. R. Dharmadasa, A. A. Tahir and K. G. U. Wijayantha, *J. Am. Ceram. Soc.*, 2011, **94**, 3540 – 3546.
83. C. Piccirillo, R. Binions and I. P. Parkin, *Eur. J. Inorg. Chem.*, 2007, **25**, 4050 – 4055.
84. L. McElwee-White, *Dalton Trans.*, 2006, **45**, 5327 – 5333.

-
85. I. A. Hassan, A. Ratnasothy, D. S. Bhachu, S. Sathasivam and C. J. Carmalt, *Aust. J. Chem.*, 2013, **66**, 1274 – 1280.
 86. C. Edusi, G. Sankar and I. P. Parkin, *Chem. Vap. Depos.*, 2012, **18**, 126 – 132.
 87. C. J. Carmalt, *Sustainable Manufacturing of Transparent Conducting Oxide (TCO) Inks and Thin Films*, 2014, EPSRC Grant, EP/L017709/1.
 88. A. C. Jones, *J. Mater. Chem.*, 2002, **12**, 2576 – 2590.
 89. J. Hu and R. G. Gordon, *J. Appl. Phys.*, 1992, **72**, 5381 – 5392.
 90. H. Li, H. Liu, J. Wang, S. Yao, X. Cheng, R. I. Boughton, *Mater. Lett.*, 2004, **58**, 3630 – 3633.
 91. D. S. Bhachu, G. Sankar and I. P. Parkin, *Chem. Mater.*, 2012, **24**, 4704 – 4710.
 92. J. S. Matthews, O. O. Onakoya, T. S. Ouattara and R. J. Butcher, *Dalton Trans.*, 2006, **31**, 3806 – 3811.
 93. J. S. Kim, H. A. Marzouk, P. J. Reucroft and C. E. Hamrin, *Thin Solid Films*, 1992, **217**, 133 – 137.
 94. M. A. Malik, M. Afzaal and P. O'Brien, *Chem. Rev.*, 2010, **110**, 4417 – 4446.
 95. K. Ramasamy, V. L. Kuznetsov, K. Gopal, M. A. Malik, J. Raftery, P. P. Edwards and P. O'Brien, *Chem. Mater.*, 2013, **25**, 266 – 276.
 96. L. G. Bloor, C. J. Carmalt and D. Pugh, *Coord. Chem. Rev.*, 2011, **255**, 1293 – 1318.
 97. P. Marchand and C. J. Carmalt, *Coord. Chem. Rev.*, 2013, **257**, 3202 – 3221.
 98. S. L. James, C. J. Adams, C. Bolm, D. Braga, P. Collier, T. Friščić, F. Grepioni, K. D. M. Harris, G. Hyett, W. Jones, A. Krebs, J. Mack, L. Maini, A. G. Orpen, I. P. Parkin, W. C. Shearouse, J. W. Steed and D. C. Waddell, *Chem. Soc. Rev.*, 2012, **41**, 413 – 447.

Chapter 2

Experimental Procedures

*This chapter serves to report the experimental details for the synthesis, characterisation and depositions presented in this thesis. The first section describes the experimental procedures used to synthesise the ligands (**L1**) – (**L4**) and complexes (**1**) – (**14**) reported and the details of their characterisation. The second section describes the AACVD technique employed and the successful characterisation of the films deposited from both the synthesised complexes and the commercially available zinc triflate precursor.*

2.1 Introduction

In this thesis, 14 zinc complexes, (**1**) – (**14**) and four ligands, (**L1**) – (**L4**) have been synthesised and zinc oxide (ZnO) thin films have been deposited from both commercial and synthesised precursors. This chapter contains two main sections, the first of which presents the experimental procedures and details for the 14 synthesised complexes and four synthesised ligands. These are reported in the order as they are presented in this thesis, firstly the zinc oxane complexes reported in Chapter 4, followed by the β -iminoester ligands and subsequent zinc β -iminoesterate complexes discussed in Chapter 5. The second main section discusses the set-up and procedures used for the deposition and characterisation of the doped and undoped ZnO thin films deposited by aerosol assisted chemical vapour deposition (AACVD). This includes the thin films deposited using zinc triflate, $[\text{Zn}(\text{OTf}_2)_2]$ in Chapter 3, zinc oxane complexes in Chapter 4 and zinc β -iminoesterate complexes in Chapter 5 as novel AACVD precursors.

2.2 Synthesis

2.2.1 General Procedures

Caution: Diethylzinc is a pyrophoric substance which may ignite spontaneously in air. All manipulations involving the formation of the zinc complexes were performed under a dry dinitrogen atmosphere using standard Schlenk line techniques or in a Mbraun glovebox. All solvents used were stored in alumina columns and dried with anhydrous engineering equipment, such that water concentrations were less than 10 ppm.

Diethylzinc was obtained by Sigma Aldrich in a Sure-PacTM system and stored in a glovebox. Diethylzinc (1M solution in hexanes) and diethylzinc (15 wt.% in toluene) were obtained from Sigma Aldrich and stored under nitrogen. Methyl acetoacetate, acetylacetone, ethyl acetoacetate, and *tert*-butyl acetoacetone were obtained from Sigma Aldrich, degassed *via* the freeze-pump-thaw technique and stored over activated molecular sieves. Isopropylamine, methylamine solution (33 wt.% in absolute ethanol), isobutylamine, isopentylamine and K-10 montmorillonite clay were obtained from Sigma Aldrich and used as supplied. The synthesised β -iminoester

ligands (**L1**) - (**L4**) discussed and used as reactants in Chapter 5 were also degassed *via* the freeze-pump-thaw technique and stored over activated molecular sieves.

2.2.2 Characterisation Measurements

^1H and ^{13}C NMR spectra were obtained on a Bruker Avance III 600 cryo spectrometer and were recorded in CDCl_3 or C_6D_6 as stated. The C_6D_6 solvent was degassed *via* the freeze-pump-thaw technique and stored over activated molecular sieves. ^1H and ^{13}C chemical shifts are reported relative to SiMe_4 (δ 0.00). Variable temperature ^1H NMR was obtained on a Bruker Avance III 400 equipped with a BCU-X at 22 and 75 °C. Mass spectroscopy was performed on a Thermo Finnigan MAT900 XP operating in EI and CI mode. Single crystal X-ray diffraction datasets were collected on a SuperNova (dual source) Atlas diffractometer. Single crystals were selected, mounted on a nylon loop and kept at 150 K during data collection. The datasets were collected using either monochromated Cu K_α radiation ($\lambda = 1.54184 \text{ \AA}$) or monochromated Mo K_α ($\lambda = 0.71073 \text{ \AA}$). All single crystal X-ray diffraction datasets were collected and solved by Dr. Caroline E. Knapp.

2.2.3 Zinc Oxane Complexes

Detailed experimental procedures for the synthesis of zinc complexes (**1**) – (**8**) and their characterisation details are given below. These complexes are presented and discussed in Chapter 4.

2.2.3.1 Synthesis of Zinc Oxane Trimer Complexes

2.2.3.1.1 Synthesis of $[(\text{Zn}(\text{Et})(\text{OC}(\text{OMe})\text{CHC}(\text{Me})\text{O}))_3]$ (**1**)

Diethylzinc (9.76 mmol, 1.21 g) was added to dry hexane (10 mL) at -78 °C. Dry methyl acetoacetate (9.76 mmol, 1.13 g) was added dropwise to the diethylzinc solution. The resulting solution was brought to room temperature and stirred for 48 hours. Hexane was partially removed *in vacuo* and the remaining solution was left at -18 °C for 24 hours. The product crystallised out as off-white crystals. Yield: 1.86 g, 91%. ^1H NMR δ/ppm (C_6D_6): 0.55 (q, 6H, CH_2CH_3 , $J = 8.0 \text{ Hz}$), 1.47 (t, 9H, CH_2CH_3 , $J = 8.00 \text{ Hz}$), 1.90 (s, 9H, CCH_3), 3.27 (s, 9H, OCH_3), 4.95 (s, 3H, CCHC).

$^{13}\text{C}\{^1\text{H}\}$ NMR δ/ppm (C_6D_6): 1.0 (CH_2CH_3), 12.5 (CH_2CH_3), 27.5 (CCH_3), 51.1 (OCH_3), 89.3 (CCHC), 174.0 (COCH_3), 184.4 (CCH_3). **Anal. Calcd. for $\text{C}_{21}\text{H}_{36}\text{O}_9\text{Zn}_3$:** C, 40.12; H, 5.77. **Found:** C, 40.21; H, 5.89.

2.2.3.1.2 Synthesis of $[(\text{Zn}(\text{Et})(\text{OC}(\text{Me})\text{CHC}(\text{Me})\text{O}))_3]$ (2)

Diethylzinc (9.76 mmol, 1.21 g) was added to dry hexane (10 mL) at -78°C . Dry acetylacetone (9.76 mmol, 0.98 g) was added dropwise to the diethylzinc solution. The resulting solution was brought to room temperature and stirred for 48 hours. Hexane was fully removed *in vacuo* and the product was isolated as an off-white solid. Yield: 1.71 g, 90%. ^1H NMR δ/ppm (C_6D_6): 0.57 (q, 6H, CH_2CH_3 , $J = 8.2$ Hz), 1.48 (t, 9H, CH_2CH_3 , $J = 8.2$ Hz), 1.79 (s, 18H, CCH_3), 5.03 (s, 3H, CCHC). $^{13}\text{C}\{^1\text{H}\}$ NMR δ/ppm (C_6D_6): 1.0 (CH_2CH_3), 12.4 (CH_2CH_3), 28.3 (CCH_3), 102.0 (CCHC), 193.1 (CCH_3). **Anal. Calcd. for $\text{C}_{21}\text{H}_{36}\text{O}_6\text{Zn}_3$:** C, 43.44; H, 6.25. **Found:** C, 43.09; H, 6.77.

2.2.3.1.3 Synthesis of $[(\text{Zn}(\text{Et})(\text{OC}(\text{OEt})\text{CHC}(\text{Me})\text{O}))_3]$ (3)

Diethylzinc (9.76 mmol, 1.21 g) as a 1 M solution in hexanes (9.76 mL) was added to dry hexane (5 mL) at -78°C . Dry ethyl acetoacetate (9.76 mmol, 1.27 g) was added dropwise to the diethylzinc solution. The resulting solution was brought to room temperature and stirred for 48 hours. Hexane was fully removed *in vacuo* and the product was isolated as an off-white solid. Yield: 1.92 g, 88%. ^1H NMR δ/ppm (C_6D_6): 0.44 (q, 6H, ZnCH_2CH_3 , $J = 8.0$ Hz), 0.92 (t, 9H, OCH_2CH_3 , $J = 7.1$ Hz), 1.38 (t, 9H, ZnCH_2CH_3 , $J = 8.0$ Hz), 1.93 (s, 9H, CCH_3), 3.85 (q, 6H, OCH_2CH_3 , $J = 7.1$ Hz), 4.95 (s, 3H, CCHC). $^{13}\text{C}\{^1\text{H}\}$ NMR δ/ppm (C_6D_6): 2.7 (ZnCH_2CH_3), 11.9 (ZnCH_2CH_3), 14.1 (OCH_2CH_3), 27.6 (CCH_3), 60.5 (OCH_2CH_3), 89.6 (CCHC), 173.6 (COCH_2CH_3), 184.2 (CCH_3). **Anal. Calcd. for $\text{C}_{24}\text{H}_{42}\text{O}_9\text{Zn}_3$:** C, 42.98; H, 6.31. **Found:** C, 42.83; H, 5.72.

2.2.3.1.4 Synthesis of $[(\text{Zn}(\text{Et})(\text{OC}(\text{O}^t\text{Bu})\text{CHC}(\text{Me})\text{O}))_3]$ (4)

Diethylzinc (9.76 mmol, 1.21 g) as a 1 M solution in hexanes (9.76 mL) was added to dry hexane (5 mL) at -78°C . Dry *tert*-butyl acetoacetate (9.76 mmol, 1.54 g) was added dropwise to the diethylzinc solution. The resulting solution was brought to room

temperature and stirred for 48 hours. Hexane was fully removed *in vacuo* and the product was isolated as an off-white solid. Yield: 2.25 g, 91%. ^1H NMR δ /ppm (C_6D_6): 0.37 (q, 6H, CH_2CH_3 , $J = 8.2$ Hz), 1.31 (s, 27H, $\text{C}(\text{CH}_3)_3$), 1.33 (t, 9H, CH_2CH_3 , $J = 8.2$ Hz), 1.94 (s, 9H, CCH_3), 4.90 (s, 3H, CCHC). $^{13}\text{C}\{^1\text{H}\}$ NMR δ /ppm (C_6D_6): 3.4 (CH_2CH_3), 11.7 (CH_2CH_3), 27.6 (CCH_3), 28.4 ($\text{C}(\text{CH}_3)_3$), 80.9 ($\text{C}(\text{CH}_3)_3$), 91.0 (CCHC), 173.8 ($\text{COC}(\text{CH}_3)_3$), 183.2 (CCH_3). **Anal. Calcd. for $\text{C}_{30}\text{H}_{54}\text{O}_9\text{Zn}_3$:** C, 47.73; H, 7.21. **Found:** C, 46.93; H, 6.97.

2.2.3.2 Synthesis of Zinc Oxane Cluster Complexes

2.2.3.2.1 Synthesis of $[(\text{Zn}(\text{OC}(\text{OMe})\text{CHC}(\text{Me})\text{O})_2\text{Zn}(\text{Et})\text{OEt})_2]$ (5)

Diethylzinc (9.76 mmol, 1.21 g) as a 1 M solution in hexanes (9.76 mL) was added to dry hexane (5 mL) at -78°C . Dry methyl acetoacetate (9.76 mmol, 1.13 g) was added dropwise to the diethylzinc solution and upon warming to room temperature was stirred for 48 hours. O_2 (5 mL) was added to the flask at -78°C and upon warming to room temperature was stirred for 15 minutes. Liquid N_2 was used to freeze the solution and the flask purged with N_2 . Upon thawing, the solution was stirred for 24 hours at room temperature. Hexane was fully removed *in vacuo* and the product was isolated as an off-white solid. Yield: 1.85 g, 87%. ^1H NMR δ /ppm (C_6D_6): 0.62 (q, 4H, $J = 8.0$ Hz, ZnCH_2CH_3), 1.33 (t, 6H, $J = 7.0$ Hz, OCH_2CH_3), 1.60 (t, 6H, $J = 8.0$ Hz, ZnCH_2CH_3), 1.90 (s, 12H, CCH_3), 3.33 (s, 12H, OCH_3), 3.87 (q, 4H, $J = 7.0$ Hz, CH_2CH_3), 4.99 (s, 4H, CCHC). $^{13}\text{C}\{^1\text{H}\}$ NMR δ /ppm (C_6D_6): 2.2 (ZnCH_2CH_3), 12.6 (ZnCH_2CH_3), 19.7 (OCH_2CH_3), 27.3 (CCH_3), 50.6 (OCH_3), 61.3 (OCH_2CH_3), 87.0 (CCHC), 173.6 (COCH_3), 183.3 (CCH_3). **Anal. Calcd. for $\text{C}_{28}\text{H}_{48}\text{O}_{14}\text{Zn}_4$:** C, 38.64; H, 5.56. **Found:** C, 38.45; H, 5.64. **MS:** m/z $[\text{M} - \text{Zn}_2\text{O}_5\text{C}_{13}\text{H}_{27}]^+$: 474.87; $[\text{M} - \text{Zn}_3\text{O}_8\text{C}_{18}\text{H}_{34}]^+$: 294.97.

2.2.3.2.2 Synthesis of $[(\text{Zn}(\text{OC}(\text{Me})\text{CHC}(\text{Me})\text{O})_2\text{Zn}(\text{Et})\text{OEt})_2]$ (6)

Diethylzinc (9.76 mmol, 1.21 g) as a 1 M solution in hexanes (9.76 mL) was added to dry hexane (5 mL) at -78°C . Dry acetylacetone (9.76 mmol, 0.98 g) was added dropwise to the diethylzinc solution and upon warming to room temperature was stirred for 48 hours. O_2 (5 mL) was added to the flask at -78°C and upon warming to

room temperature was stirred for 15 minutes. Liquid N₂ was used to freeze the solution and the flask purged with N₂. Upon thawing, the solution was stirred for 24 hours at room temperature. Hexane was partially removed *in vacuo* and the remaining solution left at -18 °C for 24 hours. The product crystallised out as off-white crystals. Yield: 1.66 g, 84%. ¹H NMR δ/ppm (C₆D₆): 0.69 (br, 4H, ZnCH₂CH₃), 1.42 (t, 6H, *J* = 7.0 Hz, OCH₂CH₃), 1.61 (br, 6H, ZnCH₂CH₃), 1.79 (s, 24H, CCH₃), 3.80 (q, 4H, *J* = 7.0 Hz, OCH₂CH₃), 5.06 (s, 4H, CCHC). ¹³C{¹H} NMR δ/ppm (C₆D₆): 2.7 (ZnCH₂CH₃), 12.9 (ZnCH₂CH₃), 20.1 (OCH₂CH₃), 28.1 (CCH₃), 61.1 (OCH₂CH₃), 100.6 (CCHC), 193.1 (CCH₃). **Anal. Calcd. for C₂₈H₄₈O₁₀Zn₄**: C, 41.71; H, 6.00. **Found**: C, 42.06; H, 5.92. **MS**: *m/z* [M + C₃H₅]⁺: 847.04; [M - C₈H₂₀]⁺: 691.11; [M - Zn₂O₄C₁₃H₂₇]⁺: 426.91; [M - Zn₃O₆C₁₈H₃₄]⁺: 263.00.

2.2.3.2.3 Synthesis of [(Zn(OC(OEt)CHC(Me)O)₂Zn(Et)OEt)₂] (7)

Diethylzinc (9.76 mmol, 1.21 g) as a 1 M solution in hexanes (9.76 mL) was added to dry hexane (5 mL) at -78 °C. Dry ethyl acetoacetate (9.76 mmol, 1.27 g) was added dropwise to the diethylzinc solution and upon warming to room temperature was stirred for 48 hours. O₂ (5 mL) was added to the flask at -78 °C and upon warming to room temperature was stirred for 15 minutes. Liquid N₂ was used to freeze the solution and the flask purged with N₂. Upon thawing, the solution was stirred for 24 hours at room temperature. Hexane was fully removed *in vacuo* and the product was isolated as an off-white solid. Yield: 1.91 g, 85%. ¹H NMR δ/ppm (C₆D₆): 0.62 (q, 4H, *J* = 8.0 Hz, ZnCH₂CH₃), 0.96 (t, 12H, *J* = 7.1 Hz, COCH₂CH₃), 1.37 (t, 6H, *J* = 7.1 Hz, ZnOCH₂CH₃), 1.61 (t, 6H, *J* = 8.0 Hz, ZnCH₂CH₃), 1.92 (s, 12H, CCH₃), 3.92 (m, 8H, COCH₂CH₃), 3.97 (m, 4H, ZnOCH₂CH₃), 4.99 (s, 4H, CCHC). ¹³C{¹H} NMR δ/ppm (C₆D₆): 2.2 (ZnCH₂CH₃), 12.7 (ZnCH₂CH₃), 14.4 (COCH₂CH₃), 19.8 (ZnOCH₂CH₃), 27.3 (CCH₃), 59.7 (COCH₂CH₃), 61.3 (ZnOCH₂CH₃), 87.3 (CCHC), 173.2 (COCH₂CH₃), 183.0 (CCH₃). **Anal. Calcd. for C₃₂H₅₆O₁₄Zn₄**: C, 41.49; H, 6.09. **Found**: C, 40.88; H, 5.70. **MS**: *m/z* [M - Zn₂O₅C₁₄H₂₉]⁺: 518.98; [M - Zn₃O₈C₂₀H₃₈]⁺: 323.02.

2.2.3.2.4 Synthesis of [(Zn(OC(O^tBu)CHC(Me)O)₂Zn(Et)OEt)₂] (8)

Diethylzinc (9.76 mmol, 1.21 g) as a 1 M solution in hexanes (9.76 mL) was added to dry hexane (5 mL) at -78 °C. Dry *tert*-butyl acetoacetate (9.76 mmol, 1.54 g) was added dropwise to the diethylzinc solution and upon warming to room temperature was stirred for 48 hours. O₂ (5 mL) was added to the flask at -78 °C and upon warming to room temperature was stirred for 15 minutes. Liquid N₂ was used to freeze the solution and the flask purged with N₂. Upon thawing, the solution was stirred for 24 hours at room temperature. Hexane was partially removed *in vacuo* and the remaining solution left at -18 °C for 24 hours. The product crystallised out as off-white crystals. Yield: 2.09 g, 83%. ¹H NMR δ/ppm (C₆D₆): 0.58 (q (br), 4H, ZnCH₂CH₃), 1.44 (s, 36H, C(CH₃)₃), 1.51 (t (br), 6H, OCH₂CH₃), 1.66 (t, 6H, *J* = 8.1 Hz, ZnCH₂CH₃), 1.92 (s, 12H, CCH₃), 4.02 (q, 4H, *J* = 7.1 Hz, OCH₂CH₃), 4.96 (s, 4H, CCHC). ¹³C{¹H} NMR δ/ppm (C₆D₆): 1.8 (ZnCH₂CH₃), 13.1 (ZnCH₂CH₃), 19.8 (OCH₂CH₃), 27.4 (CCH₃), 28.7 (C(CH₃)₃), 61.4 (OCH₂CH₃), 79.7 (C(CH₃)₃), 88.7 (CCHC), 173.4 (COC(CH₃)₃), 182.1 (CCH₃). **Anal. Calcd. for C₄₀H₇₂O₁₄Zn₄:** C, 46.26; H, 6.99. **Found:** C, 46.43; H, 7.27. **MS: m/z** [M – Zn₂O₅C₁₆H₃₃]⁺: 601.05; [M – Zn₃O₈C₂₄H₄₆]⁺: 379.04.

2.2.4 Synthesis of Zinc β-Iminoesterate Complexes

Detailed experimental procedures for the synthesis of β-iminoester ligands (L₁) – (L₄) and zinc β-iminoesterate complexes (9) – (14) and their characterisation details are given below. These complexes are presented and discussed in Chapter 5.

2.2.4.1 Synthesis of β-Iminoester Ligands

2.2.4.1.1 Synthesis of MeC(NHⁱPr)CHC(O)OEt (L₁)

Isopropylamine (150 mmol, 12.89 mL) was added dropwise to ethyl acetoacetate (75 mmol, 9.49 mL) dispersed over K-10 montmorillonite clay (40 g) in a 3-necked round-bottom flask fitted with an overhead mechanical stirrer. The reaction slurry initially gave out heat and was stirred at room temperature for 6 hours. The product was extracted by washing with dichloromethane (3 × 50 mL) and filtered. The solvent was removed *in vacuo* to yield pale orange liquid. Yield: 11.17 g, 87%. ¹H NMR δ/ppm

(CDCl₃): 1.18 (d, 6H, $J = 6.4$ Hz, (CH₃)₂), 1.21 (t, 3H, $J = 7.1$ Hz, CH₃CH₂), 1.91 (s, 3H, CH₃C), 3.65 (m, 1H, (CH₃)₂CH), 4.05 (q, 2H, $J = 7.1$ Hz, CH₃CH₂), 4.36 (s, 1H, CHCO), 8.47 (s (broad), 1H, NH). ¹³C{¹H} NMR δ/ppm (CDCl₃): 14.8 (CH₃CH₂), 19.3 (CH₃C), 24.2 ((CH₃)₂), 44.5 (CH(CH₃)₂), 58.3 (CH₃CH₂), 81.8 (CHCO), 160.9 (q) (CNH), 170.7 (q) (CO). MS: m/z [M+H]⁺: 172.16.

2.2.4.1.2 Synthesis of MeC(NHMe)CHC(O)OEt (L₂)

Methylamine (150 mmol, 4.66 g) as a 33wt.% solution in ethanol (18.67 mL) was added dropwise to ethyl acetoacetate (75 mmol, 9.49 mL) dispersed over K-10 montmorillonite clay (60 g) in a 3-necked round-bottom flask fitted with an overhead mechanical stirrer. The reaction slurry initially gave out heat and was stirred at room temperature for 6 hours. The product was extracted by washing with dichloromethane (3 × 50 mL) and filtered. The solvent was removed *in vacuo* to yield a light yellow liquid. Yield: 8.58 g, 80%. ¹H NMR δ/ppm (CDCl₃): 1.20 (t, 3H, $J = 7.1$ Hz, CH₃CH₂), 1.87 (s, 3H, CH₃C), 2.86 (d, 3H, $J = 5.2$ Hz, CH₃NH), 4.04 (q, 2H, $J = 7.1$ Hz, CH₃CH₂), 4.42 (s, 1H, CHCO), 8.44, (s (broad), 1H, NH). ¹³C{¹H} NMR δ/ppm (CDCl₃): 14.7 (CH₃CH₂), 19.3 (CH₃C), 29.6 (CH₃NH), 58.3 (CH₃CH₂), 81.9 (CHCO), 162.9 (q) (CNH), 170.7 (q) (CO). MS: m/z [M+H]⁺: 144.10.

2.2.4.1.3 Synthesis of MeC(NHⁱBu)CHC(O)OEt (L₃)

Isobutylamine (100 mmol, 9.94 mL) was added dropwise to ethyl acetoacetate (50 mmol, 6.32 mL) dispersed over K-10 montmorillonite clay (30 g) in a 3-necked round-bottom flask fitted with an overhead mechanical stirrer. The reaction slurry initially gave out heat and was stirred at room temperature for 15 hours. The product was extracted by washing with dichloromethane (4 × 30 mL) and filtered. The solvent was removed *in vacuo* to yield a yellow liquid. Yield: 8.12 g, 88%. ¹H NMR δ/ppm (CDCl₃): 0.93 (d, 6H, $J = 6.7$ Hz, (CH₃)₂CH), 1.21 (t, 3H, $J = 7.1$ Hz, CH₃CH₂), 1.76 (m, 1H, (CH₃)₂CH), 1.87 (s, 3H, CH₃C), 2.98 (t, 2H, $J = 6.4$ Hz, CH₂NH), 4.05 (q, 2H, $J = 7.1$ Hz, CH₃CH₂), 4.39 (s, 1H, CHCO), 8.65 (s (broad), 1H, NH). ¹³C{¹H} NMR δ/ppm (CDCl₃): 14.8 (CH₃CH₂), 19.6 (CH₃C), 20.2 ((CH₃)₂CH), 29.4 ((CH₃)₂CH), 50.7 (CH₂NH), 58.3 (CH₃CH₂), 81.8 (CHCO), 162.1 (q) (CNH), 170.8 (q) (CO). MS: m/z [M+H]⁺: 186.10.

2.2.4.1.4 Synthesis of MeC(NH(CH₂)₂^{*i*}Pr)CHC(O)OEt (L₄)

Isopentylamine (60 mmol, 6.96 mL) was added dropwise to ethyl acetoacetate (30 mmol, 3.79 mL) dispersed over K-10 montmorillonite clay (20 g) in a 3-necked round-bottom flask fitted with an overhead mechanical stirrer. The reaction slurry initially gave out heat and was stirred at room temperature for 15 hours. The product was extracted by washing with dichloromethane (3 × 30 mL) and filtered. The solvent was removed *in vacuo* to yield a dark orange liquid. Yield: 5.43 g, 90%. ¹H NMR δ/ppm (CDCl₃): 0.89 (d, 6H, *J* = 6.7 Hz, (CH₃)₂CH), 1.22 (t, 3H, *J* = 7.1 Hz, CH₃CH₂), 1.43 (q, 2H, *J* = 7.1 Hz, CHCH₂), 1.67 (m, 1H, (CH₃)₂CH), 1.89 (s, 3H, CH₃C), 3.18 (q, 2H, *J* = 6.5 Hz, CH₂NH), 4.05 (q, 2H, *J* = 7.1 Hz, CH₃CH₂), 4.40 (s, 1H, CHCO), 8.50 (s (broad), 1H, NH). ¹³C{¹H} NMR δ/ppm (CDCl₃): 14.8 (CH₃CH₂), 19.5 (CH₃C), 22.5 ((CH₃)₂CH), 25.6 ((CH₃)₂CH), 39.3 (CH₂CH), 41.2 (CH₂NH), 58.3 (CH₃CH₂O), 81.8 (CHCO), 162.1 (q) (CNH), 170.8 (q) (CO). MS: *m/z* [M+H]⁺: 200.11.

2.2.4.2 Synthesis of Homoleptic Zinc β-Iminoesterate Complexes

Complex (9) has previously been synthesised and as such is labelled and presented first. This is discussed further in Chapter 5.2.2.1 and Chapter 5.2.2.1.1.

2.2.4.2.1 Synthesis of [Zn(OC(OEt)CHC(Me)N^{*i*}Pr)₂] [Zn(L₁)₂] (9)

Diethylzinc (8.76 mmol, 1.08 g) as a 15 wt.% toluene solution (7.88 mL) was added to dry toluene (10 mL) at -78 °C. L₁ (17.52 mmol, 3.00 g) was added dropwise to the diethylzinc solution. The resulting solution was brought to room temperature and stirred for 24 hours. Toluene (~15 mL) was partially removed *in vacuo* and the remaining solution was left at -18 °C for 48 hours. The product crystallised out as yellow tinted crystals. Yield: 3.01 g, 85%. ¹H NMR δ/ppm (CDCl₃): 1.09 (d, 6H, *J* = 5.4 Hz, (CH₃)₂CH), 1.10 (d, 6H, *J* = 5.4 Hz, (CH₃)₂CH), 1.23 (t, 6H, *J* = 7.1 Hz, CH₃CH₂), 1.98 (s, 6H, CH₃C), 3.85 (m, 2H, (CH₃)₂CH), 4.08 (q, 4H, *J* = 7.1 Hz, CH₃CH₂), 4.30 (s, 2H, CHCO). ¹³C{¹H} NMR δ/ppm (CDCl₃): 15.0 (CH₃CH₂), 22.4 (CH₃C), 24.8 ((CH₃)₂CH), 49.8 ((CH₃)₂CH), 59.2 (CH₃CH₂), 78.00 (CHCO), 170.5 (q) (CN), 171.0 (q) (CO). Anal. Calcd. for C₁₈H₃₂N₂O₄Zn: C, 53.27; H, 7.95; N, 6.90. Found: C, 52.57; H, 8.13; N, 7.01. MS: *m/z* [M]⁺: 405.52.

2.2.4.2.2 Synthesis of [Zn(OC(OEt)CHC(Me)NMe)₂] [Zn(L₂)₂] (10)

Diethylzinc (10.47 mmol, 1.29 g) as a 15 wt.% toluene solution (9.43 mL) was added to dry toluene (10 mL) at -78 °C. L₂ (20.95 mmol, 3.00 g) was added dropwise to the diethylzinc solution. The resulting solution was brought to room temperature and stirred for 24 hours. Toluene (~15mL) was partially removed *in vacuo* and the remaining solution was left at -18 °C for 48 hours. The product crystallised out as yellow tinted crystals. Yield: 2.63 g, 72%. ¹H NMR δ/ppm (CDCl₃): 1.25 (t, 6H, *J* = 7.1 Hz, CH₃CH₂), 1.95 (s, 6H, CH₃C), 3.01 (s, 6H, CH₃N), 4.09 (q, 4H, *J* = 7.1 Hz, CH₃CH₂), 4.36 (s, 2H, *J* = 7.1 Hz, CHCO). ¹³C{¹H} NMR δ/ppm (CDCl₃): 14.9 (CH₃CH₂), 21.7 (CH₃C), 37.7 (CH₃N), 59.4 (CH₃CH₂), 77.8 (CHCO), 171.9 (q) (CN), 174.5 (q) (CO). MS: m/z [M]⁺: 349.09.

2.2.4.2.3 Synthesis of [Zn(OC(OEt)CHC(Me)NⁱBu)₂] [Zn(L₃)₂] (11)

Diethylzinc (3.24 mmol, 0.40 g) as a 15 wt.% toluene solution (2.91 mL) was added to dry toluene (10 mL) at -78 °C. L₃ (6.48 mmol, 1.20 g) was added dropwise to the diethylzinc solution. The resulting solution was brought to room temperature and stirred for 48 hours. Toluene was removed *in vacuo* and the product was isolated as an orange coloured oil. Yield: 0.95 g, 67%. ¹H NMR δ/ppm (CDCl₃): 0.86 (dd, 12H, *J* = 4.4, 2.1 Hz, CH₃CH), 1.22 (t, 6H, *J* = 7.1 Hz, CH₃CH₂), 1.66 (m, 2H, CH₃CH), 1.93 (s, 6H, CH₃C), 3.00 (m, 4H, CH₂CH), 4.06 (m, 4H, CH₃CH₂), 4.28 (s, 2H, CHCO). ¹³C{¹H} NMR δ/ppm (CDCl₃): 14.9 (CH₃CH₂), 20.6 (CHCH₃), 20.8 (CHCH₃), 22.8 (CH₃C), 30.6 (CH₂CH), 58.4 (CH₂CH), 59.2 (CH₃CH₂), 77.9 (CHCO), 171.4 (q) (CN), 172.4 (q) (CO). MS: m/z [M]⁺: 433.12.

2.2.4.2.4 Synthesis of [Zn(OC(OEt)CHC(Me)N(CH₂)₂ⁱPr)₂] [Zn(L₄)₂] (12)

Diethylzinc (3.01 mmol, 0.37 g) as a 15 wt.% toluene solution (2.71 mL) was added to dry toluene (10 mL) at -78 °C. L₄ (6.02 mmol, 1.20 g) was added dropwise to the diethylzinc solution. The resulting solution was brought to room temperature and stirred for 48 hours. Toluene was removed *in vacuo* and the product was isolated as an orange coloured oil. Yield: 0.96 g, 69%. ¹H NMR δ/ppm (CDCl₃): 0.86 (dd, 12H, *J* = 2.9, 3.7 Hz, CH₃CH), 1.23 (t, 6H, *J* = 7.1 Hz, CH₃CH₂), 1.35 (dt, 4H, *J* = 7.6, 8.1,

6.8 Hz, $\text{CH}_2\text{CH}_2\text{CH}$), 1.55 (m, 2H, CH_2CH), 1.94 (s, 6H, CH_3C), 3.19 (m, 2H, CH_2CH), 3.29 (m, 2H, CH_2CH), 4.07 (m, 4H, $\text{CH}_3\text{CH}_2\text{O}$), 4.30 (s, 2H, CHCO). $^{13}\text{C}\{^1\text{H}\}$ NMR δ/ppm (CDCl_3): 15.0 (CH_3CH_2), 22.1 (CH_3C), 22.7 (CHCH_3), 22.8 (CHCH_3), 26.1 (CHCH_3), 40.7 (NCH_2), 48.6 (CH_2CH), 59.2 (CH_3CH_2), 77.9 (CHCO), 171.4 (q) (CN), 172.2 (q) (CO). MS: m/z [M] $^+$: 461.15.

2.2.4.3 Synthesis of Heteroleptic Zinc β -Iminoesterate Complexes

2.2.4.3.1 Synthesis of $[(\text{Zn}(\text{OC}(\text{OEt})\text{CHC}(\text{Me})\text{N}^i\text{Pr})(\text{Et}))_2][(\text{Zn}(\text{L}_1)(\text{Et}))_2]$ (13)

Diethylzinc (5.84 mmol, 0.72 g) as a 15 wt.% toluene solution (5.26 mL) was added to dry toluene (10 mL) at -78°C . L_1 (5.84 mmol, 1.00 g) was added dropwise to the diethylzinc solution. The resulting solution was brought to room temperature and stirred for 24 hours. Toluene was partially removed *in vacuo* and the remaining solution was left at -18°C for 48 hours. The product crystallised out as yellow tinted crystals. Yield: 1.17 g, 75%. ^1H NMR δ/ppm (C_6D_6): 0.32 (br, 4H, ZnCH_2CH_3), 0.93 (d, 12H, $J = 6.4$ Hz, $(\text{CH}_3)_2\text{CH}$), 1.09 (t, 6H, $J = 7.1$ Hz, OCH_2CH_3), 1.28 (br, 6H, ZnCH_2CH_3), 1.61 (s, 6H, CH_3C), 3.44 (m, 2H, $(\text{CH}_3)_2\text{CH}$), 4.03 (q, 4H, $J = 7.1$ Hz, OCH_2CH_3), 4.57 (s, 2H, CHCO). $^{13}\text{C}\{^1\text{H}\}$ NMR δ/ppm (C_6D_6): 4.8 (ZnCH_2CH_3), 11.2 (ZnCH_2CH_3), 14.9 (OCH_2CH_3), 22.2 (CH_3C), 25.6 ($(\text{CH}_3)_2\text{CH}$), 49.4 ($(\text{CH}_3)_2\text{CH}$), 59.5 (OCH_2CH_3), 79.6 (CHCO), 170.3 (q) (CN), 172.2 (q) (CO). MS: m/z [M] $^+$: 530.25.

2.2.4.3.2 Synthesis of $[(\text{Zn}(\text{OC}(\text{OEt})\text{CHC}(\text{Me})\text{N}(\text{CH}_2)_2^i\text{Pr})(\text{Et}))_2][(\text{Zn}(\text{L}_4)(\text{Et}))_2]$ (14)

Diethylzinc (5.02 mmol, 0.62 g) as a 15 wt.% toluene solution (4.52 mL) was added to dry toluene (15 mL) at -78°C . L_4 (5.02 mmol, 1.00 g) was added dropwise to the diethylzinc solution. The resulting solution was brought to room temperature and stirred for 42 hours. Toluene was partially removed *in vacuo* and the remaining solution was left at -18°C for 48 hours. The product crystallised out as yellow tinted crystals. Yield: 0.98 g, 67%. ^1H NMR δ/ppm (C_6D_6): 0.21 (q (br), 4H, $J = 8.1$ Hz, ZnCH_2CH_3), 0.81 (d, 12H, $J = 6.6$ Hz, $(\text{CH}_3)_2\text{CH}$), 1.09 (t, 6H, $J = 7.1$ Hz, OCH_2CH_3),

1.20 (t (br), 6H, $J = 8.1$ Hz, ZnCH_2CH_3), 1.25 (m, 4H, NCH_2CH_2), 1.41 (m, 4H, NCH_2CH_2), 1.61 (s, 6H, CH_3C), 2.98 (m, 2H, $(\text{CH}_3)_2\text{CH}$), 4.04 (q, 4H, $J = 7.1$ Hz, OCH_2CH_3), 4.62 (s, 2H, CHCO). $^{13}\text{C}\{^1\text{H}\}$ NMR δ/ppm (C_6D_6): 5.7 (ZnCH_2CH_3), 10.8 (ZnCH_2CH_3), 14.9 (OCH_2CH_3), 21.8 (CH_3C), 22.8 ($(\text{CH}_3)_2\text{CH}$), 26.6 (NCH_2CH_2), 41.9 (NCH_2CH_2), 49.2 ($(\text{CH}_3)_2\text{CH}$), 59.6 (OCH_2CH_3), 79.6 (CHCO), 172.6 (q) (CN), 172.7 (q) (CO).

2.3 Chemical Vapour Deposition

2.3.1 Analysis Methods

2.3.1.1 Precursor Thermal Decomposition Analysis

The thermal decomposition properties of zinc complexes used in AACVD were determined by thermal gravimetric analysis (TGA) and differential scanning calorimetry (DSC). The experiment ran concurrently from room temperature to 600 °C under helium using a Netzsch STA 449 C Jupiter Thermo-microbalance. For $[\text{Zn}(\text{OTf})_2]$ and synthesised complexes (**9**) and (**10**), the studies were run in open aluminium pans. For complex (**6**), the study was performed in a sealed pan which was pierced prior to running the analysis.

2.3.1.2 Film Analysis Methods

X-ray diffraction (XRD) patterns were recorded using a Bruker D8 Discover X-ray diffractometer using monochromatic $\text{Cu } K_{\alpha 1}$ and $\text{Cu } K_{\alpha 2}$ radiation of wavelengths 1.54056 and 1.54439 Å respectively, emitted in an intensity ratio of 2:1 with a voltage of 40 kV and a current of 40 mA. The incident beam angle was 1° and data was collected between 10° and 66° 2θ with a step size of 0.05° at 0.5 s/step. Scanning electron microscopy (SEM) was performed using a Philips XL30 FEG operating in both plan and cross section mode at varying instrument magnifications from $\times 10,000$ to $\times 50,000$, as stated. Film thickness was estimated using a Filmetrics F20 thin film measurement system. X-ray photoelectron spectroscopy (XPS) surface and depth profiling was performed using a Thermo Scientific K-Alpha XPS system using monochromatic $\text{Al } K_{\alpha}$ radiation at 1486.6 eV X-ray source. Etching was achieved using an Ar ion etch beam at 1 KeV with a current of 1.55 μA . All SEM images and

XPS data were collected by the surface analysis technicians at the NSG European Technical Centre, Lathom, UK. CasaXPS software was used to analyse the data with binding energies referenced to an adventitious C 1s peak at 284.8 eV. UV/Vis/NIR transmission spectra were recorded using a PerkinElmer Lambda 950 spectrometer in the range of 250/300 – 1400 nm with an air background. Where appropriate, sheet resistance measurements were recorded using the Van der Pauw method and Hall Effect measurements made to determine the mobility and free carrier concentrations of the deposited films.

2.3.2 Thin Film Deposition

2.3.2.1 Chemical Vapour Deposition Rig

Depositions discussed in this thesis were carried out in a horizontal, cold-walled reactor system, a schematic of which is shown in Figure 2.1.

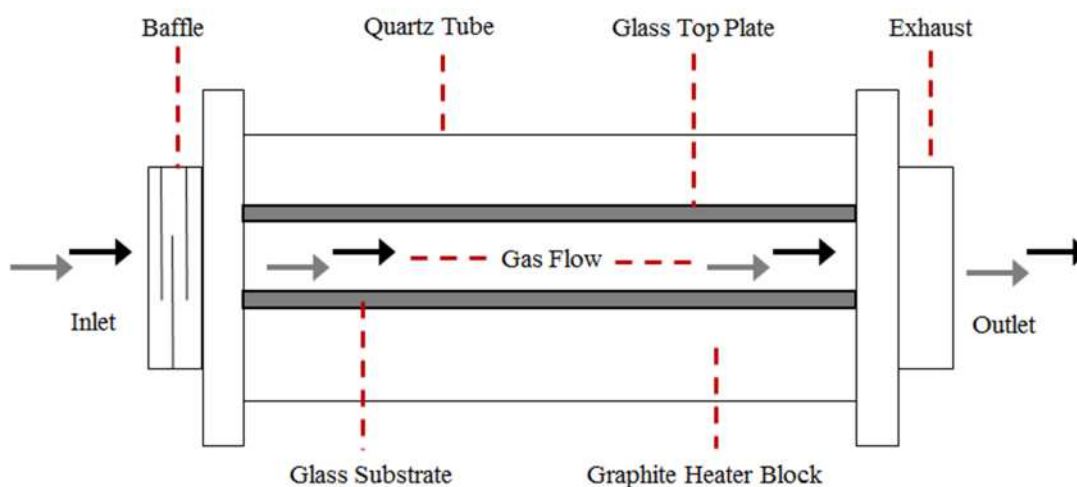


Figure 2.1: Horizontal cold-walled CVD reactor.

The reactant vapour and carrier gas are delivered to the reaction chamber through a brass baffle which is used to ensure a laminar gas flow. Once inside the chamber, the flow of gas is located between two glass plates. The first is the substrate, located below the gas flow and where the film deposition occurs. The substrate rests on a graphite block which is fitted with a Whatman cartridge heater, used to heat the substrate to the required deposition temperature. A second glass plate is held 6 mm above the glass

substrate and is used to quash any air turbulence and ensure the laminar gas flow to the exhaust is maintained. The technique used for depositions discussed in this thesis was AACVD.

2.3.2.2 Aerosol Assisted Chemical Vapour Deposition Delivery

As discussed in Chapter 1.4.3.1, AACVD differs from conventional CVD in how the precursor is delivered to the CVD chamber, a schematic of the set-up is shown in Figure 2.2.

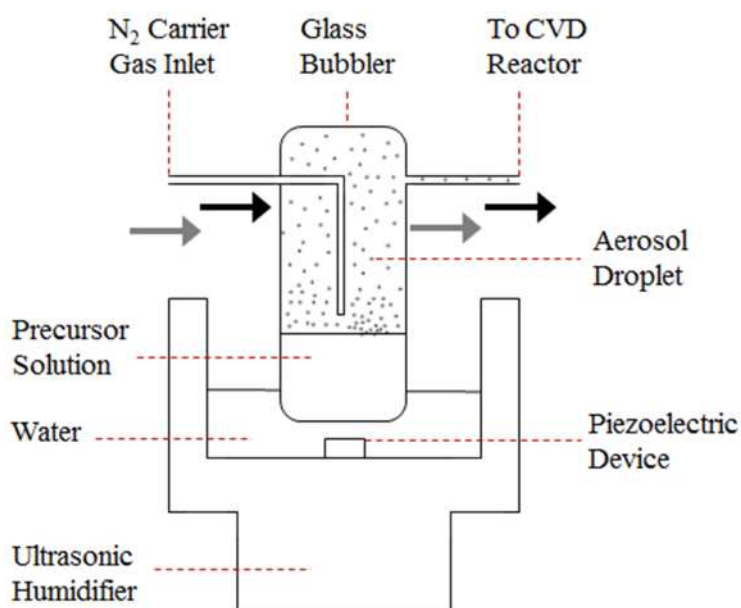


Figure 2.2: AACVD bubbler set-up.

The precursor was first dissolved in a suitable dry solvent, as stated below for each precursor and held in a glass bubbler. A liquifog® piezo ultrasonic atomizer was used to vaporise the precursor solution, the process of which was also described in Chapter 1.4.3.1. The N₂ carrier gas enters the bubbler where the generated aerosol mist is located. This flow of carrier gas through the system allows for the aerosol to be transported from the outlet of the bubbler to the inlet of the CVD reactor.

2.3.2.3 General Procedures

Caution: Fumes produced during the CVD of zinc compounds can potentially be toxic and corrosive and all dispositions should be carried out in a fume hood.

Nitrogen (99.99%) was obtained from BOC and used as supplied. Films were deposited onto Pilkington NSG float glass substrates (145 mm × 45 mm × 4 mm) with a 25 nm barrier layer of crystalline SiO₂. This barrier layer is used to prevent ions from the glass material leaching into the deposited film. The glass substrate was cleaned prior to deposition using isopropyl alcohol and acetone and dried in air. Heating of the system was carried out under a flow of N₂. Depositions were performed under atmospheric pressure and initiated upon the generation of an aerosol and its delivery to the CVD chamber. Once all the precursor solution had been transported to the CVD reactor the glass substrates were allowed to cool under a flow of nitrogen to below 100 °C before being removed. Coated substrates were handled and stored in air.

2.3.2.4 AACVD from [Zn(OTf)₂]

Zinc triflate was procured from Sigma-Aldrich and aluminium acetylacetonate from Merck Millipore, both used as supplied. Methanol was used as the solvent and dried over magnesium methoxide and distilled under nitrogen. ZnO thin films were deposited from a precursor solution of [Zn(OTf)₂] (0.5 g, 1.38 mmol) dissolved in dry methanol (30 mL). Aluminum doping was achieved by the addition of [Al(acac)₃] (0.022 g, 0.069 mmol) to [Zn(OTf)₂] (0.5 g, 1.38 mmol) in methanol (30 mL). Initial investigations were carried out to determine the optimal flow rate of N₂ and substrate temperature. These were determined to be 1.2 Lmin⁻¹ and 600 °C respectively. Deposition times varied between 30 and 35 minutes.

2.3.2.5 AACVD from Zinc Complex (6)

All manipulations to (6) were carried out under inert conditions either in a Mbraun Unilab glovebox or using standard Schlenk line conditions. [(Zn(OC(Me)CHC(Me)O)₂Zn(Et)O(Et))₂] (0.87 mmol, 0.7 g) (6) was dissolved in dry toluene (30 mL) inside a glass bubbler under N₂ and stirred for 10 minutes. An optimal N₂ flow rate and substrate temperature of 1.2 Lmin⁻¹ and 450 °C respectively were

used. Dry toluene had been stored in an alumina column and dried with anhydrous engineering equipment such that the water concentration were below 10 ppm. Deposition times varied between 30 and 40 minutes.

2.3.2.6 AACVD from $[\text{Zn}(\text{L}_1)_2]$ (**9**) and $[\text{Zn}(\text{L}_2)_2]$ (**10**)

$[\text{Zn}(\text{L}_1)_2]$ (1.23 mmol, 0.5 g) (**9**) was dissolved in dry toluene (20 mL) inside a glass bubbler under N_2 and stirred for 10 minutes. Depositions from precursor (**9**) were also carried out in dry dioxane and dry hexane. Depositions from $[\text{Zn}(\text{L}_2)_2]$ (1.43 mmol, 0.5 g) (**10**) were carried out under the same conditions in dry toluene and dry dioxane. An optimal N_2 flow rate and substrate temperature of 1 Lmin^{-1} and 450°C respectively were used. Dry solvents used in these depositions had been stored in an alumina column and dried with anhydrous engineering equipment such that the water concentration were below 10 ppm. Deposition times varied between 25 and 35 minutes.

2.4 Conclusion

This chapter has described the synthesis and characterisation of zinc oxane complexes (**1**) – (**8**), β -iminoester ligands (**L1**) – (**L4**) and zinc β -iminoesterate complexes (**9**) – (**14**). The experimental details of the AACVD of doped and undoped ZnO films from $[\text{Zn}(\text{OTf})_2]$, the zinc oxane $[(\text{Zn}(\text{OC}(\text{Me})\text{CHC}(\text{Me})\text{O})_2\text{Zn}(\text{Et})\text{O}(\text{Et}))_2]$ (**6**) and the zinc β -iminoesterates $[\text{Zn}(\text{L}_1)_2]$ (**9**) and $[\text{Zn}(\text{L}_2)_2]$ (**10**) have also been presented.

Chapter 3

AACVD of Zinc Oxide and Aluminium Doped Zinc Oxide Thin Films from Zinc Triflate

This chapter describes the novel use of zinc triflate (trifluoromethanesulfonate), $[\text{Zn}(\text{OTf})_2]$ as a precursor in the AACVD of transparent and conductive ZnO thin films. $[\text{Zn}(\text{OTf})_2]$ is shown to be a highly suitable AACVD precursor which exhibits a number of ideal precursor properties. Aluminium-doped zinc oxide (AZO) thin films with high transparency and high conductivity were also successfully deposited when aluminium acetylacetonate $[\text{Al}(\text{acac})_3]$ was added to the precursor solution. The work presented in this chapter has also been used as the descriptive example given in a patent application for the process of depositing metal oxide thin films from metal sulfonates.

3.1 Introduction

ZnO thin films have significant potential to replace ITO in a number of current TCO applications, as described in Chapter 1.2, however, there are a number of challenges to overcome. One of the most significant challenges is the lack of suitable CVD precursors which exhibit the ideal precursor properties defined in Chapter 1.5.1. The most widely used precursor for the CVD of ZnO is diethylzinc, (a) in Figure 3.1. Despite being commercially available and chemically pure, there are a number of significant issues related to its use, not least its pyrophoric nature.

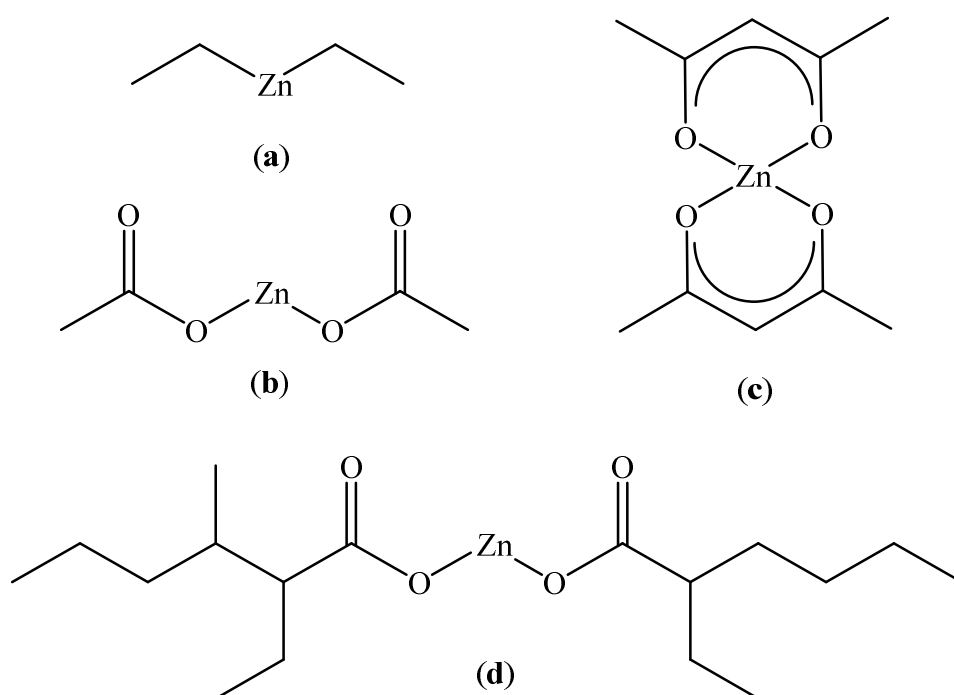


Figure 3.1: Commercially available zinc complexes used as CVD precursors, namely: (a) diethylzinc, (b) zinc acetate, (c) zinc acetylacetonate and (d) zinc 2-ethylhexanoate.

The most commonly used alternative commercial compound is zinc acetate, shown in Figure 3.1 (b). With the exception of a limited number of investigations using zinc acetylacetonate and zinc 2-ethylhexanoate, shown in Figure 3.1 (c) and (d) respectively, alternative commercially available zinc CVD precursors are limited. Some researchers suggest that the limited investigations into alternative commercial precursors is due to carbon contamination in the deposited ZnO films.¹ However, the alternatives offer a number of advantages over diethylzinc including greater stability,

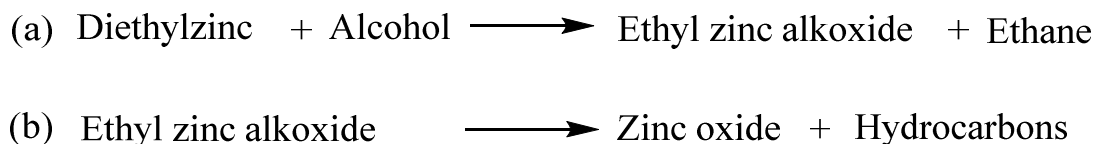
ease of handling and lower cost. The use of these compounds as CVD precursors is reviewed in this chapter. One zinc compound which is used widely as a catalyst in organic chemistry but has not been investigated for use as a CVD precursor for ZnO is zinc triflate, $[\text{Zn}(\text{OTf})_2]$. This chapter demonstrates that zinc triflate exhibits strong potential for use as an AACVD precursor for the deposition of ZnO thin films.

3.1.1 Zinc Complexes as ZnO CVD Precursors

3.1.1.1 Alkyl Zinc Compounds

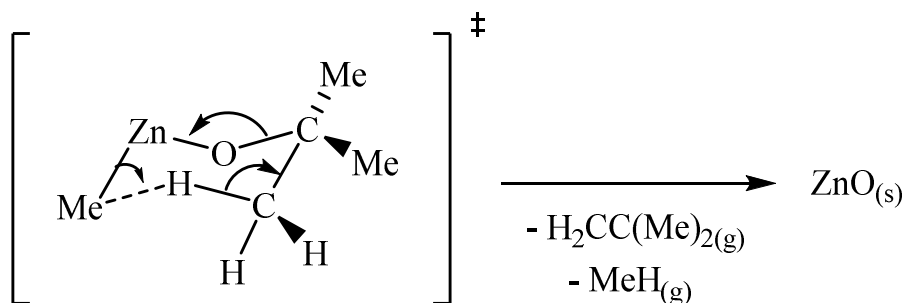
Alkyl zinc compounds were first discovered and identified by Edward Frankland in 1849 in the reaction of granulated zinc with ethyl iodide.² These were discovered in quite a notable reaction when Franklin investigated the effect of water upon the solid alkyl zinc which had formed, resulting in the formation of ZnO but also flames of several feet and some signs of zinc poisoning. The synthesis and further reactions of the newly discovered alkyl zinc compounds were investigated in the years following their discovery, including their reaction with oxygen to form ZnO. The proposed reaction mechanism put forward by Abraham³ and Davis⁴ suggested that the reaction proceeds *via* a radical mechanism with oxygen insertion between the Zn-C bond forming the alkoxides or peroxides species, such as $[\text{RZn}(\text{OOR})]$, $[\text{Zn}(\text{OOR})_2]$ and $[\text{Zn}(\text{OR})_2]$. However, recent studies suggest this is not the case and an alternative mechanism was proposed involving the direct attack of O_2 at the Zn centre.⁵

ZnEt_2 has become the most widely used precursor for the deposition of ZnO films *via* CVD routes. It is an example of a dual-source reaction system, as discussed in Chapter 1.5.2, in which an additional precursor acting as an oxygen source is required to allow for the *in situ* reaction to form ZnO. A wide variety of oxygen precursors have been used including oxygen,⁶ nitrogen dioxide,⁷ nitric oxide,⁸ and carbon dioxide⁹ gases. Alternatively, oxygen sources have also come from a variety of vaporised liquids including *tert*-butanol,¹⁰ methanol¹¹ or water vapour.¹² Van Deelen *et al.*¹³ investigated the deposition of ZnO thin films from the reaction between ZnEt_2 and *tert*-butanol. They considered the reaction mechanism to proceed according to Scheme 3.1, *via* the formation of alkyl zinc alkoxide species, as just discussed. At higher temperatures or partial pressures of *tert*-butanol, it was believed that the alkoxide undergoes a second reaction to form a bis(alkoxide).¹⁴



Scheme 3.1: Formation of ZnO from ZnEt₂ and an alcohol.¹³

The alkyl zinc alkoxide is believed to undergo intramolecular decomposition *via* a six member cyclic transition state (as shown in Scheme 3.2 for [MeZn(OⁱBu)]), to form the desired ZnO thin film whilst eliminating the gaseous byproducts of an alkene and methane.¹⁵ As part of their work, van Deelen *et al.*¹³ modelled this reaction using computational fluid dynamics flow simulations and found that the deposition profiles involving the formation of this intermediate species fits well with experimental results.



Scheme 3.2: Decomposition mechanism of [MeZn(OⁱBu)] alkyl zinc alkoxide.¹⁵

Recent investigations into the oxygenation reactions of zinc alkyls have shown the reaction to afford heterocubanes.¹⁶ Jana *et al.*¹⁷ studied the reactions of ZnMe₂, ZnEt₂ and Zn^{*i*}Pr₂ with oxygen and have isolated structures of mono(heterocubane) or bis(heterocubane) structures, as shown in Figure 3.2. The structure of the heterocubane products were found to depend on the identity of the alkyl zinc and on the presence or absence of water during the reaction. Further investigations are required and Hollingsworth *et al.*¹⁸ highlight the problem faced in the study of these reactions in that they are generally uncontrollably fast and so highly challenging to isolate the reaction intermediates. Further discussions on the zinc oxane products that result from the reactions of ZnEt₂ are presented in Chapter 4 as an introduction and prelude to the work presented there.

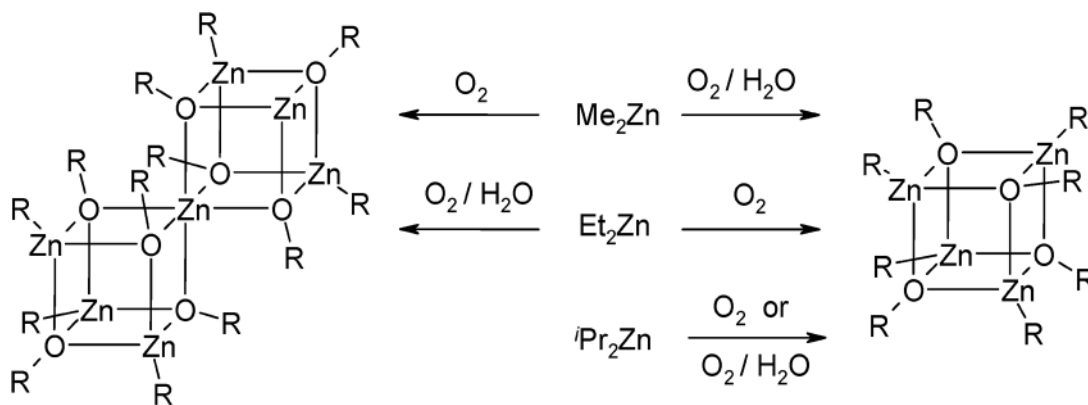


Figure 3.2: Synthesis of mono and bis(heterocubanes) from the reaction of ZnMe_2 , ZnEt_2 and Zn^iPr_2 with O_2 or O_2 and H_2O .¹⁷

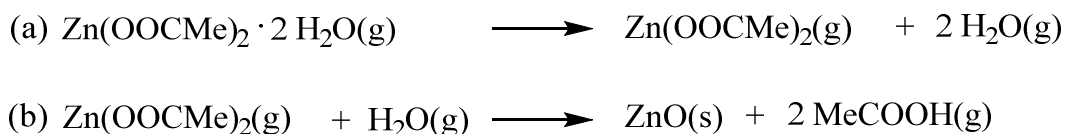
Despite being relatively expensive and not single-source, ZnEt_2 is by far the most common CVD precursor for ZnO films. It is commercially available, of high purity, has a good growth rate and does not require a high substrate temperature for deposition. It is also synthesised commercially *via* an organoaluminium route² and available neat or in pre-mixed solutions of varying concentrations in a number of solvents. When external dopants are introduced to the system, ZnEt_2 has also been shown to easily yield doped ZnO films *via* a number of the CVD routes including MOCVD,¹⁹ LPCVD²⁰ and AACVD.¹¹

However, its high reactivity is also a disadvantage and results in a number of issues, particularly in terms of its commercial application. Its highly pyrophoric nature makes it difficult to handle, allows for ample opportunity for undesired pre-reactions and any tiny leaks of air into the system can cause significant issues to the deposition process.²¹ As a result, the composition, uniformity and the reproducibility of the films produced can be difficult to control. These factors limit the commercial applicability of ZnEt_2 . Park *et al.*²² have put claim *via* a patent to one way of limiting the reactivity of ZnEt_2 . The reactivity of alkyl zincs is reduced when dissolved in a solvent, however, the solvent and ZnEt_2 will still have different vapour pressures. The authors present an invention in which two organic solvents, such as octane and pentane are used in a ratio in which they match the vapour pressure of the alkyl zinc from 95 to 99%. This allowed ZnO to be deposited *via* APCVD with the use of an oxidiser gas.

Another route to reducing and overcoming the issues related to the use of ZnEt_2 as a CVD precursor is the synthesis of more stable, less pyrophoric and potentially single-source zinc precursors. This method is discussed in detail in the two synthesis chapters of this thesis, Chapter 4 and Chapter 5. The main alternative commercial CVD precursor however, is zinc acetate.

3.1.1.2 Zinc Acetate

Zinc acetate $[\text{Zn}(\text{OOCMe})_2]$ is a precursor that has the potential to be used as a single-source precursor but is most commonly used in a dual-source set-up. It has been used in a number of techniques including sol-gel²³ and spray pyrolysis,²⁴ but has also been widely applied in CVD.^{25,26} The starting material exists as a dihydrate and is first dried to remove the water. In MOCVD, $[\text{Zn}(\text{OOCMe})_2]$ is then sublimed by heating to 180-200 °C or evaporated at its melting point of 245 °C and carried in either a N_2 carrier gas or air to be reacted with water to form a ZnO film,²⁷ as illustrated in Scheme 3.3.



Scheme 3.3: Deposition of ZnO from zinc acetate dihydrate $[\text{Zn}(\text{OOCMe})_2] \cdot 2\text{H}_2\text{O}$.²⁷

Other researchers^{28,29} believe that $[\text{Zn}(\text{OOCMe})_2]$ oligomerizes on sublimation to form zinc oxyacetate, $[\text{Zn}_4\text{O}(\text{OOCMe})_6]$, also referred to as basic zinc acetate, which has the tetrameric structure shown in Figure 3.3.³⁰ This complex is believed to decompose to form ZnO by fragmentation of the O-C bonds starting at 200 °C,³¹ however, substrate temperatures ideally need to be greater than 400 °C to ensure decomposition to ZnO. Further investigations using $[\text{Zn}(\text{OOCMe})_2]$ in both air and N_2 carrier gas have been carried out by Jain *et al.*³² Their results suggests ZnO is formed from two simultaneous reactions which occur at different rates depending on the deposition conditions. One reaction involves $[\text{Zn}(\text{OOCMe})_2]$ and the other involves $[\text{Zn}_4\text{O}(\text{OOCMe})_6]$, both of which were found to reach the heated substrate.

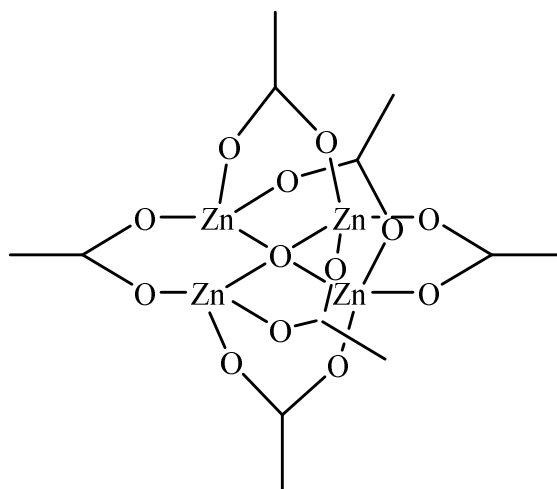


Figure 3.3: Structure of zinc oxyacetate $[\text{Zn}_4\text{O}(\text{OOCMe})_6]$.³⁰

$[\text{Zn}(\text{OOCMe})_2]$ was found to readily undergo clean decomposition during AACVD where the solvent is thought to also act as a proton donor.³³ Films were found to have transparencies $> 80\%$ to visible light, with resistances in the $\text{k}\Omega$ region and a dominant (002) peak in the XRD pattern, illustrating preferred orientation along the c-axis, particularly at higher temperatures. Thin films deposited employing zinc acetate by O'Brien *et al.*³⁴ by AACVD were hexagonal wurtzite ZnO with a spherical grain structure consistent with island growth with a sheet resistance of $17 \text{ k}\Omega/\square$ and $520 \text{ k}\Omega/\square$ when deposited at 400°C and 425°C respectively. The increase in resistivity at higher temperatures was attributed to CVD process factors. Although zinc $[\text{Zn}(\text{OOCMe})_2]$ is the most widely employed commercially available alternative to ZnEt_2 , zinc acetylacetonate and zinc 2-ethylhexanoate have also been investigated.

3.1.1.3 Zinc Acetylacetonate

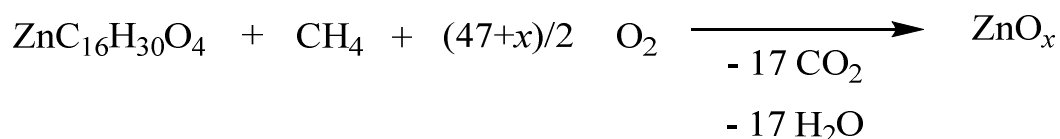
Zinc acetylacetonate $[\text{Zn}(\text{O}_2\text{C}_5\text{H}_7)_2]$ has been used to deposit ZnO thin films *via* APCVD and it undergoes decomposition between 80°C and 120°C .³⁵ This temperature range was used since TGA studies revealed $[\text{Zn}(\text{C}_5\text{H}_7\text{O}_2)_2]$ starts to decompose at about 85°C but melts at 124°C .¹ Once decomposed, oxidation *via* a number of sources including oxygen,³⁶ air,³⁷ hydrogen peroxide³⁸ and ozone³⁹ can occur. The ZnO has also been successfully doped with aluminium using aluminium acetylacetonate.^{38,1} Aluminium doped ZnO thin films have been deposited with transparency $> 80\%$ and a sheet resistance as low as $35 \Omega/\square$, however, a number of

reports describe the films as being of a ‘milky’ transparency.^{37,38} In this same work it was noted that as the amount of oxygen precursor supplied to the deposition increased, so did the crystallinity due to the removal of carbon contamination.³⁸ $[\text{Zn}(\text{O}_2\text{C}_5\text{H}_7)_2]$ has also successfully been used to deposit ZnO and Cu doped ZnO thin films *via* AACVD.⁴⁰ Precursors were dissolved in methanol and transported using a nitrogen carrier gas. The films deposited were highly transparent at around 85% transparency but were highly resistive with a sheet resistivity of 52.4 k Ω .

3.1.1.4 Zinc 2-Ethylhexanoate

Zinc 2-ethylhexanoate, $[\text{Zn}(\text{OOCCH}(\text{C}_2\text{H}_5)\text{C}_4\text{H}_9)_2]$ can be prepared by the reaction between ZnO and 2-ethylhexanoic acid and has also been used for the MOCVD of ZnO.⁴¹ Compressed air was used as both the reactant and carrier gas as oxygen gas was found to cause premature oxidation of the precursor. Films deposited below 400 °C were found to be translucent but transparent and crystalline when deposited above 400 °C.

Most studies however, use $[\text{Zn}(\text{OOCCH}(\text{C}_2\text{H}_5)\text{C}_4\text{H}_9)_2]$ in the combustion CVD (CCVD) of ZnO thin films. Li *et al.*⁴² dissolved $[\text{Zn}(\text{OOCCH}(\text{C}_2\text{H}_5)\text{C}_4\text{H}_9)_2]$ in ethanol which was atomised into droplets and carried in methane gas to a flame. The droplets were vaporised and reacted with the O_2 in the air to form ZnO, as shown in Scheme 3.4.



Scheme 3.4: Deposition of ZnO from zinc 2-ethylhexanoate



Stoichiometric thin films of ZnO were also deposited by CCVD by supplying dry oxygen to the system.⁴³ Polley and Carter⁴⁴ have also investigated the effect of deposition temperature and concentrations of the $[\text{Zn}(\text{OOCCH}(\text{C}_2\text{H}_5)\text{C}_4\text{H}_9)_2]$ precursor solution. CCVD of ZnO was achieved with substrate temperatures between

180 °C to 850 °C and solution concentrations of 0.0025, 0.005, 0.01, 0.02 and 0.04 M. The depositions yielded three different microstructures, as shown in Figure 3.4. Low substrate temperature and low precursor concentrations were found to favour the growth of amorphous ZnO, represented by Zone A. Smooth crystalline and small grained thin films were favoured at moderate substrate temperatures and low precursor concentrations, as represented by Zone T. At higher temperature, crystalline films grow with larger grain sizes, and falls into Zone II.

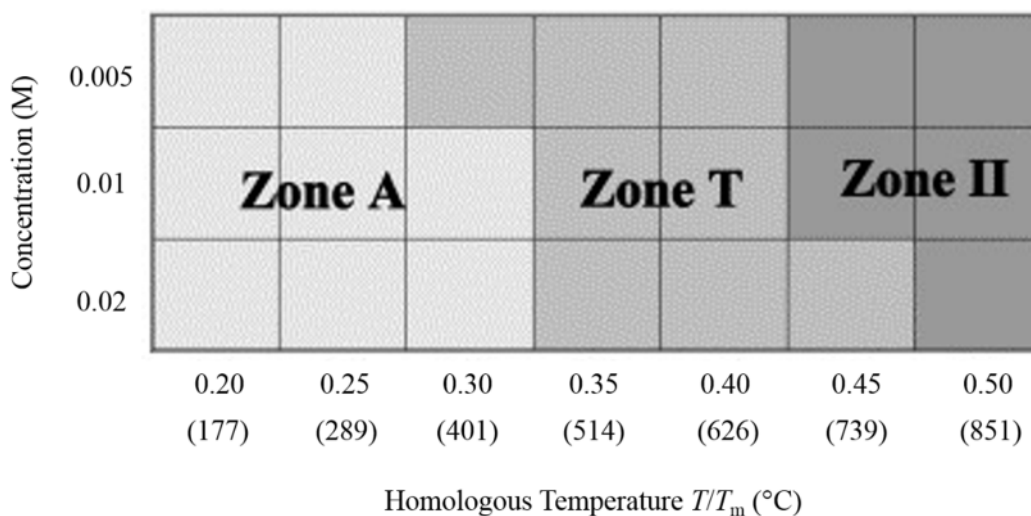


Figure 3.4: Deposition matrix of ZnO from zinc 2-ethylhexanoate



One relatively inexpensive and commercially available zinc complex which has not been used as a CVD precursor, possibly because of its lack of volatility is zinc triflate $[\text{Zn}(\text{OTf})_2]$.

3.1.1.5 Zinc Triflate

Zinc triflate is the most commonly used name for the zinc salt of trifluoromethanesulfonic acid, zinc trifluoromethanesulfonate $[\text{Zn}(\text{OTf})_2]$, shown in Figure 3.5. Dinnebier *et al.*⁴⁵ have successfully determined the crystal structure of $[\text{Zn}(\text{OTf})_2]$ using high-resolution synchrotron X-ray powder diffraction data. Zinc triflate is a Lewis ‘superacid’ catalyst⁴⁶ and has been used in a wide variety of organic reactions^{47,48,49} including carbonyl addition reactions, such as Henry reactions⁵⁰ and

alkylations such as Friedel-Crafts reactions.⁵¹ Zinc triflate has also appeared in the literature as the starting material in the synthesis of zinc β -ketoiminates, a class of complexes which are discussed further in Chapter 5.⁵²

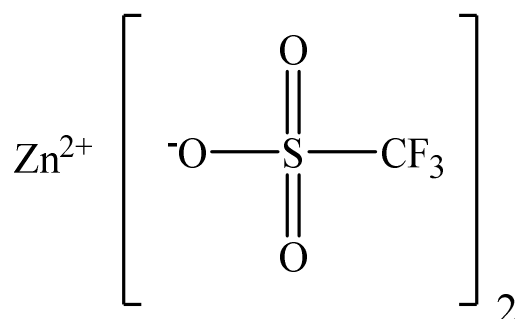
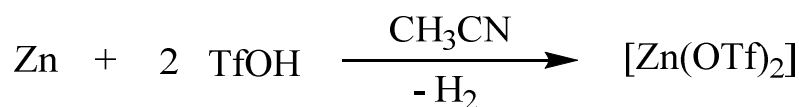
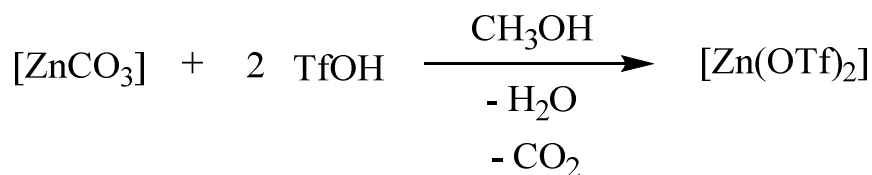


Figure 3.5: Zinc triflate [Zn(OTf)₂].

[Zn(OTf)₂] can be synthesised either by the reaction of zinc metal with two equivalence of triflic acid, as shown in Scheme 3.5 or by the reaction of zinc carbonate with two equivalence of triflic acid, as shown in Scheme 3.6.⁵³



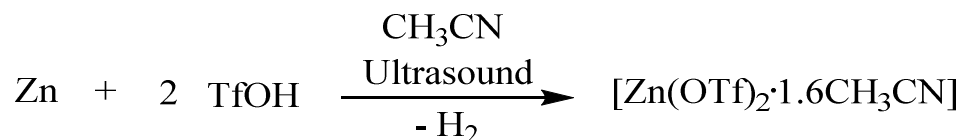
Scheme 3.5: Synthesis of zinc triflate [Zn(OTf)₂] from Zn metal.⁵³



Scheme 3.6: Synthesis of zinc triflate [Zn(OTf)₂] from zinc carbonate [ZnCO₃].⁵³

Legrave *et al.*⁵⁴ have also employed a method using ultrasonic activation to yield zinc triflate almost quantitatively from zinc dust and two equivalence of triflic acid in acetonitrile, as shown in Scheme 3.7. The reaction was carried out in different solvents yielding the salts [Zn(OTf)₂•4H₂O] and [Zn(OTf)₂•6DMF] when water and DMF

respectively were used as the solvents. Moreover, $[\text{Zn}(\text{OTf})_2]$ is also available commercially.



Scheme 3.7: Ultrasonic activated synthesis of zinc triflate $[\text{Zn}(\text{OTf})_2]$ from zinc metal.⁵⁴

$[\text{Zn}(\text{OTf})_2]$ contains both Zn and O atoms and has the potential to be used as a single-source precursor, however, like zinc acetate and zinc acetylacetonate, it is likely to require an additional oxygen source. $[\text{Zn}(\text{OTf})_2]$ offers a number of advantages, including being available commercially, of good purity, air stable and offers ease of handling. Given the limited number of commercially available and air stable precursors that have been used for the deposition of ZnO thin films, it was surprising that no reports of using $[\text{Zn}(\text{OTf})_2]$ as a CVD precursor were available in the literature. The results presented herein, further characterise $[\text{Zn}(\text{OTf})_2]$ to determine the performance of the complex in meeting other ideal precursors properties such as solubility for AACVD and its thermal stability and decomposition. The results expand on the literature with the novel use of $[\text{Zn}(\text{OTf})_2]$ as a precursor in the successful AACVD of ZnO thin films.

3.2 Results and Discussion

3.2.1 Precursor Properties

3.2.1.1 Solubility and Solvent Choice

Zinc triflate was added to a number of solvents that are typically used in the AACVD process in order to investigate its solubility. $[\text{Zn}(\text{OTf})_2]$ was not readily soluble in toluene, isopropanol, ethyl acetate and hexane. However, in all three of the polar protic solvents that zinc triflate was added to, namely water, methanol and ethanol, the complex was found to be fully and readily soluble. From these three solvents, methanol was selected as the solvent of choice. An initial study employing water as

the solvent was not successful as aerosol generation from the precursor solution proved near impossible and the deposition of a film could not be realised. With methanol, aerosol generation was facile and the precursor was successfully carried into the reactor using the solvent. By employing methanol as the solvent, the requirement that $[\text{Zn}(\text{OTf})_2]$ be soluble in a suitable solvent was met.

3.2.1.2 Thermal Gravimetric Analysis

Thermal gravimetric analysis (TGA) and differential scanning calorimetry (DSC) was performed on the $[\text{Zn}(\text{OTf})_2]$ precursor (17 mg, 4.68×10^{-5} mol) between room temperature (23 °C) and 600 °C in a helium atmosphere, as shown in Figure 3.6.

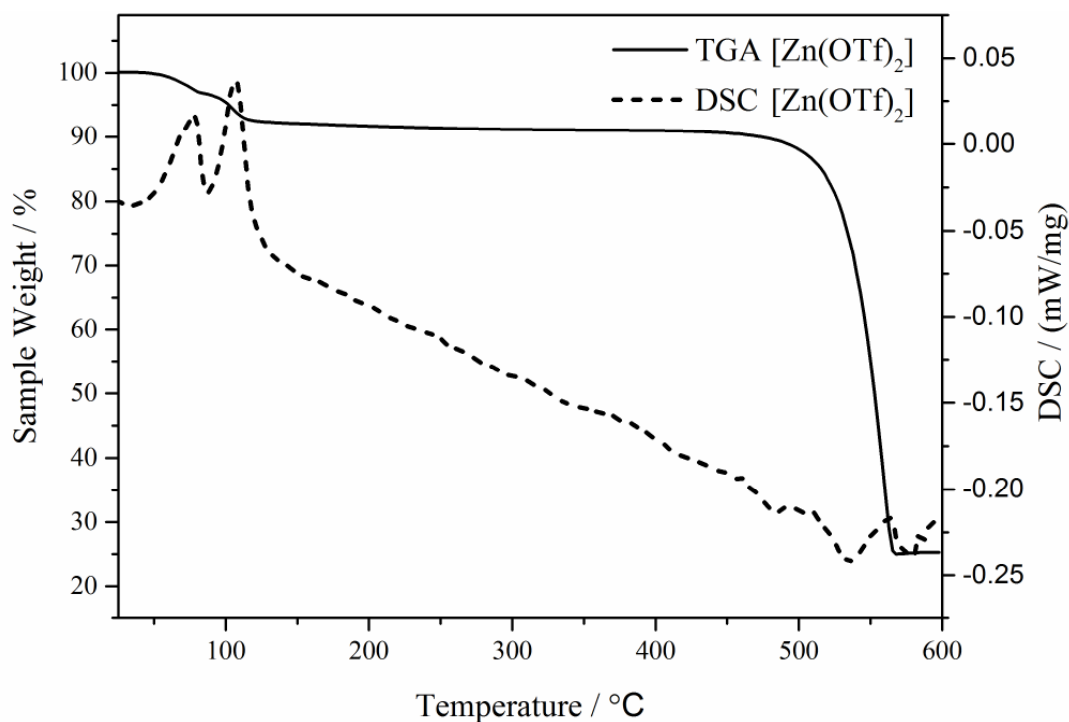


Figure 3.6: Thermal gravimetric analysis (TGA) and differential scanning calorimetry (DSC) of $[\text{Zn}(\text{OTf})_2]$.

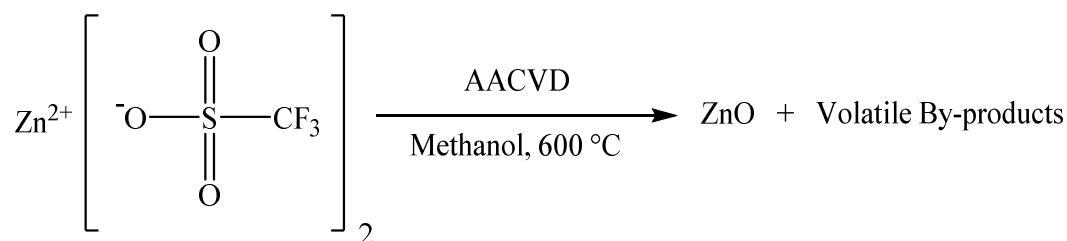
The initial mass loss observed in the TGA profile occurred between 40 and 120 °C and represented a 7 – 8% reduction in mass. Since $[\text{Zn}(\text{OTf})_2]$ is a hygroscopic powder, the mass lost is likely to be the loss of a residual solvent and water. It is likely that two residuals are lost as this would correspond with the two peaks observed in the DSC

thermogram. The mass is then stable until the onset of the decomposition of $[\text{Zn}(\text{OTf})_2]$ occurring at 500 °C. A clean decomposition in a single step was observed, predominantly between 520 – 565 °C. The DSC shows an initial energy requirement for the decomposition followed by an energy release. The calculated residual mass for ZnO from $[\text{Zn}(\text{OTf})_2]$ is 22.4% which compares very well to an observed residual mass of 22.7%, once the initial mass loss resulting from the residues is accounted for. This is a strong indication of clean decomposition of $[\text{Zn}(\text{OTf})_2]$ to ZnO. From the TGA profile it can be seen that decomposition occurs in a clean one step process to a mass corresponding to ZnO, illustrating the thermal suitability of $[\text{Zn}(\text{OTf})_2]$ as a Zn precursor. The residual masses for all complexes used as AACVD precursors presented in this thesis are shown in Appendix Table 7.1.

The decomposition temperature of $[\text{Zn}(\text{OTf})_2]$ is notably higher than many other precursors, including those synthesised and described in Chapter 4 and Chapter 5 but also those commercially available. For example, the decomposition of anhydrous zinc acetate is observed to occur between 150 and 282 °C.⁵⁵ The thermal analysis demonstrates that $[\text{Zn}(\text{OTf})_2]$ satisfies the ideal precursor property for clean decomposition. It also suggests that due to the high thermal stability of $[\text{Zn}(\text{OTf})_2]$, an elevated substrate temperature, above the 500 °C that decomposition of $[\text{Zn}(\text{OTf})_2]$ is observed to begin, will be required.

3.2.2 AACVD of ZnO and AZO Thin Films

ZnO thin films were successfully deposited from the AACVD of $[\text{Zn}(\text{OTf})_2]$ in methanol at 600 °C onto silica coated float-glass substrates, according to Scheme 3.8.

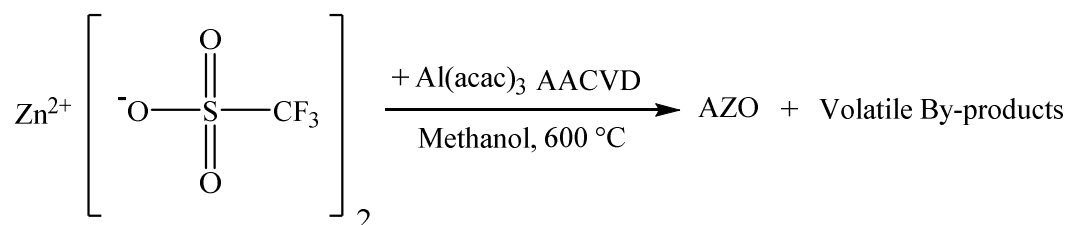


Scheme 3.8: AACVD of ZnO from $[\text{Zn}(\text{OTf})_2]$.

Studies into the optimal substrate temperature and nitrogen carrier gas flow rates were performed. Below 300 °C no deposition occurred. From 400 – 550 a non-adherent white crystalline powder was deposited which was believed to be unreacted starting material. With increasing temperature, the amount of powder deposition decreased with transparent film coverage increasing up to 600 °C. Increasing the temperature from 600 °C to 630 °C had no effect on the film deposited. Higher temperatures were not attempted as to avoid warping of the float-glass substrate. Similarly, the flow rate of the N₂ carrier gas into the reaction chamber was investigated between 0.5 and 4 Lmin⁻¹ and optimised at 1.2 Lmin⁻¹.

The deposited films were adherent to the glass substrate, passing the Scotch Tape test but removed upon scratching with a steel stylus. The films also exhibited good uniformity and coverage of the substrate. Solubility testing of the films indicated that the films were insoluble in organic solvents including THF, ethanol, methanol and toluene but decomposed in nitric acid. The films appeared highly transparent with a light brown tint, indicative of some carbon contamination. For each reaction, film deposition was observed to occur on both the glass substrate and the top plate held 6 mm above the substrate surface. The deposition on the top plate, measured to be 50-70 °C lower in temperature than that of the substrate, is attributed to thermophoretic effects.⁵⁶

The potential of this facile route is exemplified in the successful deposition of aluminium doped ZnO (AZO) thin films when aluminium acetylacetonate [Al(acac)₃] was added as a dopant source to the [Zn(OTf)₂] in methanol, as shown in Scheme 3.9.



Scheme 3.9: AACVD of aluminium zinc oxide (AZO) from [Zn(OTf)₂] and [Al(acac)₃].

The level of Al dopant introduced was investigated by the addition of [Al(acac)₃] in varying ratios to [Zn(OTf)₂] of between 0.02 – 0.2 molar ratio. The best functional

properties of high transparency and high electrical conductivity were observed for AZO films deposited when Al was added in a Al:Zn atomic ratio of 0.05:1. The aluminium doping of these films was found to be 7 at.% as determined by XPS. The physical properties of the AZO films were similar to those observed for the undoped ZnO films. All films were well adhered to the glass substrate, passing the Scotch Tape test but removed upon scratching with a steel stylus. Deposition was also observed to occur on both the substrate and top place, with good uniformity and coverage observed for the film deposited on the substrate. The films were insoluble in THF, ethanol, methanol and toluene but decomposed when in nitric acid. All films had a very light tint, indicative of minimal carbon contamination and appeared highly transparent, as later analysis confirmed.

3.2.3 Aside: Alternative Deposition Methods

The use of $[\text{Zn}(\text{OTf})_2]$ as an APCVD precursor was also attempted at the European Technical Centre of NSG in Lathom, Lancashire. However, as expected the attempts were unsuccessful given the lack of vaporisation from $[\text{Zn}(\text{OTf})_2]$. As an alternative, the $[\text{Zn}(\text{OTf})_2]$ was dissolved in methanol and used as a liquid injection (LI)CVD precursor. However, this also failed as the $[\text{Zn}(\text{OTf})_2]$ solidified before entering the CVD reactor and blocked the pipes in the rig. Finally, spray depositions of $[\text{Zn}(\text{OTf})_2]$ were investigated but again, as expected failed to deposit films given the high decomposition temperature required as observed in the TGA of $[\text{Zn}(\text{OTf})_2]$.

3.2.4 Film Characterisation

The deposited films were characterized by glancing-angle X-ray powder diffraction (XRD), X-ray photoelectron spectroscopy (XPS) and scanning electron microscopy (SEM). Optical and electrical measurements were also carried out in order to determine the functional properties of the deposited films. UV/Vis/NIR spectroscopy was used to determine the transparency of the films with four-point probe and hall effect measurements made to determine the sheet resistances, carrier concentrations, mobility and resistivity of the ZnO and AZO thin films.

3.2.4.1 X-ray Diffraction

Glancing-angle X-ray diffraction (XRD) patterns of the films were recorded and are shown in Figure 3.7. As expected, the peaks for the ZnO film confirm the formation of the hexagonal wurtzite crystal structure of ZnO. Significant preferred orientation was observed along the (002) plane resulting from the packing of the crystallites occurring along the c -axis direction, perpendicular to the underlying substrate.

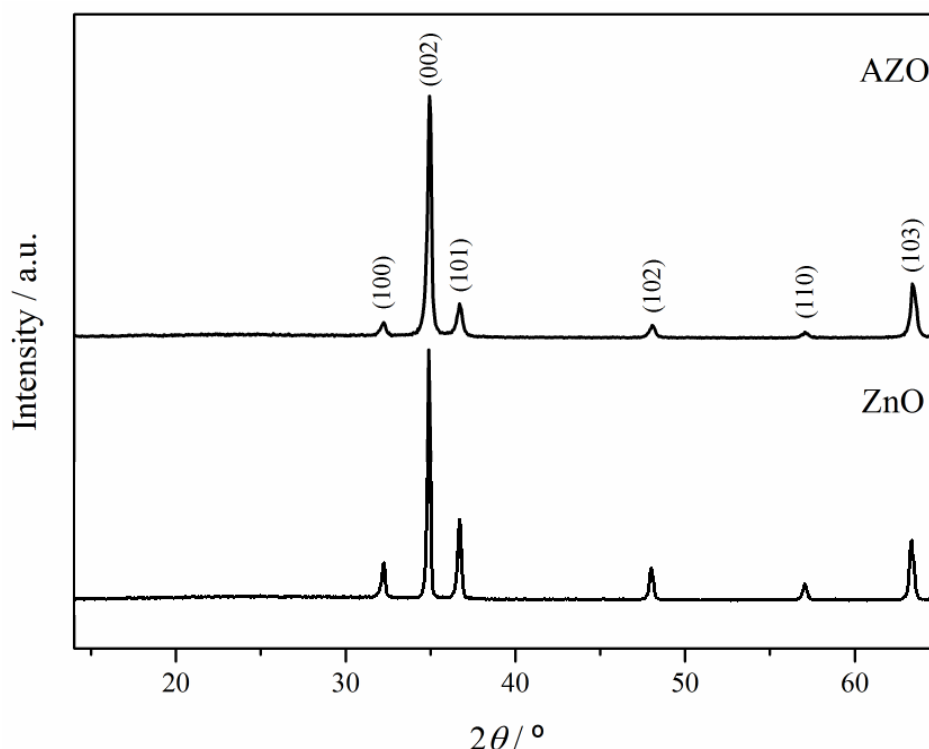


Figure 3.7: XRD pattern of the deposited ZnO and AZO from $[\text{Zn}(\text{OTf})_2]$ in methanol.

The same crystal structure was also observed for the AZO film. Upon doping of Al into the ZnO matrix there is a small (up to 0.1°) but observable shifting of the 2θ peak values to slightly higher values. This shifting results from the difference in ionic radius between the Zn^{2+} and Al^{3+} ions of 0.72 and 0.53 Å respectively.⁵⁷ For example, in the pattern for ZnO the (002) peak appears at 34.90° compared to 34.95° in the pattern for AZO. Hou *et al.*⁵⁸ have previously reported the 2θ peak values to shift to higher values in line with increasing Al doping. This shift is indicative of Al doping and is consistent with XPS analysis.

3.2.4.2 X-ray Photoelectron Spectroscopy

XPS of the ZnO films deposited from $[\text{Zn}(\text{OTf})_2]$ at 600 °C confirmed the presence of Zn and O and were consistent with XRD results that solely ZnO had been deposited. Peaks were observed for the Zn $2p_{1/2}$ and $2p_{3/2}$ states at 1045.3 and 1022.2 eV binding energy respectively, as expected with an intensity ratio of 1:2 and an energy gap of 23.1 eV,⁵⁹ as shown in Figure 3.8. The O 1s peak in the XPS data can be fitted by a Gaussian distribution and centered at 532.0 eV as expected.⁶⁰ For films doped with Al, the Al $2p_{1/2}$ and $2p_{3/2}$ peaks were observed at 75.1 and 74.7 eV respectively. These appear in a 1:2 ratio of intensity with an energy gap of 0.41 eV consistent with the value for Al^{3+} incorporation⁶¹ as shown in Figure 3.9. The peaks at 1045.7 and 1022.6 eV correspond to Zn $2p_{1/2}$ and $2p_{3/2}$, respectively, again in the 1:2 ratio, with an energy gap of 23.1 eV as expected.⁵⁹

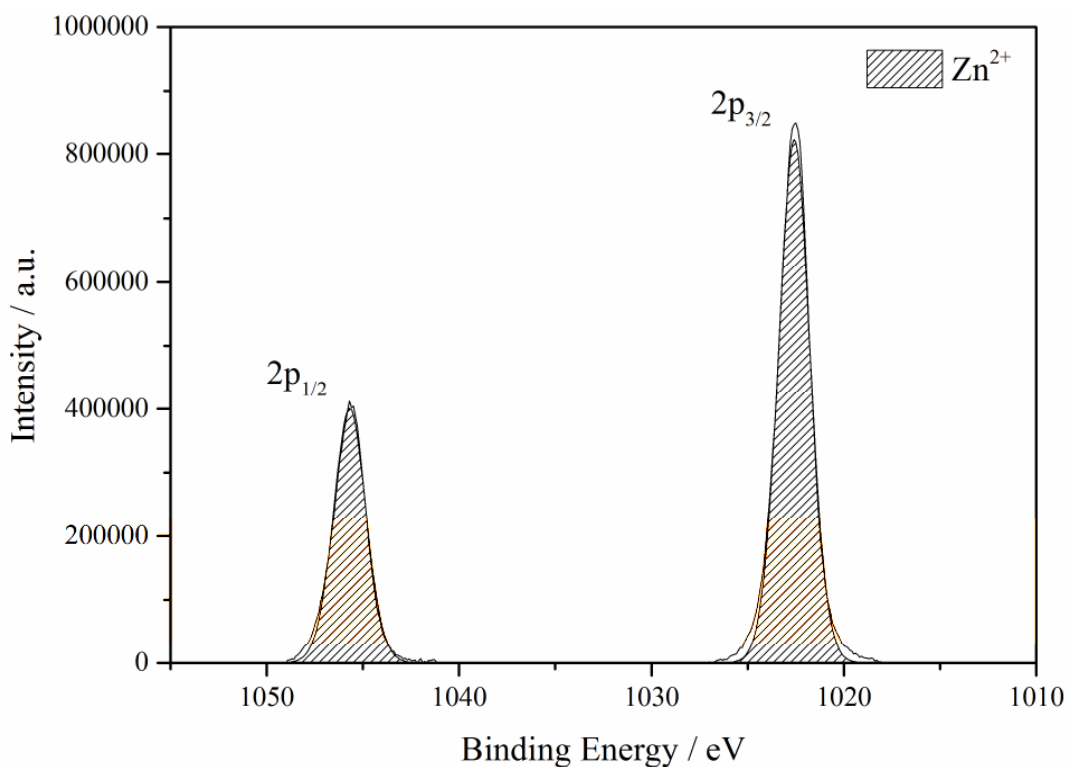


Figure 3.8: XPS of Zn 2p from an AZO film from $[\text{Zn}(\text{OTf})_2]$ and $[\text{Al}(\text{acac})_3]$.

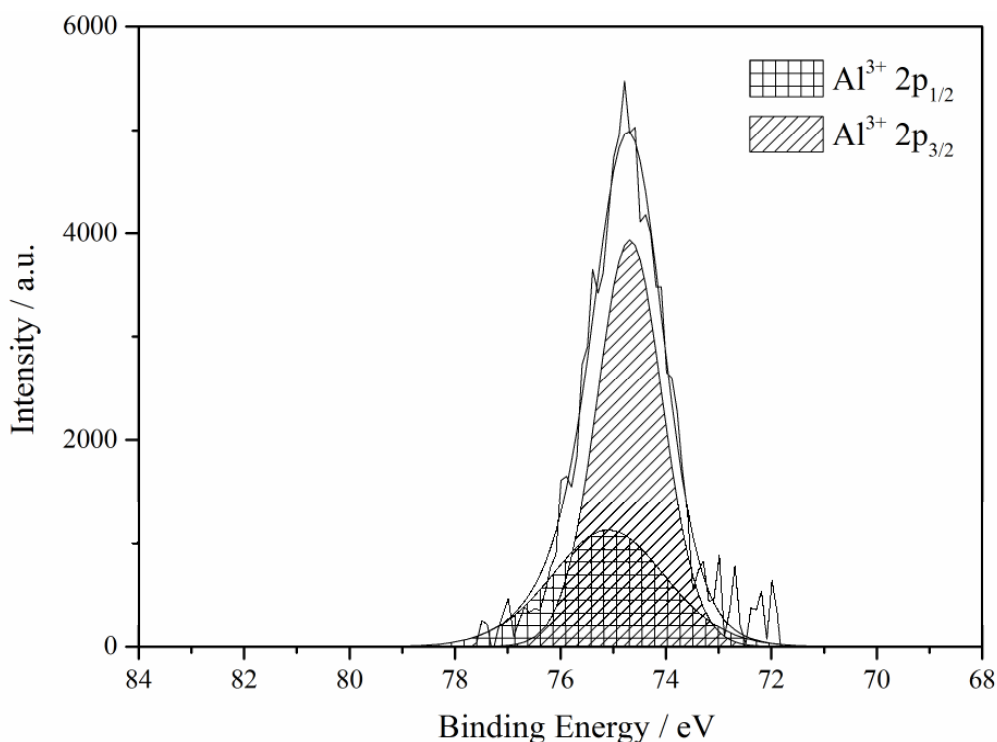


Figure 3.9: XPS of Al 2p from an AZO film deposited from [Zn(OTf)₂] and [Al(acac)₃].

3.2.4.2.1 Depth Profiling

Using scan mode, a depth profile for the ZnO and AZO samples were obtained. A 30 second etch time per level was used with 180 levels of total etching. The spectral regions for Zn 2p, O 1s, Al 2p and C 1s were scanned as well as a survey spectrum to detect any additional elements. The depth profile for the ZnO film is shown in Figure 3.10. The sample was shown to be predominantly ZnO with the presence of carbon and sulfur also found in the film. The ZnO thin film contained approximately 4 at.% sulfur contamination, originating from the triflate precursor. Carbon contamination was also present throughout the film at levels of approximately 7 at.% but significantly higher at 37 at.% closer to the surface of the film. The depth profile for AZO film deposited from [Zn(OTf)₂] and [Al(acac)₃] is shown in Figure 3.11 reveals the sample to be predominantly ZnO with an average Al doping concentration of 7 at.%. Carbon contamination was also detected throughout the AZO film but at a low level of 3 at.%. The carbon level was again much higher at 41 at.% closer to the surface of the film but this was observed to drop off much quicker than was observed for the ZnO film. The AZO film was also found to be free from the sulfur contamination that was present in the ZnO thin film.

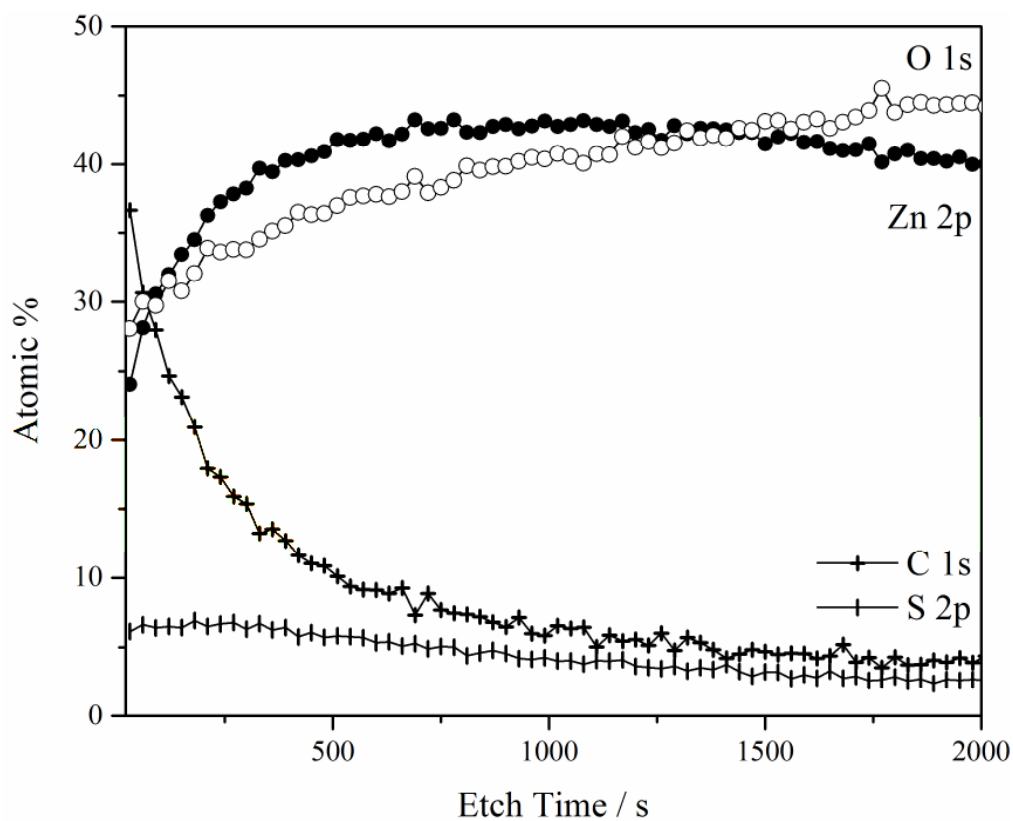


Figure 3.10: XPS depth profile for a ZnO thin film deposited from $[\text{Zn}(\text{OTf})_2]$.

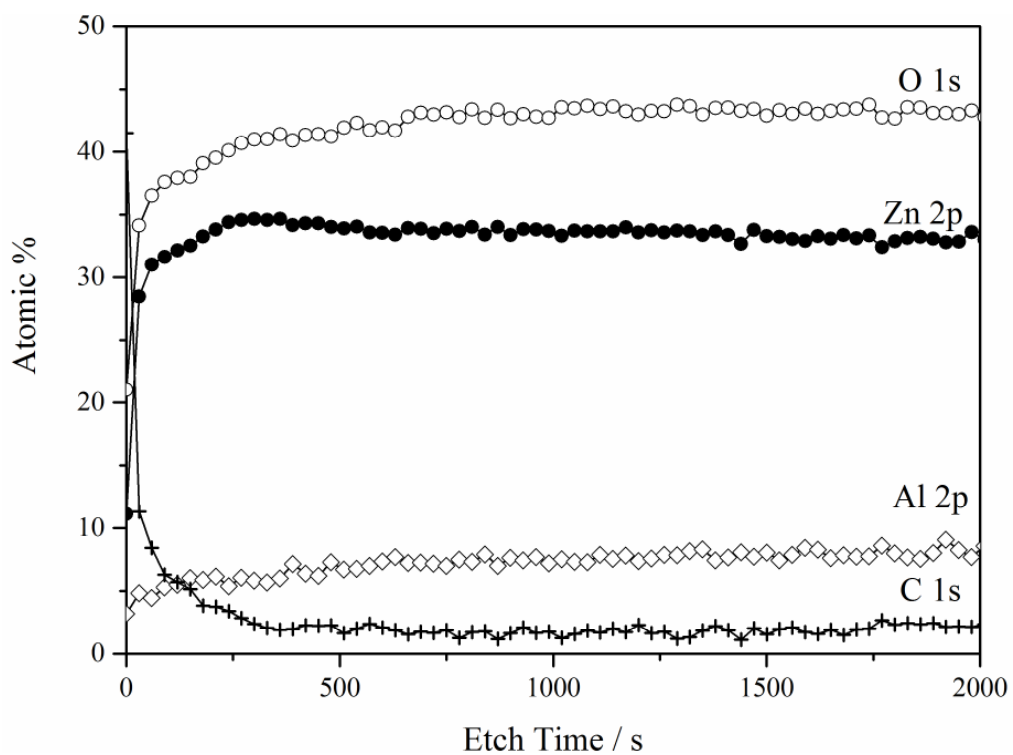


Figure 3.11: XPS depth profile for an AZO thin film deposited from $[\text{Zn}(\text{OTf})_2]$ and $[\text{Al}(\text{acac})_3]$.

3.2.4.3 Scanning Electron Microscopy

Scanning electron microscopy (SEM) images were taken to determine surface morphology and height profiles of the deposited films. Figure 3.12 (a) and (b) are plane view images at $\times 10,000$ magnification of ZnO and AZO respectively.

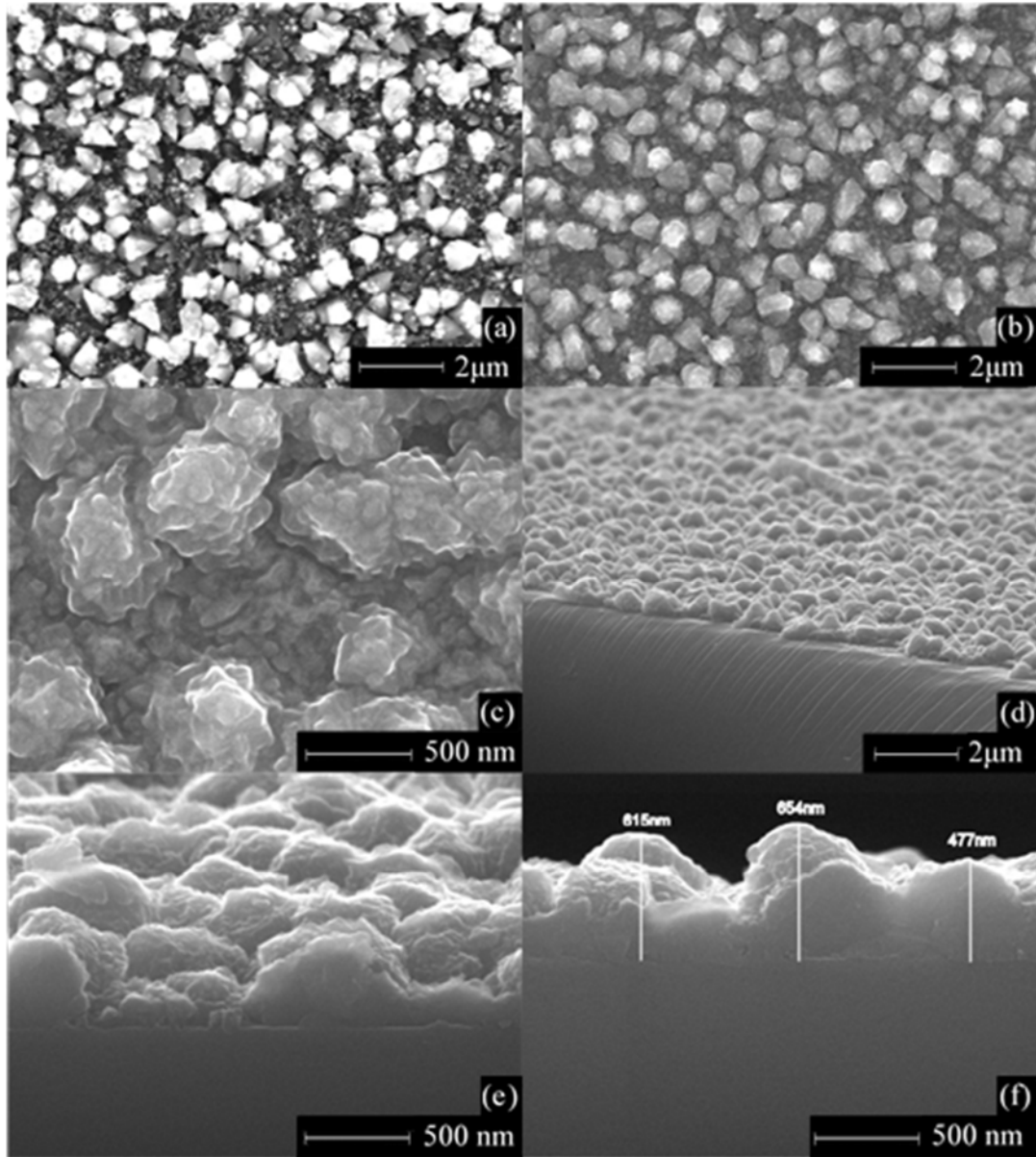


Figure 3.12: Plane view (a) – (c) and cross section (d) – (f) SEM images of (a) ZnO and (b) – (f) AZO films deposited at 600 °C by AACVD from $[\text{Zn}(\text{OTf})_2]$ in methanol.

The images show a film structure of rounded agglomerated particles which is indicative of a Volmer-Weber type island growth mechanism. This occurs when

depositing particles have a stronger attraction to themselves as opposed to the substrate, forming a film as the gaps between the islands fill. Figure 3.12 (c), a plane view image of the AZO film at $\times 50,000$ magnification shows in greater detail the particle cluster growth of the film. The surface morphology of the ZnO films appears not to change upon doping with Al. Cross section images of the films were also taken. Figure 3.12 (d) and (e) are cross section images at an 80° tilt at $\times 10,000$ magnification and $\times 50,000$ magnification respectively. These images show that the coatings consist of larger agglomerates of particles with smaller groupings of particles between these larger agglomerates. The particle clusters are quite pronounced with noticeable height differences, as shown in Figure 3.12 (f), a cross section image at 90° tilt at $\times 50,000$ magnification. The lowest thickness of film was 250 nm with the highest cluster point being 655 nm. Film thickness was also measured using a Filmetrics analyzer system and for the AZO films a thickness range of 470 – 500 nm was recorded. The ZnO films were thinner, 450 – 470 nm, but had the same pattern of varying heights of agglomerate clusters.

3.2.4.4 Functional Properties

3.2.4.4.1 Optical Properties

The transmission characteristics of the ZnO and AZO films were investigated using UV/vis/near IR spectrometry, recorded between 250 and 1400 nm, as shown in Figure 3.13. The ZnO film has an average transparency of 79%, which peaks at 80% in the visible light region. The AZO film was found to have a slightly higher average transparency at 83%, which peaks at 85% in the visible light region. The AZO film has a transparency greater than the 80% in the visible light region, the benchmark value often quoted for films to be described as highly transparent.⁶²

3.2.4.4.1.1 Band Gap

The sharp decrease in transmission of the deposited films between 300 and 400 nm is a result of the onset of fundamental adsorption. This has been used to estimate the optical band gap of the films using the Tauc relation⁶³ in Equation 3.1. The estimate

is made by finding the intercept of the $h\nu$ axis from a line of steepest gradient for the linear region of a $(\alpha h\nu)^{1/2}$ vs. $h\nu$ plot, as shown in Figure 3.13 (Inset).

$$\alpha h\nu = A(h\nu - E_g)^n \quad \text{Equation 3.1}$$

In Equation 3.1, A is a constant, α is the molar extinction coefficient, $h\nu$ is the photon energy, E_g is the band gap and $n = 1/2$ for a direct allowed transition. The band gap of the ZnO and AZO films were determined to be 3.7 and 3.9 eV respectively.

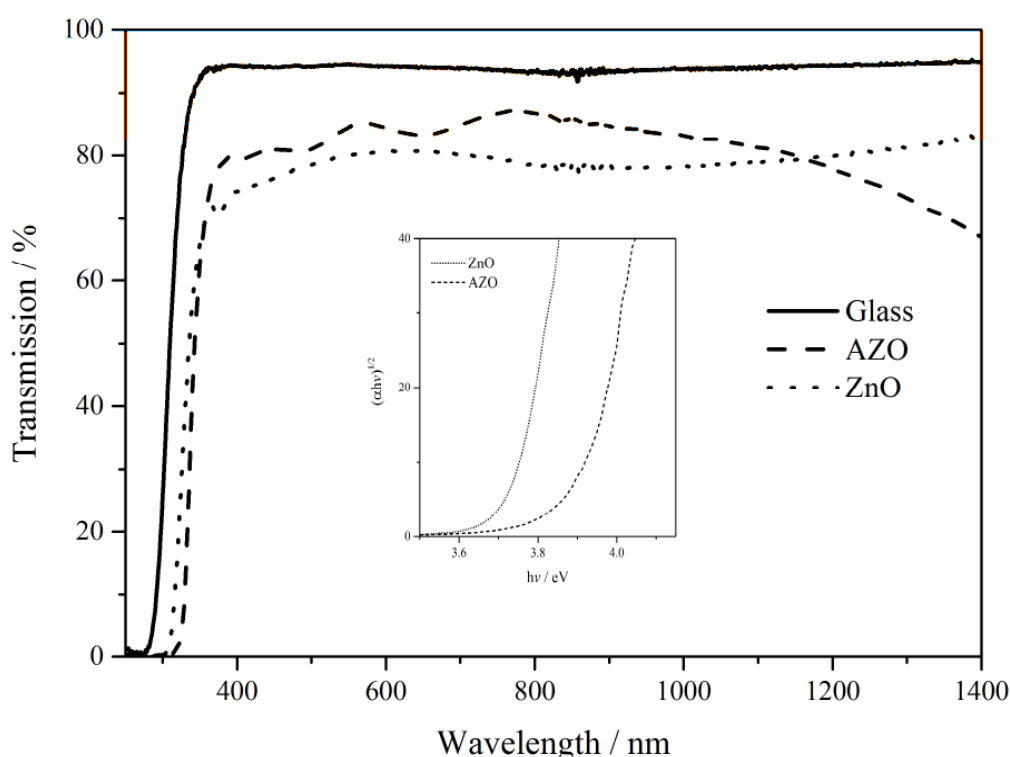


Figure 3.13: Transmission spectra for ZnO and AZO films deposited from $[\text{Zn}(\text{OTf})_2]$ and $[\text{Al}(\text{acac})_3]$ Inset: Tauc plots for ZnO and AZO films.

The band gap increases slightly upon doping with Al as a result of the Burstein-Moss effect.^{64,65} The doping by aluminium gives rise to additional electrons which populate the lower levels of the conduction band, resulting in an increased band gap. The band gap value of 3.7 eV determined for the ZnO film is greater than the 3.37 eV value for bulk ZnO.⁶⁶ Higher band gaps for ZnO thin films are also reported in the literature, for example, Bhachu *et al.*⁶⁷ also report a band gap value of 3.7 eV for ZnO thin films

deposited *via* AACVD from ZnEt_2 in methanol. Purica *et al.*³⁵ also report higher than expected bandgaps for ZnO thin films and attribute the phenomenon to the presence of a polycrystalline phase of different grain sizes. The increased band gap for these films is likely to be as a result of the impurities present as observed in the XPS results.

3.2.4.4.2 Electrical Properties

Four-point probe measurements were taken of the ZnO and AZO films deposited at 600 °C. Both films were highly conductive with sheet resistances of 70 Ω/\square for ZnO, decreasing to 15 Ω/\square for the AZO film doped with Al at 7 at.%. The value for the AZO film is comparable with other reported literature values for AZO deposited by AACVD, where a minimum sheet resistance of 18 Ω/\square was achieved at an Al doping of 6 at.%. The film however had a lower transparency of 72% across the visible light region and was deposited using zinc acetate dehydrate as a precursor.⁶⁸ AZO thin films with a lower sheet resistance have been realised *via* alternative deposition techniques, for example a rf magnetron sputtered AZO thin film with a 4.3 at.% doping of Al has been reported with a sheet resistance as low as 4.9 Ω/\square .⁶⁹

The electrical properties are noticeably improved for the AZO thin films as a result of increased carrier concentration and mobility of the carriers. The ZnO films had a carrier concentration of $2.24 \times 10^{20} \text{ cm}^{-3}$, mobility value of $9.3 \text{ cm}^2 (\text{V s})^{-1}$ and resistivity of $2.86 \times 10^{-3} \Omega \text{ cm}$. The doped AZO films had an increased carrier concentration and mobility of $3.03 \times 10^{20} \text{ cm}^{-3}$ and $10.5 \text{ cm}^2 (\text{V s})^{-1}$ respectively resulting in a decrease in the observed resistivity to $1.96 \times 10^{-3} \Omega \text{ cm}$. Although these electrical results are promising, there is still a long way to go before they match those of ITO. Thin films of ITO deposited by spray CVD have been reported with a resistivity as low as $2.6 \times 10^{-4} \Omega \text{ cm}$ ⁷⁰ and as low as $1.4 \times 10^{-4} \Omega \text{ cm}$ for those deposited by AACVD.⁷¹

3.3 Potential of Triflate Precursors

Initial studies into the potential use of magnesium triflate [$\text{Mg}(\text{OTf})_2$] as a CVD precursor were also performed. The decomposition properties of [$\text{Mg}(\text{OTf})_2$] were investigated using TGA and DSC and the profiles were found to have a similar pattern

to those observed for $[\text{Zn}(\text{OTf})_2]$, as shown in Figure 3.14. Once the loss of residual solvent and/or water is taken account for, a clean one step decomposition was observed, which occurred at around 80 °C lower than it did for $[\text{Zn}(\text{OTf})_2]$. $[\text{Mg}(\text{OTf})_2]$ was also found to be readily soluble in water, ethanol and methanol, which was also the case for $[\text{Zn}(\text{OTf})_2]$. These results suggest the potential use of other metal triflates, including $[\text{Mg}(\text{OTf})_2]$ as CVD precursors.

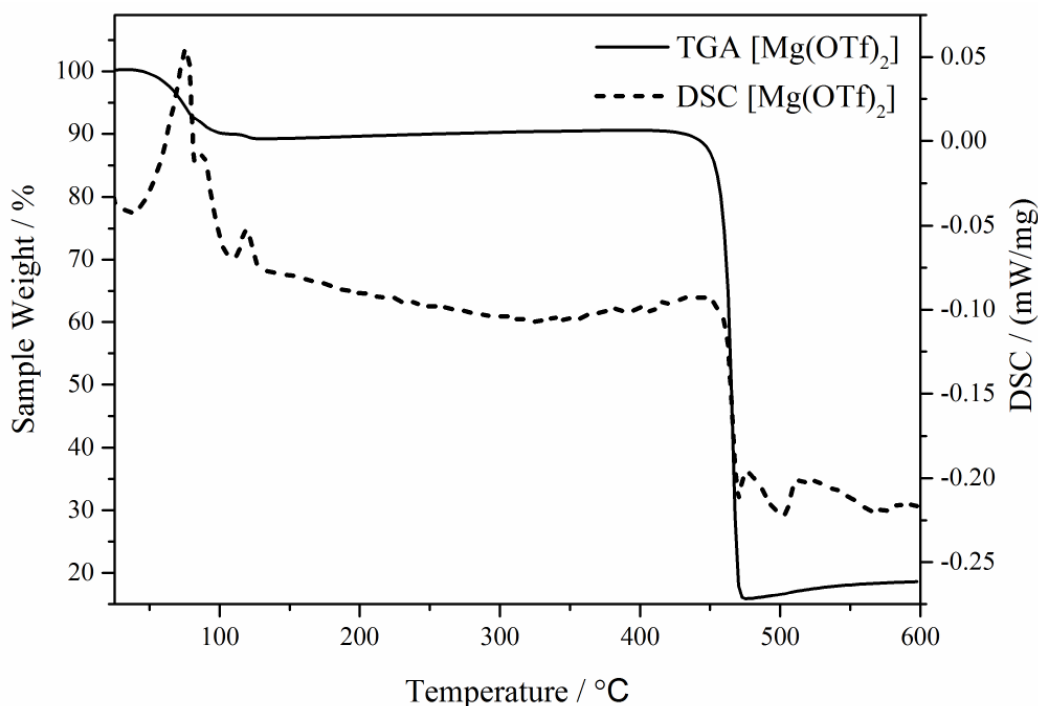


Figure 3.14: Thermal Gravimetric Analysis (TGA) and Differential Scanning Calorimetry (DSC) for $[\text{Mg}(\text{OTf})_2]$.

A PCT (patent cooperation treaty) application was filed by the Intellectual Property Portfolio team at NSG in February 2015 based on the work presented in this chapter. The patent application relates to the process of depositing metal oxide films from metal sulfonate precursors, preferentially metal triflate precursors, in an oxygenated solvent using an atomised solution such as AACVD. The $[\text{Zn}(\text{OTf})_2]$ system presented in this thesis was used throughout the patent application as the given example.

3.4 Conclusion

This work reports the first deposition of ZnO from [Zn(OTf)₂] *via* AACVD. TGA and DSC analysis of [Zn(OTf)₂] showed the precursor to have good thermal and decomposition properties and although sulfur and carbon contamination were observed, ZnO films with a transparency of 79% and a low sheet resistance of 70 Ω/\square were deposited. When [Al(acac)₃] was added to the precursor solution at a ratio of 0.05:1 of Al:Zn, AZO films free of sulfur contamination and reduced carbon contamination were deposited. Optimal coverage and adherence was observed using a deposition temperature of 600 °C resulting in films with the crystalline hexagonal wurtzite crystal structure of ZnO with significant preferred orientation was observed along the (002) plane. At a Al doping ratio of 7 at.%, as confirmed by XPS, AZO films with an average transparency of 83% and a low sheet resistance of 15 Ω/\square were deposited. The results have been used as the basis of a PCT patent application covering the deposition of metal oxide films from metal sulfonate precursors.

3.5 References

1. A. Nebatti, C. Pflitsch, B. Curdts, B. Atakan, *Mater. Sci. Semicond. Process.*, 2015, **39**, 467 – 475.
2. D. Seyferth, *Organometallics*, 2001, **20**, 2940 – 2955.
3. M. H. Abraham, *J. Chem. Soc.*, 1960, 4130 – 4135.
4. A. G. Davies and B. P. Roberts, *J. Chem. Soc. B*, 1968, 1074 – 1078.
5. J. Lewiński, W. Śliwiński, M. Dranka, I. Justyniak and J. Lipkowski, *Angew. Chem.*, 2006, **118**, 4944 – 4947.
6. A. P. Roth and D. F. Williams, *J. Appl. Phys.*, 1981, **52**, 6685 – 6692.
7. C. K. Lau, S. K. Tiku and K. M. Lakin, *J. Electrochem. Soc.*, 1980, **127**, 1843 – 1847.
8. X. Li, Y. Yan, T. A. Gessert, C. DeHart, C. L. Perkins D. Young and T. J. Coutts, *Electrochem. Solid-State Lett.*, 2003, **6**, C56 – C58.
9. Z. Fu, B. Lin and J. Zu, *Thin Solid Films*, 2002, **402**, 302 – 306.
10. O. Pagni, N. N. Somhlahllo, C. Weichsel and A. W. R. Leitch, *Phys. B Condens. Matter*, 2006, **376** – **377**, 749 – 751.
11. S. D. Ponja, S. Sathasivam, I. P. Parkin and C. J. Carmalt, *RSC Adv.*, 2014, **4**, 49723 – 49728.
12. S. Nicolay, M. Benkhaira, L. Ding, J. Escarre, G. Bugnon, F. Meillaud and C. Ballif, *Sol. Energy Mater. Sol. Cells*, 2012, **105**, 46 – 52.
13. J. van Deelen, A. Illiberi, B. Kniknie, H. Steijvers, A. Lankhorst and P. Simons, *Surf. Coat. Technol.*, 2013, **230**, 239 – 244.
14. B. Hahn, G. Heindel, E. Pschorr-Schoberer and W. Gebhardt, *Semicond. Sci. Technol.*, 1998, **13**, 788 – 791.
15. J. Auld, D. J. Houlton, A. C. Jones, S. A. Rushworth, M. Azad Malik, P. O'Brien and G. W. Critchlow, *J. Mater. Chem.*, 1994, **4**, 1249 – 1253.
16. J. Lewiński, W. Marciniak, J. Lipkowski and I. Justyniak, *J. Am. Chem. Soc.*, 2003, **125**, 12698 – 12699.
17. S. Jana, R. J. F. Berger, R. Fröhlich, T. Pape and N. W. Mitzel, *Inorg. Chem.*, 2007, **46**, 4293 – 4297.
18. N. Hollingsworth, A. L. Johnson, A. Kingsley, G. Kociok-Köhn and K. C. Molloy, *Organometallics*, 2010, **29**, 3318 – 3326.
19. N. G. Nguyen, V. T. T. Ho and L.-S. Hong, *Appl. Phys. Lett.*, 2013, **102**, 181912(1) – 181912(4).
20. W.-H. Kim, W. J. Maeng, M.-K. Kim and H. Kim, *J. Electrochem. Soc.*, 2011, **158**, D495 – D499.
21. H. Liang and R. G. Gordon, *J. Mater. Sci.*, 2007, **42**, 6388 – 6399.
22. S. Park, J. Park, Y. Z. Yoo, J. Y. Lee, S. H. Kim, G. S. Yoon, M. W. Kim, H. S. Shin, S. H. Yoo, S. D. Lee, S. I. Lee and S. J. Yim, 2014, Patent EP2719795A1, CN103710680A and US2014009443.
23. M. Ohyama, H. Kouzuka and T. Yoko, *Thin Solid Films*, 1997, **306**, 78 – 85.
24. E. Bacaksiz, M. Parlak, M. Tomakin, A. Özçelik, M. Karakiz and M. Altunbaş, *J. Alloys Compd.*, 2008, **466**, 447 – 450.
25. J. Lu, Z. Ye, L. Wang, J. Huang, and B. Zhao, *Mater. Sci. Semicond. Process.*, 2002, **5**, 491 – 496.
26. M. Labeau, P. Rey, J. L. Deschanvres, J. C. Joubert and G. Delabougliise, *Thin Solid Films*, 1992, **213**, 94 – 98.
27. T. Maruyama and J. Shionoya, *J. Mater. Sci. Lett.*, 1992, **11**, 170 – 172.

28. G. L. Mar, P. Y. Timbrell and R. N. Lamb, *Chem. Mater.*, 1995, **7**, 1890 – 1896.
29. A. K. Gyani, O. F. Z. Khan, P. O'Brien and D. S. Urch, *Thin Solid Films*, 1989, **182**, L1 – L4.
30. H. Koyama and Y. Saito, *Bull. Chem. Soc. Jpn.*, 1954, **27**, 112 – 114.
31. L. G. Mar, P. Y. Timbrell and R. N. Lamb, *Thin Solid Films*, 1993, **223**, 341 – 347.
32. S. Jain, T. T. Kodas and M. Hampden-Smith, *Chem. Vap. Depos.*, 1998, **4**, 51 – 59.
33. M. R. Waugh, G. Hyett and I. P. Parkin, *Chem. Vap. Depos.*, 2008, **14**, 366 – 372.
34. S. O'Brien, M. G. Nolan, M. Çopuroglu, J. A. Hamilton, I. Povey, L. Pereira, R. Martins, E. Fortunato and M. Pemble, *Thin Solid Films*, 2010, **518**, 4515 – 4519.
35. M. Purica, E. Budianu, E. Rusu, M. Danila and R. Gavrila, *Thin Solid Films*, 2002, **403 – 404**, 485 – 488.
36. Y. Kashiwaba, F. Katahira, K. Haga, T. Sekiguchi and H. Watanabe, *J. Cryst. Growth*, 2000, **221**, 431 – 434.
37. T. Minami, H. Sato, H. Sonohara, S. Takata, T. Miyata and I. Fukuda, *Thin Solid Films*, 1994, **253**, 14 – 19.
38. H. Sato, T. Minami, T. Miyata, S. Takata and M. Ishii, *Thin Solid Films*, 1994, **246**, 65 – 70.
39. K. Haga, F. Katahira and H. Watanabe, *Thin Solid Films*, 1999, **343 – 344**, 145 – 147.
40. G. Walters and I. P. Parkin, *Appl. Surf. Sci.*, 2009, **255**, 6555 – 6560.
41. N. D. Kumar, M. N. Kamalasanan and S. Chandra, *Appl. Phys. Lett.*, 1994, **65**, 1373 – 1375.
42. Z.-Y. Li, F. Xu, Q.-H. Wu, and J. Li, *Appl. Surf. Sci.*, 2008, **255**, 2859 – 2863.
43. T. A. Polley, W. B. Carter and D. B. Poker, *Thin Solid Films*, 1999, **357**, 132 – 136.
44. T. A. Polley and W. B. Carter, *Thin Solid Films*, 2001, **384**, 177 – 184.
45. R. Dinnebier, N. Sofina, L. Hildebrandt and M. Jansen, *Acta Cryst. B*, 62, 467 – 473.
46. J.-F. Gal, C. Iacobucci, I. Monfardini, L. Massi, E. Duñach and S. Olivero, *J. Phys. Org. Chem.*, 2013, **26**, 87 – 97.
47. J. Yang, M. R. Karver, W. Li, S. Sahu, and N. K. Devaraj, *Angew. Chem. Int. Ed.*, 2012, **51**, 5222 – 5225.
48. S. Murarka and A. Studer, *Org. Lett.*, 2011, **13**, 2746 – 2749.
49. M. Viji and R. Nagarajan, *RSC Adv.*, 2012, **2**, 10544 – 10549.
50. C. Palomo, M. Oiarbide and A. Laso, *Angew. Chem. Int. Ed.*, 2005, **44**, 3881 – 3884.
51. S.-F. Lu, D.-M. Du and J. Xu, *Org. Lett.*, 2006, **8**, 2115 – 2118.
52. D. M. Granum, P. J. Riedel, J. A. Crawford, T. K. Mahle, C. M. Wyss, A. K. Begei, N. Arulsamy, B. S. Pierce and M. P. Mehn, *Dalton Trans.*, 2011, **40**, 5881 – 5890.
53. P. Ham, J. Deng, S. Selvakumar and M. P. Sibi, Zinc Trifluoromethanesulfonate in *Encyclopedia of Reagents for Organic Synthesis*, John Wiley & Sons, Ltd, 2011, pp. 1 – 11.
54. N. Legrave, A. Couhert, S. Olivero, J.-R. Desmurs and E. Duñach, *Eur. J. Org. Chem.*, 2012, **5**, 901 – 904.

-
55. A. V. Ghule, K. Ghule, C.-Y. Chen, W.-Y. Chen, S.-H. Tzing, H. Chang and Y.-C. Ling, *J. Mass Spectrom.*, 2004, **39**, 1202 – 1208.
 56. C. E. Knapp, G. Hyett, I. P. Parkin and C. J. Carmalt, *Chem. Mater.*, 2011, **23**, 1719 – 1726.
 57. R. K. Shukla, A. Srivastava, A. Srivastava, and K. C. Dubey, *J. Cryst. Growth*, 2006, **294**, 427 – 431.
 58. Q. Hou, F. Meng and J. Sun, *Nanoscale Res. Lett.*, 2013, **8**, 144(1) – 144(8).
 59. B. S. Shaheen, H. G. Salem, M. A. El-Sayed and N. K. Allam, *J. Phys. Chem. C*, 2013, **117**, 18502 – 18509.
 60. R. Ayouchi, D. Leinen, F. Martín, M. Gabas, E. Dalchiele and J. R. Ramos-Barrado, *Thin Solid Films*, 2003, **426**, 68 – 77.
 61. H. Alarcón, M. Hedlund, E. M. J. Johansson, H. Rensmos, A. Hagfeldt and G. Boschloo, *J. Phys. Chem. C*, 2007, **111**, 13267 – 13274.
 62. S. Kaleemulla, N. M. Rao, M. G. Joshi, A. S. Reddy, S. Uthanna and P. S. Reddy, *J. Alloys Compd.*, 2010, **504**, 351 – 356.
 63. J. Tauc, *Mater. Res. Bull.*, 1968, **3**, 37 – 46.
 64. E. Burstein, *Phys. Rev.*, 1954, **93**, 632 – 633.
 65. T. S. Moss, *Proc. Phys. Soc. Sect. B*, 1954, **67**, 775 – 782.
 66. S. T. Tan, B. J. Chen, X. W. Sun, W. J. Fan, H. S. Kwok, X. H. Zhang and S. J. Chua, *J. Appl. Phys.*, 2005, **98**, 013505(1) – 013505(5).
 67. D. S. Bhachu, G. Sankar and I. P. Parkin, *Chem. Mater.*, 2012, **24**, 4704 – 4710.
 68. X.-J. Qin, S.-H.-Z. Han, L. Zhao, H.-T. Zuo and S.-T. Song, *J. Inorg. Mater.*, 2011, **26**, 607 – 612.
 69. N. Hirahara, B. Onwona-Agyeman and M. Nakao, *Thin Solid Films*, 2012, **520**, 2123 – 2127.
 70. T. Kondo, Y. Sawada, H. Funakubo, K. Akiyama, T. Kiguchi, M. Wang and T. Uchida, *Electrochem. Solid-State Lett.*, 2009, **12**, D42 – D44.
 71. K. Maki, N. Komiya and A. Suzuki, *Thin Solid Films*, 2003, **445**, 224 – 228.

Chapter 4

Synthesis of Zinc Oxane Complexes and the AACVD of Zinc Oxide Thin Films

*This chapter describes the synthesis of zinc oxane complexes of two structural types. Zinc trimer complexes $[(\text{Zn}(\text{Et})(\text{OC}(\text{R})\text{CHC}(\text{Me})\text{O}))_3]$ (**1**) – (**4**) where $\text{R} = \text{OMe}$ (**1**), Me (**2**), OEt (**3**) and O^tBu (**4**) were synthesised following an ethane elimination reaction between ZnEt_2 and the corresponding dicarbonyl compound. Zinc oxane clusters $[(\text{Zn}(\text{OC}(\text{R})\text{CHC}(\text{Me})\text{O})_2\text{Zn}(\text{Et})\text{OEt})_2]$ (**5**) – (**8**) with a face-shared, corner-removed, inversion-related, bis-heterocubane central structure, where $\text{R} = \text{OMe}$ (**5**), Me (**6**), OEt (**7**) and O^tBu (**8**) were synthesised following the selective in situ oxidation of solutions of (**1**) – (**4**) respectively. The oxane complexes were isolated and characterised with crystal structures determined for zinc oxane (**1**), (**6**) and (**8**). As a proof of concept, (**6**) was employed as a single-source precursor in the AACVD of hexagonal wurtzite ZnO thin films.*

4.1 Introduction

As discussed in Chapter 3, the most widely used precursor for ZnO thin films is ZnEt_2 , a precursor which requires an additional oxygen source to form the desired material.^{1,2} The *in situ* species in these reactions are alkylzinc alkoxides, which can also be isolated as single-source precursors for ZnO.³ It was also discussed in Chapter 3 that when dioxygen was used as the oxygen source the alkylzinc alkoxides were observed to form heterocubane structures.⁴ The structural diversity of these complexes is significantly increased when oxygen containing organic ligands are used as the oxygen source. This chapter investigates such reactions and the wide structural motifs of the zinc oxane products.

Prochowicz *et al.*⁵ define zinc oxanes as compounds, either molecular or aggregated, with Zn-O-Zn bonds and pendant organic substituents. These complexes are of interest for use in a number of applications including as initiators for ring opening polymerisation reactions,⁶ as potential precursors towards photoluminescent materials⁷ and as single-source precursors for the growth of ZnO nanocrystals.⁸ One particular noteworthy investigation found that zinc oxane compounds with different core structures resulted in ZnO nanoparticles with different morphologies, sizes and aspect ratios.⁹ Zinc oxanes are also of interest as potential single-source precursors for CVD applications,¹⁰ particularly so given their high number of Zn-O bonds. Synthesising precursors with the desired properties for CVD applications is a growing challenge,^{11,12} and one in which zinc oxane complexes may offer some potential.

4.1.1 Zinc Oxane Structures

There is also academic interest in zinc oxane complexes, including in the diversity of their central motifs, a selection of which are shown in Figure 4.1. These can include ring structures such as those seen in Figure 4.1 (a) – (c) as well as cubane motifs, shown in Figure 4.1 (d) – (f). A variety of zinc oxane central structures can result from the reactions of oxygen containing ligands with ZnEt_2 but also the further oxidation of these products by O_2 . As eluded to in Chapter 3.1.1.1, the mechanism for oxygenation has evolved as more investigations begin to reveal a greater understanding of the reaction. A mechanism for the insertion of dioxygen into a Zn-C bond has been proposed by Lewiński *et al.*¹³ and is shown in Scheme 4.1. The oxygen

is believed to enter the first coordination sphere of the alkylzinc species, before an attack of the O_2 molecule results in an electron transfer occurring from the Zn-C bond onto the O_2 molecule creating a radical pair.¹⁴

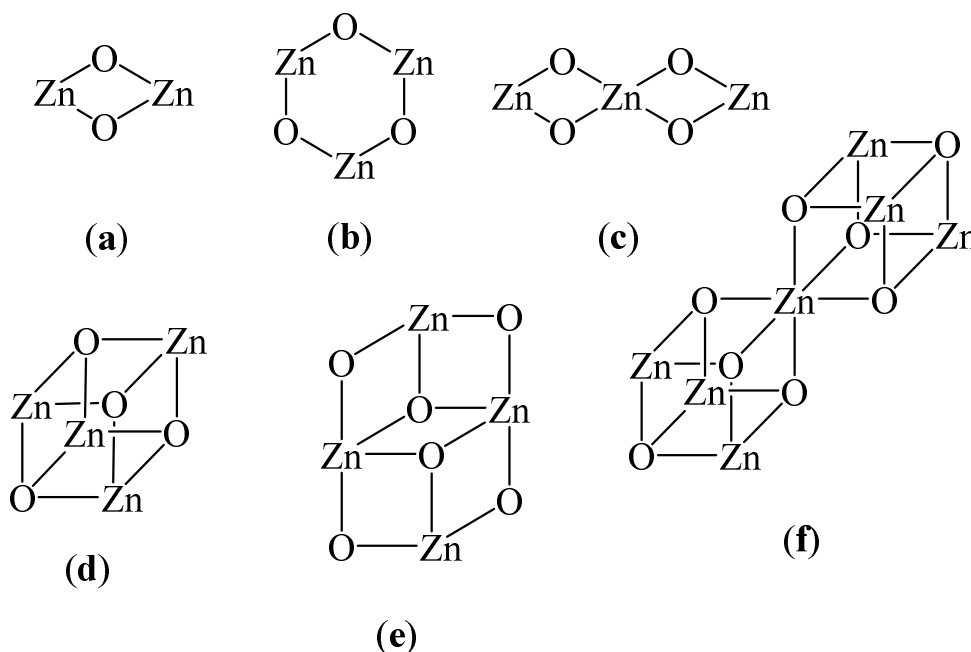
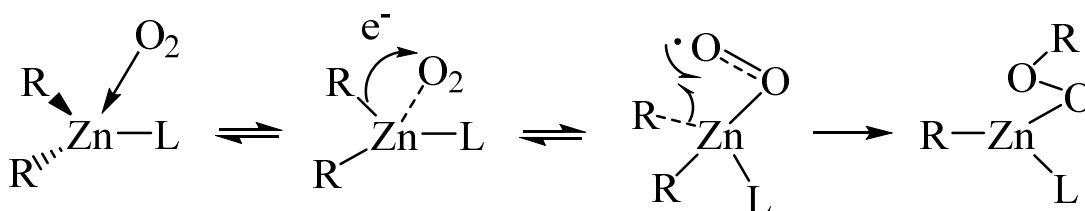


Figure 4.1: Rings and cubanes structures commonly found at the centre of zinc oxanes complexes.⁵

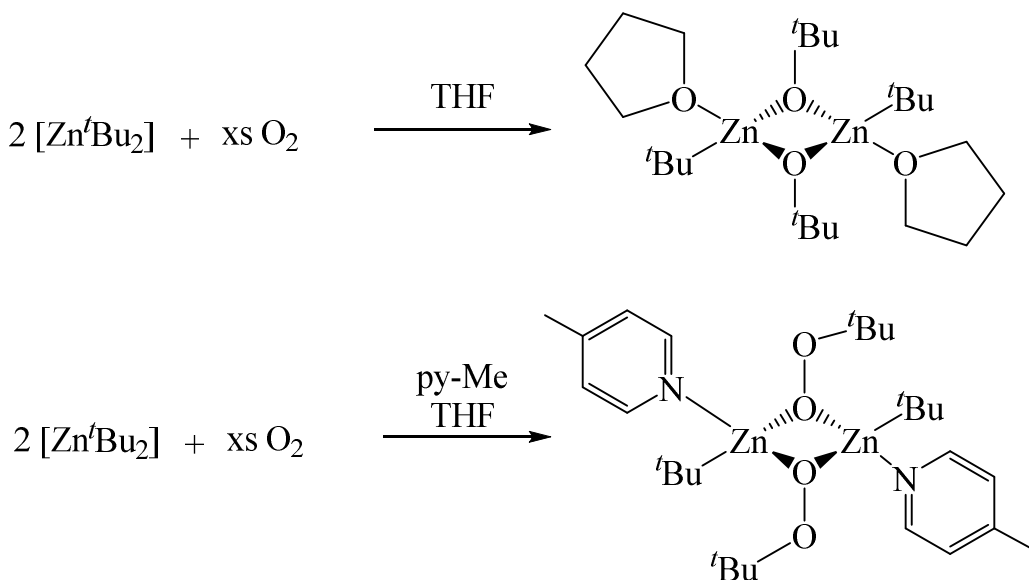
Homolysis of the O-O bond is then believed to occur leading to the zinc oxane species.¹⁵ Factors including coordination state of the Zn, steric factors and π -interactions are believed to have significant effects on the reactions.^{13,16} The resulting zinc oxane products will tend to form a cyclic or cubane core.



Scheme 4.1: Proposed reaction pathway for O_2 insertion into a Zn-C bond.¹³

4.1.1.1 Cyclic Structures

Zinc oxanes with a central four membered Zn_2O_2 cyclic centre have been synthesised from the reaction between Zn^tBu_2 and O_2 with THF or 4-methylpyridine (py-Me), as shown in Scheme 4.2.¹³



Scheme 4.2: Synthesis of $[(\text{Zn}(^t\text{Bu})\text{O}^t\text{Bu}(\text{thf}))_2]$ and $[(\text{Zn}(^t\text{Bu})\text{OO}^t\text{Bu}(\text{py-Me}))_2]$.¹³

In thf, the adduct $[\text{Zn}^t\text{Bu}_2(\text{THF})]$ is believed to form, which undergoes selective oxidation of one Zn-C bond to form the centrosymmetric $[\text{Zn}^t\text{Bu}(\text{O}^t\text{Bu})(\text{thf})]_2$ dimer, as shown in Scheme 4.2 (a). However, in the presence of py-Me, the $[(\text{Zn}^t\text{Bu}(\text{OO}^t\text{Bu})(\text{py-Me}))_2]$ *tert*-butylperoxide dimer forms, as shown in Scheme 4.2 (b). It is suggested that the ligand stabilises the selective oxygen insertion species, leading to the OO^tBu bridging ligand in (b). Although both reactions illustrate the selective oxidation of the initial species, the reactions also illustrate the influence of the donor ligand on the resulting reaction product.

Lewiński *et al.*¹⁷ also using Zn^tBu_2 synthesised the trimer zinc oxane product $[(\text{Zn}(^t\text{Bu})\text{O}^t\text{Bu})_3]$ via the solvated dimeric alkoxide $[(\text{Zn}(^t\text{Bu})\text{O}^t\text{Bu}(\text{THF}))_2]$. The trimer species has a core of three Zn atoms and three O atoms and although initial assumptions might lead to the idea that a six membered Zn_3O_3 ring would form, this is not the case. The complex forms a core motif shown in Figure 4.2, formed of one and a half of the Zn_2O_2 units.

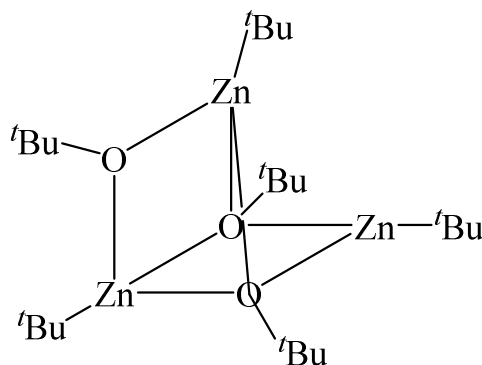
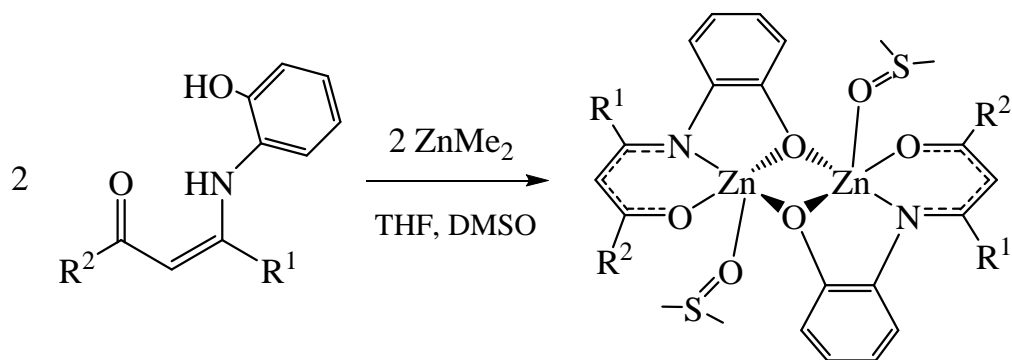


Figure 4.2: Structure of $[(\text{Zn}^t\text{BuO}^t\text{Bu})_3]$.¹⁷

In this complex, one Zn centre is three coordinate, whilst two Zn centres are four coordinate. Likewise, one O centre is three coordinate, whilst two O centres are four coordinate. As is shown in Section 4.1.1.1.1, when chelating ligands are involved, trimer species are observed to form a six membered Zn_3O_3 zinc oxane ring.

4.1.1.1.1 Cyclic Structures with Chelating Ligands

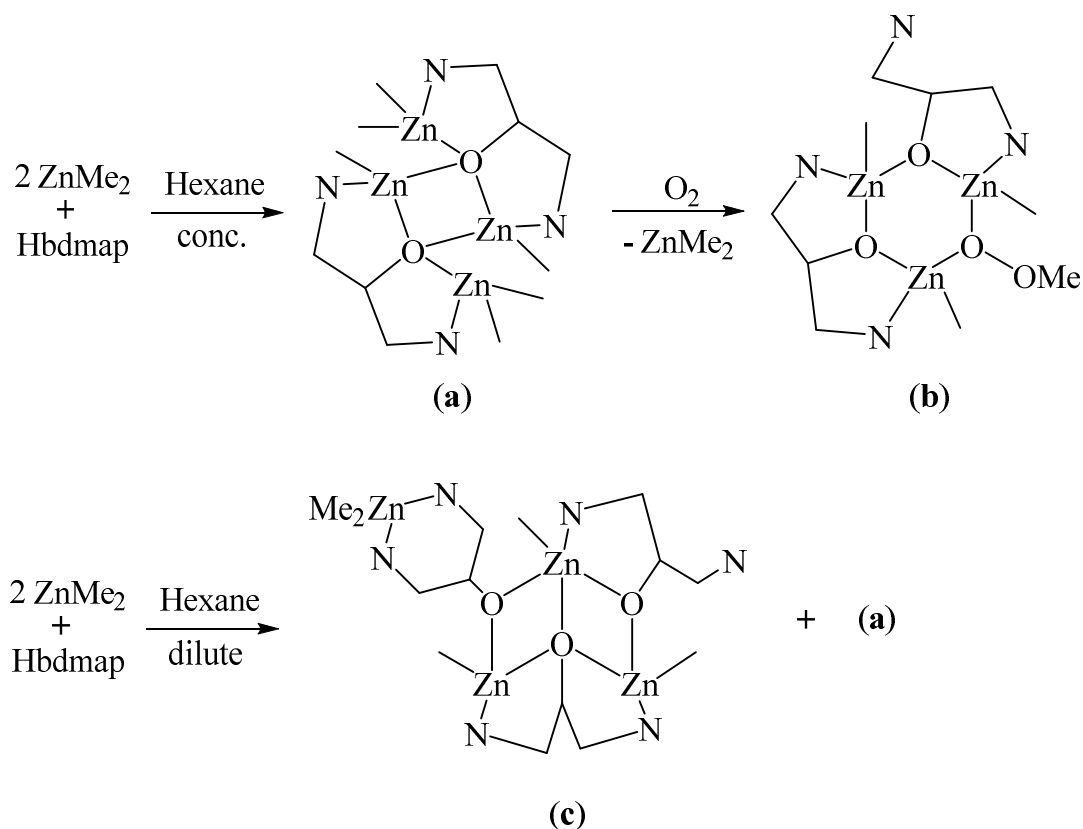
Zinc oxane complexes with a central Zn_2O_2 core have also been synthesised using bidentate ligands such as the ketoiminate ligand, as shown in Scheme 4.3.¹⁸ The use of bidentate ligands can have a strong influence on the geometry and coordination of the reaction products due to the constraints and the inflexibility of the ring structures formed. The use of the ketoiminate in the synthesis of zinc complexes is also discussed in greater detail in Chapter 5 as a prelude to the work presented there.



(a) $\text{R}^1, \text{R}^2 = \text{Me}$: (b) $\text{R}^1 = \text{Me}, \text{R}^2 = \text{Ph}$: (c) $\text{R}^1, \text{R}^2 = \text{Ph}$.

Scheme 4.3: Synthesis of $[(\text{LxZn}(\text{DMSO}))_2]$.¹⁸

Hollingsworth *et al.*¹⁹ investigated the structure of the aminoalcoholate products from the reaction of ZnMe_2 and the chelating ligand 1,3-bis(dimethylamino)-2-propanol (Hbdmap). Scheme 4.4 illustrates a selection of the reactions products and a variety of the zinc oxane structures at the core of these complexes.



Scheme 4.4: Synthesis of $[(\text{MeZn}(\text{bdmap})\text{ZnMe}_2)_2]$ (a), $[(\text{MeZn}(\text{bdmap}))_2\text{MeZnOOMe}]$ (b) and $[(\text{MeZn}(\text{bdmap}))_3\text{ZnMe}_2]$ (c).¹⁹

In a concentrated solution, the 2:1 reaction between ZnMe_2 and Hbdmap leads to the formation of an adduct with a core Zn_2O_2 zinc oxane ring, as shown in Scheme 4.4 (a). Upon the addition of dry O_2 , a ZnMe_2 molecule is lost and a complex with a central six membered Zn_3O_3 zinc oxane ring forms, as shown in Scheme 4.4 (b). However, in a dilute solution of the same 2:1 reaction a product with a motif of two Zn_2O_2 rings which share a Zn-O side forms, as shown in Scheme 4.4 (c). These reactions act to illustrate how simple changes in reaction conditions can have significant effects on the products formed and their coordination. Further investigations into organozinc aminoalcoholates have led to a wider variety of products and central structural

motifs,¹⁰ including two with an eight membered Zn_4O_8 boat-like core, an illustration of which is shown in Figure 4.3. Typically, Zn_4O_4 cores would form cubane structures, as will be discussed in Section 4.1.1.2. However, the donor amine group on the ligand fills the coordination sphere of the Zn centres, stopping the formation of Zn-O bonds and preventing the formation of a cubane core. The ring structure is highly puckered with long range interactions between opposite Zn and O atoms of between 3.435 and 3.626 Å.

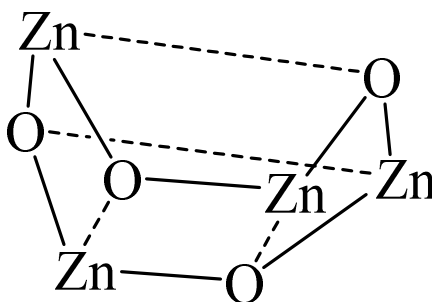
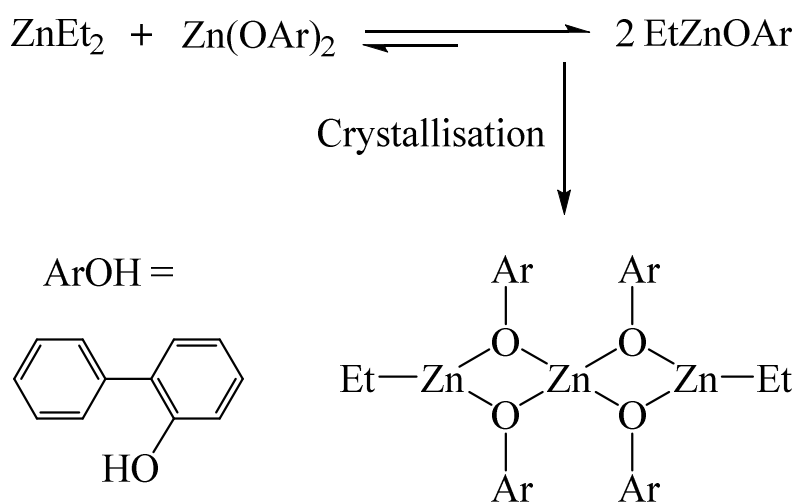


Figure 4.3: Structure of an eight membered Zn_4O_4 ring.¹⁰

Zinc oxane complexes with a central core of two Zn_2O_2 rings in which one Zn centre is shared by both ring systems are also known. One example of this is the zinc oxane $[(\text{EtZn})_2\text{Zn}(\text{OAr})_4]$ shown in Scheme 4.5.²⁰



Scheme 4.5: Synthesis of $[(\text{EtZn})_2\text{Zn}(\text{OAr})_4]$.²⁰

As the molecular formula suggests, the complex is an adduct of two Et-Zn groups bridging outer O atoms of a central $\text{Zn}(\text{OAr})_4$ core. The complex is a less soluble product from the reaction between ZnEt_2 and 2-phenylphenol (ArOH) in which $[\text{EtZn}(\text{OAr})]$ is formed. As previously mentioned, other zinc oxanes are observed to have a core cubane structure.

4.1.1.2 Cubane Structures

Cubane structures have been previously described in Chapter 3.1.1.1, where Jana *et al.*⁴ found the reaction of alkyl zinc complexes such as ZnMe_2 and ZnEt_2 with O_2 resulted in the formation of cubane structures. The structure of the resulting cubane was found to be dependant on the absence of water molecules. Zinc oxane compounds with a core cubane structure of Zn and O have also been synthesised from the reactions of alkylzinc compounds and oxygen containing ligands. These ligands have the potential to cause distortions in the resulting cubane, particularly so if the ligand is bulky or chelating.¹⁸ Zinc oxane cubanes are readily synthesised, for example, the reaction between ZnEt_2 and dry $t\text{BuOH}$ resulted in the synthesis of the $[(\text{Zn}(\text{Et})(\text{O}^t\text{Bu}))_4]$ cubane, the structure of which is shown in Figure 4.4.²¹

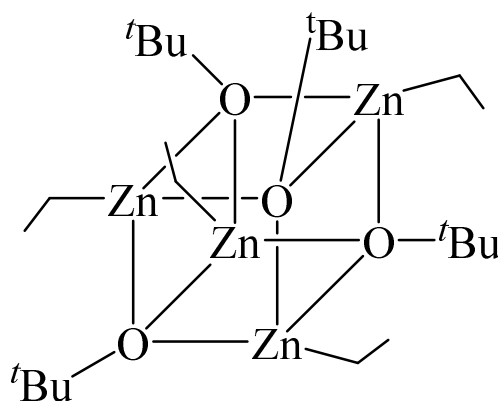
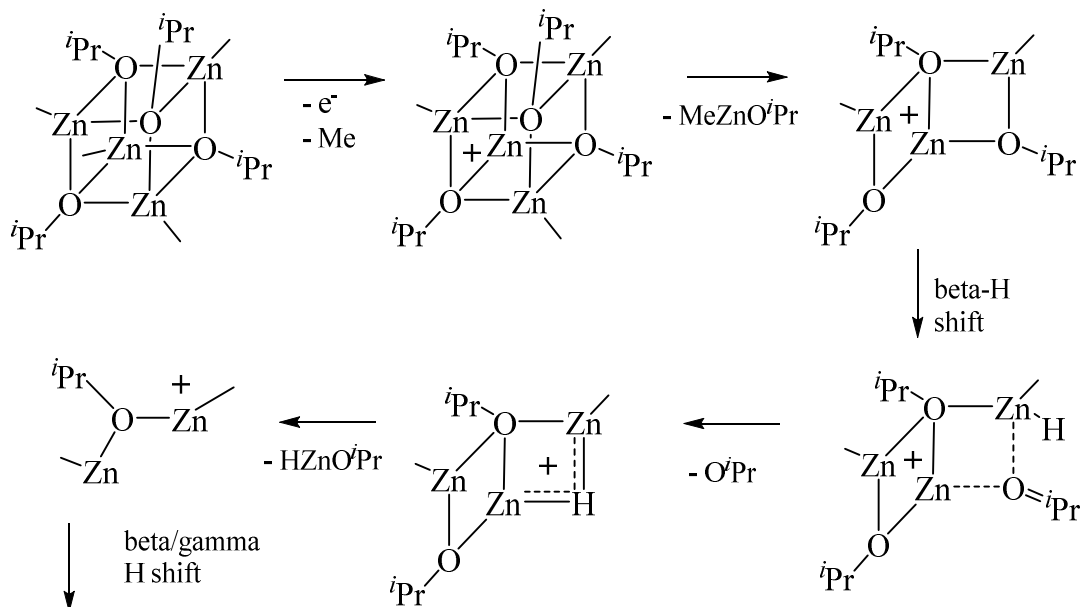


Figure 4.4: Structure of $[(\text{Zn}(\text{Et})(\text{O}^t\text{Bu}))_4]$.²¹

Investigations into the synthesis and use of a similar cubane, $[(\text{Zn}(\text{Me})(\text{O}^i\text{Pr}))_4]$ was carried out by Polarz *et al.*²² Their investigations included studying the decomposition of the cubane core by mass spectroscopy, the details of the proposed mechanism are given in Scheme 4.6. Although the reaction is initiated by ionisation in mass

spectroscopy, thermal gravimetric analysis (TGA) also provides evidence to support the proposed mechanism.



Scheme 4.6: Suggested decomposition of $[(\text{Zn}(\text{Me})(\text{O}^i\text{Pr}))_4]$.²²

Bis-cubanes in which two cubanes share a Zn corner have also been realised, for example $[(\text{ZnEt})_6\text{Zn}(\text{OMe})_8]$, shown in Figure 4.5.²³

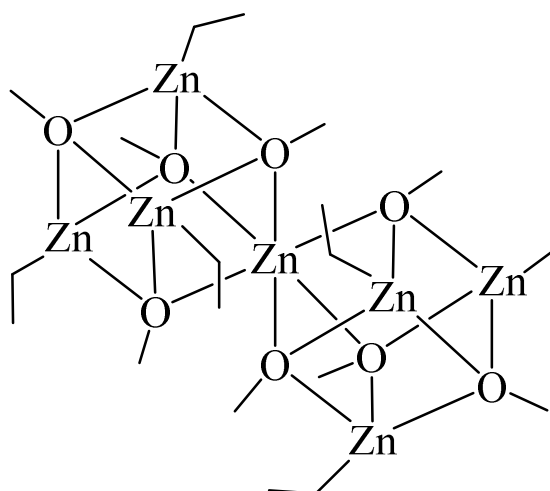
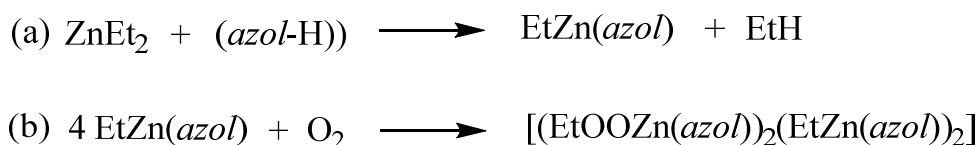


Figure 4.5: Structure of $[(\text{ZnEt})_6\text{Zn}(\text{OMe})_8]$.²³

The product forms from the reaction between ZnEt_2 and MeOH in heptane, however, reactions by Jana *et al.*⁴ suggest that a small amount of H_2O must also be present in order for this structure to form. As well as bis-cubane structures, defective cubane structures have also been realised from similar reactions of ZnEt_2 with bulkier and chelating O containing ligands.

4.1.1.2.1 Defective Cubane Structures

Lewiński *et al.*²⁴ synthesised a defective cubane in a two-step reaction, as shown in Scheme 4.7.



Scheme 4.7: Synthesis of $[(\text{EtOOZn(azol)})_2(\text{EtZn(azol)})_2]$, where Hazol is 1-aziridine ethanol.²⁴

First, ZnEt_2 was reacted with 1 mol equivalence of 1-aziridine ethanol (Hazol), forming the EtZn(azol) aggregate. This aggregate reacted with 0.25 mol of O_2 forming the $[(\text{EtOOZn(azol)})_2(\text{EtZn(azol)})_2]$ defective cubane, the structure of which is shown in Figure 4.6.

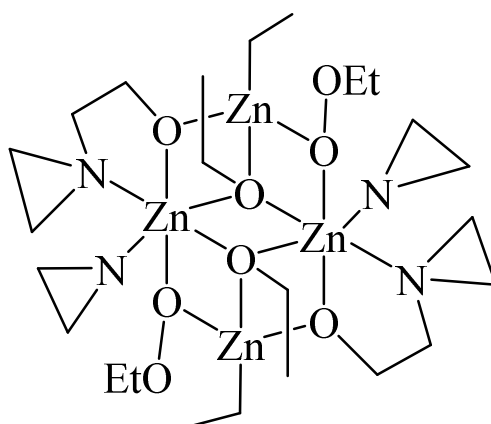


Figure 4.6: Structure of $[(\text{EtOOZn(azol)})_2(\text{EtZn(azol)})_2]$, where Hazol is 1-aziridine ethanol.²⁴

The authors describe the core of the complex as an inversion-related, corner-removed face-shared cube. Other reactions have also lead to zinc oxane complexes with a similar core structure. For example, the reaction of $[\text{Et}(\text{Zn})(\text{OMal})]$ (where MalOH is maltol, $\text{O}(\text{CH}_2)_2(\text{CO})(\text{COH})(\text{CMe})$) and O_2 lead to the synthesis of $[\text{Zn}_4(\text{Et})_2(\text{OEt})_2(\text{OMal})_4]$, the structure of which shown in Figure 4.7.

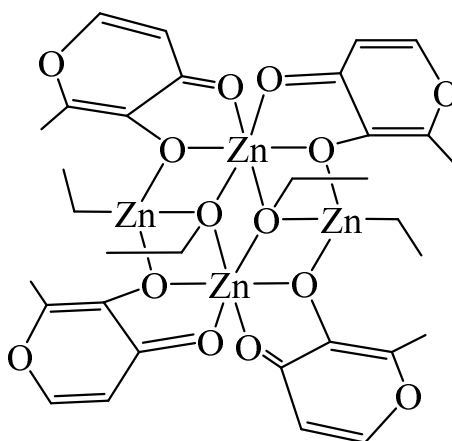


Figure 4.7: Structure of $[\text{Zn}_4(\text{Et})_2(\text{OEt})_2(\text{OMal})_4]$, where MalOH is maltol.²⁵

Zinc oxane complexes with defective cubane cores have also been synthesised avoiding the use of ZnEt_2 . $[\text{Zn}_4(\text{OMe})_2(\text{acac})_6]$ was synthesised from the reaction between zinc acetylacetonate and titanium ethoxide, the structure of which can be seen in Figure 4.8.

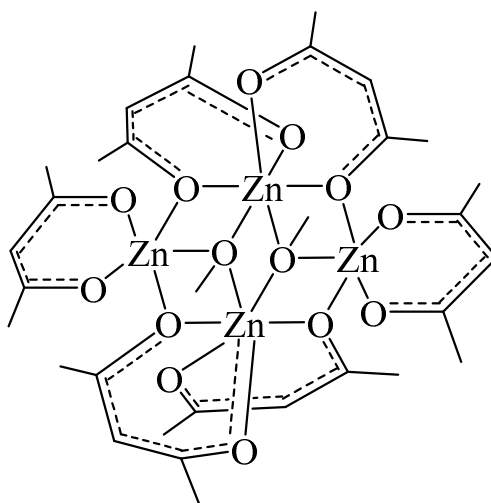


Figure 4.8: Structure of $[\text{Zn}_4(\text{OMe})_2(\text{acac})_6]$.²⁶

Two Zn centres are found in a six coordinate distorted octahedral geometry, whilst two are found in a five coordinate distorted trigonal bipyramidal coordination geometry.

In this chapter, the synthesis, isolation and characterisation of zinc oxane complexes with a six membered Zn_3O_3 central ring as the central motif, as well as zinc oxane complexes with a defective face-shared, corner-removed bis-heterocubane core are reported. AACVD studies as a proof of concept have also been performed using a synthesised zinc oxane complex.

4.2 Results and Discussion

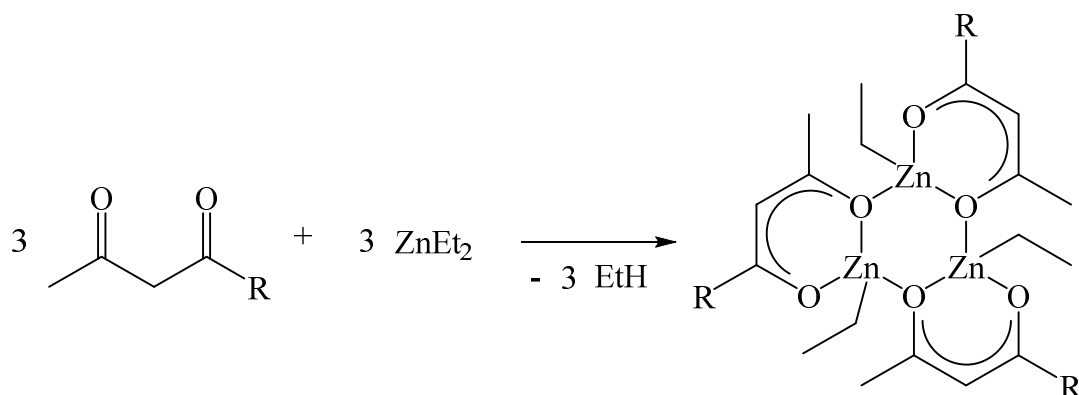
Zinc oxane complexes of two structural types have been synthesised and are presented in this chapter. Trimeric complexes of the type $[(\text{Zn}(\text{Et})(\text{OC}(\text{R})\text{CHC}(\text{Me})\text{O}))_3]$ where $\text{R} = \text{OMe}$ (**1**), Me (**2**), OEt (**3**) and O^tBu (**4**) were formed in a 1:1 reaction between ZnEt_2 and the corresponding dicarbonyl compound. Upon the controlled addition of a small volume of O_2 to solutions of (**1**) – (**4**) in hexanes, zinc oxane clusters of the type $[(\text{Zn}(\text{OC}(\text{R})\text{CHC}(\text{Me})\text{O})_2\text{Zn}(\text{Et})\text{OEt})_2]$ where $\text{R} = \text{OMe}$ (**5**), Me (**6**), OEt (**7**) and O^tBu (**8**) were synthesised. The complexes were isolated and characterised with crystal structures determined for complexes (**1**), (**6**) and (**8**). The thermal decomposition of (**6**) was investigated and the complex was used as a single-source precursor in the AACVD of ZnO thin films. The films were characterised and used to determine the suitability of (**6**) as a CVD precursor.

4.2.1 Synthesis of Zinc Oxane Complexes

4.2.1.1 Synthesis of Zinc Oxane Trimer Complexes

Zinc oxane trimer complexes of the type $[(\text{Zn}(\text{Et})(\text{OC}(\text{R})\text{CHC}(\text{Me})\text{O}))_3]$ where $\text{R} = \text{OMe}$ (**1**), Me (**2**), OEt (**3**) and O^tBu (**4**) were synthesised *via* the ethane elimination reaction of a 1:1 molar equivalence of ZnEt_2 and the corresponding dicarbonyl compound according to Scheme 4.8. Zinc oxane $[(\text{Zn}(\text{Et})(\text{OC}(\text{OMe})\text{CHC}(\text{Me})\text{O}))_3]$ (**1**) crystallised out as off-white crystals in a yield of 91% from a concentrated solution in hexane held at -18°C . Zinc oxanes $[(\text{Zn}(\text{Et})(\text{OC}(\text{R})\text{CHC}(\text{Me})\text{O}))_3]$ (**2**) – (**4**) where

R = Me (**2**), OEt (**3**) and O^tBu (**4**) were isolated as off-white solids upon the removal of hexane in yield of 90%, 88% and 91% respectively.



R = (**1**) OMe: (**2**) Me: (**3**) OEt: (**4**) O^tBu.

Scheme 4.8: Synthesis of zinc trimer complexes [(Zn(Et)(OC(R)CHC(Me)O))₃] (1**) – (**4**).**

¹H, ¹³C and HSQC (heteronuclear single quantum correlation) NMR spectroscopy were used in the characterisation of (**1**) – (**4**) with similar chemical shifts observed for corresponding proton and carbon environments in each complex. Elemental analysis was also used to characterise the trimer complexes and the crystal structure of (**1**) was determined *via* single crystal X-ray diffraction. Reactions forming (**1**) – (**4**) are shown to be highly selective and high yielding. This appears contrary to the idea that ZnEt₂ reacts in a way such that numerous products will result from its reaction. However, this has also been reported in similar reactions in which trimer species are also believed to exist in solution.²⁴ This is believed to result from the low temperature addition of the reactants but also the preference of the reaction pathway for reaction at sites of low coordination, as described in Section 4.1.1. Complexes (**1**) – (**4**) were all found to be highly pyrophoric when exposed to air.

4.2.1.1.1 Synthesis of [(Zn(Et)(OC(OMe)CHC(Me)O))₃] (**1**)

[(Zn(Et)(OC(OMe)CHC(Me)O))₃] (**1**) was synthesised by the 1:1 molar addition of dry methyl acetoacetate to ZnEt₂ in dry hexane under inert conditions. The addition was performed at -78 °C to account for the pyrophoricity of ZnEt₂. The solution was stirred and upon warming to room temperature the evolution of a gas, believed to be

the ethane reaction by-product was observed. The solution was stirred for 48 hours and concentrated *via* the removal of hexane *in vacuo*. The product crystallised out as off-white crystals after the solution was held at -18 °C for 24 hours with a yield of 91%.

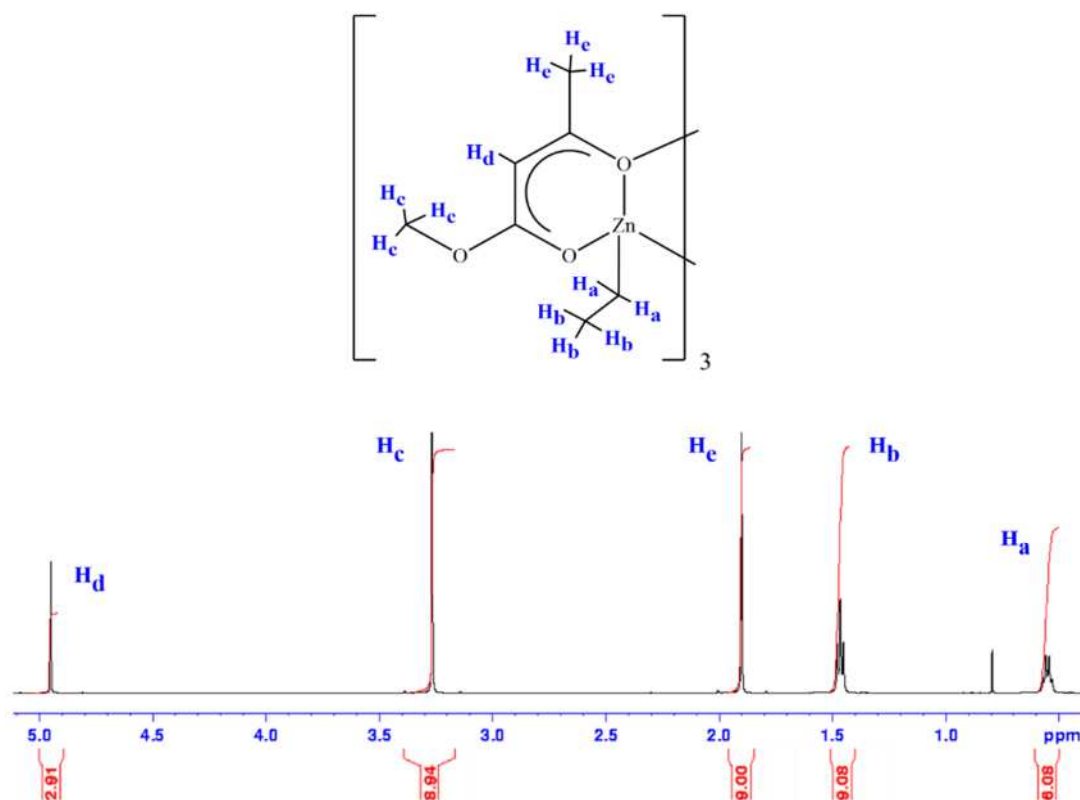


Figure 4.9: ^1H NMR spectrum of $[(\text{Zn}(\text{Et})(\text{OC}(\text{OMe})\text{CHC}(\text{Me})\text{O}))_3]$ (**1**).

The synthesis of (**1**) was confirmed using ^1H and ^{13}C NMR spectroscopy. In the ^1H NMR spectrum, each resonance was assigned to an expected proton environment in (**1**) and was present with the correct integration pattern and splitting, as shown in Figure 4.9. The peaks associated with the ethyl groups attached to the Zn centre correspond to the quartet at 0.55 ppm and triplet at 1.47 ppm for the CH_2 and CH_3 protons respectively. There are three peaks associated with the ligand bound to the Zn centre through two O atoms. The singlet at 1.90 ppm corresponds to the protons of the CH_3 methyl group attached to the ZnO_2C_3 ring with the singlet at 4.95 ppm corresponding to the CH proton attached directly to the ring structure. The protons of the OCH_3 methoxide group are associated to the singlet peak at 3.27 ppm.

The ^{13}C NMR was also fully assigned with all carbon environments in (**1**) associated with predicted peaks in the obtained spectrum. $^1\text{H} - ^{13}\text{C}$ HSQC NMR was performed and used to correlate the proton and carbon environments. The peaks associated with the ethyl groups attached to the Zn centre appear at 1.0 and 12.5 ppm for the $\underline{\text{CH}}_2$ and $\underline{\text{CH}}_3$ carbon environments respectively. The peaks for the $\text{O}\underline{\text{CH}}_3$ and $\underline{\text{CH}}_3$ carbon environments that bond to the chelating ring appear at 51.1 and 27.5 ppm respectively. The three carbon environments in the six member chelate rings, $\text{C}\underline{\text{CH}}\text{C}$, $\underline{\text{COCH}}_3$ and $\underline{\text{CCH}}_3$ are associated to the peaks at 89.3, 174.0 and 184.4 ppm respectively.

The ^1H NMR spectrum in Figure 4.9 also suggests high purity of the crude product, negating the need for further recrystallisation procedures. Elemental analysis also confirms good agreement between the C and H ratios for the product. The calculated elemental analysis of C and H in (**1**) is 40.12 and 5.77% respectively, which compares well to the obtained values of 40.21 and 5.89% respectively.

The crystal structure of zinc oxane $[(\text{Zn}(\text{Et})(\text{OC}(\text{OMe})\text{CHC}(\text{Me})\text{O}))_3]$ (**1**) was determined *via* single crystal X-ray diffraction and is shown in Figure 4.10. The details of the determined crystallographic data are given in Table 4.1 with selected bond lengths and angles given in Table 4.2. Compound (**1**) crystallised as a trimer in the monoclinic space group $P2_1/n$. The complex has three zinc centres all of which have the same distorted tetrahedral coordination environment. Zn(1) has a distorted tetrahedral geometry from the formation of four bonds. One coordination site is occupied by a bound terminal ethyl group, which remains from the original ZnEt_2 compound. Two coordination sites are filled by the bidentate $(\text{OC}(\text{OMe})\text{CHC}(\text{Me})\text{O})$ ligand which bonds through O(1) and O(2) and forms puckered a six membered ZnO_2C_3 ring. Zn(1) also forms a bond to O(4) on the $(\text{OC}(\text{OMe})\text{CHC}(\text{Me})\text{O})$ ligand around Zn(2). Zn(2) and Zn(3) make similar bonds to O(7) and O(1) respectively, forming a puckered six membered Zn_3O_3 ring in the centre of (**1**). The highly distorted nature of the tetrahedral coordination around the Zn centres in (**1**) results largely from the constraints of the central Zn_3O_3 ring and the three outer ZnO_2C_3 rings, as well as the presence of the three terminal ethyl groups. This is illustrated by the deviation from the 109.5° expected for bond angles around a perfect tetrahedron, which is expected for complexes of this type. The range of the bond angles around the Zn centres is greater than 47° from the O(4)-Zn(2)-O(7) angle measuring $87.46(4)^\circ$ to the O(4)-Zn(2)-C(13) angle measuring $135.11(5)^\circ$.

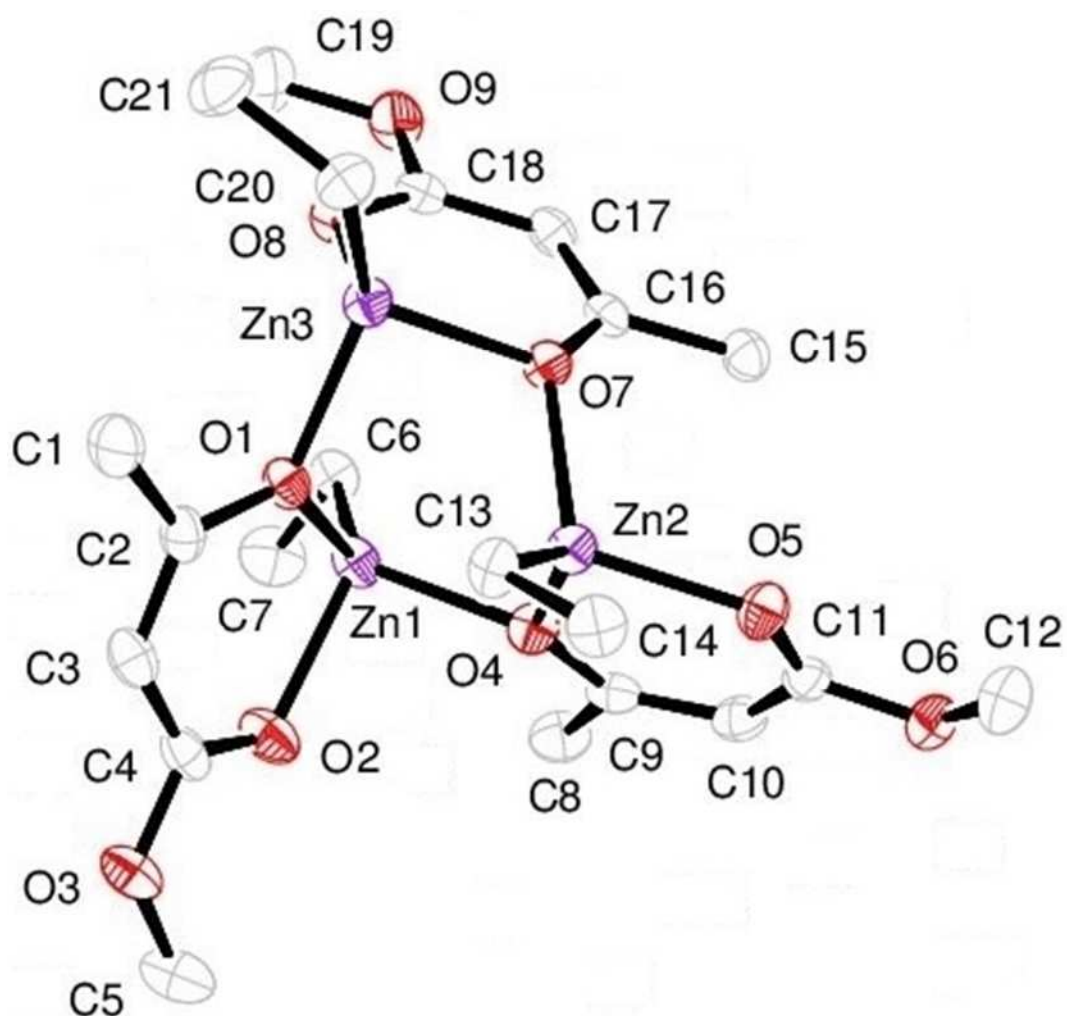


Figure 4.10: X-ray crystal structure of $[(\text{Zn}(\text{Et})(\text{OC}(\text{OMe})\text{CHC}(\text{Me})_3)]$ (1).

Table 4.1: Crystallographic data for $[(\text{Zn}(\text{Et})(\text{OC}(\text{OMe})\text{CHC}(\text{Me})_3)]$ (1).

Crystal System	Monoclinic	
Space Group	$P2_1/n$	
Volume	$2647.74(3) \text{ \AA}^3$	
Unit Cell Dimensions	$a = 14.33392(8) \text{ \AA}$	$\alpha = 90^\circ$
	$b = 9.09638(5) \text{ \AA}$	$\beta = 97.3126(6)^\circ$
	$c = 20.47334(14) \text{ \AA}$	$\gamma = 90^\circ$

**Table 4.2: Selected bond lengths (Å) and angles (°) for
[(Zn(Et)(OC(OMe)CHC(Me))₃)] (1).**

Zn(1)-O(1)	2.0489(9)	Zn(3)-O(7)	2.0367(9)
Zn(1)-O(2)	2.0562(10)	Zn(3)-O(8)	2.0409(10)
Zn(1)-O(4)	2.0710(10)	Zn(3)-C(20)	1.9761(14)
Zn(1)-C(6)	1.9676(14)	O(1)-C(2)	1.3176(16)
Zn(2)-O(4)	2.047(9)	O(2)-C(4)	1.2368(18)
Zn(2)-O(5)	2.0229(10)	O(3)-C(5)	1.431(2)
Zn(2)-O(7)	2.0980(9)	C(1)-C(2)	1.497(2)
Zn(2)-C(13)	1.9707(13)	C(2)-C(3)	1.363(2)
Zn(3)-O(1)	2.0698(10)	C(3)-C(4)	1.421(2)
O(1)-Zn(1)-O(2)	91.53(4)	O(5)-Zn(2)-O(7)	110.91(4)
O(1)-Zn(1)-O(4)	97.79(4)	O(5)-Zn(2)-C(13)	113.49(5)
O(1)-Zn(1)-C(6)	121.96(5)	O(7)-Zn(2)-C(13)	115.63(5)
O(2)-Zn(1)-O(4)	91.36(4)	O(1)-Zn(3)-O(7)	90.37(4)
O(2)-Zn(1)-C(6)	121.74(5)	O(1)-Zn(3)-O(8)	96.72(4)
O(4)-Zn(1)-C(6)	124.15(5)	O(1)-Zn(3)-C(20)	131.77(5)
O(4)-Zn(2)-O(5)	90.01(4)	O(7)-Zn(3)-O(8)	90.23(4)
O(4)-Zn(2)-O(7)	87.46(4)	O(7)-Zn(3)-C(20)	122.45(5)
O(4)-Zn(2)-C(13)	135.11(5)	O(8)-Zn(3)-C(20)	115.44(5)

The O(1)-Zn(1)-O(2), O(4)-Zn(2)-O(5) and O(7)-Zn(3)-O(8) angles formed by the bidentate (OC(OMe)CHC(Me)O) ligands measure 91.53(4), 90.01(4) and 90.23(4)°

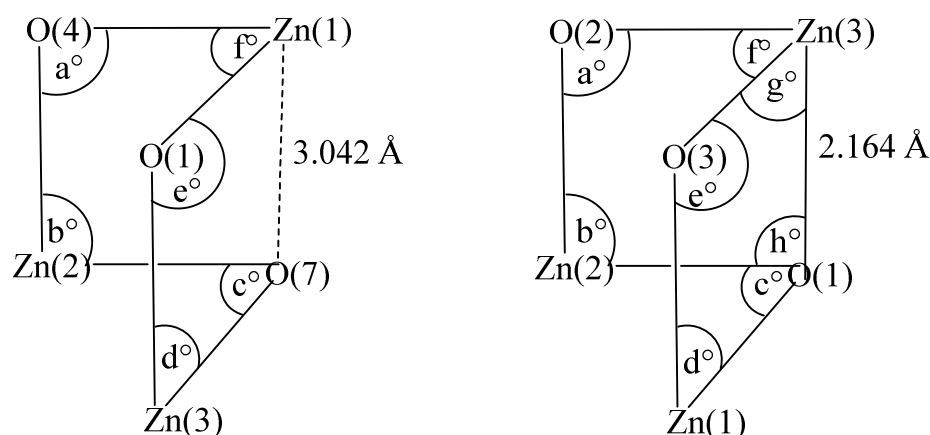
respectively. The angles have similar values $< 109.5^\circ$ due to the constraints of the ring systems formed in (1) and the resulting reduction in steric interaction from the terminal ethyl groups. Each Zn centre also forms two more Zn-O bonds which form the six sides of the central Zn_3O_3 ring. One set of angles, O(1)-Zn(1)-O(4), O(4)-Zn(2)-O(7) and O(1)-Zn(3)-O(7) are internal bond angles in the ZnO_2C_3 rings and measure $97.79(4)$, $87.46(4)$ and $90.37(4)^\circ$ respectively. The third set, O(2)-Zn(1)-O(4), O(5)-Zn(2)-O(7) and O(1)-Zn(3)-O(8) have less restrictions as they do not form internal angles in any ring system and measure $91.36(4)$, $110.91(4)$ and $96.72(4)^\circ$ respectively.

The remaining three angles about each zinc centre all feature the Zn-C bond to a terminal ethyl group. These angles are all $> 109.5^\circ$ resulting in the reduced steric hindrance of the terminal ethyl group. These angles counterbalanced the angles smaller than 109.5° that have just been discussed. Since the ethyl group ligand is not part of any formed rings there is greater flexibility to allow for the angles $> 109.5^\circ$. The variation in bond angles about each zinc is dependent on the differing effects and constraints of the ring structures in (1). Around Zn(1), the O(1)-Zn(1)-C(6), O(2)-Zn(1)-C(6) and O(4)-Zn(1)-C(6) angles measure $121.96(5)$, $121.74(5)$ and $124.15(5)^\circ$ respectively. Likewise, around Zn(2), the O(4)-Zn(2)-C(13), O(5)-Zn(2)-C(13) and O(6)-Zn(2)-C(13) bond angles all measure greater than 109.5° at $135.11(5)$, $113.49(5)$ and $115.63(5)^\circ$ respectively. This is also the case around Zn(3) in which the O(1)-Zn(3)-C(20), O(7)-Zn(3)-C(20) and O(8)-Zn(3)-C(20) measure $131.77(5)$, $122.45(5)$ and $115.44(5)^\circ$ respectively.

As would be expected, the shortest bond about each Zn centre is the Zn-C bond to the terminal ethyl groups which measure $1.9676(14)$, $1.9707(13)$ and $1.9761(14)$ Å for the Zn(1)-C(6), Zn(2)-C(13) and Zn(3)-C(20) bonds respectively. These lengths are as expected for bonds of this type. Two bonds about each Zn are to the bidentate (OC(OMe)CHC(Me)O) ligands. The Zn(1)-O(1), Zn(1)-O(2), Zn(2)-O(4), Zn(2)-O(5), Zn(3)-O(7) and Zn(3)-O(8) bonds measure $2.0489(9)$, $2.0562(10)$, $2.047(9)$, $2.0229(10)$, $2.0367(9)$ and $2.0409(10)$ Å respectively. These bonds are all relatively similar in length and are comparable to other bonds of this type in similar environments. The longest bonds around each Zn atom are the bridging Zn-O which connect the monomer units and form the central Zn_3O_3 ring. These bonds are the Zn(1)-O(4), Zn(2)-O(7) and Zn(3)-O(1) bonds, which measure $2.0710(10)$, $2.0980(9)$ and $2.0698(10)$ Å respectively. The longer and shorter bonds that form the central

Zn_3O_3 ring are therefore alternating. The delocalised nature of the ZnO_2C_3 rings in **(1)** is also illustrated by the shorter bond lengths within the ring structures. For example, the O(1)-C(2) and O(2)-C(4) bonds in the ZnO_2C_3 ring measure 1.3176(16) and 1.2368(18) Å respectively, which are shorter than the O(3)-C(5) bond of 1.431(2) Å. Similarly, the C(2)-C(3) and C(3)-C(4) bonds of 1.363(2) and 1.421(2) Å respectively are shorter than the C(1)-C(2) of 1.497(2) Å.

Zinc oxane complexes with the central Zn_3O_3 six membered ring motif observed in **(1)** are relatively rare in the published literature. Each Zn and O atom in the central Zn_3O_3 ring motif in **(1)** form the same four bonds as each of the other Zn and O atoms. This results from **(1)** being formed of three identical $(\text{Zn}(\text{Et})(\text{OC}(\text{OMe})\text{CHC}(\text{Me})\text{O}))$ monomer units, which is often not the case.¹⁹ An alternative motif for a central Zn_3O_3 core was observed in the $[(\text{Zn}(\text{tBu})\text{O}^t\text{Bu})_3]$ complex synthesised by Lewiński *et al.*,¹⁷ which was described in Section 4.1.1.1. A highly distorted representation of the Zn_3O_3 core of **(1)** is shown in Figure 4.11 (a) in order to directly compare it to the Zn_3O_3 core of the literature $[(\text{Zn}(\text{tBu})\text{O}^t\text{Bu})_3]$ complex, as shown in Figure 4.11 (b).



(a) Zinc oxane **(1)**

(b) Lewinski *et al.*

$a^\circ = 108.89(4)$
 $b^\circ = 87.46(4)$
 $c^\circ = 102.74(4)$
 $d^\circ = 90.37(4)$
 $e^\circ = 115.32(4)$
 $f^\circ = 97.79(4)$

$a^\circ = 93.54(19)$ $g^\circ = 85.8(2)$
 $b^\circ = 77.4(2)$ $h^\circ = 95.46(19)$
 $c^\circ = 91.85(18)$
 $d^\circ = 83.44(18)$
 $e^\circ = 92.4(2)$
 $f^\circ = 83.81(19)$

Figure 4.11: Highly distorted representation of **(1) for comparison of bond angles to the literature complex $[(\text{Zn}^t\text{BuO}^t\text{Bu})_3]$.¹⁷**

The Zn_3O_3 central six membered ring in **(1)** is confirmed by comparison of the bond angles to equivalent bond angles in the $[(\text{Zn}(\text{tBu})\text{O}^t\text{Bu})_3]$ complex. All bond angles in **(1)** are noticeably larger than the corresponding angle in $[(\text{Zn}(\text{tBu})\text{O}^t\text{Bu})_3]$. This is as expected since the internal bond angles in a Zn_3O_3 central six membered ring would be larger than the internal angles of the central motif observed in $[(\text{Zn}(\text{tBu})\text{O}^t\text{Bu})_3]$. Confirmation is also provided by the distance between Zn(1) and O(7) in **(1)** being 3.042 Å. This is greater than the length of a Zn-O bond and significantly larger than the 2.164 Å observed for the Zn(3)-O(1) bond in $[(\text{Zn}(\text{tBu})\text{O}^t\text{Bu})_3]$. A highly puckered folded confirmation of the inner ring in $[(\text{Zn}(\text{tBu})\text{O}^t\text{Bu})_3]$ is facilitated by the unidentate nature of the ligands. This allows for the opposite Zn and O atoms to be in close proximity and the formation of a bonding interaction. However, in complex **(1)**, the chelating nature of the $(\text{OC}(\text{OMe})\text{CHC}(\text{Me})\text{O})$ ligand and its steric rigidity reduces the degree of puckering. This prevents the close proximity and the formation of a bond between the diagonally opposite Zn and O atoms, allowing for the distorted Zn_3O_3 six membered ring motif observed in **(1)**.

4.2.1.1.2 Synthesis of $[(\text{Zn}(\text{Et})(\text{OC}(\text{Me})\text{CHC}(\text{Me})\text{O}))_3]$ (**2**)

The 1:1 molar addition of dry acetylacetone to ZnEt_2 following the procedure employed for the synthesis of **(1)** resulted in the synthesis of $[(\text{Zn}(\text{Et})(\text{OC}(\text{Me})\text{CHC}(\text{Me})\text{O}))_3]$ (**2**). The product was isolated as an off-white solid with a 90% yield.

The successful synthesis of **(2)** was confirmed using ^1H and ^{13}C NMR spectroscopy with each proton and carbon environment in **(2)** assigned to peaks in the obtained spectra and the expected splitting pattern and ratio also observed in the ^1H spectrum. The peaks associated with the ethyl group protons attached to the Zn centre correspond to the quartet at 0.57 ppm and triplet at 1.48 ppm for the CH_2 and CH_3 protons respectively. The singlet at 1.79 ppm corresponds to the 18 protons of the CH_3 methyl groups attached to the ZnO_2C_3 rings with the singlet at 5.03 ppm corresponding to the CH proton environment attached directly to the ZnO_2C_3 ring.

The ^{13}C NMR was also fully assigned with all carbon environments in **(2)** associated with predicted peaks in the obtained spectrum. $^1\text{H} - ^{13}\text{C}$ HSQC NMR was performed and used to correlate the proton and carbon environments. In the ^{13}C NMR spectra,

the peaks associated with the ethyl group carbons attached to the Zn atoms appear at 1.0 and 12.4 ppm for the $\underline{\text{CH}}_2$ and $\underline{\text{CH}}_3$ environments respectively. The methyl $\text{C}\underline{\text{CH}}_3$ carbon environment attached to the ZnO_2C_3 ring appears at 28.3 ppm with the $\text{C}\underline{\text{CH}}\text{C}$ and $\underline{\text{CCH}}_3$ carbon environments in the ring corresponding to the peaks at 102.0 and 193.1 ppm. Elemental analysis of (2) also exhibits fair agreement between the calculated C and H ratios of 43.44 and 6.25% respectively and the obtained values of 43.09 and 6.77% respectively.

4.2.1.1.3 Synthesis of $[(\text{Zn}(\text{Et})(\text{OC}(\text{OEt})\text{CHC}(\text{Me})\text{O}))_3]$ (3)

The 1:1 molar addition of dry ethyl acetoacetate to ZnEt_2 following the procedure employed for the synthesis of (1) resulted in the synthesis of $[(\text{Zn}(\text{Et})(\text{OC}(\text{OEt})\text{CHC}(\text{Me})\text{O}))_3]$ (3). The product was isolated as an off-white solid with a 88% yield.

^1H and ^{13}C NMR spectroscopy was used to confirm the successful synthesis of (3) with all proton and carbon environments assigned to peaks in the obtained spectra. The peaks in the ^1H spectrum were also present in the expected ratios and splitting patterns. The ethyl group protons attached to the Zn centre appear as a quartet at 0.44 ppm and a triplet at 1.38 ppm for the $\text{C}\underline{\text{H}}_2$ and $\text{C}\underline{\text{H}}_3$ protons respectively. The ethoxide group protons appear as a triplet at 0.92 ppm and a quartet at 3.85 ppm for the $\text{C}\underline{\text{H}}_3$ and $\text{C}\underline{\text{H}}_2$ protons respectively. The singlets at 1.93 and 4.95 ppm correspond to the $\text{C}\underline{\text{H}}_3$ methyl group protons attached to the ZnO_2C_3 rings and the $\text{C}\underline{\text{H}}$ proton attached directly to the ZnO_2C_3 ring respectively.

$^1\text{H} - ^{13}\text{C}$ HSQC NMR was also performed and used to correlate the proton and carbon environments. In the ^{13}C NMR, the ethyl group carbons attached to the Zn atoms appear at 2.7 and 11.9 ppm for the $\underline{\text{CH}}_2$ and $\underline{\text{CH}}_3$ environments respectively. The peaks for the ethoxide group carbon environments appear at 14.1 and 60.5 ppm for the $\underline{\text{CH}}_3$ and $\underline{\text{CH}}_2$ environments respectively. The peaks for the $\text{C}\underline{\text{CH}}_3$ methyl group carbon environment attached to the ZnO_2C_3 ring appears at 27.6 ppm. The $\text{C}\underline{\text{CH}}\text{C}$, $\underline{\text{COCH}}_2\text{CH}_3$ and $\underline{\text{CCH}}_3$ carbon environments in the chelate ligand ring appear at 89.6, 173.6 and 184.2 ppm respectively. The obtained elemental analysis of (3) for C and H values of 42.83 and 5.72% also compares reasonably to the calculated values of 42.98 and 6.31% respectively.

4.2.1.1.4 Synthesis of [(Zn(Et)(OC(O'Bu)CHC(Me)O))₃] (4)

The 1:1 molar addition of dry *tert*-butyl acetoacetate to ZnEt₂ following the procedure employed for the synthesis of (1) resulted in the synthesis of [(Zn(Et)(OC(O'Bu)CHC(Me)O))₃] (4). The product was isolated as an off-white solid with a 91% yield.

The successful synthesis of (4) was confirmed using ¹H and ¹³C NMR spectroscopy in which all expected proton and carbon environments were successfully assigned to peaks in the obtained spectra. In the ¹H spectrum, all peaks were also present in the expected ratios and with the correct splitting patterns. The ethyl group protons attached to the Zn centre appear as a quartet at 0.37 ppm and a triplet at 1.33 ppm for the CH₂ and CH₃ protons respectively. The protons associated with the *tert*-butoxide group appear as a singlet at 1.31 ppm for the C(CH₃)₃ environment. The singlets at 1.94 and 4.90 ppm correspond to the CH₃ methyl group protons attached to the ZnO₂C₃ rings and the CH proton attached directly to the ZnO₂C₃ ring respectively.

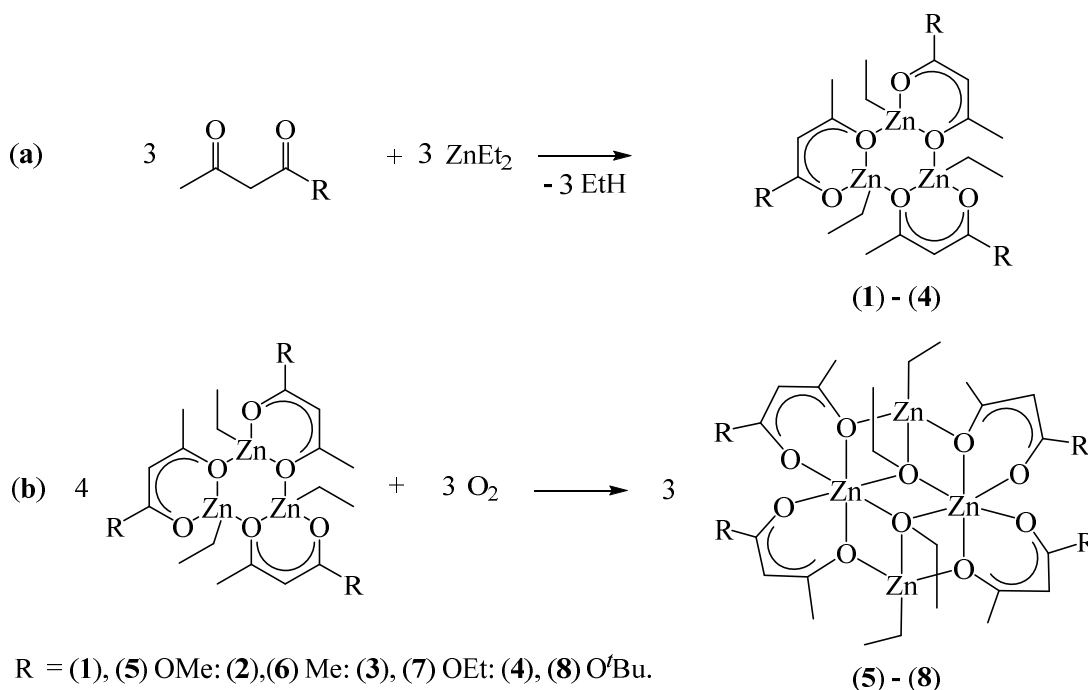
The ¹³C NMR was also fully assigned with all carbon environments in (4) associated with predicted peaks in the obtained spectrum. ¹H – ¹³C HSQC NMR was performed and used to correlate the proton and carbon environments. In the ¹³C NMR, the ethyl group carbons attached to the Zn atoms appear at 3.4 and 11.7 ppm for the CH₂ and CH₃ environments respectively. The peaks associated with the *tert*-butoxide group appear at 28.4 and 80.9 ppm for the C(CH₃)₃ and C(CH₃)₃ environments respectively. The three carbon environments in the six member chelate rings of CCHC, COC(CH₃)₃ and CCH₃ are associated to the peaks at 91.0, 173.8 and 183.2 ppm respectively. The obtained elemental analysis of (4) for C and H values of 46.93 and 6.97% respectively exhibits reasonable agreement to the calculated values of 47.73 and 7.21% respectively.

The zinc oxane trimer complexes (1) – (4) underwent further reaction when exposed to controlled amount of O₂ gas to yield zinc oxane clusters (5) – (8).

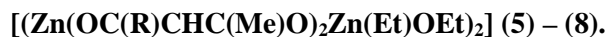
4.2.1.2 Synthesis of Zinc Oxane Cluster Complexes

Zinc oxane cluster complexes of the type [(Zn(OC(R)CHC(Me)O)₂Zn(Et)OEt)₂] where R = OMe (5), Me (6), OEt (7) and O'Bu (8) were synthesised *via* a 1:1 ethane

elimination reaction between ZnEt_2 and the corresponding dicarbonyl compound followed by an *in situ* oxygen insertion reaction of 0.25 molar equivalence, as shown in Scheme 4.9.



Scheme 4.9: Synthesis of zinc oxane cluster complexes



Step one of the reaction is carried out following the same procedure forming (1) – (4), described in Section 4.2.1.1. Controlled addition of O_2 then occurs in which O_2 is believed to insert into the Zn-O bond between Zn and the terminal ethyl group. This reaction leads to the bridging ethoxide groups observed in (5) – (8) and the formation of the ring structures at the centre of the clusters. However, only half of the terminal ethyl groups in the *in situ* trimer species of (1) – (4) are oxidised. This leaves the remaining two terminal ethyl groups on Zn centres in (5) – (8) unchanged. These groups also exhibited reluctance to further immediate oxidation when exposed to air over a period of hours. However, they did degrade when exposed to air overnight. As such, complexes (5) – (8) were all found to be only mildly air sensitive, exhibiting significantly greater stability towards air than the zinc trimers (1) – (4).

Zinc oxane clusters (**5**) and (**7**) were isolated as off-white solids upon the removal of hexane in yields of 87 and 85% respectively. Zinc oxane clusters (**6**) and (**8**) crystallised out of concentrated solutions in hexane held at -18 °C as off-white crystals in yields of 84 and 83% respectively. ^1H , ^{13}C and HSQC NMR spectroscopy were used in the characterisation of (**5**) – (**8**) with similar chemical shifts observed for corresponding proton and carbon environments in the complexes. As will be described, features such as peak broadening and the presence of additional broad peaks also appear in the ^1H NMR spectra. Elemental analysis and mass spectroscopy were also used in the characterisation of these complexes and the crystal structure of (**6**) and (**8**) were also determined *via* single crystal X-ray diffraction.

4.2.1.2.1 Synthesis of $[(\text{Zn}(\text{OC}(\text{OMe})\text{CHC}(\text{Me})\text{O})_2\text{Zn}(\text{Et})\text{OEt})_2]$ (**5**)

The synthesis of $[(\text{Zn}(\text{OC}(\text{OMe})\text{CHC}(\text{Me})\text{O})_2\text{Zn}(\text{Et})\text{OEt})_2]$ (**5**) was initiated by the addition of dry methyl acetoacetate to ZnEt_2 in dry hexane under inert conditions. The addition was performed at -78 °C to account for the pyrophoricity of ZnEt_2 . The solution was stirred and upon warming to room temperature the evolution of a gas, believed to be the ethane reaction by-product was observed. The solution was stirred for 48 hours, after which it was again cooled to -78 °C and a small volume of oxygen was added to the flask. The solution was warmed to room temperature and stirred for 15 minutes before being frozen and the flask purged with nitrogen. After stirring for 24 hours at room temperature, the hexane was removed *in vacuo* and the product isolated as an off-white solid.

The synthesis of (**5**) was confirmed using ^1H and ^{13}C NMR spectroscopy. In the ^1H NMR spectrum shown in Figure 4.12, each resonance was assigned to an expected proton environment and was present with the correct splitting pattern. The peaks associated with the ethyl groups attached to the Zn atoms correspond to the quartet at 0.62 ppm and triplet at 1.60 ppm for the CH_2 and CH_3 protons respectively. The ethoxide groups in the centre of the cluster correspond to the triplet at 1.33 ppm and quartet at 3.87 ppm for the CH_3 and CH_2 protons respectively. The three singlets for the proton environments associated with the four bidentate ligand bound through two O atoms appear at 1.90, 3.33 and 4.9 ppm for the CCH_3 , OCH_3 and CCHC protons respectively.

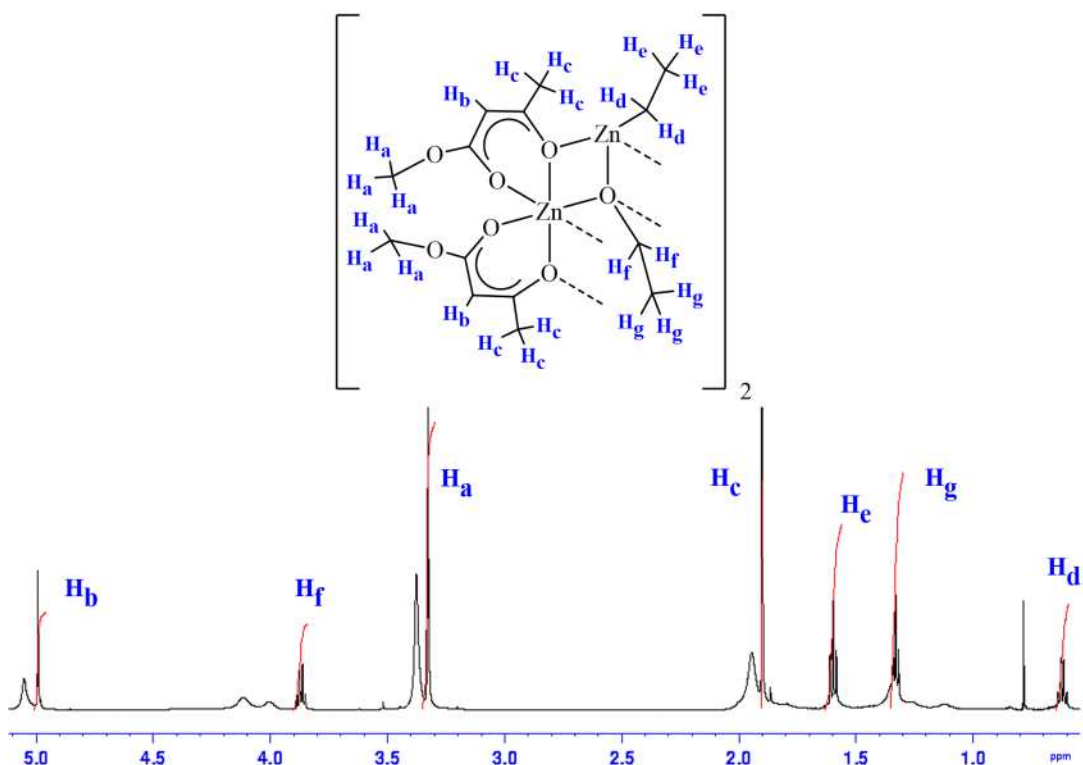


Figure 4.12: ^1H NMR spectrum of $[(\text{Zn}(\text{OC}(\text{OMe})\text{CHC}(\text{Me})\text{O})_2\text{Zn}(\text{Et})\text{OEt})_2]$ (**5**).

However, also present in the ^1H spectrum, as shown in Figure 4.12, are broader peaks absent of splitting patterns. Due to the nature of the system and the high reactivity of both ZnEt_2 and the intermediate trimer (**1**), it is possible that side products have also been synthesised and a product mixture is present. However, the broad nature of the peaks and their association to sharp peaks with splitting patterns suggest they may represent the intermediate exchanging or rotations of the proton environments in the system. These features were investigated further using variable temperature ^1H NMR, which was performed at 75°C and is shown in Figure 4.13. The spectrum illustrates that upon heating the broad and sharp peaks converge into a single broad peak. This suggests the peaks represent equivalent protons and the broad peaks in Figure 4.12 result from the fluxional processes.

^{13}C NMR also confirmed the successful synthesis of (**5**) with all carbon environments in (**5**) associated with predicted peaks in the obtained spectrum. $^1\text{H} - ^{13}\text{C}$ HSQC NMR was also performed and used to correlate the proton and carbon environments. The peaks associated with the ethyl group carbons attached to the Zn atom appear at 2.2 and 12.6 ppm for the $\underline{\text{C}}\text{H}_2$ and $\underline{\text{C}}\text{H}_3$ environments respectively. The ethoxide groups

in the centre of the cluster correspond to the peaks at 19.7 and 61.3 ppm for the $\underline{\text{CH}}_3$ and $\underline{\text{CH}}_2$ carbon environments respectively. The peaks for the $\text{C}\underline{\text{CH}}\text{C}$, $\underline{\text{COCH}}_3$ and $\underline{\text{CCH}}_3$ carbon environments in the four ZnO_2C_3 rings appear at 87.0, 173.6 and 183.3 ppm respectively. The peaks for the $\underline{\text{CH}}_3$ and $\text{O}\underline{\text{CH}}_3$ carbon environments for the groups bound to the ZnO_2C_3 rings appear at 27.3 and 50.6 ppm respectively.

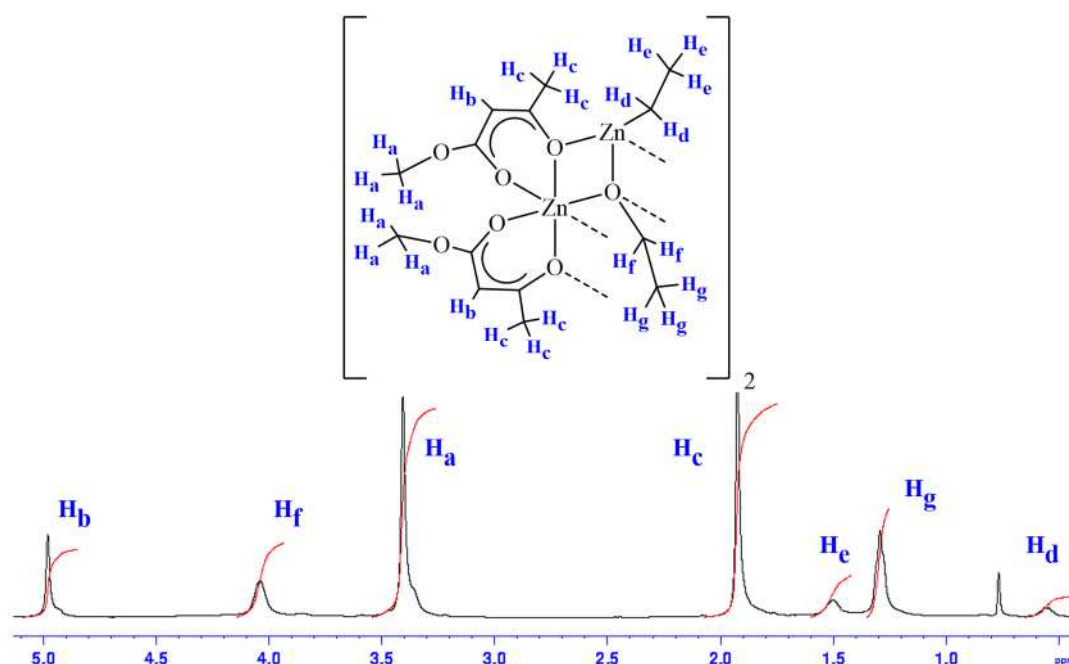


Figure 4.13: ^1H NMR spectrum of $[(\text{Zn}(\text{OC}(\text{OMe})\text{CHC}(\text{Me})\text{O})_2\text{Zn}(\text{Et})\text{OEt})_2]$ (**5**) recorded at $75\text{ }^\circ\text{C}$.

Elemental analysis also confirms good agreement between the calculated C and H ratios for (**5**) of 38.64 and 5.56% respectively and the obtained values of 38.45 and 5.64% respectively. The mass spectrum of (**5**) also exhibits peaks not as single isolated peaks but rather as a series of peaks with varying intensities, resulting from the isotopic nature of Zn and C. Peaks were observed with the predicted isotopic pattern at m/z 474.87 and 294.97 for the $[\text{M} - \text{Zn}_2\text{O}_5\text{C}_{13}\text{H}_{27}]^{+}$ and $[\text{M} - \text{Zn}_3\text{O}_8\text{C}_{18}\text{H}_{34}]^{+}$ fragments of (**5**).

4.2.1.2.2 Synthesis of $[(\text{Zn}(\text{OC}(\text{Me})\text{CHC}(\text{Me})\text{O})_2\text{Zn}(\text{Et})\text{OEt})_2]$ (**6**)

The synthesis of $[(\text{Zn}(\text{OC}(\text{Me})\text{CHC}(\text{Me})\text{O})_2\text{Zn}(\text{Et})\text{OEt})_2]$ (**6**) resulted from the reaction between dry acetylacetone and ZnEt_2 following the procedure employed for

the synthesis of (**5**). The product crystallised out of a concentrated solution in hexane as off-white crystals in a yield of 84%.

The successful synthesis of (**6**) was confirmed using ^1H and ^{13}C NMR spectroscopy, in which all expected proton and carbon environments were successfully assigned to peaks in the obtained spectra. $^1\text{H} - ^{13}\text{C}$ HSQC NMR was performed and used to correlate the proton and carbon environments. In the ^1H NMR spectrum, the peaks associated with the ethyl groups attached to the Zn atoms correspond to broad peaks at 0.69 and 1.61 ppm for the CH_2 and CH_3 protons respectively. The peaks corresponding to the ethoxide groups in the centre of the cluster are the triplet at 1.42 ppm and quartet at 3.80 ppm for the CH_3 and CH_2 protons respectively. The CCH_3 and CCH proton environments associated with the four bidentate ligands bound through two O atoms appear as singlets at 1.79 and 5.06 ppm respectively. Unlike in (**5**), no additional peaks were observed but the peaks in the ^1H spectrum appear broad. As in the case with (**5**), this feature is likely to result from the intermediate exchanging or rotations of the proton environments in the system.

The ^{13}C NMR was also fully assigned with all carbon environments in (**6**) associated with predicted peaks in the obtained spectrum. The peaks associated with the ethyl group carbons attached to the Zn atoms appear at 2.7 and 12.9 ppm for the CH_2 and CH_3 environments respectively. The ethoxide groups in the centre of the cluster correspond to the peaks at 20.1 and 61.1 ppm for the CH_3 and CH_2 carbon environments respectively. The peaks for the CCH and CCH_3 carbon environments in the four ZnO_2C_3 rings appear at 100.6 and 193.1 ppm respectively with the peak for the CH_3 carbons bound to the rings present at 28.1 ppm.

Elemental analysis also confirmed good agreement between the calculated C and H ratios for (**6**) of 41.71 and 6.00% respectively and the obtained values of 42.06 and 5.92% respectively. In the mass spectrum of (**6**), the peaks appear not as single isolated peaks but rather as a series of peaks with varying intensities, resulting from the isotopic nature of Zn and C. The mass spectrum of (**6**) contained a peak at m/z 847.04 with the predicted isotopic pattern for the mass ion of the cluster in combination with an adduct from the reagent gas, $[\text{M} + \text{C}_3\text{H}_5]^+$. The mass spectrum for (**6**) also shows peaks with the expected isotopic pattern at m/z 691.11, 426.91 and 263.00 for the $[\text{M} - \text{C}_8\text{H}_{20}]^+$, $[\text{M} - \text{Zn}_2\text{O}_4\text{C}_{13}\text{H}_{27}]^+$ and $[\text{M} - \text{Zn}_3\text{O}_6\text{C}_{18}\text{H}_{34}]^+$ respectively.

The crystal structure of the zinc oxane cluster $[(\text{Zn}(\text{OC}(\text{Me})\text{CHC}(\text{Me})\text{O})_2\text{Zn}(\text{Et})\text{OEt})_2]$ (**6**) was determined *via* single crystal X-ray diffraction and is shown in Figure 4.14. The determined crystallographic data is given in Table 4.3 with selected bond lengths and angles given in Table 4.4. Complex (**6**) crystallised as a centrosymmetric cluster in the triclinic $P\bar{1}$ space group. The cluster has four Zn centres, two of which are unique and two which are symmetrically equivalent. The Zn centres in (**6**) also have two different coordination modes: Zn(1) is in a distorted octahedral geometry whilst Zn(2) is in a distorted tetrahedral geometry, the same coordination environment as the Zn centres in the trimer $[(\text{Zn}(\text{Et})(\text{OC}(\text{OMe})\text{CHC}(\text{Me})\text{O}))_3]$ (**1**).

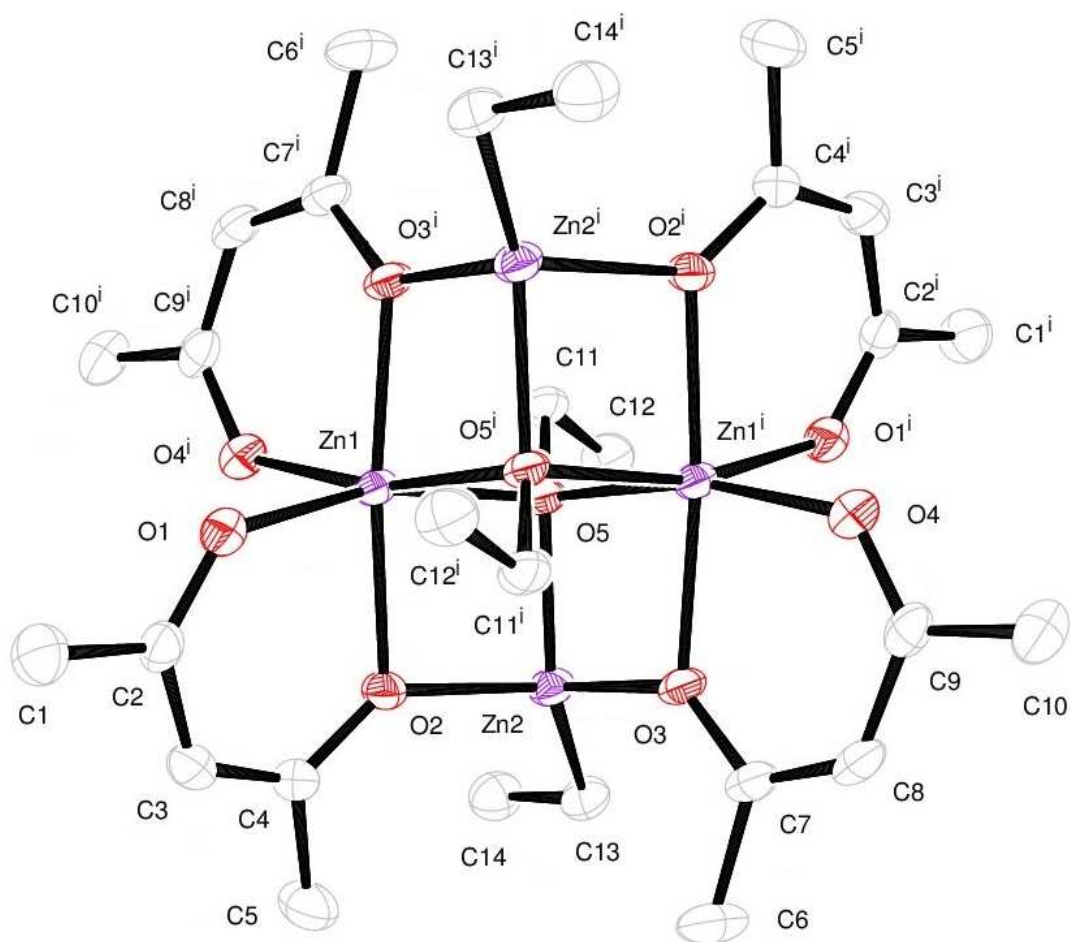


Figure 4.14: X-ray crystal structure of $[(\text{Zn}(\text{OC}(\text{Me})\text{CHC}(\text{Me})\text{O})_2\text{Zn}(\text{Et})\text{OEt})_2]$ (**6**).
(Symmetry operator: $i = -x, -y, -z$.)

Table 4.3: Crystallographic data for $[(\text{Zn}(\text{OC}(\text{Me})\text{CHC}(\text{Me})\text{O})_2\text{Zn}(\text{Et})\text{OEt})_2]$ (**6**).

Crystal System	Triclinic	
Space Group	$P\bar{1}$	
Volume	838.34(11) Å ³	
Unit Cell Dimensions	$a = 9.3721(7)$ Å	$\alpha = 99.361(5)^\circ$
	$b = 9.9549(6)$ Å	$\beta = 113.292(6)^\circ$
	$c = 10.5962(7)$ Å	$\gamma = 104.798(6)^\circ$

Zn(1) achieves its distorted octahedral geometry through the formation of six Zn-O bonds. Four of these bonds are formed from the bonding of two bidentate (OC(Me)CHC(Me)O) ligands. The first of these ligands bonds to Zn(1) through O(1) and O(2) and the second through O(3ⁱ) and O(4ⁱ). The bonding of these chelate ligands forms two puckered ZnO₂C₃ rings, in which Zn(1) is common to both. The remaining two coordination sites around Zn(1) are occupied by the bonding of two bridging ethoxide groups through O(5) and O(5ⁱ). The Zn(1)-O(5ⁱ) and Zn(1)-O(5ⁱ) bonds, along with their symmetrically equivalent bonds form a Zn₂O₂ centrosymmetric ring at the centre of (**6**). Zn(2) exists in a distorted tetrahedral geometry, forming three Zn-O bonds and one Zn-C bond. Zn(2) bonds to O(2) and O(3), which are both atoms in two different ZnO₂C₃ rings. Zn(2) also bonds to O(5), one of the bridging ethoxide groups in the central centrosymmetric Zn₂O₂ ring. These bonds and their symmetrically equivalent form four additional outer Zn₂O₂ rings in the cluster. One Zn-O bond from each of these four outer Zn₂O₂ rings is also shared with the central Zn₂O₂ ring. This forms a central structure in the cluster which appears as a face-shared, inversion-related, bis-heterocubane in which a counter corner is missing from each cubane. The remaining coordination site around Zn(2) is occupied by the bonding of a terminal ethyl group.

**Table 4.4: Selected bond lengths (Å) and angles (°) for
[(Zn(OC(Me)CHC(Me)O)₂Zn(Et)OEt)₂] (6).**

Zn(1)-O(1)	2.0536(18)	Zn(2)-O(3)	2.0778(17)
Zn(1)-O(2)	2.0921(16)	Zn(2)-O(5)	2.0006(15)
Zn(1)-O(3 ⁱ)	2.0704(16)	Zn(2)-C(13)	1.971(3)
Zn(1)-O(4 ⁱ)	2.0657(18)	O(1)-C(2)	1.259(3)
Zn(1)-O(5)	2.1217(17)	O(5)-C(11)	1.438(3)
Zn(1)-O(5 ⁱ)	2.1537(17)	C(1)-C(2)	1.502(4)
Zn(2)-O(2)	2.0720(17)	C(2)-C(3)	1.259(3)
O(1)-Zn(1)-O(2)	86.93(7)	O(5)-Zn(1)-O(3 ⁱ)	93.43(6)
O(1)-Zn(1)-O(3 ⁱ)	100.42(7)	O(5)-Zn(1)-O(4 ⁱ)	98.42(7)
O(1)-Zn(1)-O(4 ⁱ)	92.26(7)	O(5 ⁱ)-Zn(1)-O(3 ⁱ)	78.65(6)
O(1)-Zn(1)-O(5)	162.82(7)	O(5 ⁱ)-Zn(1)-O(4 ⁱ)	166.47(6)
O(1)-Zn(1)-O(5 ⁱ)	90.12(7)	O(2)-Zn(2)-O(3)	93.68(7)
O(2)-Zn(1)-O(3 ⁱ)	172.61(7)	O(2)-Zn(2)-O(5)	82.51(7)
O(2)-Zn(1)-O(4 ⁱ)	92.72(7)	O(2)-Zn(2)-C(13)	125.89(10)
O(2)-Zn(1)-O(5)	79.20(6)	O(3)-Zn(2)-O(5)	82.05(6)
O(2)-Zn(1)-O(5 ⁱ)	100.71(7)	O(3)-Zn(2)-C(13)	118.96(9)
O(3 ⁱ)-Zn(1)-O(4 ⁱ)	87.82(7)	O(5)-Zn(2)-C(13)	139.47(9)

Zn(1) makes six bonds, the longest of which are Zn(1)-O(5) and Zn(1)-O(5ⁱ) which form sides in the central Zn₂O₂ ring at 2.1217(17) and 2.1537(17) Å respectively. The Zn(1)-O(1) and Zn(1)-O(4ⁱ) bonds which form sides of the ZnO₂C₃ rings are shorter

at 2.0536(18) and 2.0657(18) Å respectively. The Zn(1)-O(2) and Zn(1)-O(3ⁱ) bonds which form sides in the ZnO₂C₃ rings and outer Zn₂O₂ rings have intermediate lengths of 2.0921(16) and 2.0704(16) Å respectively. The distorted nature of the octahedral coordination around Zn(1) results from the sterics of the cluster and the constraints of the ZnO₂C₃ and Zn₂O₂ rings. The three angles between opposite bonds, namely O(1)-Zn(1)-O(5), O(2)-Zn(1)-O(3ⁱ) and O(5ⁱ)-Zn(1)-O(4ⁱ) are all less than 180° at 162.82(7), 172.61(7) and 166.47(6)° respectively. The formation of the ring systems pull these bonds closer to one another than would occur in perfect octahedral coordination, reducing the angles between them. These smaller angles are counterbalanced by deviations observed in the adjacent angles. The bond angles inside the Zn₂O₂ rings are the smallest angles about Zn(1), where O(2)-Zn(1)-O(5) and O(5ⁱ)-Zn(1)-O(3ⁱ) have angles of 79.20(6) and 78.65(6)° respectively. The O(1)-Zn(1)-O(2) and O(3ⁱ)-Zn(1)-O(4ⁱ) bond angles inside the ZnO₂C₃ rings are also less than 90°, measuring 86.93(7) and 87.82(7)° respectively. The angle that exhibits greatest increased deviation from 90° is O(2)-Zn(1)-O(5ⁱ) at 100.71(7)°. This angle has less constraints as it does not form part of an outer Zn₂O₂ ring. The corresponding opposite angle of O(5)-Zn(1)-O(3ⁱ) measures 93.43(6)°. This difference is believed to result from the deviation in angles caused by the sterics of the terminal ethyl groups in the cluster. O(1)-Zn(1)-O(3ⁱ) and O(5)-Zn(1)-O(4ⁱ) also show large increased deviation from 90° measuring 100.42(7) and 98.42(7)° respectively. This minimises the steric interaction in (6) whilst also allowing for the constraints of the formed rings. The remaining O(1)-Zn(1)-O(5ⁱ), O(1)-Zn(1)-O(4ⁱ) and O(2)-Zn(1)-O(4ⁱ) angles around the zinc in a distorted octahedral coordination measure close to the expected 90° angle at 90.12(7), 92.26(7) and 92.72(7)° respectively. The bond lengths and angles around Zn(1) are similar to corresponding lengths and angles in analogous complexes and are as expected for Zn centres in this coordination environment.^{25,27,28}

Zn(2) makes four bonds, the longest of which are Zn(2)-O(2) and Zn(2)-O(3) which are part of the outer Zn₂O₂ rings and as expected, have similar values of 2.0720(17) and 2.0778(17) Å respectively. The Zn(2)-O(5) bond which connects Zn(2) to the bridging ethoxide group in the central Zn₂O₂ ring and forms a shared side of two outer Zn₂O₂ rings is slightly shorter at 2.0006(15) Å. As expected, the Zn(2)-C(13) bond is the shortest at 1.971(3) Å. The distorted nature of the tetrahedral coordination around Zn(2) results from the sterics of the cluster and the constraints of the ZnO₂C₃ and

Zn₂O₂ rings. The angles with increased deviation from 109.5° are O(2)-Zn(2)-C(13), O(3)-Zn(2)-C(13) and O(5)-Zn(2)-C(13) which measure 125.89(10), 118.96(9) and 139.47(9)° respectively. The angles all involve the Zn(2)-C(13) bond between the Zn(2) and the terminal ethyl group, which has greater flexibility and is not constrained by other bonds. The steric tension caused by the ethyl group is reduced with the increased bond angles. The O(5)-Zn(2)-C(13) angle exhibits the greatest deviation as there is greater steric reduction from maximising this angle. This increased deviation from 109.5° is counterbalanced by three angles which are noticeably smaller. O(2)-Zn(2)-O(5) and O(3)-Zn(2)-O(5) have the smallest bond angles around Zn(2) which measure 82.51(7) and 82.05(6)° respectively. These angles are both internal angles in an outer Zn₂O₂ ring and as expected, have similar values to each other. The O(2)-Zn(2)-O(3) bond angle is greater at 93.68(7)° but still smaller than 109.5°. This angle is constrained by the two Zn₂O₂ rings that the Zn(2)-O(2) and Zn(2)-O(3) bonds form part of. The bond lengths and angles around Zn(2) are similar to corresponding lengths and angles in analogous complexes and are as expected for Zn centres in this coordination environment.^{25,27,28}

The delocalised nature of the ZnO₂C₃ rings in (6) is also illustrated by the shorter bond lengths within the ring structures. For example, the O(1)-C(2) bond in the ZnO₂C₃ ring measures 1.259(3) Å which is shorter than the O(5)-C(11) bond of 1.438(3) Å. Similarly, the C(2)-C(3) bond of 1.417(4) Å is shorter than the C(1)-C(2) of 1.502(4) Å.

4.2.1.2.3 Synthesis of [(Zn(OC(OEt)CHC(Me)O)₂Zn(Et)OEt)₂] (7)

The synthesis of [(Zn(OC(OEt)CHC(Me)O)₂Zn(Et)OEt)₂] (7) resulted from the reaction between dry ethyl acetoacetate and ZnEt₂ following the procedure employed for the synthesis of (5). The product crystallised out of a concentrated solution in hexane as off-white crystals in a yield of 85%.

The synthesis of (7) was confirmed using ¹H and ¹³C NMR spectroscopy. In the ¹H NMR spectrum shown in Figure 4.15, each resonance was assigned to an expected proton environment and was present with the correct splitting pattern. The peaks associated with the ethyl groups attached to the two Zn atoms correspond to the quartet at 0.62 ppm and triplet at 1.61 ppm for the CH₂ and CH₃ protons respectively. The

ethoxide groups in the centre of the cluster correspond to the triplet at 1.37 ppm and quartet at 3.97 ppm for the $\underline{\text{CH}}_3$ and $\underline{\text{CH}}_2$ protons respectively. The ethoxide groups on the four bidentate ligands correspond to the triplet at 0.96 ppm and quartet at 3.92 ppm for the $\underline{\text{CH}}_3$ and $\underline{\text{CH}}_2$ protons respectively. The CCH_3 and CCHC proton environments associated with the ZnO_2C_3 rings appear as singlets at 1.92 and 4.99 ppm respectively.

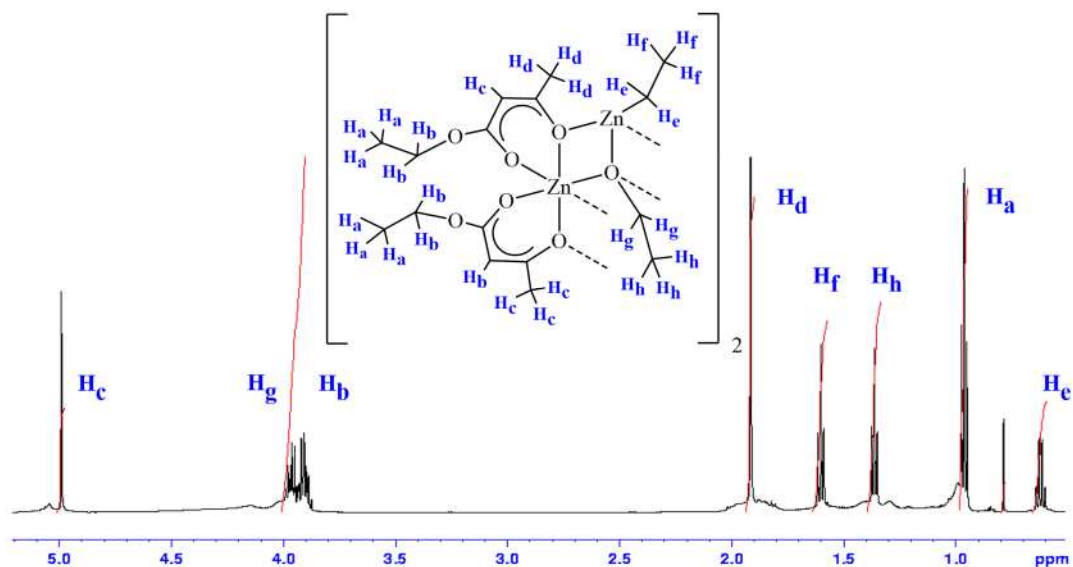


Figure 4.15: ^1H NMR spectrum of $[(\text{Zn}(\text{OC}(\text{OEt})\text{CHC}(\text{Me})\text{O})_2\text{Zn}(\text{Et})\text{OEt})_2]$ (**7**).

However, Figure 4.15 also illustrates the broadness of peaks close to the baseline of the spectrum. As has been suggested for the additional peaks in (**5**) and broadness of peaks in (**6**), this likely results as a feature from the intermediate exchanging or rotations of the proton environments in (**7**).

^{13}C NMR also confirmed the successful synthesis of (**7**) with all carbon environments in (**7**) associated with predicted peaks in the obtained spectrum. $^1\text{H} - ^{13}\text{C}$ HSQC NMR was also performed and used to correlate the proton and carbon environments. The peaks associated with the ethyl group carbons attached to the Zn atoms appear at 2.2 and 12.7 ppm for the $\underline{\text{CH}}_2$ and $\underline{\text{CH}}_3$ environments respectively. The ethoxide groups in the centre of the cluster correspond to the peaks at 19.8 and 61.3 ppm for the $\underline{\text{CH}}_3$ and $\underline{\text{CH}}_2$ carbon environments respectively. The peaks for the ethoxide group carbon environments attached to the ZnO_2C_3 rings appear at 14.4 and 59.7 ppm for the $\underline{\text{CH}}_3$

and $\underline{\text{CH}}_2$ environments respectively. The peak for the $\text{C}\underline{\text{CH}}_3$ methyl group carbon environment attached to the chelate rings appears at 27.3 ppm. The peaks for the $\text{C}\underline{\text{CH}}\text{C}$, $\underline{\text{C}}\text{OCH}_2\text{CH}_3$ and $\underline{\text{C}}\text{CH}_3$ carbon environments in the bidentate ligand rings appear at 87.3, 173.2 and 183.0 ppm respectively.

The obtained elemental analysis of (7) for C and H values of 40.88 and 5.70% respectively exhibits slight agreement to the calculated values of 41.49 and 6.09% respectively. The mass spectrum of (7) also exhibits peaks not as single isolated peaks but rather as a series of peaks with varying intensities, resulting from the isotopic nature of Zn and C. Peaks are observed with the predicted isotopic pattern at m/z 518.98 and 323.02 for the $[\text{M} - \text{Zn}_2\text{O}_5\text{C}_{14}\text{H}_{29}]^{+}$ and $[\text{M} - \text{Zn}_3\text{O}_8\text{C}_{20}\text{H}_{38}]^{+}$ fragments of (7).

4.2.1.2.4 Synthesis of $[(\text{Zn}(\text{OC}(\text{O}^t\text{Bu})\text{CHC}(\text{Me})\text{O})_2\text{Zn}(\text{Et})\text{OEt})_2]$ (8)

The synthesis of $[(\text{Zn}(\text{OC}(\text{O}^t\text{Bu})\text{CHC}(\text{Me})\text{O})_2\text{Zn}(\text{Et})\text{OEt})_2]$ (8) resulted from the reaction between dry *tert*-butyl acetoacetate and ZnEt_2 following the procedure employed for the synthesis of (5). The product crystallised out of a concentrated solution in hexane as off-white crystals in a yield of 83%.

The synthesis of (8) was confirmed using ^1H and ^{13}C NMR spectroscopy, with each proton and carbon environment assigned to peaks observed in the obtained spectra. $^1\text{H} - ^{13}\text{C}$ HSQC NMR was performed and used to correlate the proton and carbon environments. In the ^1H NMR spectrum, the peaks associated with the ethyl groups attached to the Zn atoms correspond to a broad quartet at 0.58 ppm and triplet at 1.66 ppm for the $\text{C}\underline{\text{H}}_2$ and $\text{C}\underline{\text{H}}_3$ protons respectively. The ethoxide groups in the centre of the cluster correspond to a broad triplet at 1.51 ppm and quartet at 4.02 ppm for the $\text{C}\underline{\text{H}}_3$ and $\text{C}\underline{\text{H}}_2$ protons respectively. The peaks for the $\text{C}\underline{\text{CH}}_3$ and $\text{C}\underline{\text{CH}}\text{C}$ proton environments of the four bidentate ligands bound through O atoms appear at 1.92 and 4.96 ppm respectively. The protons associated with the *tert*-butoxide group appear as a singlet at 1.44 ppm for the $\text{C}(\text{C}\underline{\text{H}}_3)_3$ environment. Unlike in (5), no additional peaks were observed but as for complexes (6) and (7), the peaks in the ^1H NMR spectrum for (8) appear broad. This feature is also likely to result from the intermediate exchanging or rotations of the proton environments in the system.

In the ^{13}C NMR spectrum of (**8**), the peaks associated with the ethyl groups attached directly to the Zn atoms appear at 1.8 and 13.1 ppm for the $\underline{\text{C}}\text{H}_2$ and $\underline{\text{C}}\text{H}_3$ environments respectively. The ethoxide groups correspond to the peaks at 19.8 and 61.4 ppm for the $\underline{\text{C}}\text{H}_3$ and $\underline{\text{C}}\text{H}_2$ carbon environments respectively. The peak for the $\underline{\text{C}}\text{H}_3$ carbon environment bound to the bidentate ligand rings appear at 27.3 and 27.4 ppm. The three carbon environments in the ZnO_2C_3 rings of $\underline{\text{C}}\underline{\text{C}}\text{HC}$, $\underline{\text{C}}\text{OC}(\text{CH}_3)_3$ and $\underline{\text{C}}\text{CH}_3$ are associated to the peaks at 88.7, 173.4 and 182.1 ppm respectively. The peaks associated with the *tert*-butoxide group appear at 28.7 and 79.7 ppm for the $\text{C}(\underline{\text{C}}\text{H}_3)_3$ and $\underline{\text{C}}(\text{CH}_3)_3$ environments respectively.

Elemental analysis also confirms good agreement between the calculated C and H ratios for (**8**) of 46.26 and 6.99% respectively and the obtained values of 46.43 and 7.27% respectively. The mass spectrum of (**8**) also exhibits peaks not as single isolated peaks but rather as a series of peaks with varying intensities, resulting from the isotopic nature of Zn and C. Peaks are observed with the predicted isotopic pattern at m/z 601.05 and 379.04 for the $[\text{M} - \text{Zn}_2\text{O}_5\text{C}_{16}\text{H}_{33}]^{+}$ and $[\text{M} - \text{Zn}_3\text{O}_8\text{C}_{24}\text{H}_{46}]^{+}$ fragments of (**8**).

The crystal structure of the zinc oxane cluster $[(\text{Zn}(\text{OC}(\text{O}^t\text{Bu})\text{CHC}(\text{Me})\text{O})_2\text{Zn}(\text{Et})\text{OEt})_2]$ (**8**) was determined *via* single crystal X-ray diffraction and is shown in Figure 4.16. Two $(\text{OC}(\text{O}^t\text{Bu})\text{CHC}(\text{Me})\text{O})$ chelate ligands bonding through O(2), O(4), O(1ⁱ) and O(5ⁱ) have been removed from Figure 4.15 for clarity. The determined crystallographic data is given in Table 4.5 with selected bond lengths and angles given in Table 4.6. Complex (**8**) crystallised as a centrosymmetric cluster in the triclinic $P\bar{1}$ space group. The cluster has four Zn centres, two of which are unique and two which are symmetrically equivalent. The Zn centres in (**8**) also have two different coordination modes. Zn(1) is in a distorted octahedral geometry whilst Zn(2) is in a distorted tetrahedral geometry, the same coordination environment as the Zn centres in the trimer $[(\text{Zn}(\text{Et})(\text{OC}(\text{OMe})\text{CHC}(\text{Me})\text{O}))_3]$ (**1**).

Zn(1) achieves its distorted octahedral geometry through the formation of six Zn-O bonds. Four of these bonds are formed from the bonding of two bidentate $(\text{OC}(\text{O}^t\text{Bu})\text{CHC}(\text{Me})\text{O})$ ligands. The first of these ligand bonds to Zn(1) through O(1) and O(2) and the second through O(2) and O(4). The bonding of these chelate ligands forms two puckered ZnO_2C_3 rings, in which Zn(1) is common to both. The remaining

two coordination sites around Zn(1) are occupied by the bonding of two bridging ethoxide groups through O(7) and O(7ⁱ). The Zn(1)-O(7) and Zn(1)-O(7ⁱ) bonds, along with their symmetrically equivalent bonds form a Zn₂O₂ centrosymmetric ring at the centre of (8).

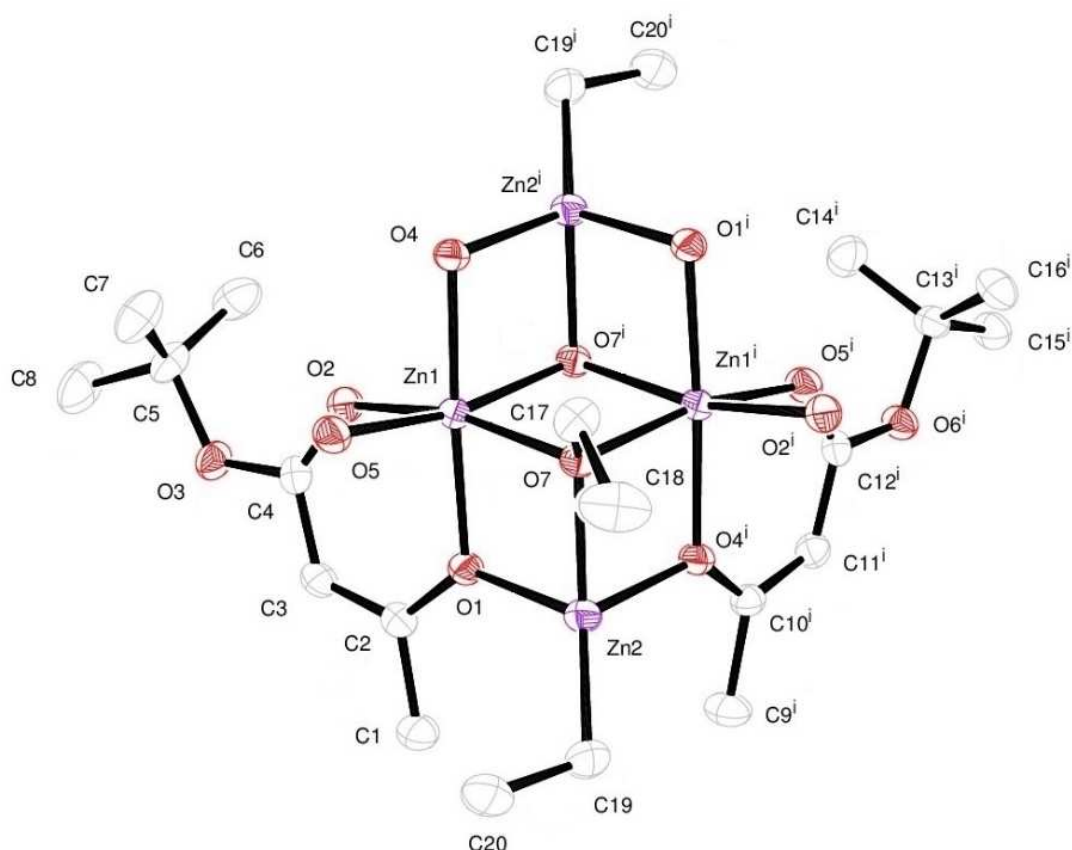


Figure 4.16: X-ray crystal structure of $[(\text{Zn}(\text{OC}(\text{O}'\text{Bu})\text{CHC}(\text{Me})\text{O})_2\text{Zn}(\text{Et})\text{OEt})_2]$ (8), two $(\text{OC}(\text{O}'\text{Bu})\text{CHC}(\text{Me})\text{O})$ chelate ligands bonding through O(2), O(4), O(1ⁱ) and O(5ⁱ) have been removed for clarity. (Symmetry operator: $i = -X, -Y, -Z$.)

Zn(2) exists in a distorted tetrahedral geometry, forming three Zn-O bonds and one Zn-C bond. Zn(2) bonds to O(1) and O(4ⁱ), which are both atoms in two different ZnO₂C₃ rings. Zn(2) also bonds to O(7), one of the bridging ethoxide groups in the central centrosymmetric Zn₂O₂ ring. These bonds and their symmetrically equivalent form four additional outer Zn₂O₂ rings in the cluster. One Zn-O bond from each of these four outer Zn₂O₂ rings is also shared with the central Zn₂O₂ ring. As with compound (6), this compound forms a central structure in the cluster which appears as a face-shared, inversion-related, bis-heterocubane in which a counter corner is

missing from each cubane. The remaining coordination site around Zn(2) is filled by the bonding of a terminal ethyl group.

Table 4.5: Crystallographic data for [(Zn(OC(O'Bu)CHC(Me)O)₂Zn(Et)OEt)₂] (8).

Crystal System	Triclinic	
Space Group	$P\bar{1}$	
Volume	2455.44(12) Å ³	
Unit Cell Dimensions	$a = 11.2864(2)$ Å	$\alpha = 110.060(3)^\circ$
	$b = 13.2409(4)$ Å	$\beta = 90.455(2)^\circ$
	$c = 17.7760(5)$ Å	$\gamma = 99.460(2)^\circ$

Zn(1) makes six bonds, the longest of which are Zn(1)-O(7) and Zn(1)-O(7ⁱ) which form sides in the central Zn₂O₂ ring at 2.1300(14) and 2.0874(14) Å respectively. The Zn(1)-O(2) and Zn(1)-O(5) bonds which form sides of the ZnO₂C₃ rings are shorter at 2.0796(15) and 2.0549(14) Å respectively. This compares to the Zn(1)-O(1) and Zn(1)-O(4) bonds which form sides in both the ZnO₂C₃ rings and outer Zn₂O₂ rings with have lengths of 2.0823(14) and 2.0730(14) Å respectively. The distorted nature of the octahedral coordination around Zn(1) results from the sterics of the cluster and the constraints of the ZnO₂C₃ and Zn₂O₂ rings. The three angles between opposite bonds, namely O(1)-Zn(1)-O(4), O(2)-Zn(1)-O(7) and O(5)-Zn(1)-O(7ⁱ) are all less than 180° at 176.70(6), 166.48(6) and 166.94(6)° respectively. The formation of the ring systems pull these bonds closer to one another than would occur in perfect octahedral coordination, reducing the angles between them. These smaller angles are counterbalanced by deviations observed in the adjacent angles. The bond angles inside the Zn₂O₂ rings are the smallest angles about Zn(1), where O(1)-Zn(1)-O(7) and O(4)-Zn(1)-O(7ⁱ) have angles of 79.79(5) and 80.03(5)° respectively. The angles which show the greatest increased deviation from 90° are O(1)-Zn(1)-O(7ⁱ) and O(4)-Zn(1)-O(7), which measure 98.41(6) and 97.13(6)° respectively. These angles also form part

of the inner face-shared bis-heterocubane but due to the missing corners on each heterocubane the angles have increased flexibility.

Table 4.6: Selected bond lengths (Å) and angles (°) for [(Zn(OC(O^tBu)CHC(Me)O)₂Zn(Et)OEt)₂] (8).

Zn(1)-O(1)	2.0823(14)	Zn(2)-O(4 ⁱ)	2.0660(14)
Zn(1)-O(2)	2.0796(15)	Zn(2)-O(7)	2.0255(14)
Zn(1)-O(4)	2.0730(14)	Zn(2)-C(19)	1.974(2)
Zn(1)-O(5)	2.0549(14)	O(1)-C(2)	1.306(2)
Zn(1)-O(7)	2.1300(14)	O(3)-C(5)	1.480(3)
Zn(1)-O(7 ⁱ)	2.0874(14)	C(1)-C(2)	1.506(3)
Zn(2)-O(1)	2.0644(14)	C(2)-C(3)	1.360(3)
O(1)-Zn(1)-O(2)	86.76(6)	O(4)-Zn(1)-O(7)	97.13(6)
O(1)-Zn(1)-O(4)	176.70(6)	O(4)-Zn(1)-O(7 ⁱ)	80.03(5)
O(1)-Zn(1)-O(5)	94.26(6)	O(5)-Zn(1)-O(7)	94.87(6)
O(1)-Zn(1)-O(7)	79.79(5)	O(5)-Zn(1)-O(7 ⁱ)	166.94(6)
O(1)-Zn(1)-O(7 ⁱ)	98.41(6)	O(1)-Zn(2)-O(4 ⁱ)	93.71(6)
O(2)-Zn(1)-O(4)	96.28(6)	O(1)-Zn(2)-O(7)	82.69(6)
O(2)-Zn(1)-O(5)	87.45(6)	O(1)-Zn(2)-C(19)	123.89(9)
O(2)-Zn(1)-O(7)	166.48(6)	O(4 ⁱ)-Zn(2)-O(7)	81.65(6)
O(2)-Zn(1)-O(7 ⁱ)	96.37(6)	O(4 ⁱ)-Zn(2)-C(19)	124.50(8)
O(4)-Zn(1)-O(5)	87.16(6)	O(7)-Zn(2)-C(19)	136.22(9)

The O(1)-Zn(1)-O(5) and O(2)-Zn(1)-O(4) bond angles inside the ZnO_2C_3 rings measure $94.26(6)$ and $96.28(6)^\circ$ respectively. These angles result from the sterics and rigidity of the ring systems, the bulk of the inner cluster and the sterics of the *tert*-butoxide group on the (OC(O^tBu)CHC(Me)O) ligands. The O(2)-Zn(1)-O(7ⁱ) and O(5)-Zn(1)-O(7) bonds between the Zn_2O_2 ring and the ZnO_2C_3 rings measure $96.37(6)$ and $94.87(6)^\circ$ respectively. These bonds are constrained by the ring systems but are greater than 90° to reduce the steric interaction of the terminal ethyl groups on the bridging ethoxide groups and the *tert*-butoxide group on the (OC(O^tBu)CHC(Me)O) ligands. The remaining O(1)-Zn(1)-O(2), O(4)-Zn(1)-O(5) and O(2)-Zn(1)-O(5) angles around the zinc in a distorted octahedral coordination measure $86.76(6)$, $87.16(6)$ and $87.45(6)^\circ$ respectively. These bond angles are outside of ring structures and with increased flexibility, counterbalance the angles greater than 90° . The bond lengths and angles around Zn(1) are similar to corresponding lengths and angles in analogous complexes and are as expected for Zn centres in this coordination environment.^{25,27,28}

As in the structure of (6), Zn(2) in this complex makes four bonds, the longest of which are Zn(2)-O(1) and Zn(2)-O(4ⁱ) which are part of the outer Zn_2O_2 rings and as expected, have similar values of $2.0644(14)$ and $2.0660(14)$ Å respectively. The Zn(2)-O(7) bond which connects Zn(2) to the bridging ethoxide group in the central Zn_2O_2 ring and forms a shared side of two outer Zn_2O_2 rings is slightly shorter at $2.0255(14)$ Å. As expected, the Zn(2)-C(19) bond is the shortest at $1.974(2)$ Å. The angles with increased deviation from 109.5° are O(1)-Zn(2)-C(19), O(4ⁱ)-Zn(2)-C(19) and O(7)-Zn(2)-C(19) which measure $123.89(9)$, $124.50(8)$ and $136.22(9)^\circ$ respectively. The angles all involve the Zn(2)-C(19) bond between the Zn(2) and the terminal ethyl group, which has greater flexibility and is not constrained by other bonds. The steric tension caused by the ethyl group is reduced with the increased bond angles. The O(7)-Zn(2)-C(19) angle exhibits the greatest deviation as there is greater steric reduction from maximising this angle. This increased deviation from 109.5° is counterbalanced by three angles which are noticeably smaller. O(1)-Zn(2)-O(7) and O(4ⁱ)-Zn(2)-O(7) have the smallest bond angles around Zn(2) which measure $82.69(6)$ and $81.65(6)^\circ$ respectively. These angle are both internal angles in an outer Zn_2O_2 ring and as expected, have similar values to each other. The O(1)-Zn(2)-O(4ⁱ) bond angle is greater at $93.71(6)^\circ$ but still smaller than 109.5° . This angle is constrained by the two

Zn₂O₂ rings that the Zn(2)-O(1) and Zn(2)-O(4ⁱ) bonds form part of. The bond lengths and angles around Zn(2) are similar to corresponding lengths and angles in analogous complexes and are as expected for Zn centres in this coordination environment.^{25,27,28}

The delocalised nature of the ZnO₂C₃ rings in **(8)** is also illustrated by the shorter bond lengths within the ring structures. For example, the O(1)-C(2) bond in the ZnO₂C₃ ring measures 1.306(2) Å which is shorter than the O(3)-C(5) bond of 1.480(3) Å. Similarly, the C(2)-C(3) bond of 1.360(3) Å is shorter than the C(1)-C(2) of 1.506(3) Å.

4.2.1.3 Crystal Structure Comparison of [(Zn(OC(Me)CHC(Me)O)₂Zn(Et)OEt)₂] (**6**) and [(Zn(OC(O^tBu)CHC(Me)O)₂Zn(Et)OEt)₂] (**8**)

Zinc oxane compounds **(6)** and **(8)** are both centrosymmetric clusters which crystallise in the triclinic *P* $\bar{1}$ space group. They each have four Zn atoms, two of which are unique and two of which are symmetrically equivalent. Two of these Zn atoms are in a distorted octahedral geometry whilst two have a distorted tetrahedral geometry. Both clusters also have a centrosymmetric Zn₂O₂ ring, four bound bidentate ligands and a central structure which appears as a face-shared, inversion-related, bis-heterocubane in which a counter corner is missing from each cubane. It is the rigidity of the formed ligand rings and the presence of terminal ethyl groups in both complexes which cause large deviation from the expected geometries about the octahedral and tetrahedral centres.

The bond lengths around Zn(1) and Zn(2) were observed to be similar in compounds **(6)** and **(8)** and both have a similar order of length of their corresponding bonds. For example, the longest bond lengths around Zn(1) in both are the two Zn-O bonds that form the central Zn₂O₂ ring. This is also the case around Zn(2), where the Zn-C bond to the terminal ethyl group is the shortest, whilst the longest bonds are to the two O atoms on the bidentate ligands.

The zinc oxane clusters differ by the R group on their four bound (OC(R)CHC(Me)O) bidentate ligands. In **(6)**, R is a methyl group, however in **(8)** it is a much larger *tert*-butoxide group. The increased bulk of the *tert*-butoxide group in **(8)** increases the

steric hindrance, affecting the coordination arrangement in the complex. An example of where the effects can be observed is the internal bond angle around Zn(1) of the two ZnO_2C_3 rings formed by the $(\text{OC}(\text{R})\text{CHC}(\text{Me})\text{O})$ bidentate ligands. In **(6)** $\text{O}(1)\text{-Zn}(1)\text{-O}(2)$ and $\text{O}(3^i)\text{-Zn}(1)\text{-O}(4^i)$ bonds measure $86.93(7)$ and $87.82(7)^\circ$ respectively, whilst the equivalent bonds in **(8)** of $\text{O}(1)\text{-Zn}(1)\text{-O}(5)$ and $\text{O}(2)\text{-Zn}(1)\text{-O}(4)$ measure $94.26(6)$ and $96.28(6)^\circ$ respectively.

Differences in the bond angles around Zn(2) are also observed, for example in the range observed in the bond angles involving the Zn-C bond to the terminal ethyl group. In **(6)**, the range involving this bond is from $118.96(9)$ to $139.47(9)^\circ$ for the $\text{O}(3)\text{-Zn}(2)\text{-C}(13)$ and $\text{O}(5)\text{-Zn}(2)\text{-C}(13)$ bonds respectively. In **(8)**, the range is from $123.89(9)$ to $136.22(9)^\circ$ for the $\text{O}(1)\text{-Zn}(2)\text{-C}(19)$ and $\text{O}(7)\text{-Zn}(2)\text{-C}(19)$ bonds respectively. The range in **(8)** is less due to the reduced freedom to avoid steric interaction as a result of the bulkier *tert*-butoxide group.

4.2.2 AACVD Precursors Study

The zinc trimer complexes **(1)** – **(4)** were found to be highly pyrophoric, offering little to overcome the issues related to the use of ZnEt_2 as a CVD precursor. However, zinc oxanes **(5)** – **(8)** were observed to offer much greater stability towards air and in doing so moving closer to meeting the desired properties for precursors as described in Chapter 1.5.1. Zinc oxane cluster $[(\text{Zn}(\text{OC}(\text{Me})\text{CHC}(\text{Me})\text{O})_2\text{Zn}(\text{Et})\text{OEt})_2]$ **(6)** was selected as the complex to be investigated for its potential use as a precursor in the AACVD of zinc oxide thin films as it is the most characterised of the zinc oxanes compounds. The characterisation of **(6)** by ^1H and ^{13}C NMR, MS, EA and a description of its crystal structure have been presented in Section 4.2.1.2.2. The thermal decomposition properties of **(6)** were studied before its application in the AACVD system.

4.2.2.1 Thermal Gravimetric Analysis

The thermal decomposition properties $[(\text{Zn}(\text{OC}(\text{Me})\text{CHC}(\text{Me})\text{O})_2\text{Zn}(\text{Et})\text{OEt})_2]$ **(6)** were investigated by thermal gravimetric analysis (TGA) and differential scanning

calorimetry (DSC) between room temperature (23 °C) and 600 °C in a helium atmosphere, as shown in Figure 4.17.

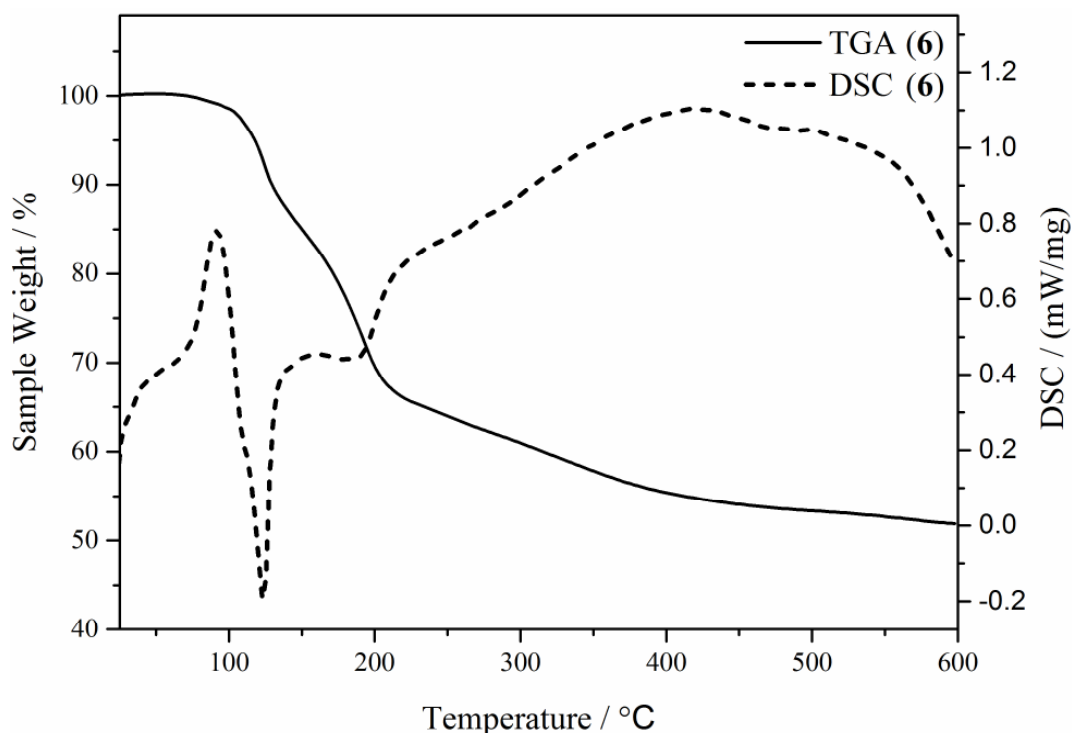


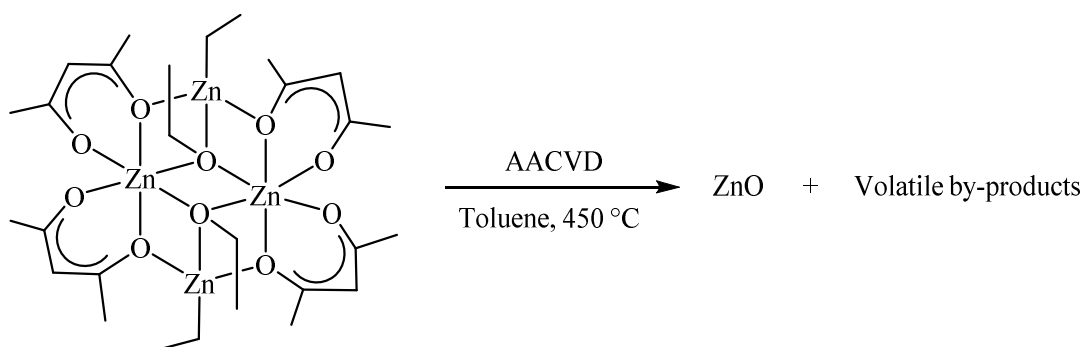
Figure 4.17: Thermal gravimetric analysis (TGA) and differential scanning (DSC) of zinc complex $[(\text{Zn}(\text{OC}(\text{Me})\text{CHC}(\text{Me})\text{O})_2\text{Zn}(\text{Et})\text{OEt})_2]$ (6).

The TGA and DSC profiles illustrate that (6) does not undergo a one-step, clean decomposition as an ideal CVD precursor would. Instead, the profiles illustrate that the decomposition is more complex and less complete than is desirable. Mass loss is observed to begin at 100 °C with the complex losing around 28% of its mass between 100 and 200 °C. However, the peak in the DSC and small dip in the TGA may suggest that part of this mass loss is associated with the evaporation of solvent. The loss of the two ethyl groups and two ethoxide groups may also occur in this region which would represent an 18.4% reduction in mass. The gradient of the TGA reduces at around 200 °C and remains steady until around 400 °C, during which time the complex loses around 14% of its mass. The gradient reduces again at around 400 °C and the complex loses around 4% of its mass until the heating stops at 600 °C. The residual mass at 600 °C is 51.8%, which is 11.4% higher than the 40.4% residual mass calculated for complete decomposition of (6) to ZnO. This additional mass indicates a potential for

significant contamination and the overall decomposition profile indicates that compound (**6**) may be unsuitable as a CVD precursor. The residual masses for all complexes used as AACVD precursors presented in this thesis are shown in Appendix Table 7.1.

4.2.3 AACVD of ZnO Thin Films

Zinc oxane $[(\text{Zn}(\text{OC}(\text{Me})\text{CHC}(\text{Me})\text{O})_2\text{Zn}(\text{Et})\text{OEt})_2]$ (**6**) was successfully employed as a single-source precursor in the AACVD of ZnO thin films as shown in Scheme 4.10. Initial studies into the effect of varying the substrate temperature between 400 and 600 °C and the N_2 carrier gas flow rates were carried out. Optimal coverage of the silica-coated float glass substrate was achieved using a temperature of 450 °C and an N_2 flow rate of 1 Lmin^{-1} . The films were also annealed post deposition at 600 °C for 6 hours. The films before they were annealed are referred to as ‘as deposited’ and following the heating treatment as ‘annealed’ films. All films were strongly adherent, passing the Scotch© tape test and only being removed upon intense scratching with a steel scalpel. The films were also insoluble in common organic solvents (acetone, toluene and 2-propanol) but dissolved in nitric acid.



Scheme 4.10: AACVD of $[(\text{Zn}(\text{OC}(\text{Me})\text{CHC}(\text{Me})\text{O})_2\text{Zn}(\text{Et})\text{OEt})_2]$ (**6**).

The as deposited films were very dark brown in colour, indicative of significant carbon content in the films, as later XPS analysis confirmed. This is likely to result from the incomplete decomposition of (**6**) whilst in the CVD chamber. Upon annealing, films appeared highly transparent and all brown coloration of the films had been removed. The films were characterised using X-ray photoelectron spectroscopy (XPS),

glancing-angle X-ray powder diffraction (XRD), scanning electron microscopy (SEM), UV/Vis/NIR transmission spectroscopy and two-point probe electrical measurements.

4.2.3.1 X-ray Photoelectron Spectroscopy

X-ray photoelectron spectroscopy (XPS) was performed on the as deposited and annealed thin film deposited from (6). The characteristic Zn 2p peaks for the Zn 2p_{1/2} and 2p_{3/2} states were fitted using a Gaussian/Lorentzian product distribution and are shown in Figure 4.18 for the annealed ZnO film deposited from (6). As expected, they appear at 1044.8 and 1021.7 eV binding energy respectively with an intensity ratio of 1:2 and an energy gap of 23.1 eV.²⁹ The O 1s peak was also fitted by a Gaussian distribution and as expected, was centred at 530.7 eV.

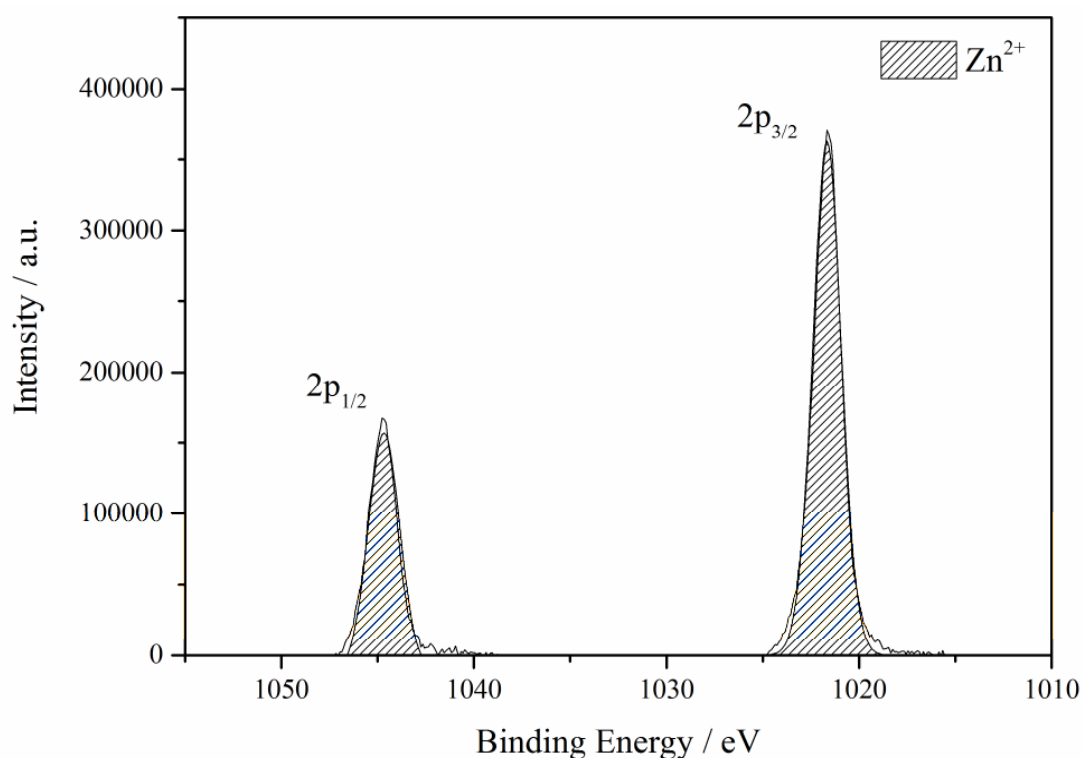


Figure 4.18: XPS of Zn 2p from a ZnO thin film deposited from [(Zn(OC(Me)CHC(Me)O)₂Zn(Et)OEt)₂] (6).

Using scan mode, depth profiles for the as deposited and annealed films from (6) were also obtained, as shown in Figure 4.19. The as deposited film is observed to be heavily

carbon contaminated throughout with an average carbon content of 65 at.%. Some carbon contamination was expected due to the TGA results but this level of carbon contamination is rarely seen, with the exception of some reported levels of surface carbon contamination of deposited ZnO thin films. Upon annealing, the carbon level observed in the film falls to < 1 at.%, as shown in Figure 4.19 resulting in a transparent ZnO thin film.

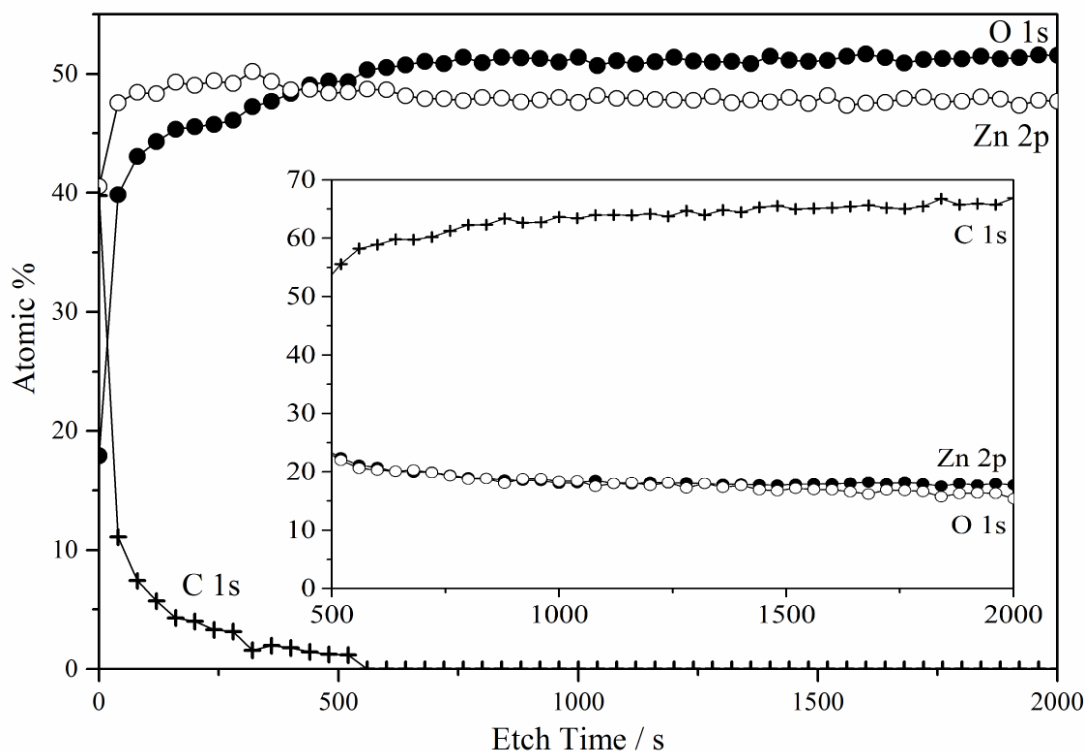


Figure 4.19: XPS depth profile for annealed films deposited from $[(\text{Zn}(\text{OC}(\text{Me})\text{CHC}(\text{Me})\text{O})_2\text{Zn}(\text{Et})\text{OEt})_2]$ (6). Inset: XPS depth profile for as deposited film.

4.2.3.2 X-ray Diffraction

Glancing-angle X-ray diffraction (XRD) patterns are shown in Figure 4.20 for the as deposited and annealed films from (6). No peaks were observed in the as deposited pattern which results for the high carbon level contained in the film. Upon annealing, peaks in the XRD pattern confirm the formation of the hexagonal wurtzite phase of ZnO. The morphology of the film was also analysed using SEM.

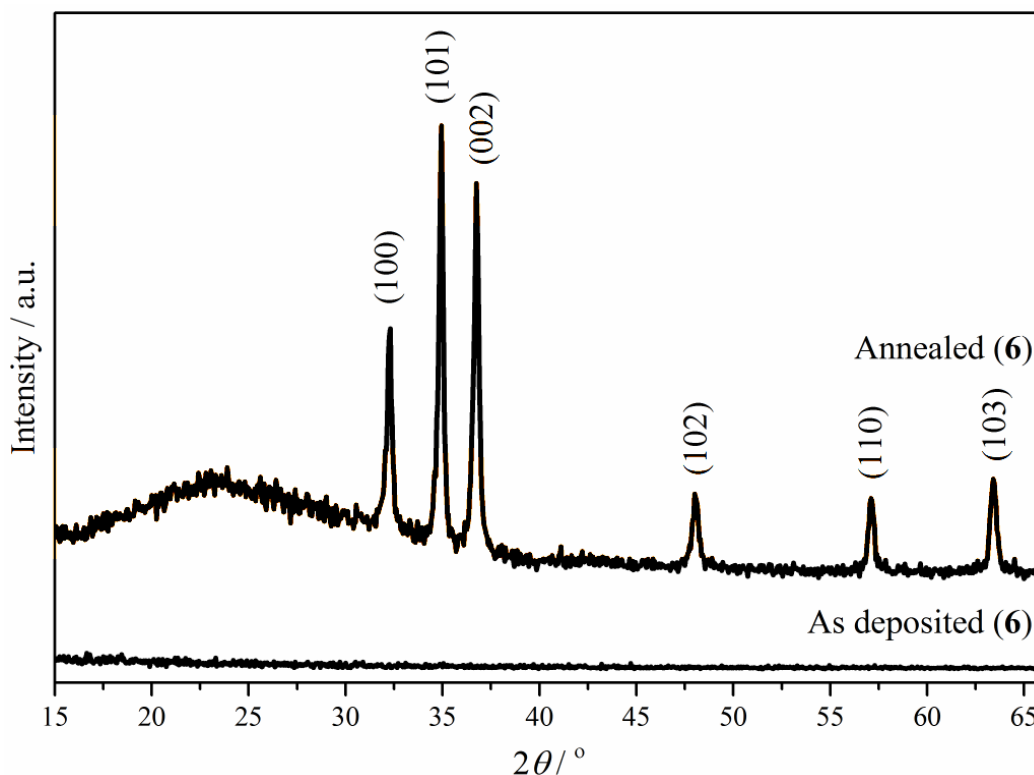


Figure 4.20: XRD patterns of as deposited and annealed films deposited from zinc complex $[(\text{Zn}(\text{OC}(\text{Me})\text{CHC}(\text{Me})\text{O})_2\text{Zn}(\text{Et})\text{OEt})_2]$ (6).

4.2.3.3 Scanning Electron Microscopy

Scanning electron microscopy (SEM) was performed on the annealed ZnO thin film deposited from (6) to determine the surface morphology of the film. The images shown in Figure 4.21 (a) – (c) reveal the surface of the film to be porous and formed of agglomerated rounded particles. This type of microstructure is suggestive of a Volmer-Weber type island growth mechanism in which the films have formed as the depositing particles agglomerate and other particles fill the gaps separating the agglomerates. There is quite a varied size distribution of agglomerate sizes, with diameters varying from < 50 nm to > 200 nm. The larger the agglomerate are in size, the less obvious the boundaries between particles and agglomerate are.

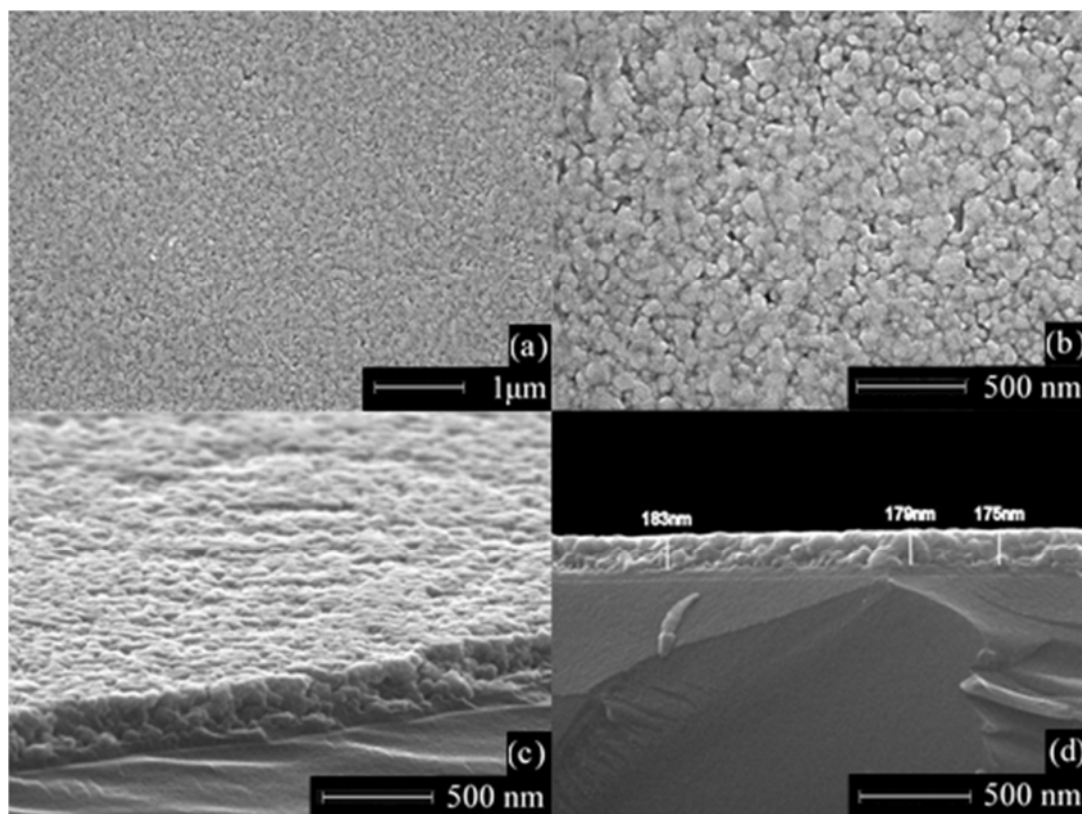


Figure 4.21: SEM images of annealed ZnO thin films deposited from $[(\text{Zn}(\text{OC}(\text{Me})\text{CHC}(\text{Me})\text{O})_2\text{Zn}(\text{Et})\text{OEt})_2]$ (6). (a) and (b) are plane view images at $\times 20,000$ and $\times 50,000$ respectively. (c) and (d) are cross section images at $\times 50,000$ with an 80° and 90° tilt respectively.

Cross section images shown in Figure (c) and (d) show the film to be porous and to have a similar structure throughout the depth of the film. The thickness of the annealed film from (6) was also determined *via* cross section SEM with a 90° tilt as seen in Figure 4.20 (d) and found to be around 180 nm.

4.2.3.4 Functional Properties

4.2.3.4.1 Electrical Properties

The as deposited and annealed films from (6) were tested for electrical conductivity but were found not to be conductive. The high level of carbon contamination is likely to be the cause for the lack of conductivity in the as deposited film. In the case of the annealed film, it is often the case that undoped ZnO thin films are either highly resistive or not conductive.³⁰ As described in Chapter 1.1.2, it is only by doping the

ZnO films using a dopant source such as Al, Ga or F that highly conductive films are produced.

4.2.3.4.2 Optical Properties

The transparency of the as deposited and annealed films from **(6)** was determined using UV/vis/near IR spectrometry, recorded between 250 and 1400 nm, as shown in Figure 4.22.

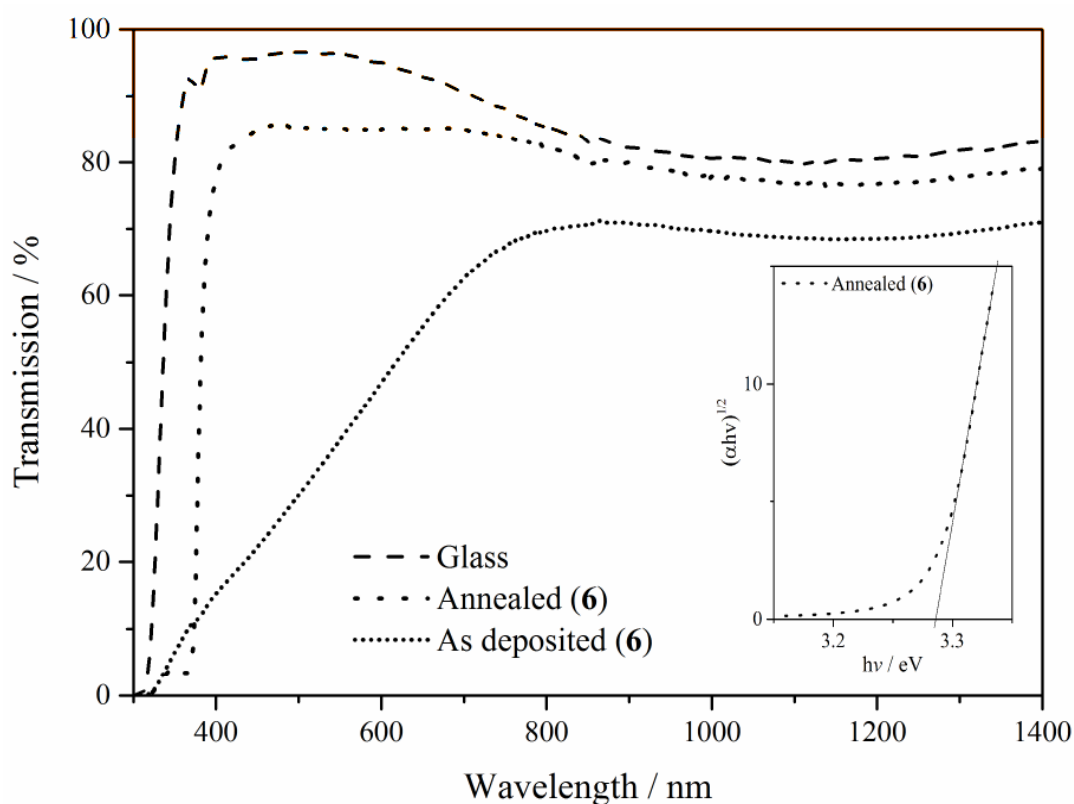


Figure 4.22: Transmission spectra observed for as deposited and annealed thin films deposited from $[(\text{Zn}(\text{OC}(\text{Me})\text{CHC}(\text{Me})\text{O})_2\text{Zn}(\text{Et})\text{OEt})_2]$ (6**). Insert: Tauc plot for annealed film.**

The as deposited film has an average transparency of 38% in the visible light region as a result of its high carbon content. After annealing, the film has an average transparency of 84% in the visible light region. This is greater than the 80% benchmark value that appears in the literature for a film to be described as highly transparent.³¹ Also apparent in Figure 4.22 is the shifting of the absorption edge of the annealed film

to a higher wavenumber relative to the float glass substrate. It is from this absorption edge that an estimate of the band gap of the film can be made.

4.2.3.4.2.1 Band Gap

The Tauc relation in Equation 4.1 can be used to estimate the band gap for the annealed film deposited from (6) using the absorption edge, the sharp decrease in transmission seen in Figure 4.22.

$$\alpha h\nu = A(h\nu - E_g)^n \quad \text{Equation 4.1}$$

In Equation 4.1, A is a constant, α is the molar extinction coefficient, $h\nu$ is the photon energy, E_g is the band gap and $n = 1/2$ for a direct allowed transition. The band gap of the annealed ZnO film was estimated to be 3.29 eV and was determined from the intercept of the $h\nu$ axis from a line of steepest gradient for the linear region of a $(\alpha h\nu)^{1/2}$ vs. $h\nu$ plot, as shown in Figure 4.21 (Inset). This value is in good agreement with the literature value of the ZnO band gap of 3.37 eV.³²

4.3 Conclusion

This chapter reports the synthesis of a family of zinc oxane complexes of two structural types. The first is a series of zinc oxane trimer complexes (1) – (4) with the formula $[(\text{Zn}(\text{Et})(\text{OC}(\text{R})\text{CHC}(\text{Me})\text{O}))_3]$, where R = OMe (1), Me (2), OEt (3) and O'Bu (4). These complexes were synthesised in a 1:1 reaction of ZnEt_2 and the corresponding dicarbonyl compound. The complexes were isolated and characterised using a number of analytical techniques including the determination of the crystal structure of (1). Compounds (1) – (4) were highly pyrophoric but upon the controlled addition of a small volume of O_2 , a selective oxidation reaction took place. These reactions resulted in the synthesis of zinc oxane clusters (5) – (8) with the formula $[(\text{Zn}(\text{OC}(\text{R})\text{CHC}(\text{Me})\text{O})_2\text{Zn}(\text{Et})\text{OEt})_2]$ (5) – (8), where R = OMe (5), Me (6), OEt (7) and O'Bu (8). These complexes were isolated and characterised and the crystal structure for (6) and (8) also determined. These complexes have a face-shared, corner-removed, inversion-related, bis-heterocubane central structure and were observed to

exhibit surprising resistance to further oxidation. As a proof of concept, (6) was employed as a single-source precursor in the AACVD of ZnO thin films. Characterisation of (6) and the resulting films however reveal that zinc oxanes of this type may not be ideal as CVD precursors.

4.4 References

1. O. Pagni, N. N. Somhlahllo, C. Weichsel and A. W. R. Leitch, *Phys. B Condens. Matter.*, 2006, **376** – **377**, 749 – 751.
2. S. D. Ponja, S. Sathasivam, I. P. Parkin and C. J. Carmalt, *RSC Adv.*, 2014, **4**, 49723 – 49728.
3. J. Auld, D. J. Houlton, A. C. Jones, S. A. Rushworth, M. A. Malik, P. O'Brien and G. W. Crichtlow, *J. Mater. Chem.*, 1994, **4**, 1249 – 1253.
4. S. Jana, R. J. F. Berger, R. Fröhlich, T. Pape and N. W. Mitzel, *Inorg. Chem.*, 2007, **46**, 4293 – 4297.
5. D. Prochowicz, K. Sokołowski and J. Lewiński, *Coord. Chem. Rev.*, 2014, **270** – **271**, 112 – 126.
6. C. Di Iulio, M. D. Jones, M. F. Mahon and D. C. Apperley, *Inorg. Chem.*, 2010, **49**, 10232 – 10234.
7. K. Sokołowski, I. Justyniak, W. Śliwiński, K. Sołtys, A. Tulewicz, A. Kornowicz, R. Moszyński, J. Lipkowski and J. Lewiński, *Chem. Eur. J.*, 2012, **18**, 5637 – 5645.
8. K. Sokołowski, I. Justyniak, W. Bury, J. Grzonka, Z. Kaszukur, Ł. Mąkowski, M. Dutkiewicz, A. Lewalska, E. Krajewska, D. Kubicki, K. Wójcik, K. J. Kurzydłowski and J. Lewiński, *Chem. Eur. J.*, 2015, **21**, 5488 – 5495.
9. T. J. Boyle, S. D. Bunge, N. L. Andrews, L. E. Matzen, K. Sieg, M. A. Rodriguez and T. J. Headley, *Chem. Mater.*, 2004, **16**, 3279 – 3288.
10. A. L. Johnson, N. Hollingsworth, G. Kociok-Köhn and K. C. Molloy, *Inorg. Chem.*, 2008, **47**, 12040 – 12048.
11. P. Marchand and C. J. Carmalt, *Coord. Chem. Rev.*, 2013, **257**, 3202 – 3221.
12. L. McElwee-White, *Dalton Trans.*, 2006, **45**, 5327 – 5333.
13. J. Lewiński, W. Śliwiński, M. Dranka, I. Justyniak and J. Lipkowski, *Angew. Chem.*, 2006, **118**, 4944 – 4947.
14. K. Budny-Godlewski, D. Kubicki, I. Justyniak and J. Lewiński, *Organometallics*, 2014, **33**, 5093 – 5096.
15. J. Lewiński, W. Bury, M. Dutkiewicz, M. Maurin, I. Justyniak and J. Lipkowski, *Angew. Chem. Int. Ed.*, 2008, **47**, 573 – 576.
16. Ł. Mąkowski, K. Zelga, R. Petrus, D. Kubicki, P. Zarzycki, P. Sobota, J. Lewiński, *Chem. Eur. J.*, 2014, **20**, 14790 – 14799.
17. J. Lewiński, M. Dutkiewicz, M. Lesiuk, W. Śliwiński, K. Zelga, I. Justyniak and J. Lipkowski, *Angew. Chem. Int. Ed.*, 2010, **49**, 8266 – 8269.
18. C. Di Iulio, M. Middleton, G. Kociok-Köhn, M. D. Jones and A. L. Johnson, *Eur. J. Inorg. Chem.*, 2013, **9**, 1541 – 1554.
19. N. Hollingsworth, A. L. Johnson, A. Kingsley, G. Kociok-Köhn and K. C. Molloy, *Organometallics*, 2010, **29**, 3318 – 3326.
20. P. Sobota, R. Petrus, K. Zelga, Ł. Mąkowski, D. Kubicki and J. Lewiński, *Chem. Commun.*, 2013, **49**, 10477 – 10479.
21. S. C. Moratti and J. Simpson, *Acta Crystallogr. Sect. E*, 2007, **63**, m2444 – m2444.
22. S. Polarz, A. Roy, M. Merz, S. Halm, D. Schröder, L. Schneider, G. Bacher, F. E. Kruis and M. Driess, *Small*, 2005, **1**, 540 – 552.
23. M. Ishimori, T. Hagiwara, T. Tsuruta, Y. Kai, N. Yasuoka, N. Kasai, *Bull. Chem. Soc. Jpn.*, 1976, **49**, 1165 – 1166.
24. J. Lewiński, W. Marciniak, J. Lipkowski and I. Justyniak, *J. Am. Chem. Soc.*, 2003, **125**, 12698 – 12699.

-
25. R. Petrus and P. Sobota, *Organometallics*, 2012, **31**, 4755 – 4762.
 26. G. A. Seisenbaeva, M. Kritikos and V. G. Kessler, *Polyhedron*, 2003, **22**, 2581 – 2586.
 27. J. Dekker, A. Schouten, P. H. M. Budzelaar, J. Boersma and G. J. M. van Der Kerk, *J. Organomet. Chem.*, 1987, **320**, 1 – 12.
 28. J. Boersma, A. L. Spek and J. G. Noltes, *J. Organomet. Chem.*, 1974, **81**, 7 – 15.
 29. B. S. Shaheen, H. G. Salem, M. A. El-Sayed N. K. Allam, *J. Phys. Chem. C*, 2013, **117**, 18502 – 18509.
 30. R. Romero, M. C. López, D. Leinen, F. Martín and J. R. Ramos-Barrado, *Mater. Sci. Eng. B*, 2004, **110**, 87 – 93.
 31. S. Kaleemulla, N. M. Rao, M. G. Joshi, A. S. Reddy, S. Uthanna and P. S. Reddy, *J. Alloys Compd.*, 2010, **504**, 351 – 356.
 32. S. T. Tan, B. J. Chen, X. W. Sun, W. J. Fan, H. S. Kwok, X. H. Zhang and S. J. Chua, *J. Appl. Phys.*, 2005, **98**, 013505(1) – 013505(5).

Chapter 5

Synthesis of Zinc β -Iminoesterates and the AACVD of Zinc Oxide Thin Films

*This chapter describes the synthesis of four β -iminoester ligands (**L**₁) – (**L**₄) and their subsequent reaction with diethylzinc to form zinc β -iminoesterates complexes. The synthesized complexes are of two structural types: the homoleptic $[\text{Zn}(\text{L}_x)_2]$ monomeric complexes (**9**) – (**12**) and the heteroleptic $[(\text{Zn}(\text{L}_x)\text{Et})_2]$ dimeric complexes (**13**) and (**14**) where L_x is a β -iminoester ligand. The complexes have been isolated and characterized and four single crystal X-ray diffraction structures determined. Two complexes, (**9**) and (**10**) of the $[\text{Zn}(\text{L}_x)_2]$ type were used for the first time as single source zinc β -iminoesterate precursors in the AACVD of ZnO thin films. Upon analysis, it is shown that the organic ligand attached to the N moiety of the zinc complex has a significant effect on the level of carbon incorporated into the deposited thin film. After annealing, highly transparent hexagonal wurtzite ZnO thin films were produced.*

5.1 Introduction

β -Ketoiminate complexes have been the subject of investigation for their application as catalysts in a variety of polymerisation reactions including ethylene polymerisation and ring opening polymerisation^{1,2,3} due to the nature of the β -ketoiminate ligands. There has been a growing interest in the use of metal β -ketoiminates as precursors in the deposition of metal oxide thin films, a use for which they exhibit great potential.

Metal β -ketoiminates are synthesised by the reaction of the metal containing precursor with the β -ketoimine ligand of the general structure shown in Figure 5.1. The β -ketoimine ligand is chelating and bonds to the metal centre through both the N and O atoms. Driving the reaction forward is believed to be the stability of the β -ketoiminate product and the weak basicity of the β -ketoimine anions.⁴

One of the most appealing features of β -ketoiminates is the ability to alter the substituent group on more than one position in the complex. For example, both the R¹ and R² groups on the back bone of the ligand in Figure 5.1, as well as the R³ group on the nitrogen moiety can be altered. This in effect allows the electronic and steric properties of the resultant metal complex to be changed. This is achieved through selection of the amine and dicarbonyl compounds used to synthesise the ligand.

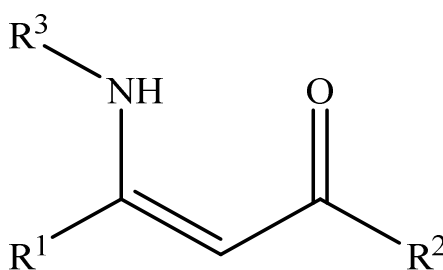


Figure 5.1: Structure of the β -ketoimine ligand.

These complexes offer a number of advantages for CVD purposes, including improved thermal stability and solubilities⁵ are achieved. Since the nitrogen is a weaker donor than oxygen, the complexes are believed to be more volatile at lower temperatures than for the all oxygen-coordinated complexes.⁶

These compounds also meet a number of the desired precursor properties discussed in Chapter 1.5.1, including the presence of the preformed Zn–O bond and the potential to be used as single-source precursors. They also offer the capability to support a tetrahedral coordination about a Zn centre and have the ability to promote reduced oligomerisation.

This introduction examines the synthesis of the β -ketoimine and β -iminoester ligands and their use in the synthesis of alkaline earth, group 13 and transition metal complexes. The synthesis and use of zinc β -ketoimine and β -iminoesterate complexes prior to this work will also be established before discussing the results presented in this chapter.

5.1.1 β -Ketoimine and β -Iminoester Ligands

β -Ketoimine and β -iminoester ligands have the general structure shown in Figure 5.2 (a) and (b) respectively and are the product of a reaction between the corresponding amine and dicarbonyl compound.

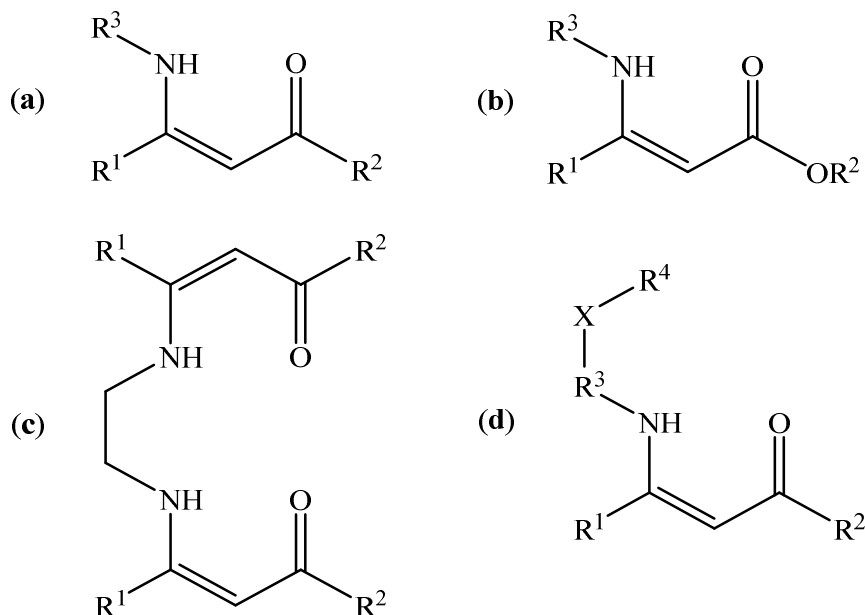


Figure 5.2: Structure of (a) a β -ketoimine ligand, (b) a β -iminoester ligand (c) a bis(β -ketoimine) ligand and (d) a patented β -ketoimine ligand, where R is a linear or branched alkyl group.

The structure of the ligand can be more elaborate, such as the bis(β -ketoimine) ligand shown in Figure 5.2 (c)⁷ in which the ligand provides four potential appendage points to a metal centre. β -Ketoimine ligands have also been the subject of a number of patents, including those of the type shown in Figure 5.2 (d) where R¹ – R⁴ are generally linear or branched alkyl groups and X is an O or S atom.⁸

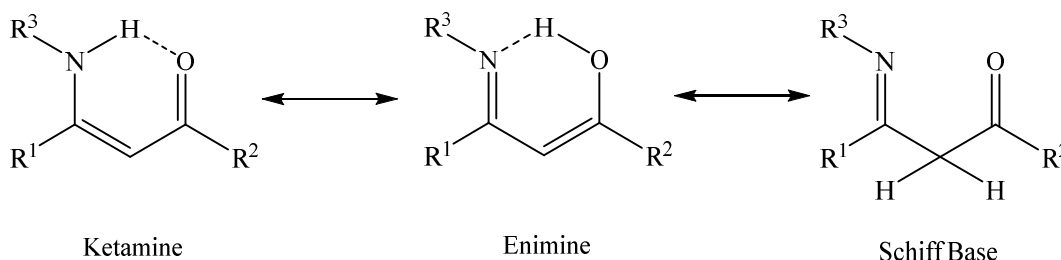
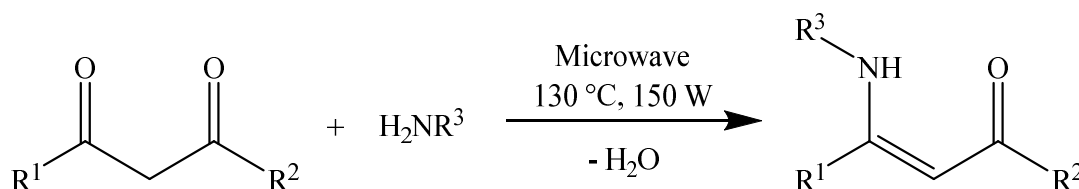


Figure 5.3: Tautomeric structures of a β -ketoimine and β -iminoester ligand.⁹

Granum *et al.*⁹ describe how three tautomeric forms of the ligand are possible, as shown in Figure 5.3. They suggest, given the characterisation of their synthesised ligands, that the best description of the ligands is that of protonated β -ketoimine ligands. Typically, these ligands are formed *via* reflux condensations reactions,¹⁰ which require reflux conditions at elevated temperature in a suitable solvent for a period of hours or days. However, alternative methods with high yields and greener credentials have also been used.

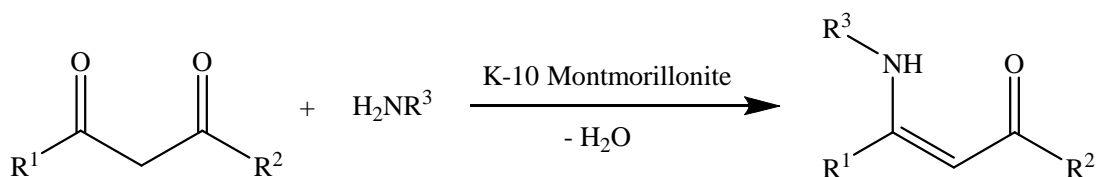
Lee *et al.*¹¹ have conducted an extensive study into the microwave accelerated preparation of these ligands, according to Scheme 5.1, expanding on earlier work by Rechsteiner *et al.*¹²



Scheme 5.1: Microwave assisted preparation of β -ketoimine ligands.¹¹

Their study involved the reaction of β -diketones with a wide variety of amines in a 1:1.1 molar ratio under solvent free conditions. Yields ranged between 59 and 100%, with higher yields obtained than those reported for conventional synthetic methods, particularly those with bulky substituents. Strauss and Rooney¹³ suggest that thermal reactions proceed optimally when they are rapidly heated to the highest tolerable temperature, held there for the shortest possible time and followed by quenching. They argue that microwave conditions are well suited to achieving this.

An alternative method of synthesis involves the use of K-10 montmorillonite, a clay composed of aluminosilicate layers which has been employed in various organic reactions¹⁴ as a solid state catalyst including condensation reactions.¹⁵ Braibante *et al.*¹⁶ were the first and as far as can be seen, the only to report its use for the synthesis of β -ketoimine and β -iminoester ligands, as shown in Scheme 5.2.



Scheme 5.2: Preparation of β -ketoimine and β -iminoester ligands employing K-10 montmorillonite as a catalyst.¹⁶

K-10 montmorillonite is an abundant and inexpensive support¹⁷ and the use of such clays are of significant interest for their ease of set-up, low cost, abundance and their potential environmental benefits.¹⁷ It is their ability to behave as an acid catalyst,¹⁵ allowing for protonation as the first reaction step and the ability to stabilise higher energy reaction intermediates¹⁸ that allow for transformations to take place.

The process is a simple stirring reaction under ambient and solvent free conditions in which the dicarbonyl compound and amine reactants have been dispersed over the K-10 montmorillonite. Although DCM is used to extract the formed ligands this method can still claim its green credentials as ambient conditions significantly reduce the consumption of energy as opposed to reflux conditions.

Commercial and environmental gains are available through the use of microwave conditions or the use of K-10 montmorillonite as the two processes are capable of

delivering a high yield of product under milder conditions than reflux condensation reactions. β -Ketoimine and β -iminoester ligands synthesised by these methods have been used in the synthesis of a wide variety of β -ketoimine and iminoesterate metal complexes.

5.1.2 β -Ketoiminates and β -Iminoesterates Metal Complexes

5.1.2.1 Commercial Importance

The commercial importance of these complexes is an important factor given, if proved successful, their value would be high. Patents have been filed not only for β -ketamine ligands but also for certain types of β -ketoiminates complexes, as shown by the two examples below. Firstly, a patent filed by Lei *et al.*¹⁹ puts claim to ‘metal complexes of tridentate β -ketoiminates’ of the type shown in Figure 5.4 (a). Each R group has specific statements but are generally organic groups where M is stated to be one of 22, mainly metallic elements including palladium, titanium, iron, zinc and copper.

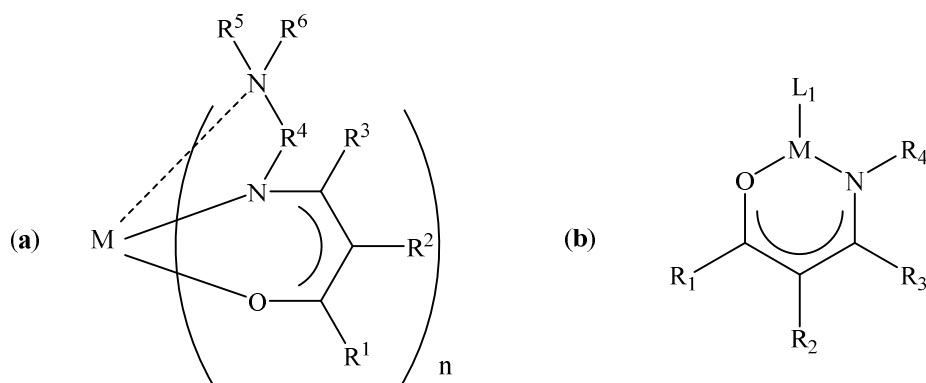
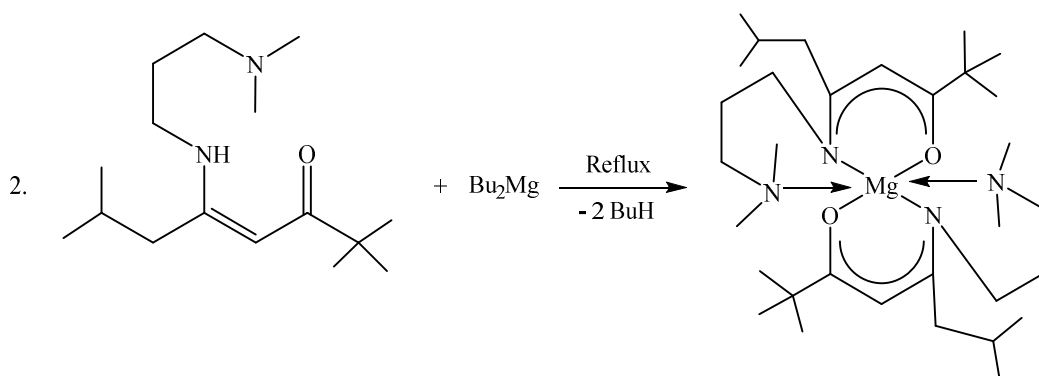


Figure 5.4: Patented metal β -ketoiminate complexes.^{19,20}

Norman²⁰ has laid claim to the ‘volatile metal β -ketoiminate complexes’ shown in Figure 5.4 (b) where M is Cu, Au, Co, Ru, Rh, Pt, In, Pd, Ni or Os, R can be hydrogens or groups such as alkyls, fluoroalkyls and halogens and L groups such as carbon monoxide, an alkyl nitrile or a silylalkyne. However, many other β -ketoiminate complexes have been synthesised and have not been patented, including a number of alkaline earth β -ketoiminates.

5.1.2.2 Alkaline Earth β -Ketoiminates

Matthews *et al.*²¹ used the dimethylaminopropyl-substituted β -ketoiminate ligand to coordinatively saturate the Mg centre of the β -ketoiminate of the complex, shown in Scheme 5.3. The reaction of dibutylmagnesium with the β -ketoiminate ligand yields the octahedral Mg complex in which the dimethylamino propyl groups form dative interactions and occupy both axial positions.

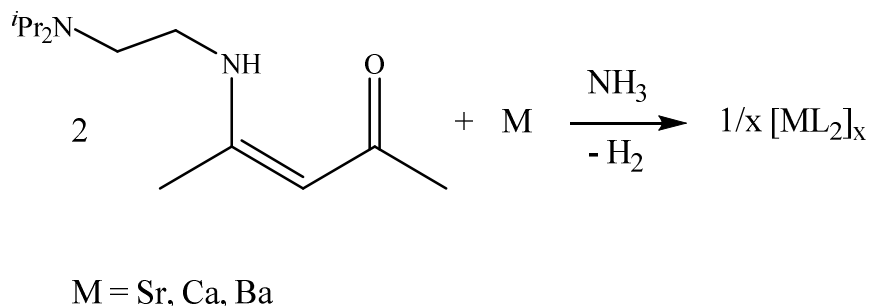


Scheme 5.3: Synthesis of magnesium β -ketoiminate complexes.²¹

TGA analysis showed the precursor to be thermally stable, decomposing in a single-step. Single-source CVD was carried out in the absence of additional oxygen which lead to the growth of stoichiometric magnesium oxide. Four-coordinate homoleptic magnesium β -ketoiminate complexes have also been synthesised and isolated as monomeric species.²²

Pasko *et al.*²³ have synthesised β -ketoiminate complexes of strontium, calcium and barium according to Scheme 5.4. Unlike other reactions seen in this introduction, the ligand was reacted directly with the metal. The metal was activated using ammonia which most likely allows for the synthesis of intermediate species such as amides and imides to form which will react with two equivalence of the β -ketoimine ligand. Yields varied from 60% where $\text{M} = \text{Sr}$ to 20% where $\text{M} = \text{Ca}$. Where M is Sr , a centrosymmetric trinuclear complex was synthesised. The central Sr was bonded to all six O atoms in the six β -ketoiminates and has trigonal antiprismatic geometry. The two outer Sr centres are six coordinate and bonded to three β -ketoiminates each

through both the N and O atoms. The ketoiminate ligand has also been extensively used in the synthesis of group 13 complexes.

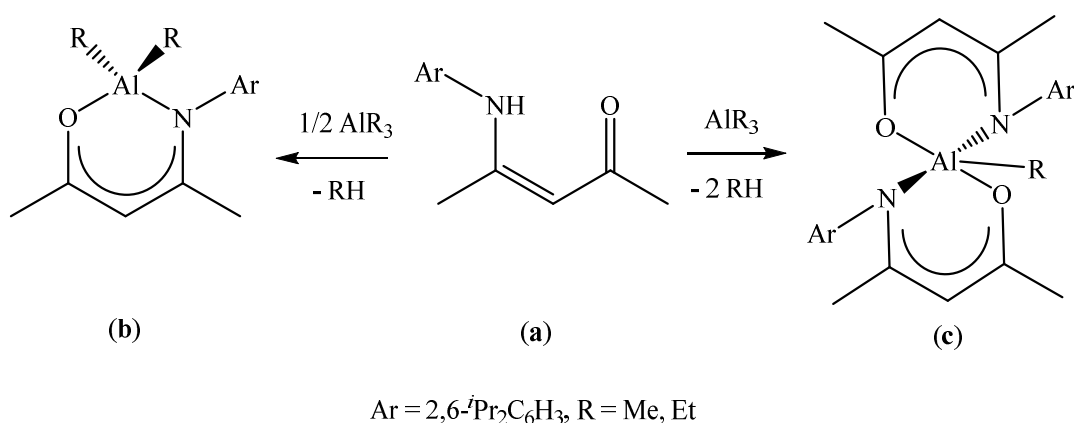


Scheme 5.4: Synthesis of strontium, cadmium and barium β -ketoiminate complexes.²³

5.1.2.3 Group 13 β -Ketoiminates

5.1.2.3.1 Aluminium β -Ketoiminate Complexes

Aluminium β -ketoiminate complexes shown in Scheme 5.5 have been synthesised for their potential application for ring opening polymerisation.²⁴ The β -ketoimine ligand (**a**) was reacted with trialkylaluminium in a 1:1 ratio to form the four coordinate complexes $[\text{AlR}_2(\text{OCMeCHCMeNAr})]$.

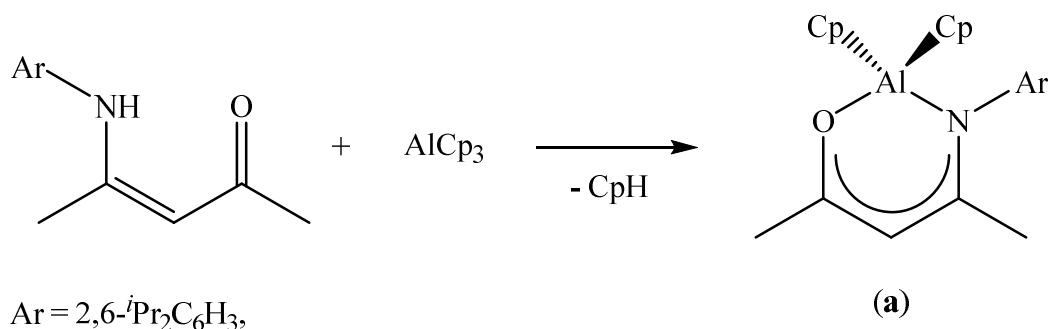


Scheme 5.5: Synthesis of aluminium β -ketoiminate complexes.²⁴

The Al centre was in a tetrahedral coordination, bonding through both the N and O of the β -ketoiminate ligand and two R groups. When a ratio of 2:1 β -ketoimine ligand to

trialkylaluminium was used, the bis(ketoiminate) complexes of the type $[\text{AlR}(\text{OCMeCHCMeNAr})_2]$, (**c**) were synthesised. The Al is now five coordinate and in a trigonal bipyramidal coordination in which the O atoms are in the axial positions. For structures of this type, only by refluxing for 3 days were reasonable yields obtained. When the lithiated ketoiminate ligand was reacted with AlCl_3 , the analogous complexes of (**b**) and (**c**) were synthesised, where $\text{R} = \text{Cl}$.

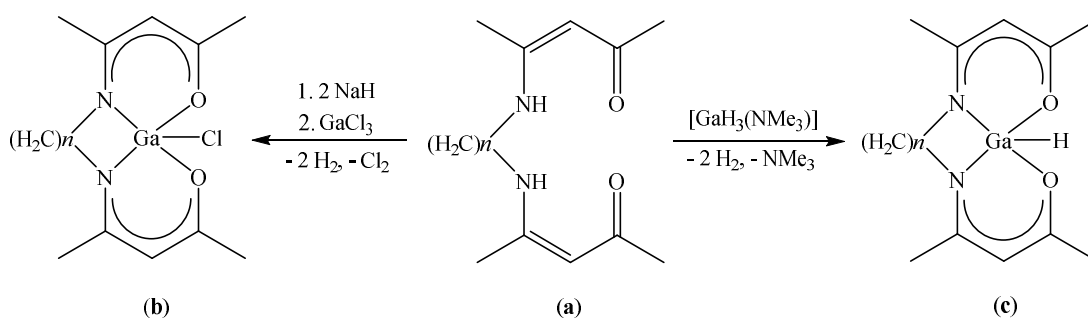
In similar work, Madura *et al.*²⁵ reacted the β -ketoiminate ligand with AlCp_3 which, after stirring for 1 day resulted in the synthesis of (**a**), as shown in Scheme 5.6. As with Figure 5.5 (**b**), the product is monomeric with aluminium in a distorted tetrahedral geometry with the chelate ring forming an envelope conformation with the Al above the plane of the C, N and O ring member atoms.



Scheme 5.6: Synthesis of aluminium β -ketoiminate complex.²⁵

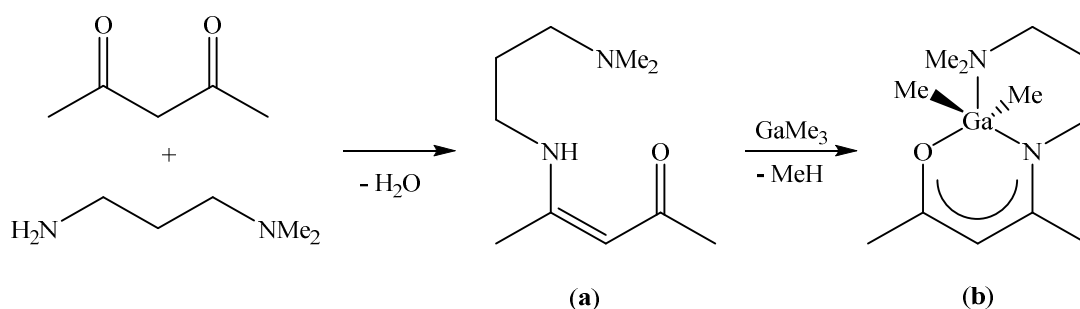
5.1.2.3.2 β -Ketoiminate Stabilised Gallium Complexes

Marchand *et al.*⁵ have demonstrated the use of bis(β -ketoimine) ligands of the type (**a**) in Scheme 5.7 in the synthesis of β -ketoiminate stabilised gallium chlorides and hydrides. For the synthesis of β -ketoiminate stabilised gallium chlorides, the first stage is the deprotonation of the β -ketoimine ligand using NaH , forming the disodium salt of the ligand. This is followed by a salt metathesis reaction with GaCl_3 to form complexes of structure (**b**) in Scheme 5.7. The β -ketoiminate stabilised gallium hydrides were synthesised by the reaction of the β -ketoimine ligand with the ethereal solution of $[\text{GaH}_3(\text{NMe}_3)]$ yielding the gallium hydride derivative, as shown in Figure 5.7 (**c**).



Scheme 5.7: Synthesis of gallium β -ketoiminate complexes, where $n = 2$ or 3.⁵

Pugh *et al.*²⁶ also synthesised a β -ketoimine ligand with the additional functionalisation of a Lewis base, as shown in Scheme 5.8 (a). After a 16 hour reflux at 150 °C, reaction of this β -ketoimine ligand and trimethylgallium resulted in the heteroleptic donor-functionalised β -ketoiminate gallium complex (b) as a gelatinous brown oil.



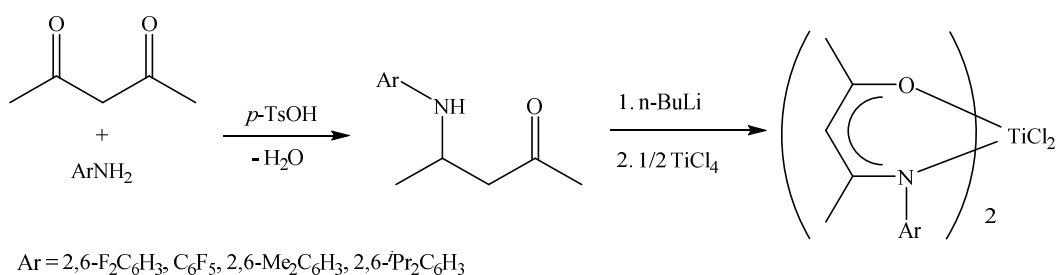
Scheme 5.8: Synthesis of gallium β -ketoiminate complexes.²⁶

The β -ketoiminates of type (c) in Scheme 5.7 and type (b) in Scheme 5.8 have also been successfully employed as AACVD precursors towards gallium oxide (Ga₂O₃) thin films.^{26,5} Transition metal β -ketoiminate complexes have also been synthesised, most notably those with group 4 metals and zinc.

5.1.2.4 Transition Metal β -Ketoiminate Complexes

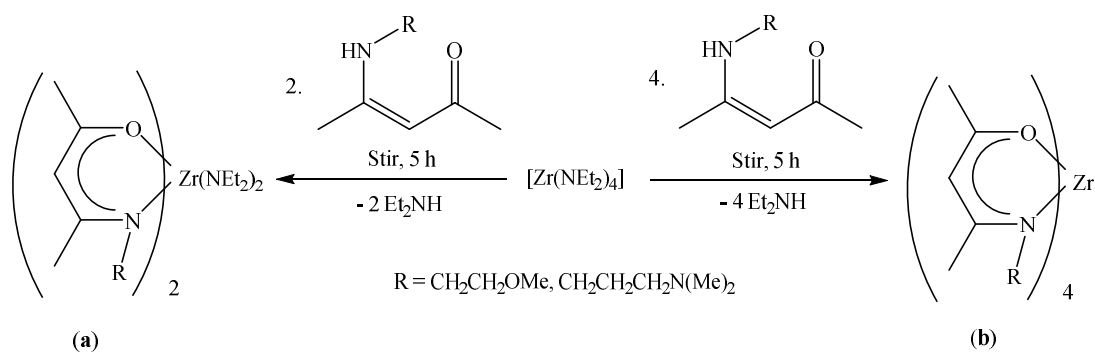
5.1.2.4.1 Group 4 Transition Metal β -Ketoiminate Complexes

Titanium β -ketoiminate complexes are generally synthesised for catalytic activities,²⁷ such as those synthesised by Xie *et al.*²⁸ shown in Scheme 5.9. The heteroleptic complexes were formed in the reaction between TiCl_4 and two equivalence of the lithium salt of the corresponding β -ketoimine ligand. The complexes form with a distorted octahedral structure where five isomeric structures are possible. Results show that these complexes are good catalysts for olefin polymerisation and the different substituents on the imino group give rise to different catalytic performances.



Scheme 5.9: Synthesis of titanium β -ketoiminate complexes.²⁸

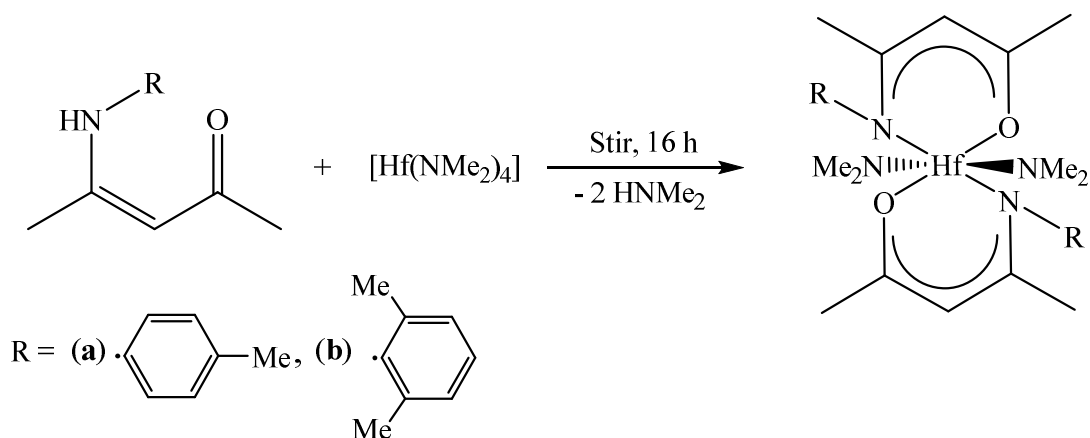
Other group 4 β -ketoiminate complexes have been synthesised for their potential use as precursors towards TiO_2 ,^{29,30} ZrO_2 ,⁴ and HfO_2 ,³¹ thin films, mainly *via* one of the CVD routes discussed in Section 1.4.3. For example, Banerjee *et al.*⁴ synthesised zirconium β -ketoiminates, as shown in Scheme 5.10.



Scheme 5.10: Synthesis of zirconium β -ketoiminate complexes.⁴

Heteroleptic amido- β -ketoiminato complexes (**a**) with a distorted octahedral geometry were formed when two equivalence of the β -ketoimine ligand was added to $[\text{Zr}(\text{NEt}_2)_4]$. These complexes were successfully used in the solution processing of ZrO_2 thin films. When four equivalence of the β -ketoimine ligand was added the homoleptic eight coordinate β -ketoiminato complexes (**b**) were observed to form, which were found to be more thermally stable than those of type (**a**).

Synthesis of the hafnium heteroleptic complexes shown in Scheme 5.11 resulted from the addition of the tetrakis(dimethylamido)hafnium to the corresponding β -ketoimine ligand at -78°C in toluene followed by a 16 hour stir at room temperature.



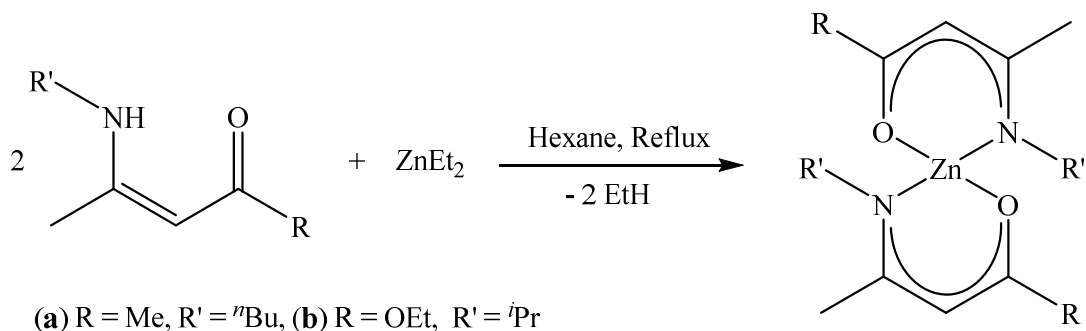
Scheme 5.11: Synthesis of hafnium β -ketoiminates for potential CVD application.³¹

Two methylamido groups remain attached at the Hf centre with two β -ketoimine ligands bonding through both O and N forming distorted octahedral complexes. Through TGA studies, the temperature of significant mass loss was found to vary by 80°C , being 120°C for (**a**) and 200°C for (**b**).

β -Ketoiminate complexes have also been synthesised for a number of other transition metal complexes including iron,⁹ titanium,³⁰ palladium³² and copper,³³ not only for catalysis but also for CVD purposes.^{34,35,36} Despite the studies above, and given the prominent nature of ZnO , there have been relatively few investigations into zinc β -ketoiminate complexes.³⁷

5.1.2.4.2 Zinc β -Ketoiminate/Iminoesterate Complexes

Matthews *et al.*³⁸ began investigating these complexes for use as AP-MOCVD precursors with the synthesis of the zinc β -ketoiminate and zinc β -iminoesterate in Scheme 5.12.



Scheme 5.12: Synthesis of a novel zinc β -ketoiminate and β -iminoesterate complex.³⁸

The synthesis of (a) and (b) in Scheme 5.12 in a yield of 71% and 61% respectively was achieved by reflux condensation for 30 minutes. The complexes have a tetrahedral Zn centre with the two ligands bonding to the Zn through both the N and O groups. Matthews *et al.* suggest that the ethoxy moiety in (b) increases electron density in the formed rings, meaning the lengths of the Zn-O and Zn-N bonds are similar. This is not the case with (a) in which the Zn-N bond is a weaker dative bond. Both complexes were found to be air stable, sublime in a single step and have low melting points, with the start of vaporisation being 150 °C for (a) and 250 °C for (b). The two complexes were successfully used as single-source AP-MOCVD precursors with the deposition of ZnO thin films without an additional oxygen source. The film from (a) had a carbon content of 26.2 at.% compared to 8.7 at.% for the film from (b), which was attributed to the ethoxy O in the β -iminoesterate acting as an additional oxygen source.

Further investigation has been carried out into both β -ketoiminate and β -iminoesterate complexes. Holmes *et al.*³⁹ deposited ZnO thin films onto silicon substrates from zinc β -ketoiminate complexes with the *n*-propyl and isopropyl moiety shown in Figure 5.5. These complexes were synthesised by addition of the corresponding ligand to ZnEt₂ at 273 K and stirring for 1 hour before being isolated in yields of 80% for (a) and 87% for (b).

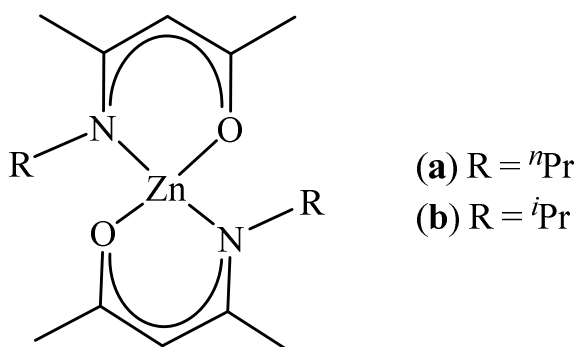
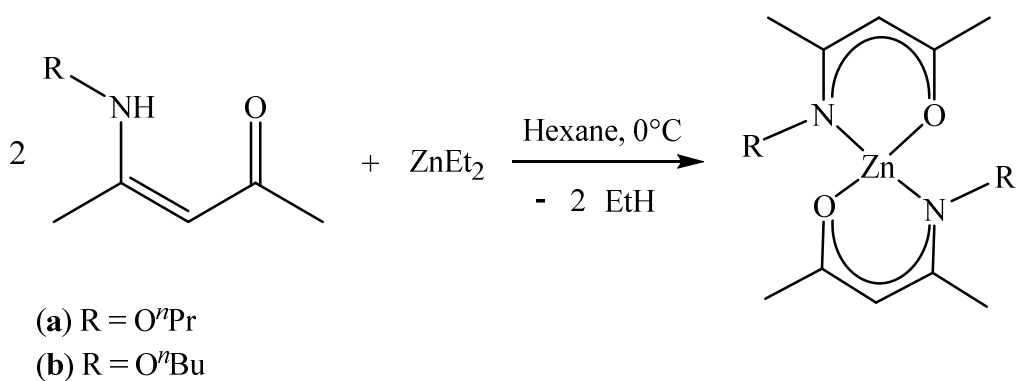


Figure 5.5: Zinc β -ketoiminate precursors used for the MOCVD of ZnO thin films.³⁹

However, they reported high carbon contamination on the surface of the ZnO thin films, ranging between 24% and 80% with higher values observed when the substrate temperature was $> 450\text{ }^{\circ}\text{C}$. Upon sputtering, carbon content was found to be approximately 10% and upon annealing, carbon contamination was reduced and the films were semiconducting. Complex (b) in Scheme 5.13 was also synthesised using zinc triflate as the starting material but the yield was much lower at 33%.⁹

Bekermann *et al.*⁶ synthesised similar zinc β -ketoiminate MOCVD precursors which contained additional O atoms as part of the imino moiety as shown in Scheme 5.13. Compounds (a) and (b) were synthesised in yields of 80% and 67% respectively.

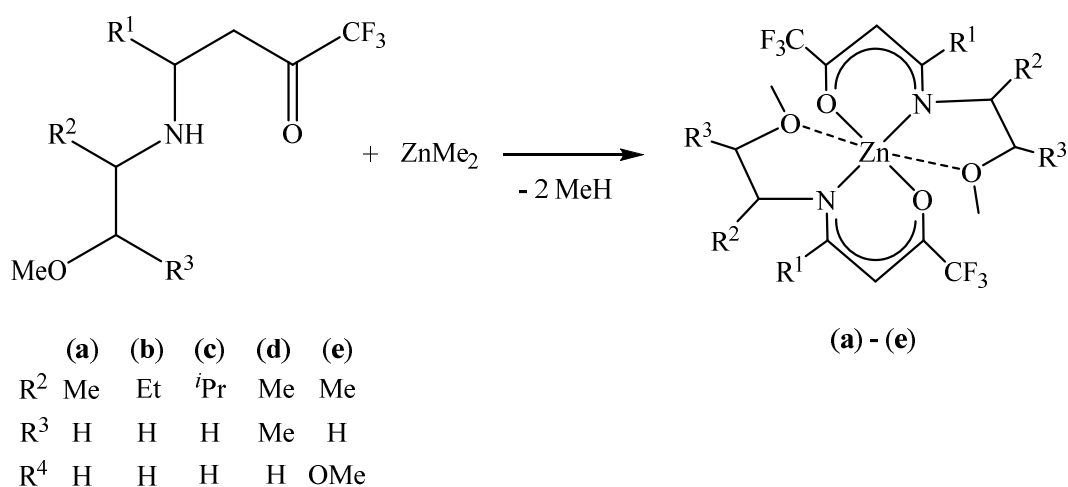


Scheme 5.13: Synthesis of zinc β -ketoiminates with additional O atoms.⁶

Positive thermal properties of the precursors were reported including ‘nearly’ one-step decomposition, low melting points and good volatility with significant mass loss starting at 130°C for (a) and at 150°C for (b). However, these complexes were not

used as single-source precursors as O_2 was used as a reactive gas. Further MOCVD studies⁴⁰ using the complexes synthesised in Scheme 5.13 describe the onset temperature of crystallisation of the ZnO hexagonal wurtzite phase being 500 °C with a single reflection observed for the (002) ZnO plane. This is indicative of (001) preferred orientation, normal to the substrate surface.

Cosham *et al.*⁴¹ have also synthesised a novel family of zinc β -ketoimine complexes in which the functionalised pendant arms allows for the two β -ketoimine ligands to bond in a tridentate chelating mode in *mer* arrangement, according to Scheme 5.14.



Scheme 5.14: Synthesis of zinc β -ketoiminates with functionalised pendant arms.⁴¹

The central Zn atom is in a six coordinate *pseudo* octahedral coordination, bonding through four O and two N atoms. The additional dative bonding to the O on the pendant arms is believed to result from the presence of the CF_3 groups on the β -ketoimine ligand. These complexes were found to exhibit clean decomposition, good volatility and low melting points and were successfully used in the AP-MOCVD of ZnO:F with 1.2% fluorine found within the deposited film.

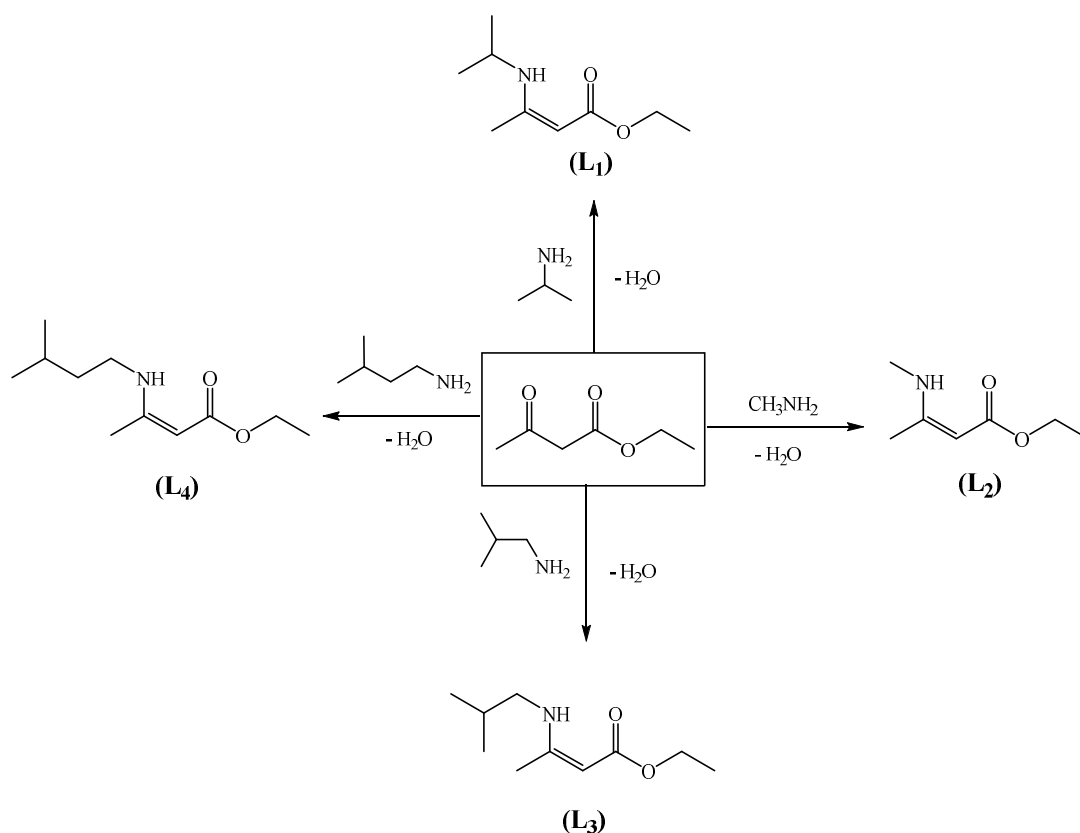
The literature reveals the wide use of the β -ketoiminate system across the periodic table and the promising use of such complexes as single-source precursors towards thin film depositions.

5.2 Results and Discussion

The results presented here describe further research into the synthesis of zinc complexes of this type and their precursor applications, which has been relatively under investigated given the potential of ZnO based thin films.³⁷ The synthesis of four β -iminoester ligands (**L**₁) – (**L**₄) is presented and their subsequent use in the synthesis of both homoleptic [Zn(L_X)₂] (**9**) – (**12**) and heteroleptic [(Zn(L_X)Et)₂] (**13**) and (**14**) zinc β -iminoesterates complexes. For the first time, results presented here also describe the use of [Zn(L_X)₂] complexes (**9**) and (**10**) as single-source precursors in the AACVD of ZnO thin films.

5.2.1 Synthesis of β -Iminoester Ligands

β -iminoester ligands (**L**₁) – (**L**₄) were successfully synthesised from the reaction between the dicarbonyl compound (ethyl acetoacetate) and the corresponding primary amine, as shown in Scheme 5.15.



Scheme 5.15: Synthesis of β -iminoester ligands (L**₁) – (**L**₄).**

The reaction is a 1:1 condensation reaction which results in the desired ligand and the elimination of a water molecule. As detailed in Section 5.1.1, there are a number of methods available for the synthesis of β -iminoester ligands. Initial investigations for the formation of the β -iminoester ligands were carried out using the more conventional method of reflux condensation. However, it was found that the reactions utilising K-10 montmorillonite as a catalyst offered a number of advantages including a higher yield, ease of set-up and the advantages associated with ambient temperature reactions. The ethyl acetoacetate was dispersed on the clay and the amine added dropwise as significant amounts of heat were given off upon addition. Once allowed to stir for the given time, as shown in Table 5.1, the product was extracted using DCM and filtered. The ligand was then isolated by the removal of DCM and water side product *in vacuo*.

Table 5.1: Stirring time and yield of synthesised β -iminoester ligands.

Ligand	Stirring Time (h)	Yield (%)
L₁	6	87
L₂	6	80
L₃	15	88
L₄	15	90

The original procedure set out by Braibante *et al.*¹⁶ was adapted significantly in this work. The yield of the ligand product on this scale was observed to increase when the primary amine was used in a 2:1 molar ratio as opposed to a 1:1.2 ratio. Using excess amine acts to ensure complete reaction of the ethyl acetoacetate, which has a high boiling point (181 °C), whilst also driving the reaction forward according to Le Chatelier's principle. The excess amine is then easily removed *in vacuo* as a result of their low to middling boiling points (< 71 °C). The stirring times for the reactions were also adapted with yields observed to decrease under shorter stirring times for (**L₃**) and (**L₄**) but not for (**L₁**) and (**L₂**). The synthesis of (**L₃**) and (**L₄**) appears to be novel, with

no indication of the synthesis of these ligands according to Reaxys (Elsevier). The ligands were isolated in high yields (80 – 90%) as shown in Table 5.1.

Characterisation and complete reaction to the β -iminoester ligand was confirmed by ^1H and ^{13}C NMR spectroscopy. All resonances in the spectra were assigned to proton and carbon peaks in the respective ligand and all peaks in the ^1H NMR have the expected integration ratio and splitting patterns. The characteristic peak for the NH proton environment is present at 8.47, 8.44, 8.65 and 8.50 ppm in the ^1H NMR for (**L1**), (**L2**), (**L3**) and (**L4**) respectively. The proton is significantly deshielded as a result of the hydrogen bonding in this environment to the highly electronegative N atom. This peak also appears broad as a result of the interconversion of the tautomeric forms of the ligand in which the proton is bonded to either the N or O atom, as shown in Figure 5.6.

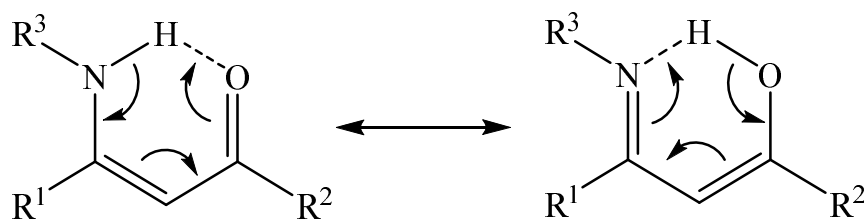


Figure 5.6: Tautomer forms of the β -iminoester ligand.

Mass spectroscopy also confirmed the successful synthesis of the β -iminoester ligands with the expected gas phase $[\text{M} + \text{H}]^+$ ions recorded at m/z values of 172.16, 144.10, 186.10 and 200.11 for (**L1**), (**L2**), (**L3**) and (**L4**) respectively. Once completely dry, as shown by the absence of a H_2O peak at 1.56 ppm in the ^1H spectrum, the ligands were used in reactions to afford zinc β -iminoesterate complexes.

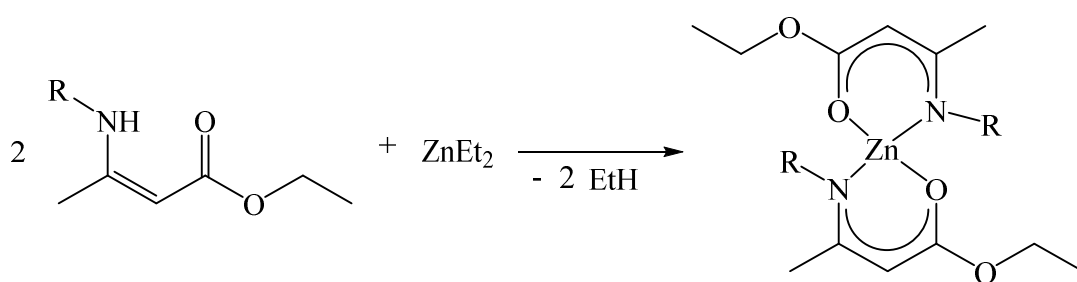
5.2.2 Synthesis of Zinc β -Iminoesterate Complexes

The reaction between ZnEt_2 and the synthesised β -iminoester ligands yielded zinc β -iminoesterates of two structural types. Homoleptic $[\text{Zn}(\text{L}_\text{X})_2]$ monomeric complexes (**9**) – (**12**) were synthesised when the ratio of β -iminoester to ZnEt_2 was 2:1. However, heteroleptic $[(\text{Zn}(\text{L}_\text{X})\text{Et})]$ dimeric complexes (**13**) and (**14**) were observed to form when

the ratio of β -iminoester to ZnEt_2 was 1:1. Complexes (**9**) – (**14**) were successfully isolated and characterised including the determination of four crystal structures.

5.2.2.1 Homoleptic Zinc β -Iminoesterate Complexes Synthesis

Zinc β -iminoesterate complexes of the type $[\text{Zn}(\text{L}_x)_2]$ (**9**) – (**12**) were synthesised *via* the ethane elimination reaction between ZnEt_2 and two equivalents of the corresponding β -iminoester ligand according to Scheme 5.16.



R = (**L**₁), (**9**) ⁱPr: (**L**₂), (**10**) Me: (**L**₃), (**11**) ⁱBu: (**L**₄), (**12**) $(\text{CH}_2)_2$ ⁱPr.

Scheme 5.16: Synthesis of zinc β -iminoesterate complexes $[\text{Zn}(\text{L}_{1-4})_2]$ (**9**) – (**12**).

The zinc complexes $[\text{Zn}(\text{L}_1)_2]$ (**9**) and $[\text{Zn}(\text{L}_2)_2]$ (**10**) crystallised out of concentrated toluene solutions held at -18 °C as yellow tinted crystals in good yields of 85% and 72% respectively. $[\text{Zn}(\text{L}_3)_2]$ (**11**) and $[\text{Zn}(\text{L}_4)_2]$ (**12**) did not crystallise out but were both isolated as orange coloured oils in yields of 67% and 69% respectively. The synthesis of (**9**) - (**12**) was confirmed *via* ¹H and ¹³C NMR and mass spectroscopy and the crystal structures of (**9**) and (**10**) were also determined *via* single crystal X-ray diffraction. Complex (**9**) has previously been synthesised by Matthews *et al.*³⁸ and as such is labelled and discussed first.

5.2.2.1.1 Synthesis of $[\text{Zn}(\text{OC}(\text{OEt})\text{CHC}(\text{Me})\text{N}^i\text{Pr})_2]$ $[\text{Zn}(\text{L}_1)_2]$ (**9**)

The addition of ligand (**L**₁) to a solution of ZnEt_2 in toluene was carried out at -78 °C given the pyrophoric nature of ZnEt_2 . The solution was stirred and allowed to warm to room temperature, during which time the evolution of a gas was observed. This evolution was attributed to the formation of ethane, the by-product of the reaction and

is one of the factors driving the reaction. After stirring at room temperature for 24 hours, the solution was concentrated *via* the removal of toluene *in vacuo*. The solution was held at $-18\text{ }^{\circ}\text{C}$ for 48 hours over which time the product had crystallised out as yellow tinted crystals.

The synthesis of (**9**) was confirmed *via* ^1H and ^{13}C NMR spectroscopy. Each resonance in the obtained ^1H spectrum was assigned to an expected proton environment, as shown in Figure 5.7, with the correct splitting and integration ratio. The protons of the isopropyl group were attributed to the doublets at 1.09 and 1.10 ppm, for the CH_3 groups protons and the multiplet at 3.85 ppm for the CH proton. The CH_3 and CH_2 protons of the ethoxide group were attributed to the triplet at 1.23 ppm and the quartet at 4.08 ppm respectively. At 1.98 ppm is the singlet for the protons of the CH_3 methyl group attached to the chelating ring, with the singlet peak at 4.30 ppm corresponding to the CH proton attached directly to the chelating ring.

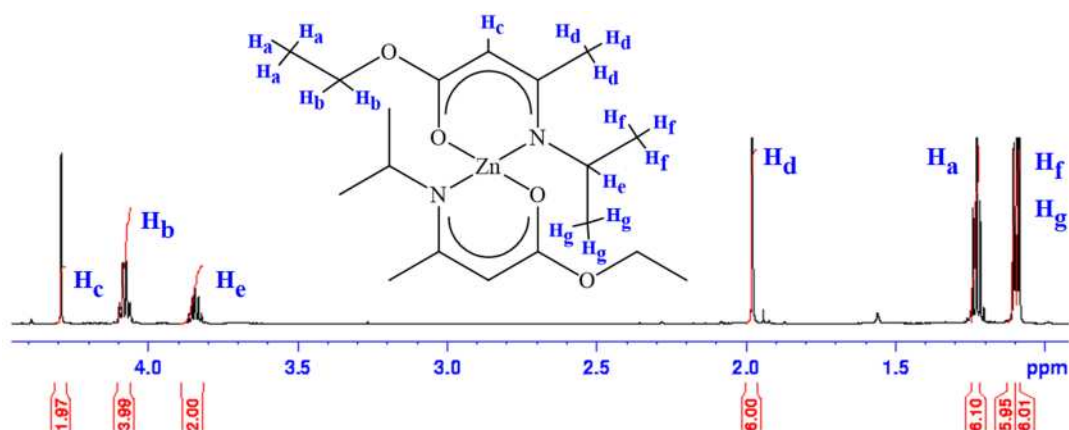


Figure 5.7: ^1H NMR spectrum of zinc β -iminoesterate complex $[\text{Zn}(\text{L}_1)_2]$ (**9**).

Peak shifting was also observed, representative of a change in chemical environment from the free ligand. The quartet associated with the CH_3CH_2 proton environment appears at 4.05 ppm for ligand (**L**₁) and shifts downfield to 4.08 ppm for (**9**). Upfield shifting was also observed, for example, the singlet associated with the CHCO proton environment appears at 4.36 ppm for ligand (**L**₁) but shifts upfield to 4.30 ppm when the six membered ZnOC_3N ring structure forms in (**9**). These shifting effects result from the bonding and closeness of each group to the Zn centre compared to their chemical environment in the free ligand. The ^1H spectrum obtained for (**9**) is also free

from the characteristic peak for the NH proton environment, which appears in the 1H spectrum of (**L**₁) as a broad singlet at 8.47 ppm. This is as expected and confirms that the reaction had gone to completion with no unreacted ligand present. There are also no peaks associated any unreacted $ZnEt_2$. The ^{13}C NMR spectrum was fully assigned with all resonance peaks assigned to carbon environments in (**9**). Both the 1H and ^{13}C NMR spectra also illustrate the high purity of the crude product, negating the need for recrystallisation. This is a significant commercial advantage in that by removing a step in the process likely allows for a greater yield of (**9**).

Successful synthesis of $[Zn(L_1)_2]$ (**9**) was also confirmed by mass spectroscopy with the spectrum obtained shown in Figure 5.8. The spectrum shows the peak corresponding to the $[M]^{++}$ gas phase ion at m/z 405.52 and one for the $[M - C_9H_{16}NO_2]^{++}$ gas phase ion at m/z 235.85. One notable feature present in the mass spectrum is that the peaks do not appear as single isolated peaks but rather as a series of peaks with varying intensities. This is illustrated in greater detail for the molecular ion in Figure 5.9 and results from the isotopic nature of Zn and C.

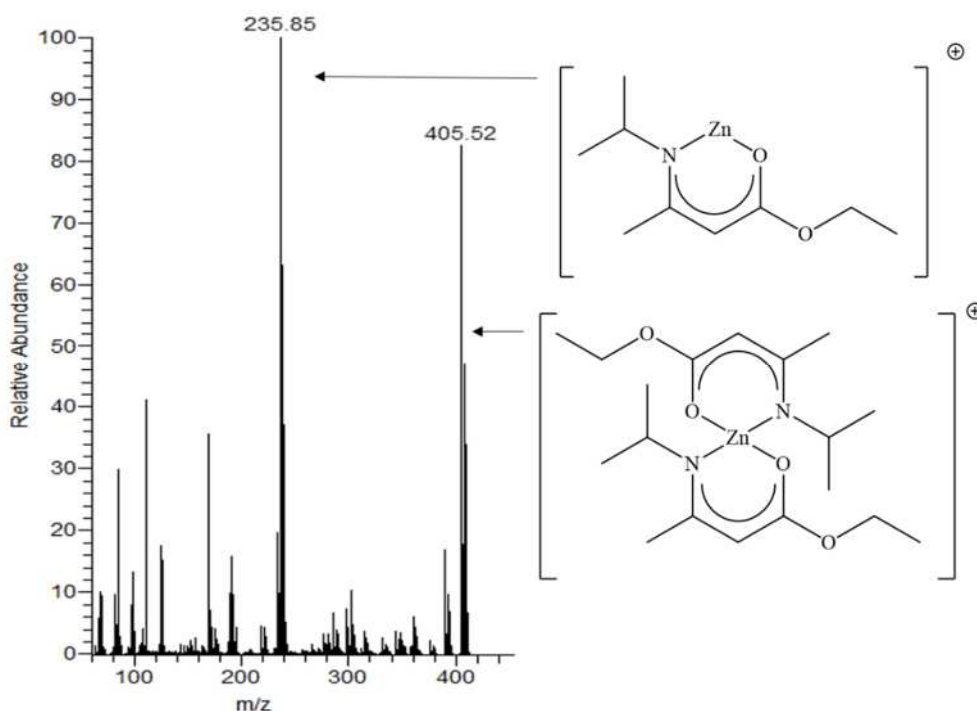


Figure 5.8: Mass spectroscopy analysis for zinc β -iminoesterate complex $[Zn(L_1)_2]$ (**9**).

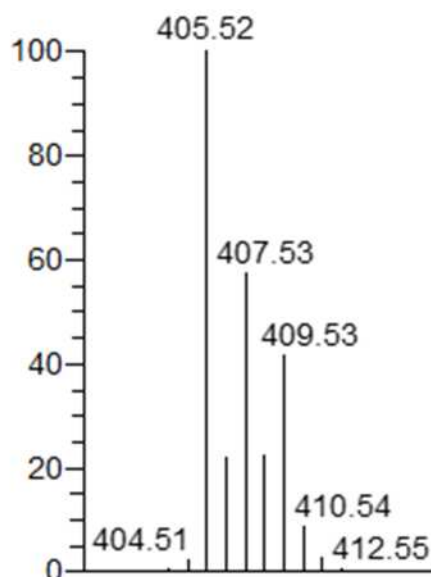


Figure 5.9: Molecular ion peak observed in the mass spectrum for $[\text{Zn}(\text{L}_1)_2]$ (**9**).

The crystal structure of complex (**9**) was determined *via* single crystal X-ray diffraction and is shown in Figure 5.10. Table 5.2 details the determined crystallographic data with selected bond lengths and angles given in Table 5.3. The crystal structure of (**9**) has been previously reported by Matthews *et al.*³⁸ and is in good agreement with the data collected. (**9**) crystallised in the monoclinic $P2_1/n$ space group with a monomeric solid state structure. Two orthogonal chelate β -iminoester ligands bond through both the N and O atoms, creating two six membered ZnOC_3N rings which are puckered in nature. The Zn atom is common to both rings and as a four coordinate centre, adopts a distorted tetrahedral geometry.

The distorted nature of the tetrahedral coordination around Zn(1) is illustrated by the variation from the 109.5° expected for bond angles in a perfect tetrahedral coordination. The bond angles about Zn(1) range from $96.63(4)$ and $97.80(4)^\circ$ for O(1)-Zn(1)-N(1) and O(2)-Zn(1)-N(2) respectively, to $129.46(5)^\circ$ as the bond angle for N(1)-Zn(1)-N(2). This is a difference of over 30° between the smallest and largest bond angles about Zn(1). The other bond angles about the centre have more middling values of $110.85(4)$, $110.24(4)$ and $111.80(4)^\circ$ for the O(1)-Zn(1)-O(2), O(1)-Zn(1)-N(2) and O(2)-Zn(1)-N(1) angles respectively. The coordination of the bound ligands impose significant restraints on the complex and the inflexibility of the ligands results

in the geometric distortion and the deviation in the bond angles observed. This range of bond angles are therefore expected for compounds of this type.

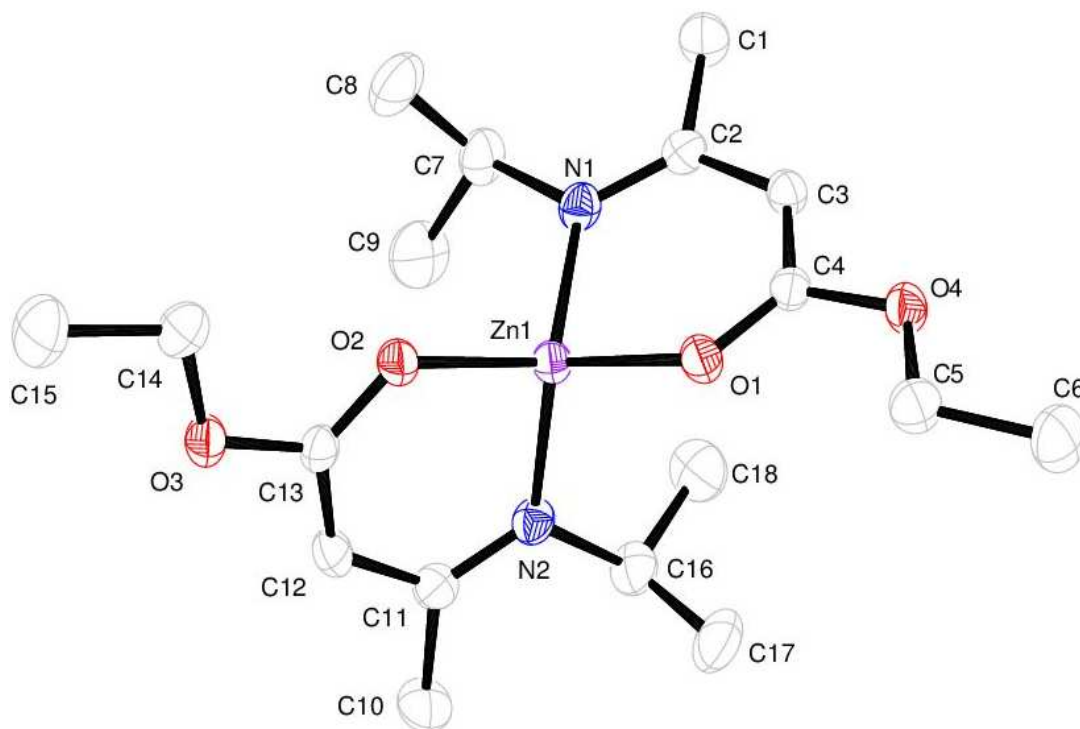


Figure 5.10: X-ray crystal structure of $[\text{Zn}(\text{OC}(\text{OEt})\text{CHC}(\text{Me})\text{N}^i\text{Pr})_2]$ (**9**).

The bond lengths surrounding the metal centre of Zn(1)-O(1), Zn(1)-O(2), Zn(1)-N(1) and Zn(1)-N(2) are 1.9766(9), 1.9645(9), 1.9692(11) and 1.9677(11) Å respectively. The bond lengths are relatively similar to those found in analogous zinc complexes of this type and are as expected for compounds of this type.^{6,38} The bond lengths in (**9**) also illustrate the delocalised nature of the two orthogonal puckered rings formed by the bonding of the β -iminoesterate ligands. Outside of the ring structures, the C-O, C-N and C-C bonds have distances typically expected for a single bond length, such as 1.4442(17), 1.4796(16) and 1.5822(2) Å for bonds O(4)-C(5), N(1)-C(7) and C(7)-C(8) respectively. However, within the ring structures they are much shorter, for example 1.2642(16), 1.3198(17) and 1.4179(17) Å for the O(1)-C(4), N(1)-C(2) and C(2)-C(3) bonds respectively. These distances are intermediate of distances typically expected for single and double C-O, C-N and C-C bonds respectively.

Table 5.2: Crystallographic data for [Zn(OC(OEt)CHC(Me)NⁱPr)₂] (9).

Crystal System	Monoclinic	
Space Group	$P2_1/n$	
Volume	2128.34(4)	
Unit Cell Dimensions	$a = 7.70990(7) \text{ \AA}$	$\alpha = 90^\circ$
	$b = 14.23748(16) \text{ \AA}$	$\beta = 91.6241(8)^\circ$
	$c = 19.39700(17) \text{ \AA}$	$\gamma = 90^\circ$

Table 5.3: Selected bond lengths (\AA) and angles ($^\circ$) for [Zn(OC(OEt)CHC(Me)NⁱPr)₂] (9).

Zn(1)-O(1)	1.9766(9)	O(4)-C(5)	1.4442(17)
Zn(1)-O(2)	1.9645(9)	N(1)-C(2)	1.3198(17)
Zn(1)-N(1)	1.9692(11)	N(1)-C(7)	1.4796(16)
Zn(1)-N(2)	1.9677(11)	C(2)-C(3)	1.4179(17)
O(1)-C(4)	1.2642(16)	C(7)-C(8)	1.5822(2)
O(1)-Zn(1)-O(2)	110.85(4)	O(2)-Zn(1)-N(1)	111.80(4)
O(1)-Zn(1)-N(1)	96.63(4)	O(2)-Zn(1)-N(2)	97.80(4)
O(1)-Zn(1)-N(2)	110.24(4)	N(1)-Zn(1)-N(2)	129.46(5)

There are a number of advantages that make this reaction potentially interesting commercially. The reaction does not require reflux conditions and even when the synthesis of (9) was investigated using reflux conditions it did not result in an

improved product yield. The synthesis under ambient conditions is beneficial since it reduces energy consumption and keeps the system relatively simple. The reaction also proceeds without an additional step to deprotonate the ligand *via* the synthesis of the ligand salt prior to reaction with ZnEt_2 , which can sometimes be the case with ligands of this type.^{26,28} These factors also hold true for the synthesis of zinc β -iminoesterate complexes (**10**) – (**14**). The purity of complex (**9**) without the need for recrystallisation also make it an interesting candidate as a potential precursor for CVD applications. This is particularly the case since (**9**) is also air stable since there are no ethyl groups attached to the zinc and the chelating ligands provide a full coordination around the metal centre.

5.2.2.1.2 Synthesis of $[\text{Zn}(\text{OC}(\text{OEt})\text{CHC}(\text{Me})\text{NMe})_2][\text{Zn}(\text{L}_2)_2]$ (**10**)

The synthesis of $[\text{Zn}(\text{L}_2)_2]$ (**10**) resulted from the reaction of ZnEt_2 and ligand (**L**₂) following the procedure employed for (**9**). The product was isolated as yellow tinted crystals and characterised using spectroscopic techniques.

^1H and ^{13}C NMR spectroscopy confirmed the synthesis of (**10**) with each proton and carbon in the complex assigned to resonances in the obtained spectra. In the ^1H NMR spectrum, the expected splitting, integration ratios and shifts from the free ligand were also observed. The CH_3 methyl group protons attached to the N were attributed to the singlet at 3.01 ppm. The CH_3 and CH_2 protons of the ethoxide group were attributed to the triplet at 1.25 ppm and the quartet at 4.09 ppm respectively. The singlet for the protons of the CH_3 methyl group attached to the chelating ring appears at 1.95 ppm whilst the singlet for the CH proton attached directly to the chelating ring appears at 4.36 ppm. As expected, the characteristic broad singlet for the NH proton environment in ligand (**L**₂) at 8.44 ppm is no longer present in the ^1H spectrum obtained for (**10**), nor are there any peaks associated unreacted ZnEt_2 . Mass spectroscopy also confirms the successfully synthesis of (**10**) with the peak corresponding to the $[\text{M}]^{++}$ gas phase molecular ion observed at m/z 349.09. This peak also has the isotopic pattern expected for this type of zinc compound.

The novel crystal structure of (**10**) was also determined using single crystal X-ray diffraction and is shown in Figure 5.11. The determined crystallographic data for (**10**) is given in Table 5.4 with selected bond lengths and angles given in Table 5.5.

$[\text{Zn}(\text{L}_2)_2]$ (**10**) is monomeric in the solid state and crystallises in the $P2_1/c$ space group. Two orthogonal bidentate β -iminoester ligands bond through both the N and O atoms to a central, four coordinate Zn atom, which, as in (**9**), adopts a distorted tetrahedral geometry.

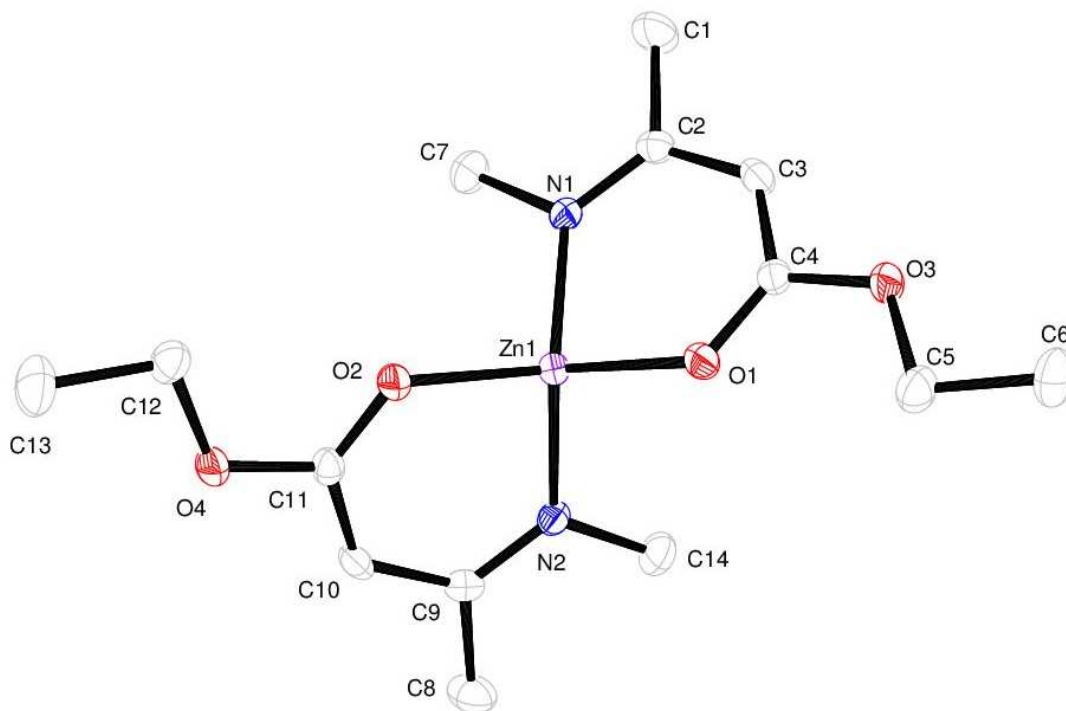


Figure 5.11: X-ray crystal structure of $[\text{Zn}(\text{OC}(\text{OEt})\text{CHC}(\text{Me})\text{NMe})_2]$ (**10**).

Table 5.4: Crystallographic data for $[\text{Zn}(\text{OC}(\text{OEt})\text{CHC}(\text{Me})\text{NMe})_2]$ (**10**).

Crystal System	Monoclinic	
Space Group	$P2_1/c$	
Volume	1680.46(16)	
Unit Cell Dimensions	$a = 6.8111(4) \text{ \AA}$	$\alpha = 90^\circ$
	$b = 20.8570(11) \text{ \AA}$	$\beta = 101.592(6)^\circ$
	$c = 12.0757(7) \text{ \AA}$	$\gamma = 90^\circ$

The bond angles about Zn(1) have a range of over 30°. The O(1)-Zn(1)-N(2) and O(2)-Zn(1)-N(1) bond angles have values of 106.58(7) and 106.60(7)° respectively, which are slightly smaller than the expected 109.5° angle for a perfect tetrahedral. However, the O(1)-Zn(1)-O(2) and N(1)-Zn(1)-N(2) angles of 122.56(6) and 131.35(7)° respectively are significant larger whilst the O(1)-Zn(1)-N(1) and O(2)-Zn(1)-N(1) angles are noticeably smaller at 96.18(7) and 96.49(6)° respectively. This range of values is expected and result from the constraints of the ring systems formed by ligands of this type.

Table 5.5: Selected bond lengths (Å) and bond angles (°) for [Zn(OC(OEt)CHC(Me)NMe)₂] (10).

Zn(1)-O(1)	1.9815(14)	O(3)-C(5)	1.443(3)
Zn(1)-O(2)	1.9726(13)	N(1)-C(2)	1.318(3)
Zn(1)-N(1)	1.9582(19)	N(1)-C(7)	1.470(3)
Zn(1)-N(2)	1.9551(18)	C(1)-C(2)	1.500(3)
O(1)-C(4)	1.266(2)	C(2)-C(3)	1.410(3)
O(1)-Zn(1)-O(2)	122.56(6)	O(2)-Zn(1)-N(1)	106.60(7)
O(1)-Zn(1)-N(1)	96.18(7)	O(2)-Zn(1)-N(2)	96.49(6)
O(1)-Zn(1)-N(2)	106.58(7)	N(1)-Zn(1)-N(2)	131.35(7)

The bond lengths surrounding the metal centre of Zn(1)-O(1), Zn(1)-O(2), Zn(1)-N(1) and Zn(1)-N(2) of 1.9815(14), 1.9726(13), 1.9582(19) and 1.9551(18) Å respectively are as expected for this type of compound and similar to those found in analogous zinc complexes.^{6,38} The delocalised nature of the two orthogonal puckered rings is also illustrated by the variation in bond lengths. Outside of the ring structures, the C-O, C-N and C-C bonds have distances typically expected for a single bond of each type, such as 1.443(3), 1.470(3) and 1.500(3) Å for bonds O(3)-C(5), N(1)-C(7) and C(1)-

C(2) respectively. However, within the ring structures they are much shorter, for example 1.266(2), 1.318(3) and 1.410(3) Å for the O(1)-C(4), N(1)-C(2) and C(2)-C(3) bonds respectively. These distances are intermediate between lengths typically expected for single and double C-O, C-N and C-C bonds respectively.

As with complex (9), the factors of purity, air stability and relative ease of synthesis also make complex (10) an interesting compound for potential use as a ZnO CVD precursor.

5.2.2.1.3 Crystal Structure Comparison of [Zn(L₁)₂] (9) and [Zn(L₂)₂] (10)

There is significant deviation from the expected bond angles for a tetrahedral centre of 109.5° in both (9) and (10). The Zn centre in (9) has bond angles from 96.63(4) to 129.46(5)°, similar to the 96.18(7) to 131.35(7)° observed in (10). These angles result from the inflexibility of the chelating ligand and the relatively small bite angle resulting from the (N(X)C(Me)CHC(OEt)O) chain where X is *i*-Pr in (9) and Me in (10). The bond angles around the central Zn atom deviate between complex (9) and (10), most notably, the O(1)-Zn(1)-O(2) bond angle in (9) measures 110.85(4)° compared to 122.56(6)° in (10). This variation results from the requirement to compensate for the reduced O(2)-Zn(1)-N(1) and O(1)-Zn(1)-N(2) bond angles in (10) of 106.60(7) and 106.58(7)° respectively, compared to the bond angles of 111.80(4) and 110.24(4)° respectively observed in (9). It is the reduced steric bulk of the methyl group on the N moiety in (10) compared to the isopropyl group on the N moiety in (9) that results in these differences.

The Zn-O and Zn-N bond lengths around Zn(1) are of similar values in both (9) and (10) and as discussed above, are as expected for this type of compound. Both compounds (9) and (10) form two orthogonal puckered rings around the Zn centre common to both rings. The length of the C-O, C-N and C-C bonds that form part of the rings are shorter than those outside, illustrating the delocalised nature of the rings in both complexes.

5.2.2.1.4 Synthesis of $[\text{Zn}(\text{OC}(\text{OEt})\text{CHC}(\text{Me})\text{N}^i\text{Bu})_2] [\text{Zn}(\text{L}_3)_2]$ (**11**)

The reaction of ZnEt_2 with ligand (**L**₃) following the procedure employed for (**9**), resulted in the synthesis of $[\text{Zn}(\text{L}_3)_2]$ (**11**). The product was isolated as an orange oil and characterised using spectroscopic techniques.

The synthesis of (**11**) was confirmed by ^1H and ^{13}C NMR spectroscopy with each proton and carbon environment in the compound assigned to peaks in the obtained spectra. The expected shifting from resonances in the free ligand was also observed, as was the predicted splitting patterns in the ^1H spectrum. The three resonances associated with the isobutyl group of the N moiety appear as the double doublet at 0.86 ppm, the multiplet at 1.66 ppm and the multiplet at 3.00 ppm and were attributed to the CH_3 , CH protons and CH_2 protons respectively. The CH_3 and CH_2 protons of the ethoxide group were attributed to the triplet at 1.22 ppm and the quartet at 4.06 ppm respectively. The singlet for the protons of the CH_3 methyl group attached to the chelating ring appears at 1.93 ppm and the singlet for the CH proton attached directly to the chelating ring appears at 4.28 ppm. The absence of the broad singlet observed at 8.65 ppm in the ^1H spectrum for the NH proton in ligand (**L**₃) also confirms the synthesis of (**11**) and absence of any remaining (**L**₃). Mass spectroscopy was also used to confirm the successful synthesis of (**11**). The expected peak for the $[\text{M}]^{++}$ gas phase molecular ion with the predicted isotopic pattern of peaks was observed at m/z 433.12. Complex (**11**) also exhibits the air stability and other properties described for complex (**9**) that make it a potentially interesting compound for potential use as a CVD precursor.

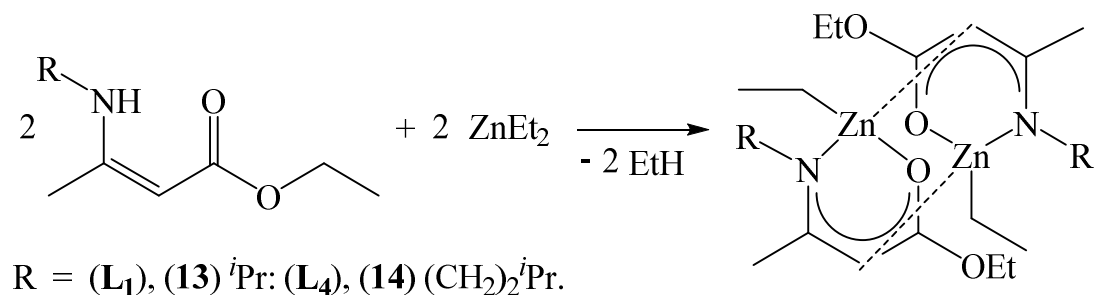
5.2.2.1.5 Synthesis of $[\text{Zn}(\text{OC}(\text{OEt})\text{CHC}(\text{Me})\text{N}(\text{CH}_2)_2^i\text{Pr})_2] [\text{Zn}(\text{L}_4)_2]$ (**12**)

$[\text{Zn}(\text{L}_4)_2]$ (**12**) was synthesised and isolated as an orange oil, following the reaction of ZnEt_2 and ligand (**L**₄) as per the procedure employed for (**9**). The product was characterised using spectroscopic techniques including ^1H and ^{13}C NMR spectroscopy, where all carbon and proton environments were assigned to predicted resonances obtained in the spectra.

The protons that form the isopentyl group of the N moiety appear across five resonance. Peaks for the \underline{CH}_3 and \underline{CH} protons appear as a double doublet and a multiplet at 0.86 and 1.55 ppm respectively. The protons of the \underline{CH}_2 group attached to the N appear at 1.35 ppm whereas the protons for the central \underline{CH}_2 group appear at two peaks, one at 3.19 and a second at 3.29 ppm, both as multiplets. The \underline{CH}_3 and \underline{CH}_2 protons of the ethoxide group were attributed to the triplet at 1.23 ppm and the quartet at 4.07 ppm respectively. The singlet for the protons of the \underline{CH}_3 methyl group attached to the chelating ring appears at 1.94 ppm whilst the singlet for the \underline{CH} proton attached directly to the chelating ring appears at 4.30 ppm. As expected, the characteristic broad singlet for the \underline{NH} proton environment in ligand (**L**₄) at 8.50 ppm is no longer present in the ¹H spectrum obtained for (**12**). Confirmation of the successful synthesis of (**12**) was also achieved using mass spectroscopy. The expected [M]⁺⁺ gas phase molecular ion was observed at *m/z* 461.15 with the predicted isotopic pattern expected for this zinc compound. Similar to (**9**), the properties of (**12**) and its synthesis make it suitable for further investigation as a potential CVD precursor towards ZnO.

5.2.2.2 Synthesis of Zinc β -Iminoesterate Dimer Complexes

Despite the synthesis of air stable, homoleptic zinc β -iminoesterate complexes as potentially suitable CVD precursors, further synthetic studies were performed. The zinc β -iminoesterate complexes of the type [(Zn(L_x)(Et))₂] (**13**) and (**14**) were synthesised *via* the ethane elimination reaction when a 1:1 ratio of ZnEt₂ and the corresponding β -iminoester ligand were reacted together, as shown in Scheme 5.17.



Scheme 5.17: Synthesis of zinc β -iminoesterates [(Zn(**L**₁)(Et))₂] (**13**) and [(Zn(**L**₄)(Et))₂] (**14**).

The aim was to establish what complexes might form upon reacting varying equivalence ratios of β -iminoester ligand with ZnEt_2 . The heteroleptic zinc complexes $[(\text{Zn}(\text{L}_1)(\text{Et}))_2]$ (**13**) and $[(\text{Zn}(\text{L}_4)(\text{Et}))_2]$ (**14**) formed as dimers in the solid state and crystallised out of concentrated toluene solutions held at -18°C as yellow tinted crystals in yields of 75% and 67% respectively. The synthesis of (**13**) and (**14**) was confirmed *via* ^1H and ^{13}C NMR spectroscopy and their crystal structures were determined *via* single crystal X-ray diffraction.

5.2.2.2.1 Synthesis of $[(\text{Zn}(\text{OC}(\text{OEt})\text{CHC}(\text{Me})\text{N}^i\text{Pr})(\text{Et}))_2]$

$[(\text{Zn}(\text{L}_1)(\text{Et}))_2]$ (**13**)

Ligand (**L1**) was added to a solution of ZnEt_2 in toluene in a 1:1 ratio at -78°C , to allow for its pyrophoric nature. Upon stirring, the solution warmed to room temperature and the evolution of a gas was observed. This gas was attributed to the formation of ethane, the by-product of the successful formation of (**13**). The solution was stirred for 24 hours, concentrated *via* the removal of toluene *in vacuo* and held at -18°C for 48 hours. During this time, $[(\text{Zn}(\text{L}_1)(\text{Et}))_2]$ (**13**) had crystallised out as yellow tinted crystals.

The synthesis of (**13**) was confirmed *via* ^1H and ^{13}C NMR spectroscopy. In the ^{13}C spectrum, a peak at an expected chemical shift was observed for each carbon environment in (**13**). This was also the case for the expected proton environments in the ^1H NMR spectrum where the resonances also had the correct splitting patterns. The protons of the ethyl group bonded to the central Zn atom appear as broader peaks at 0.32 and 1.28 ppm for the CH_2 and CH_3 protons respectively. The protons of the isopropyl group on the N atom were attributed to the doublet at 0.93 ppm for the methyl CH_3 group protons and the multiplet at 3.44 ppm to the CH proton. The CH_3 and CH_2 protons of the ethoxide group were attributed to the triplet at 1.09 ppm and the quartet at 4.03 ppm respectively. The singlet for the protons of the CH_3 methyl group attached to the chelating ring was present at 1.61 ppm and the singlet peak corresponding to the CH proton attached directly to the chelating ring appears at 4.57 ppm. The characteristic peak for the NH proton in (**L1**) was no longer present, which confirms the reaction had gone to completion and no unreacted ligand remained.

The crystal structure of (**13**) was determined using single crystal X-ray diffraction and is shown in Figure 5.12. The determined crystallographic data is given in Table 5.6 with selected bond lengths and angles shown in Table 5.7. Zinc complexes with this heteroleptic β -iminoesterate structure have not been reported before in the literature. $[(\text{Zn}(\text{L}_1)(\text{Et}))_2]$ (**13**) is centrosymmetric and crystallises in the triclinic $P\bar{1}$ space group as a dimer. The complex has two Zn atoms, one of which has been symmetrically generated. Zn(1) retains one bond to a terminal ethyl group which remains from the original ZnEt_2 compound. Two coordination sites around Zn(1) are occupied by the coordination of the bidentate ligand (L_1) which bonds through the O(1ⁱ) and N(1ⁱ) atoms. The bonding of (L_1) forms a puckered six membered ZnOC_3N ring. Zn(1) also forms a dative interaction to C(3) on the symmetry equivalent monomer unit. As such, (**13**) exists as a dimer with two dative interactions between two monomer units, in which Zn(1) adopts a highly distorted tetrahedral geometry.

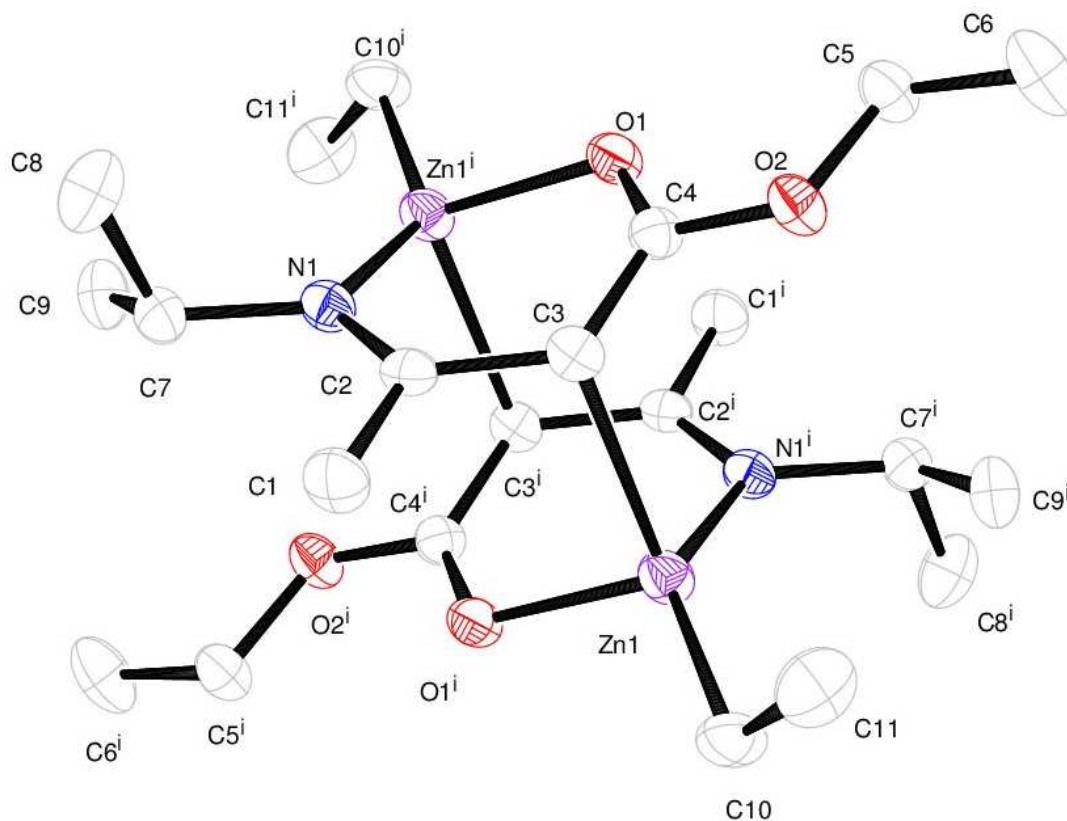


Figure 5.12: X-ray crystal structure of $[(\text{Zn}(\text{OC}(\text{OEt})\text{CHC}(\text{Me})\text{N}^i\text{Pr})(\text{Et}))_2]$ $[(\text{Zn}(\text{L}_1)(\text{Et}))_2]$ (**13**). (Symmetry operator: $i = -X, -Y, -Z$.)

The longest bond made by Zn(1) is the Zn(1)-C(3) bond between Zn(1) on one monomer to C(3) on the other, which measures 2.408(3) Å. This compares to a more typical Zn-C bond length of 1.980(3) Å for the Zn(1)-C(10) bond. The increased length of the Zn(1)-C(3) bond is highly indicative of a dative interaction between Zn(1) and C(3). Zn(1) also makes bonds to O(1ⁱ) and N(1ⁱ) of the bidentate ligand (**L**₁) which measure 2.046(2) and 2.013(2) Å respectively. These bonds are slightly longer than the analogous bonds in (**9**) and (**10**). For example the Zn(1)-O(1) and Zn(1)-N(1) bonds in (**9**) measure 1.9766(9) and 1.9692(11) Å respectively. This is likely the result of the formation of a dimer in (**13**).

**Table 5.6: Crystallographic data for [(Zn(OC(OEt)CHC(Me)NⁱPr)(Et))₂]
[(Zn(**L**₁)(Et))₂] (**13**).**

Crystal System	Triclinic	
Space Group	$P\bar{1}$	
Volume	648.68(12) Å ³	
Unit Cell Dimensions	$a = 7.9052(6)$ Å	$\alpha = 88.294(9)^\circ$
	$b = 8.2403(10)$ Å	$\beta = 75.054(7)^\circ$
	$c = 11.1073(11)$ Å	$\gamma = 68.489(9)^\circ$

The delocalised nature of the puckered ring formed by the bonding of the β -iminoesterate ligand is also illustrated by the bond lengths in (**13**). The C-O, C-N and C-C bonds within the ZnOC₃N bonded ring structure are much shorter than those bonds outside of it. The C-O, C-N and C-C bonds outside the bonded ligand ring system in complex (**13**) have distances typically expected for a single bond length, such as 1.449(3), 1.484(3) and 1.509(5) Å for the bonds of O(2)-C(5), N(1)-C(7) and C(5)-C(6) respectively. However, the C-O, C-N and C-C bonds that form part of the ring structure are much shorter due to the delocalised nature, with the O(1)-C(4), N(1)-C(2) and C(2)-C(3) bonds measuring 1.252(4), 1.315(4) and 1.443(4) Å respectively.

**Table 5.7: Selected bond lengths (Å) and angles (°) for
[(Zn(OC(OEt)CHC(Me)N^{*i*}Pr)(Et))₂] [(Zn(L₁)(Et))₂] (**13**).**

Zn(1)-O(1 ^{<i>i</i>})	2.046(2)	O(2)-C(5)	1.449(3)
Zn(1)-N(1 ^{<i>i</i>})	2.013(2)	N(1)-C(2)	1.315(4)
Zn(1)-C(3)	2.408(3)	N(1)-C(7)	1.484(3)
Zn(1)-C(10)	1.980(3)	C(2)-C(3)	1.443(4)
O(1)-C(4)	1.252(4)	C(5)-C(6)	1.509(5)
O(1 ^{<i>i</i>})-Zn(1)-N(1 ^{<i>i</i>})	93.15(9)	C(3)-Zn(1)-C(10)	108.42(12)
O(1 ^{<i>i</i>})-Zn(1)-C(3)	97.02(9)	C(4)-O(1)-Zn(1 ^{<i>i</i>})	118.80(17)
O(1 ^{<i>i</i>})-Zn(1)-C(10)	114.23(11)	Zn(1 ^{<i>i</i>})-N(1)-C(2)	120.69(19)
N(1 ^{<i>i</i>})-Zn(1)-C(3)	98.26(9)	C(4)-C(3)-C(2)	123.9(3)
N(1 ^{<i>i</i>})-Zn(1)-C(10)	138.12(13)	O(1)-C(4)-C(3)	128.6(3)

The largest bond angle about the central Zn atom in (**13**) is 138.12(13)° for N(1^{*i*})-Zn(1)-C(10), which is over 40° larger than the 93.15(9)° for the N(1^{*i*})-Zn(1)-O(1^{*i*}) angle. The N(1^{*i*})-Zn(1)-C(10) bond angle is large as it reduces the steric interaction between the terminal ethyl group on Zn(1) and the ^{*i*}Pr group on N(1^{*i*}). The O(1^{*i*})-Zn(1)-N(1^{*i*}) angle however is small due to the constraints of the formed ring system. The other angles about Zn(1) of O(1^{*i*})-Zn(1)-C(3), O(1^{*i*})-Zn(1)-C(10), N(1^{*i*})-Zn(1)-C(3) and C(3)-Zn(1)-C(10) have intermediate bonds angles of 97.02(9), 114.23(11), 98.26(9) and 108.42(12)° respectively. The deviations from 109.5° are expected in complexes of this type and result from the inflexibility of the bound chelate ligand (L₁) and the requirement to reduce the steric interaction between the ^{*i*}Pr and terminal ethyl groups.

The set-up for the synthesis of (**13**) is relatively simple and does not require reflux conditions or an additional ligand deprotonation step to allow for reaction with ZnEt_2 . These factors are beneficial for the synthesis of potential CVD precursors. However, the complex is not air or moisture stable given the presence of the ethyl groups attached to the Zn and the available decomposition pathway they allow for.

5.2.2.2.2 Synthesis of $[(\text{Zn}(\text{OC}(\text{OEt})\text{CHC}(\text{Me})\text{N}(\text{CH}_2)_2^i\text{Pr})(\text{Et}))_2][(\text{Zn}(\text{L}_4)(\text{Et}))_2]$ (**14**)

The synthesis of $[(\text{Zn}(\text{L}_4)(\text{Et}))_2]$ (**14**) was achieved from the 1:1 equivalence reaction between ligand (**L4**) and ZnEt_2 . The addition of ligand (**L4**) to ZnEt_2 in toluene was carried out at $-78\text{ }^\circ\text{C}$ and the solution allowed to warm to room temperature whilst stirring. During this time, the evolution of ethane gas, the by-product of the reaction was observed. The solution was stirred for 24 hours, concentrated *via* the removal of toluene *in vacuo* and held at $-18\text{ }^\circ\text{C}$ for 48 hours. $[(\text{Zn}(\text{L}_4)(\text{Et}))_2]$ (**14**) crystallised out of solution and was isolated as yellow tinted crystals.

^1H and ^{13}C NMR spectroscopy confirmed the synthesis of (**14**) with the expected resonances observed in both spectra. The peaks observed in the ^1H NMR spectrum also had the anticipated splitting patterns. A broad quartet and triplet were observed at 0.21 and 1.20 ppm respectively for the CH_2 and CH_3 protons for the ethyl group bonded to the Zn center. The protons of the isopentyl group on the N atom were attributed to the doublet at 0.81 ppm and the three multiplets at 1.25, 1.41 and 2.98 ppm, for the CH_3 groups, the NCH_2CH_2 , NCH_2CH_2 and CH group respectively. The CH_3 and CH_2 protons of the ethoxide group were attributed to the triplet at 1.09 ppm and the quartet at 4.04 ppm respectively. The singlet for the protons of the CH_3 methyl group attached to the chelating ring appears at 1.61 ppm whilst the singlet for the CH proton attached directly to the chelating ring appears at 4.62 ppm. The ^1H spectrum contained no broad downfield characteristic peak for the NH proton in (**L4**), confirming no unreacted (**L4**) remained.

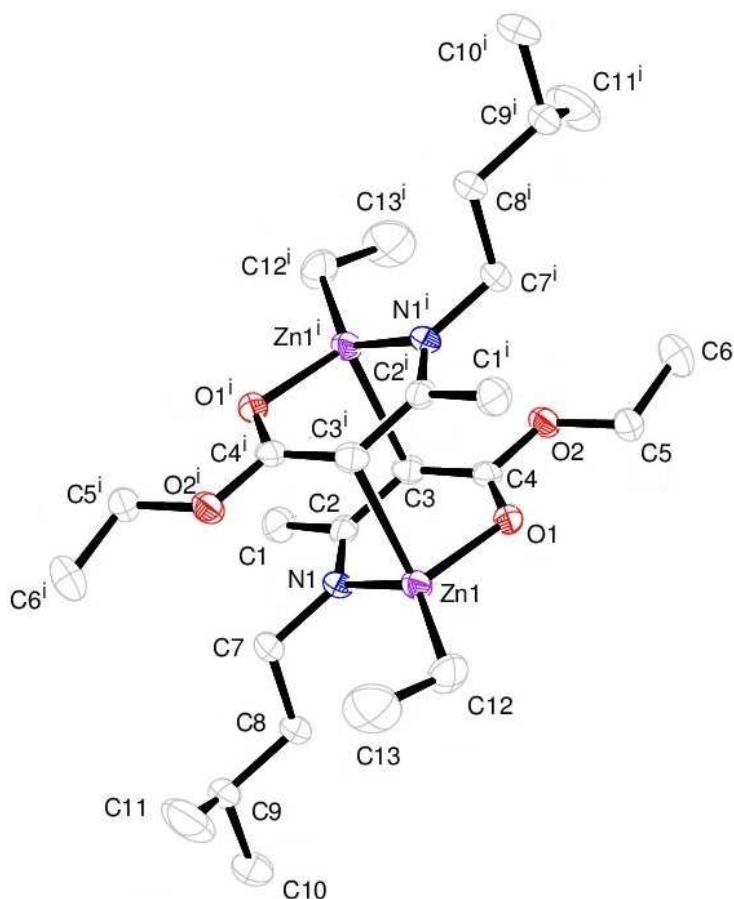


Figure 5.13: X-ray crystal structure of $[(\text{Zn}(\text{OC}(\text{OEt})\text{CHC}(\text{Me})\text{N}(\text{CH}_2)_2^i\text{Pr})(\text{Et}))_2][(\text{Zn}(\text{L}_4)(\text{Et}))_2]$ (**14**). (Symmetry operator: $i = -X, -Y, -Z$.)

Table 5.8: Crystallographic data for $[(\text{Zn}(\text{OC}(\text{OEt})\text{CHC}(\text{Me})\text{N}(\text{CH}_2)_2^i\text{Pr})(\text{Et}))_2][(\text{Zn}(\text{L}_4)(\text{Et}))_2]$ (**14**).

Crystal System	Triclinic	
Space Group	$P\bar{1}$	
Volume	$759.20(7) \text{ \AA}^3$	
Unit Cell Dimensions	$a = 7.6150(4) \text{ \AA}$	$\alpha = 79.215(4)^\circ$
	$b = 8.0888(4) \text{ \AA}$	$\beta = 76.682(4)^\circ$
	$c = 13.6777(6) \text{ \AA}$	$\gamma = 68.774(5)^\circ$

The crystal structure of (**14**) was determined using single crystal X-ray diffraction and is shown in Figure 5.13. The determined crystallographic data is given in Table 5.8 with selected bond lengths and angles shown in Table 5.9. Zinc complexes with this heteroleptic β -iminoesterate structure have not been reported before in the literature. $[(\text{Zn}(\text{L}_4)(\text{Et}))_2]$ (**14**) is centrosymmetric and crystallises in the triclinic space group $P\bar{1}$ as a dimer. The complex has two Zn atoms, one of which has been symmetrically generated. Zn(1) retains one bond to a terminal ethyl group which remains from the original ZnEt_2 compound. Two coordination sites around Zn(1) are occupied by the coordination of the bidentate ligand (**L**₄) which bonds through the O(1) and N(1) atoms. The bonding of (**L**₄) forms a puckered six membered ZnOC_3N ring. Zn(1) also forms a dative interaction to C(3ⁱ) on the symmetry equivalent monomer unit. As such, (**14**) exists as a dimer with two dative interactions between two monomer units, in which Zn(1) adopts a highly distorted tetrahedral geometry.

Table 5.9: Selected bond lengths (Å) and angles (°) for $[(\text{Zn}(\text{OC}(\text{OEt})\text{CHC}(\text{Me})\text{N}(\text{CH}_2)_2^i\text{Pr})(\text{Et}))_2]$ $[(\text{Zn}(\text{L}_4)(\text{Et}))_2]$ (14**).**

Zn(1)-O(1)	2.0278(14)	O(2)-C(5)	1.451(3)
Zn(1)-N(1)	1.9964(18)	N(1)-C(2)	1.307(3)
Zn(1)-C(3 ⁱ)	2.452(2)	N(1)-C(7)	1.468(3)
Zn(1)-C(12)	1.962(2)	C(2)-C(3)	1.430(3)
O(1)-C(4)	1.254(3)	C(7)-C(8)	1.525(3)
O(1)-Zn(1)-N(1)	92.99(7)	C(3 ⁱ)-Zn(1)-C(12)	107.44(10)
O(1)-Zn(1)-C(3 ⁱ)	96.94(7)	Zn(1)-O(1)-C(4)	119.96(13)
O(1)-Zn(1)-C(12)	121.22(9)	Zn(1)-N(1)-C(2)	122.76(14)
N(1)-Zn(1)-C(3 ⁱ)	97.02(7)	C(2)-C(3)-C(4)	124.3(2)
N(1)-Zn(1)-C(12)	133.75(10)	O(1)-C(4)-C(3)	128.35(19)

The longest bond made by Zn(1) is the Zn(1)-C(3ⁱ) bond between Zn(1) on one monomer to C(3ⁱ) on the other, which measures 2.452(2) Å. This compares to a more typical Zn-C bond length of 1.962(2) Å for the Zn(1)-C(12) bond. The increased length of the Zn(1)-C(3ⁱ) bond is highly indicative of a dative interaction between Zn(1) and C(3ⁱ). Zn(1) also makes bonds to O(1) and N(1) of the bidentate ligand (**L4**) which measure 2.0278(14) and 1.9964(18) Å respectively. These bonds are slightly longer than the analogous bonds in (**9**) and (**10**). For example the Zn(1)-O(1) and Zn(1)-N(1) bonds in (**9**) measure 1.9766(9) and 1.9692(11) Å respectively. This is likely the result of the formation of a dimer in (**14**). The delocalised nature of the puckered ring formed by the bonding of the β -iminoesterate ligand is also illustrated by the bond lengths in (**14**). The C-O, C-N and C-C bonds within the ZnOC₃N bonded ring structure are much shorter than those bonds outside of it. The C-O, C-N and C-C bonds outside the bonded ligand ring system in complex (**14**) have distances typically expected for a single bond length, such as 1.451(3), 1.468(3) and 1.525(3) Å for the bonds of O(2)-C(5), N(1)-C(7) and C(7)-C(8) respectively. However, the C-O, C-N and C-C bonds that form part of the ring structure are much shorter, due to the delocalised nature of the ring with the O(1)-C(4), N(1)-C(2) and C(2)-C(3) bonds measuring 1.254(3), 1.307(3) and 1.430(3) Å respectively.

The largest angle about Zn(1) in (**14**) is 133.75(10)° for N(1)-Zn(1)-C(12), which is over 40° larger than the 92.99(7)° for the O(1)-Zn(1)-N(1) angle. The N(1)-Zn(1)-C(12) bond angle is large as it reduces the steric interaction between the terminal ethyl group on Zn(1) and the isopentyl group on N(1). The N(1)-Zn(1)-C(12) angle however is small due to the constraints of the formed ring system. The other angles about Zn(1) of C(3ⁱ)-Zn(1)-C(12), N(1)-Zn(1)-C(3ⁱ), O(1)-Zn(1)-C(12) and O(1)-Zn(1)-C(3ⁱ) have intermediate values of 107.44(10), 97.02(7), 121.22(9) and 96.94(7)° respectively. The deviations from 109.5° are expected in complexes of this type and result from the inflexibility of the bound chelate ligand (**L4**) and the requirement to reduce the steric interaction between the isopentyl and terminal ethyl groups.

The synthesis of (**14**) was conducted without the use of reflux conditions or deprotonation of the NH proton on the free ligand prior to reaction with ZnEt₂. Despite these advantages, the use of (**14**) as a CVD precursor may not be ideal since the complex is not air or moisture stable given the presence of the ethyl groups and the low energy activation pathways these offer towards decomposition.

5.2.2.2.3 Crystal Structure Comparison of [(Zn(L₁)(Et))₂] (**13**) and [(Zn(L₄)(Et))₂] (**14**)

The bond angles around the four coordinate Zn centres in (**13**) and (**14**) both have a range that deviates significantly from the 109.5° that would be observed for a centre with perfect tetrahedral geometry. This is due to the inflexibility of the chelating ligand and the relatively small bite angle resulting from the (OC(OEt)CHC(Me)N(R)) chain where X is *i*Pr in (**13**) and (CH₂)₂*i*Pr in (**14**). However, there are differences between the respective bond angles in (**13**) and (**14**), one example being the angle between the N, Zn and the ethyl C atoms. This bond angle is the largest in both complexes as to reduce the steric conflict in the complexes and place distance between the organic ligand on the N atom and the ethyl group on the Zn atom. The N(1ⁱ)-Zn(1)-C(10) angle in (**13**) measures 138.12(13)°, compared to the N(1)-Zn(1)-C(12) bond angle of 133.75(10)° in (**14**). The isopropyl group on the N in (**9**) has a short carbonyl chain and less rotation available about its bonds. This results in the steric bulk of the ligand being in closer proximity to the ethyl group on the Zn, requiring an increased bond angle between them. However, the isopentyl group has a longer carbonyl chain with increased rotation available which causes a reduction in the steric frustration with the ethyl group on the Zn allowing for a smaller angle in the bond. This is compensated for by the angle between the O, Zn and C on the ethyl group, which measures 114.23(11)° for the O(1ⁱ)-Zn(1)-C(10) bond angle in (**13**) and 121.22(9)° for the O(1)-Zn(1)-C(12) bond angle in (**14**).

The Zn in both (**13**) and (**14**) retains one ethyl group from the ZnEt₂ whilst forming two bonds to form a puckered ZnOC₃N ring from the β -iminoester ligand and one dative bond to dimerise. The delocalised nature of the rings in both complexes is illustrated by the shorter length of the C-O, C-N and C-C bonds within the formed rings when compared to those outside of the ring structure. The bond lengths around the Zn and in the ZnOC₃N ring are of relatively similar values in (**13**) and (**14**). However, most bonds are slightly shorter in (**14**), for example the Zn(1)-O(1) and Zn(1)-N(1) bonds measure 2.0278(14) and 1.9964(18) Å respectively which compares to 2.046(2) and 2.013(2) Å for the Zn(1)-O(1ⁱ) and Zn(1)-N(1ⁱ) bonds respectively in (**13**). However (**14**) does have a slightly longer dative bond between the two monomer units with the Zn(1)-C(3ⁱ) measuring 2.452(2) Å compared to the equivalent Zn(1)-

C(3) bond measuring 2.408(3) Å in (13). As discussed above, the bond lengths in (13) and (14) are as expected for this type of compound.

5.2.2.2.4 Crystal Structure Comparison of [Zn(L₁)₂] (9) and [(Zn(L₁)(Et))₂] (13)

Zinc β -iminoesterate complexes [Zn(L₁)₂] (9) and [(Zn(L₁)(Et))₂] (13) were both synthesised *via* the ethane elimination reaction between the (L₁) β -iminoester ligand and ZnEt₂ in a 2:1 and 1:1 molar equivalence ratio respectively. The resulting crystal structures differentiate quite significantly. In (9), the ethyl groups on the Zn have been replaced by two chelate β -iminoester ligands which bond through both the O and N atoms and are orthogonal to each other. This creates a coordinatively saturated Zn metal centre with a distorted tetrahedral geometry and two six membered ZnOC₃N rings which are puckered in nature. Since the Zn has a full coordination sphere it exists in the solid state as a monomer species. In (13), only one of the ethyl ligands is replaced by a chelate β -iminoester ligands which likewise bonds through both the O and N atoms. As is the case in (9), the bonding β -iminoester ligand creates a six membered ZnOC₃N ring which is puckered in nature. However, the Zn only makes three bonds and so forms a dative bond to the central C atom in the ZnOC₃N ring of another unit to form a dimer.

The length of corresponding bonds in (9) and (13) have only a slight variation, for example, the Zn-O and Zn-N bonds in (13) are slightly longer than in (9). The Zn(1)-O(1ⁱ) and Zn(1)-N(1ⁱ) bonds in (13) measure 2.046(2) and 2.013(2) Å respectively, compared to 1.9766(9) and 1.9692(11) Å for the Zn(1)-O(1) and Zn(1)-N(1) bonds respectively in (9). This is compensated for by slightly shorter O-C and O-N bonds in the ZnOC₃N ring in (13) than in (9). The O(1)-C(4) and N(1)-C(2) bonds measure 1.252(3) and 1.315(4) Å in (13) compared to 1.2642(16) and 1.3198(17) Å for the O(1)-C(4) and N(1)-C(2) bonds respectively in (9).

Due to the different identity of ligands in (9) and (13), only the O-Zn-N bond angle of the ZnOC₃N ring is comparable about the Zn centre. In (9), the O(1)-Zn(1)-N(1) measures 96.63(4)°, which is slightly larger than the O(1ⁱ)-Zn(1)-N(1ⁱ) bond angle in (13), which measures 93.15(9)°. This ligand and its nature of bonding is common to both (9) and (13) and hence the values are similar. However, the slight discrepancy

results from the effect of the unidentate bonds formed to the Zn centre in (**13**). The Zn centres in both (**9**) and (**13**) are in a distorted tetrahedral geometry where the range of bond angles about the Zn differs significantly from the 109.5° which would be expected for a perfect tetrahedral geometry. The bond angles in (**9**) range from $96.63(4)^\circ$ for the O(1)-Zn(1)-N(1) angle, to $129.46(5)^\circ$ for the N(1)-Zn(1)-N(2) angle. The bond angles in (**13**) have an even greater range from $93.15(9)^\circ$ for the N(1ⁱ)-Zn(1)-O(1ⁱ) angle to $138.12(13)^\circ$ for the N(1ⁱ)-Zn(1)-C(10) angle. As discussed previously, this results from the inflexibility of the ligands β -iminoester ligand and the small bite angle resulting from the (N(ⁱPr)C(Me)CHC(OEt)O) chain. The range is greater in (**13**) as a result of the restrictive requirements in order to enable a dative bond to be formed with another monomer unit.

5.2.3 AACVD Precursors Study

This chapter has described the synthesis of zinc β -iminoesterate complexes which have potential to be highly appropriate CVD precursors towards ZnO thin films. [Zn(L₁)₂] (**9**) and [Zn(L₂)₂] (**10**) were selected for analysis as potential precursors for the AACVD of ZnO. The complexes were selected on the basis that they are both monomers, air stable, single-source and meet a good number of the desired precursor properties as outlined in Chapter 1.5.1. They have also been fully characterised including the determination of their crystal structure by single crystal X-ray diffraction.

5.2.3.1 Thermal Gravimetric Analysis

The thermal decomposition properties of the two β -iminoesterate complexes were determined by thermal gravimetric analysis (TGA) and differential scanning calorimetry (DSC) between room temperature (23 °C) and 500 °C in a helium atmosphere, as shown in Figure 5.14. TGA thermograms show both (**9**) and (**10**) exhibit clean, one step decomposition profiles, ideal for CVD purposes. Complex (**9**) begins to decompose at 140 °C with major loss of mass observed between 200 and 250 °C. The very slight mass loss (1.5%) observed between 85 and 115 °C results from residual toluene, as also observed in the DSC profile.

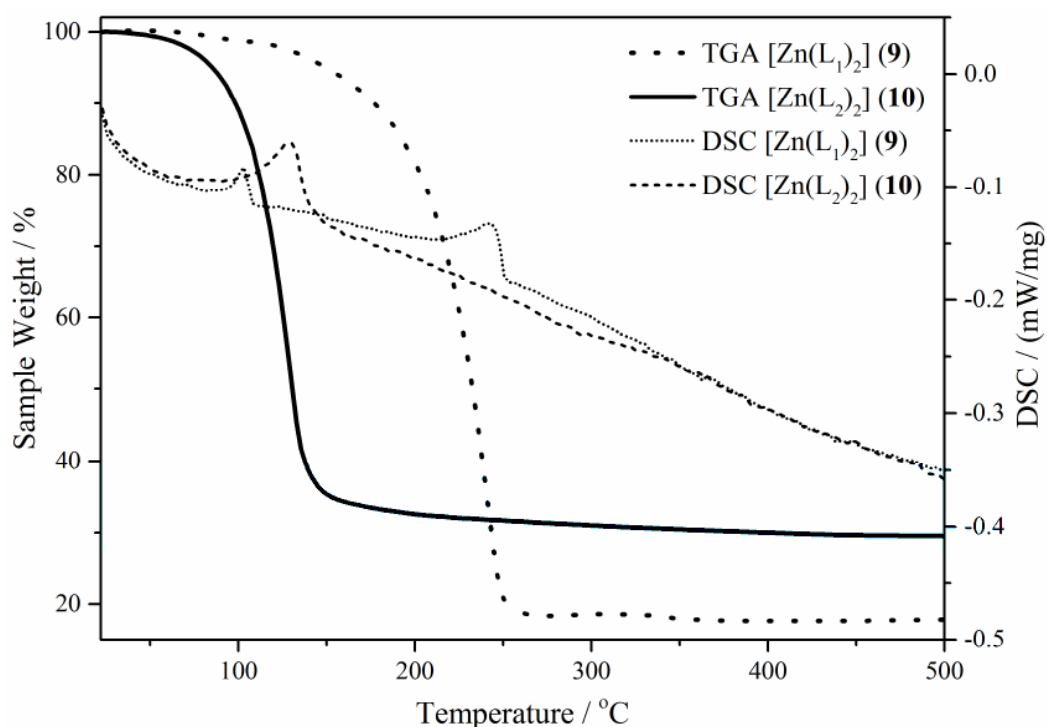
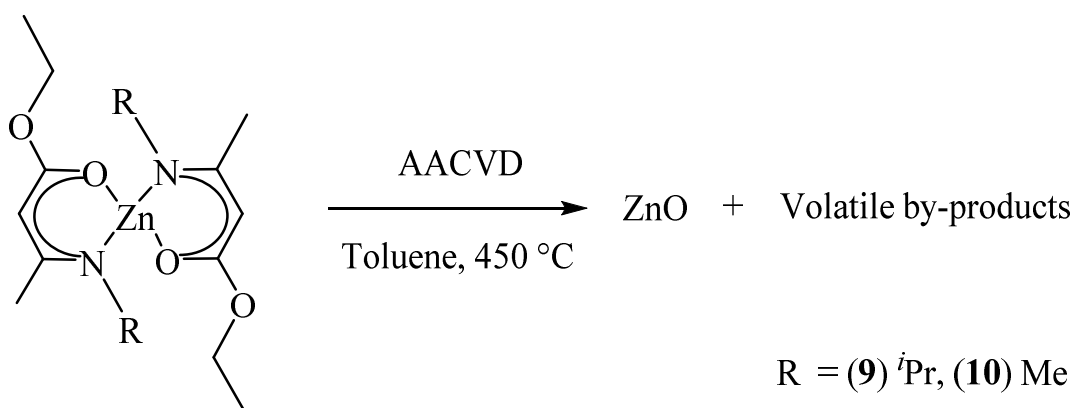


Figure 5.14: Thermal gravimetric analysis (TGA) and differential scanning calorimetry (DSC) of zinc complex [Zn(L₁)₂] (9) and [Zn(L₂)₂] (10).

The total mass loss of complex (9) was 80.2% leaving a residual mass of 19.8%. This closely matches the calculated residual mass of 20.1% for decomposition to ZnO and is a good indication of a clean decomposition to ZnO. Complex (10) begins to decompose at a much lower temperature. Significant mass loss was observed much sooner in the heating process, between 100 – 140 °C, around 100 °C lower than complex (9). This is likely to be a result of the different R groups in the complexes. The residual mass of (10) is 29.6% which is noticeably higher than the calculated residual mass for decomposition to ZnO of 23.2%. This may be suggestive that complex (10) undergoes incomplete decomposition to ZnO and could result in contamination of the deposited thin films. The residual masses for all complexes used as AACVD precursors presented in this thesis are shown in Appendix Table 7.1. Following the determination of the thermal properties of [Zn(L₁)₂] (9) and [Zn(L₂)₂] (10) the complexes were employed as AACVD precursors.

5.2.4 AACVD of ZnO Thin Films

ZnO thin films were successfully deposited onto silica-coated float glass substrates using zinc β -iminoesterate precursors $[\text{Zn}(\text{L}_1)_2]$ (**9**) and $[\text{Zn}(\text{L}_2)_2]$ (**10**) as shown in Scheme 5.18. Initial studies were used to determine the optimal deposition conditions, varying the substrate temperature between 350 and 550 °C and the N_2 flow rates between 0.8 and 2 Lmin^{-1} . It was found that the optimum deposition conditions of 450 °C and 1 Lmin^{-1} resulted in films with excellent coverage of the entire substrate. The films were also strongly adherent, passing the Scotch© tape test and only being removed upon intense scratching with a steel scalpel. The films were insoluble in common organic solvents (acetone, toluene and 2-propanol) but dissolved in nitric acid.



Scheme 5.18: AACVD of ZnO thin films from β -iminoesterate precursors $[\text{Zn}(\text{L}_1)_2]$ (**9**) and $[\text{Zn}(\text{L}_2)_2]$ (**10**).

Once deposited, the films were characterised by glancing-angle X-ray powder diffraction (XRD), scanning electron microscopy (SEM), X-ray photoelectron spectroscopy (XPS) and their thicknesses were determined using a Filmetrics F20 measurement system. Their functional properties of electrical conductance and optical properties were also studied using a two-point probe and UV/Vis/NIR transmission spectroscopy respectively. The films were then annealed at 600 °C for 6 hours and the characterization repeated. The analysis before annealing is described as ‘as deposited’ and the analysis post the heating stage as ‘annealed’.

The precursors were employed on a single-source basis in which no additional oxygen source was used. Precursors (**9**) and (**10**) exhibited excellent solubility in a range of dry solvents including toluene, hexane, dioxane and DCM. Dry toluene was selected as the solvent with depositions also carried out in dry dioxane and dry hexane as a comparison.

The as deposited films varied in their physical appearance with those deposited from (**9**) having a light brown tint as opposed to films deposited from (**10**) which were noticeably darker. This difference in appearance is suggestive of a greater carbon content in the films from (**10**). Upon annealing, the brown colour from all samples was removed and all films appeared highly transparent.

5.2.4.1 Film Thickness

Film thickness was determined using a Filmetrics F20 thin film measurement system. The as deposited film from $[\text{Zn}(\text{L}_1)_2]$ (**9**) was found to be 350 nm thick which compared to the 550 nm thickness measured for films as deposited from $[\text{Zn}(\text{L}_2)_2]$ (**10**). Upon annealing, films from both (**9**) and (**10**) were found to be between 280 and 300 nm in thickness. These figures are explained by XPS analysis which shows incorporation of carbon and nitrogen in films from (**10**) which is subsequently removed upon annealing.

5.2.4.2 X-ray Photoelectron Spectroscopy

X-ray photoelectron spectroscopy (XPS) was used to analyse the elemental composition of the thin films and confirms the presence of Zn and O in the annealed thin films deposited from zinc complexes $[\text{Zn}(\text{L}_1)_2]$ (**9**) and $[\text{Zn}(\text{L}_2)_2]$ (**10**). A Gaussian/Lorentzian product distribution was used to fit the Zn 2p peaks. The characteristic peaks for the Zn $2p_{1/2}$ and $2p_{3/2}$ states, as expected, appear at 1045.2 and 1022.2 eV binding energy respectively, with an intensity ratio of 1:2 and an energy gap of 23.0 eV as shown in Figure 5.15 for the film deposited from (**9**).⁴² Also as expected, the O 1s peak can be fitted by a Gaussian distribution centred at 531.4 eV.

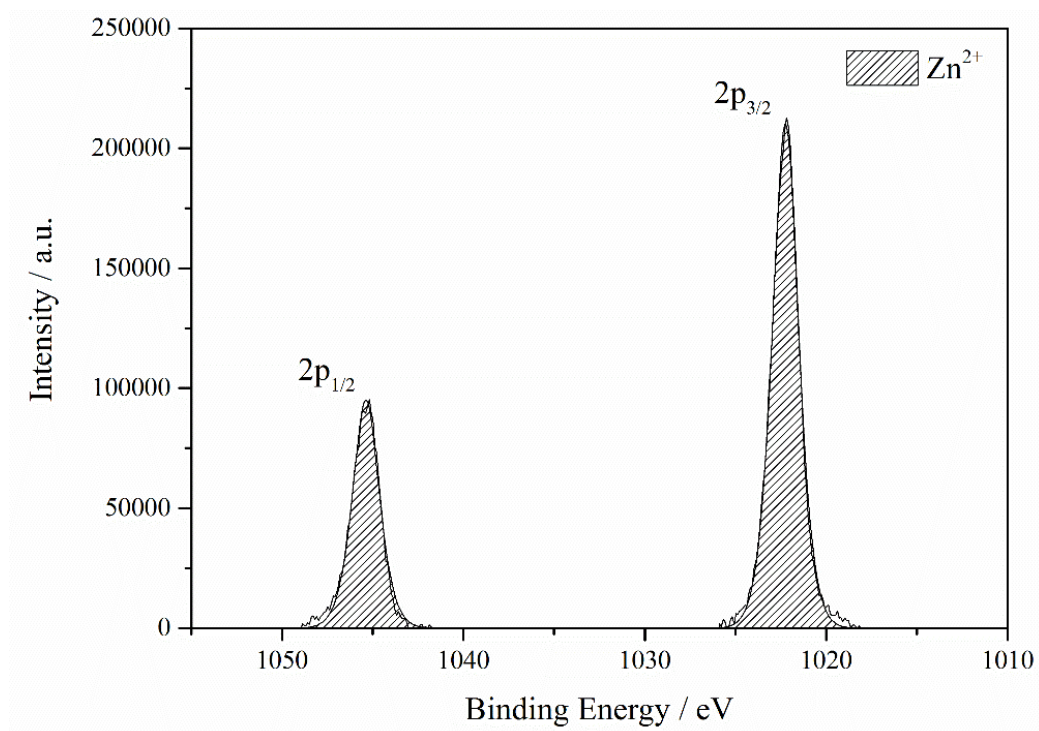


Figure 5.15: XPS of Zn 2p peaks for the Zn 2p_{1/2} and 2p_{3/2} states for a ZnO thin film deposited from [Zn(L₁)₂] (9) at 450 °C by AACVD in toluene.

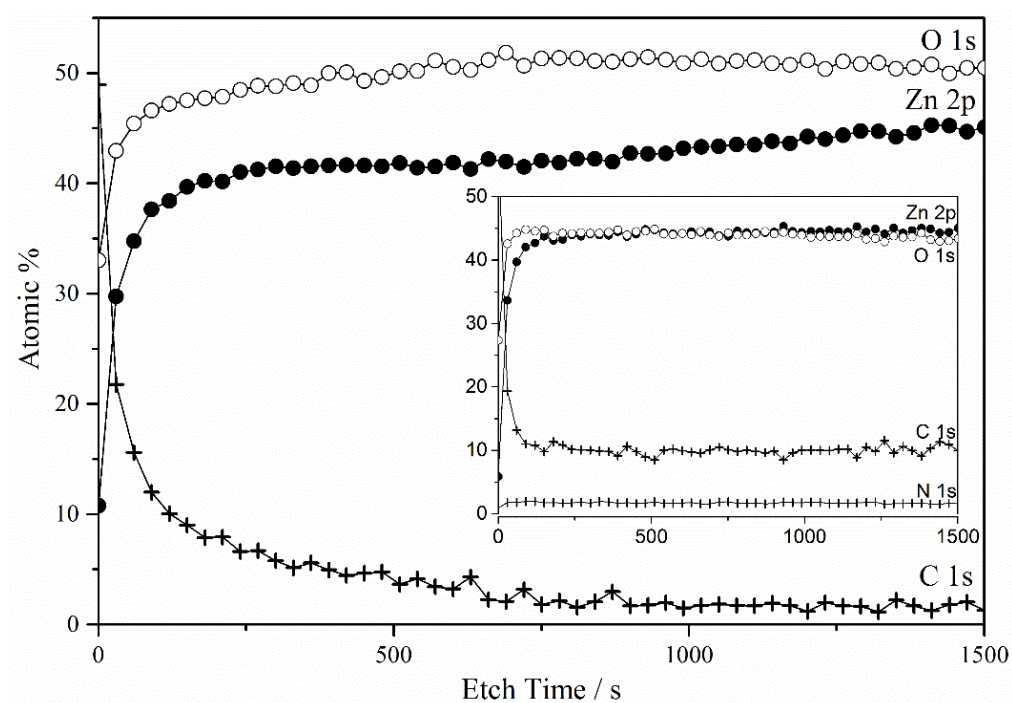


Figure 5.16: XPS depth profile for annealed films deposited from zinc complex [Zn(L₁)₂] (9). Inset: XPS depth profile for the as deposited film.

Pre-annealing, both films were found to contain carbon throughout. Etching studies were performed and the average carbon content in the as deposited films from $[\text{Zn}(\text{L}_1)_2]$ (**9**) in toluene was found to be 9.7 at.%, as shown in Figure 5.16 (inset). The level of carbon contamination could also be attributed to the identity of the solvent used. When dioxane was used, the carbon content was higher, at an average of 10.2 at.% but was found to be lower, at an average of 5.7 at.% when hexane was used. These figures are in a range comparable to the 8.7 at.% reported by Matthews *et al.*³⁸ for ZnO films deposited from (**9**) by AP-MOCVD. Upon annealing, the carbon content of the film from $[\text{Zn}(\text{L}_1)_2]$ (**9**) falls to 3.1 at.% as can be seen in Figure 5.16, resulting in a $\text{ZnO}_{1.2}$ transparent thin film.

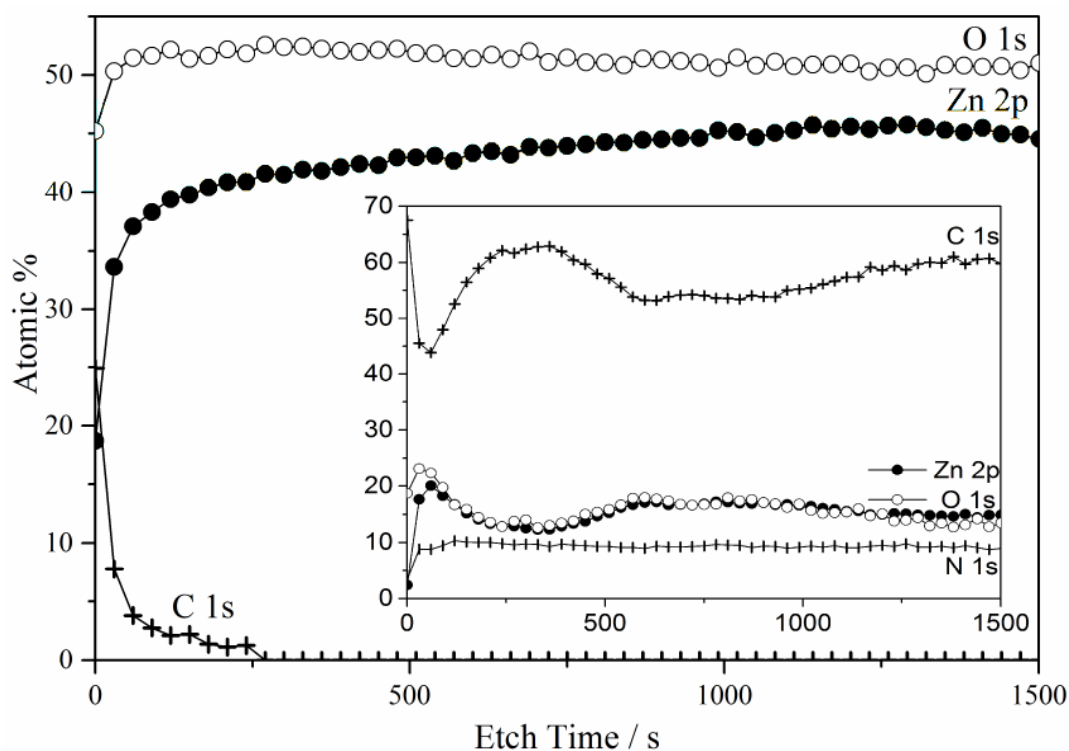


Figure 5.17: XPS depth profile for annealed films deposited from zinc complex $[\text{Zn}(\text{L}_2)_2]$ (**10**) in toluene. Inset: XPS depth profile for the as deposited film.

The carbon content in thin films deposited from $[\text{Zn}(\text{L}_2)_2]$ (**10**) was found to be 56.1 at.%, as shown in Figure 5.17 (inset). The XPS etching study also found the film to contain a significant nitrogen content at 9.0 at.%, which compares to less than 1 at.% in the thin film deposited from (**9**). This suggests that it is contamination from the

precursor that has undergone incomplete decomposition which results in the heavily contaminated ZnO thin films. The TGA thermogram for (10) discussed in Section 5.2.3.1 supports this idea. The carbon content of the film deposited from (10) fell dramatically upon annealing to 0.6 at.%, as shown in Figure 5.17 resulting in a transparent ZnO_{1.2} thin film.

These XPS figures are quite significant: simply by changing the identity of the organic ligand attached to the N on the zinc β -iminoesterate from an isopropyl group (9) to methyl group (10), the carbon content of the films increases from 9.7 at.% to 56.1 at.% for a comparable deposition. It is postulated that complex (9) with the larger isopropyl group has access to more facile decomposition routes such as hydride elimination which are not available in complex (10) with a small methyl group. This lack of facile decomposition pathways results in the contamination observed.

The carbon content reported in the literature for films deposited from similar, single-source zinc β -ketoiminate precursors by MOCVD range from approximately 10 at.%³⁹ up to 26.2 at.%.³⁸ These results widen this range from 5.7 at.% where [Zn(L₁)₂] (9) in hexane was used to 56.1 at.% where [Zn(L₂)₂] (10) in toluene was employed. The as deposited and annealed films were also analysed using X-ray diffraction.

5.2.4.3 X-ray Diffraction

Glancing-angle X-ray diffraction (XRD) patterns of the films (as deposited and annealed) deposited from [Zn(L₁)₂] (9) and [Zn(L₂)₂] (10) in toluene are shown in Figure 5.18. Upon annealing, the crystallinity of the films are observed to increase and the peaks in the XRD pattern for the annealed films from both (9) and (10) confirm the formation of the hexagonal wurtzite phase of ZnO. Similar XRD patterns are observed when dioxane and hexane were used as the solvent. The as deposited and annealed films were also analysed using scanning electron microscopy.

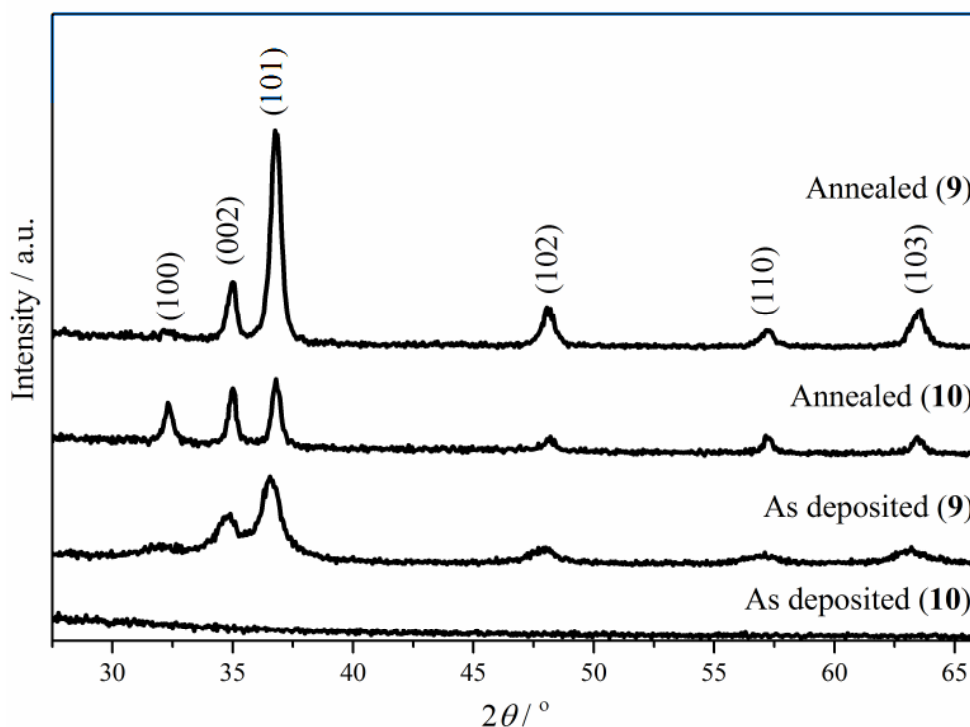


Figure 5.18: XRD patterns obtained from as deposited and annealed films deposited from zinc complex $[\text{Zn}(\text{L}_1)_2]$ (9) and $[\text{Zn}(\text{L}_2)_2]$ (10) at 450 °C by AACVD in toluene.

5.2.4.4 Scanning Electron Microscopy

The surface morphology of the films, both as deposited and annealed was determined by scanning electron microscopy (SEM) and is shown in Figure 5.19. As deposited films, Figure 5.19 (a) and (c) were dense and continuous ZnO coatings. Upon annealing, the structure of agglomerated particles becomes more evident, as can be seen in Figure 5.19 (b) and (d) – (f). This is indicative of a Volmer-Weber type island growth mechanism. This arises when the depositing particles have a stronger attraction to themselves as opposed to the underlying silica-coated float glass substrate. The SEM images also reveal the microstructure of all films showing the significant presence of grain boundaries, which is consummate with their low conductivity as will be discussed in Section 5.2.4.5.1.

The identity of the solvent was also observed to influence the microstructure of the deposited films. The use of dioxane as a solvent resulted in a greater degree of agglomeration and increased size of particle clusters, as can be seen in Figure 5.19 (d) and (f) as compared to when toluene was employed as the solvent, Figure 5.19, (b)

and (e). Finally, when $[\text{Zn}(\text{L}_4)_2]$ (**10**) was used as the precursor, the particle clusters were found to be less rounded and more elongated, as shown in Figure 5.19 (f).

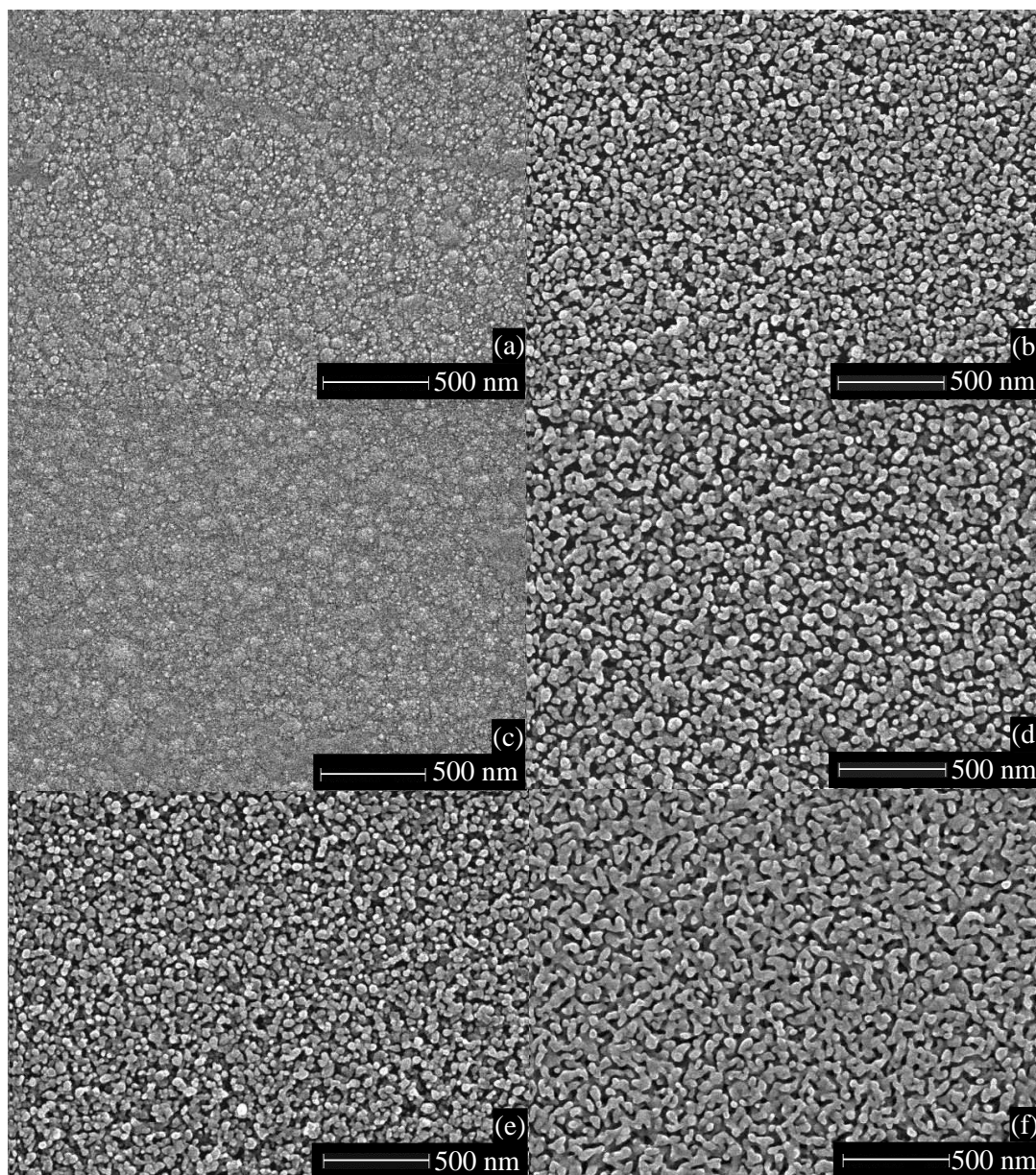


Figure 5.19: High magnification ($\times 50,000$) plane view SEM images of thin films deposited from $[\text{Zn}(\text{L}_1)_2]$ (**9**) (a) – (d) and $[\text{Zn}(\text{L}_2)_2]$ (**10**) (e) and (f). As deposited films are shown in (a) and (c) with annealed films shown in (b) and (d)-(f). Films (a), (b) and (e) were deposited using toluene as a solvent and films (c), (d) and (f) using dioxane.

5.2.4.5 Functional Properties

5.2.4.5.1 Electrical Properties

The as deposited films were not electrically conductive but became slightly conductive upon annealing. Films deposited from $[\text{Zn}(\text{L}_1)_2]$ (**9**) had a resistance of 5 M Ω and films deposited from (**10**) had a resistance of 40 M Ω . This is similar to ZnO films reported by Holmes *et al.*³⁹ who attributed the conductivity to the removal of carbon contamination. Although the films are not overly conductive this is what is typically expected for undoped ZnO, which is often highly resistive.⁴³ To significantly increase the conductivity a dopant source would be required, as described in Chapter 1.1.2.

5.2.4.5.2 Optical Properties

UV/Vis/NIR spectroscopy was employed to determine the transmission properties of the as deposited and annealed films deposited from $[\text{Zn}(\text{L}_1)_2]$ (**9**) and $[\text{Zn}(\text{L}_2)_2]$ (**10**) in toluene between 300 and 1400 nm, as shown in Figure 5.20.

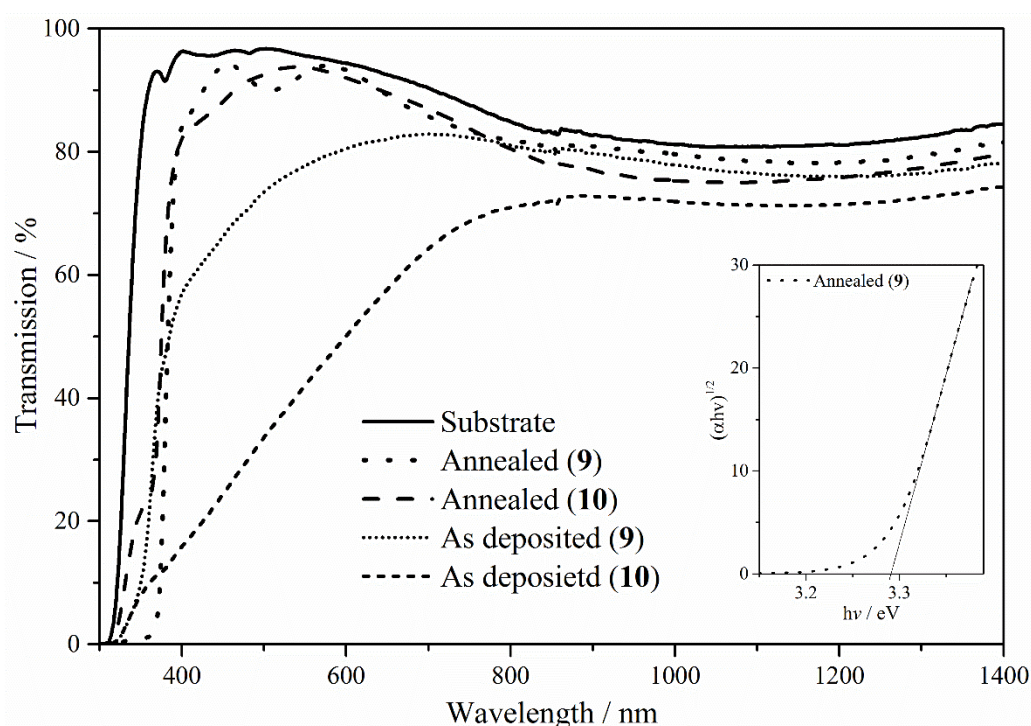


Figure 5.20: Transmission spectra observed for as deposited and annealed thin films deposited from $[\text{Zn}(\text{L}_1)_2]$ (**9**) and $[\text{Zn}(\text{L}_2)_2]$ (**10**) in toluene at 450 °C by AACVD. Insert: Tauc plot for annealed film deposited from $[\text{Zn}(\text{L}_1)_2]$ (**9**).

The film deposited from $[\text{Zn}(\text{L}_1)_2]$ (**9**) has an average transmission of 74% in the visible light region. Upon annealing, this increases above 90%, a value well above the 80% figure often quoted for a film to be described as highly transparent.⁴⁴ The transmission in the visible light region of the film from $[\text{Zn}(\text{L}_2)_2]$ (**10**) is 41% before annealing. This significantly lower transmission again results from the films high carbon content, as determined by the XPS measurements. However, upon annealing the film also has a transparency greater than 90% in the visible light region.

5.2.4.5.2.1 Band Gap

The sharp decrease in transmission of the annealed films, as seen in the UV region in Figure 5.20 is the adsorption edge of the material and is characteristic of a TCO. Using this, an estimate of the optical band gap has been made using the Tauc relation:⁴⁵

$$\alpha h\nu = A(h\nu - E_g)^n \quad \text{Equation 5.1}$$

where A is a constant, α is the molar extinction coefficient, $h\nu$ is the photon energy, E_g is the band gap and $n = 1/2$ for a direct allowed transition. Figure 5.20 (Inset) illustrates how the estimates were made from the intercept of the $h\nu$ axis from a line of steepest gradient for the linear region of a $(\alpha h\nu)^{1/2}$ vs. $h\nu$ plot. The band gap of the annealed ZnO films was determined to be 3.3 eV for the film from $[\text{Zn}(\text{L}_1)_2]$ (**9**) and 3.4 eV for the film from $[\text{Zn}(\text{L}_4)_2]$ (**10**). These values are in good agreement with the literature value of 3.37 eV.⁴⁶

5.3 Conclusion

This chapter reports the synthesis of four β -iminoester ligands (**L**₁) to (**L**₄) which were reacted with ZnEt_2 to form zinc β -iminoesterates complexes which took one of two forms. When the ratio of ligand to ZnEt_2 was 2:1 the homoleptic $[\text{Zn}(\text{L}_x)_2]$ monomeric and air-stable complexes (**9**) – (**12**) were synthesised. When the ratio of ligand to ZnEt_2 was decreased to 1:1, the air-sensitive heteroleptic $[(\text{Zn}(\text{L}_x)\text{Et})_2]$ dimeric complexes (**13**) and (**14**) formed. Zinc β -iminoesterate complexes with the heteroleptic structure of (**13**) and (**14**) have not been previously reported. All ligands and complexes were

synthesised, isolated and characterised using a number of analytical techniques. Four compounds had their structures determined by single crystal X-ray crystallography three of which are novel and have been discussed and compared in detail. Zinc β -iminoesterates (**9**) and (**10**) were also employed as single-source precursors in the first reported use of β -iminoesterates in the AACVD of ZnO thin films. It was found that by changing the organic ligand attached to the N moiety from an isopropyl group in (**9**) and a methyl group in (**10**) resulted in a dramatic increase in the level of carbon contained in the resultant film. This is believed to be due to more facile decomposition pathways such as hydride elimination available in (**9**) as opposed to (**10**). TGA was found to give a useful indication that $[\text{Zn}(\text{L}_4)_2]$ (**10**) may result in contaminated film deposition. Upon annealing, ZnO thin films with the hexagonal wurtzite structure and high transparency greater than 90% in the visible light region were produced.

5.4 References

1. J. Kim, J.-W. Hwang, Y. Kim, M. H. Lee, Y. Han and Y. Do, *J. Organomet. Chem.*, 2001 **620**, 1 – 7.
2. C. C. Roberts, B. R. Barnett, D. B. Green and J. M. Fritsch, *Organometallics*, 2012, **31**, 4133 – 4141.
3. K. A. Gerling, N. M. Rezayee, A. L. Rheingold, D. B. Green and J. M. Fritsch, *Dalton Trans.*, 2014, **43**, 16498 – 16508.
4. M. Banerjee, R. W. Seidel, M. Winter, H.-W. Becker, D. Rogalla and A. Devi, *Dalton Trans.*, 2014, **43**, 2384 – 2396.
5. P. Marchand, D. Pugh, I. P. Parkin and C. J. Carmalt, *Chem. Eur. J.*, 2014, **20**, 10503 – 10513.
6. D. Bekermann, D. Rogalla, H.-W. Becker, M. Winter, R. A. Fischer and A. Devi, *Eur. J. Inorg. Chem.*, 2010, **9**, 1366 – 1372.
7. N. Bresciani-Pahor, M. Calligaris, G. Nardin, L. Randaccio and D. Viterbo, *Acta Crystallogr. B*, 1979, **35**, 2776 – 2778.
8. S. Chang, S. T. Hwang and E. C. Hwang, 2003, Patent EP1227079A3 and US6620971B2.
9. D. M. Granum, P. J. Riedel, J. A. Crawford, T. K. Mahle, C. M. Wyss, A. K. Begej, N. Arulsamy, B. S. Pierce and M. P. Mehn, *Dalton Trans.*, 2011, **40**, 5881 – 5890.
10. S. J. W. Cummins, H. P. Fraser, J. R. Fulton, M. P. Coles and C. M. Fitchett, *Aust. J. Chem.*, 2015, **68**, 641 – 647.
11. D. H. Lee, S.-E. Park, K. Cho, Y. Kim, T. Athar, I.-M. Lee, *Tetrahedron Lett.*, 2007, **48**, 8281 – 8284.
12. B. Rechsteiner, F. Texier-Boullet and J. Hamelin, *Tetrahedron Lett.*, 1993, **34**, 5071 – 5074.
13. C. R. Strauss and D. W. Rooney, *Green Chem.*, 2010, **12**, 1340 – 1344.
14. B. S. Kumar, A. Dhakshinamoorthy and K. Pitchumani, *Catal. Sci. Technol.*, 2014, **4**, 2378 – 2396.
15. G. B. B. Varadwaj, S. Rana and K. M. Parida, *Dalton Trans.*, 2013, **42**, 5122 – 5129.
16. M. E. F. Braibante, H. S. Braibante, L. Missio and A. Andricopulo, *Synthesis*, 1994, **9**, 898 – 900.
17. A. Vaccari, *Catal. Today*, 1998, **41**, 53 – 71.
18. P. Laszlo, *Science*, 1987, **235**, 1473 – 1477.
19. X. Lei, D. P. Spence and H. Cheng, 2010, Patent US7691984B2 and EP2065364B1.
20. J. A. T. Norman, 2006, Patent, US7034169B1 and EP1676849B1
21. J. S. Matthews, O. Just, B. Obi-Johnson and W. S. Rees Jr., *Chem. Vap. Depos.*, 2000, **6**, 129 – 132.
22. T. S. Ouattara, R. J. Butcher and J. S. Matthews, *J. Coord. Chem.*, 2005, **58**, 461 – 465.
23. S. Pasko, L. G. Hubert-Pfalzgraf, P. Richard and A. Abrutis, *Inorg. Chem. Commun.*, 2005, **8**, 483 – 487.
24. R.-C. Yu, C.-H. Hung, J.-H. Huang, H.-Y. Lee and J.-T. Chen, *Inorg. Chem.*, 2002, **41**, 6450 – 6455.
25. I. D. Madura, J. Zachara, K. Leszczyńska and A. R. Kunicki, *J. Mol. Struct.*, 2010, **968**, 93 – 98.

26. D. Pugh, P. Marchand, I. P. Parkin and C. J. Carmalt, *Inorg. Chem.*, 2012, **51**, 6385 – 6395.
27. J. Chen, Y.-S. Li, J.-Q. Wu and N.-H. Hu, *J. Mol. Catal. Chem.*, 2005, **232**, 1 – 7.
28. G. Xie, Y. Li, J. Sun and C. Qian, *Inorg. Chem. Commun.*, 2009, **12**, 796 – 799.
29. S. H. Hong, S. K. Rim, I.-M. Lee, Y. S. Min, D. Kim and W. I. Lee, *Thin Solid Films*, 2002, **409**, 82 – 87.
30. S. Lim, B. Choi, Y.-S. Min, D. Kim, I. Yoon, S. S. Lee, I.-M. Lee, *J. Organomet. Chem.*, 2004, **689**, 224 – 237.
31. D. González-Flores, S. A. Patil, P. A. Medina, S. Dever, C. Uthaisar, L. W. Pineda, M. L. Montero, J. W. Ziller and B. D. Fahlman, *Inorganica Chim. Acta*, 2013, **396**, 60 – 65.
32. D.-H. Lee, M.-H. Cho, I.-H. Kwon, I.-C. Jun, I.-M. Lee and M.-J. Jin, *Catal. Commun.*, 2008, **9**, 1517 – 1520.
33. I. A. Baidina, P. A. Stabnikov, A. D. Vasiliev, S. A. Gromilov and I. K. Igumenov, *J. Struct. Chem.*, 2004, **45**, 671 – 677.
34. G. I. Zharkova, P. A. Stabnikov, I. A. Baidina, A. I. Smolentsev and S. V. Tkachev, *Polyhedron*, 2009, **28**, 2307 – 2312.
35. V. V. Krisyuk, S. V. Sysoev, Y. M. Rumyantsev, S. A. Prokhorova, E. V. Maximovskiy, M. L. Kosinova and I. K. Igumenov, *Phys. Procedia*, 2013, **46**, 174 – 182.
36. G. G. Condorelli, G. Malandrino and I. L. Fragalà, *Chem. Vap. Depos.*, 1999, **5**, 237 – 244.
37. C. Di Iulio, M. Middleton, G. Kociok-Köhn, M. D. Jones and A. L. Johnson, *Eur. J. Inorg. Chem.*, 2013, **9**, 1541 – 1554.
38. J. S. Matthews, O. O. Onakoya, T. S. Ouattara and R. J. Butcher, *Dalton Trans.*, 2006, **31**, 3806 – 3811.
39. J. Holmes, K. Johnson, B. Zhang, H. E. Katz and J. S. Matthews, *Appl. Organomet. Chem.*, 2012, **26**, 267 – 272.
40. D. Bekerman, A. Ludwig, T. Toader, C. Maccato, D. Barreca, A. Gasparotto, C. Bock, A. D. Wieck, U. Kunze, E. Tondello, R. A. Fischer and A. Devi, *Chem. Vap. Depos.*, 2011, **17**, 155 – 161.
41. S. D. Cosham, G. Kociok-Köhn, A. L. Johnson, J. A. Hamilton, M. S. Hill, K. C. Molloy and R. Castaing, *Eur. J. Inorg. Chem.*, 2015, **26**, 4362 – 4372.
42. B. S. Shaheen, H. G. Salem, M. A. El-Sayed and N. K. Allam, *J. Phys. Chem. C*, 2013, **117**, 18502 – 18509.
43. R. Romero, M. C. López, D. Leinen, F. Martín, J. R. Ramos-Barrado, *Mater. Sci. Eng. B*, 2004, **110**, 87 – 93.
44. T. Minami, *Semicond. Sci. Technol.*, 2005, **20**, S35 – S44.
45. J. Tauc, *Mater. Res. Bull.*, 1968, **3**, 37 – 46.
46. S. T. Tan, B. J. Chen, X. W. Sun, W. J. Fan, H. S. Kwok, X. H. Zhang and S. J. Chua, *J. Appl. Phys.*, 2005, **98**, 013505(1) – 013505(5).

Chapter 6

Conclusions and Future Work

6. Conclusions and Future Work

This thesis has presented work concerned with the use, reaction and design of precursors in the AACVD of doped and undoped ZnO thin films.

The investigation into the use of zinc triflate $[\text{Zn}(\text{OTf})_2]$ as a precursor in the AACVD of ZnO thin films was presented in Chapter 3. It was shown that $[\text{Zn}(\text{OTf})_2]$ offers a number of desired precursor properties including a clean decomposition and stability in air. Although $[\text{Zn}(\text{OTf})_2]$ is commercially available and can be synthesised by relatively simple procedures, Chapter 3 presents the first reported use as a precursor to ZnO thin films. The system also exhibited excellent compatibility with co-precursors and the introduction of $[\text{Al}(\text{acac})_3]$ resulted in the successful deposition of AZO thin films. The deposited films were comprehensively characterised and the AZO thin films exhibited promising functional properties for use in TCO applications. The novel use of $[\text{Zn}(\text{OTf})_2]$ and related precursors is of industrial and commercial interest and a patent application was submitted based on the results presented in Chapter 3. The use of $[\text{Zn}(\text{OTf})_2]$ offers significant potential and further work is required into the use of other metal triflates and sulfonate precursors including their decomposition properties and use in alternative CVD systems.

The use of other commercially available CVD precursors towards ZnO thin films is highly limited and despite the liabilities and pyrophoric nature of ZnEt_2 it remains the most widely used precursor. The reactions of ZnEt_2 is in itself an interesting area of chemistry and was investigated in Chapter 4. Zinc complexes of two structural types were successfully synthesised, isolated and characterised following the addition of ZnEt_2 to a range of dicarbonyl compounds. A 1:1 addition resulted in an ethane elimination reaction in which highly pyrophoric zinc oxane trimer complexes of the type $[(\text{Zn}(\text{Et})(\text{OC}(\text{R})\text{CHC}(\text{Me})\text{O}))_3]$ where R = OMe (**1**), Me (**2**), OEt (**3**) and O^tBu (**4**) were synthesised in excellent yields of 88 – 91%. The crystal structure of (**1**) was determined and revealed a six membered Zn_3O_3 ring at the centre of the complex, a motif which is relatively limited in the published literature for complexes of this type. It was shown that it is the steric rigidity of the chelating ligands that allows for the six membered Zn_3O_3 ring to form.

Upon the controlled addition of O_2 to the solutions of (**1**) – (**4**), zinc oxane cluster complexes of the type $[(\text{Zn}(\text{OC}(\text{R})\text{CHC}(\text{Me})\text{O})_2\text{Zn}(\text{Et})\text{OEt})_2]$ where R = OMe (**5**), Me

(**6**), OEt (**7**) and O^tBu (**8**) were synthesised in yields of 83 – 87%. These complexes were successfully isolated and characterised with the crystal structures of complex (**6**) and (**8**) also determined. These complexes form a central structure which appears as a face-shared, inversion-related, bis-heterocubane in which a counter corner is missing from each cubane. These reactions are of interest as they provide a further example of the selective oxidation of Zn-C bonds, the mechanism of which is not fully understood. Zinc oxanes clusters (**5**) – (**8**) were also found to undergo slow decomposition despite the presence of Zn-Et groups still present in the complex. As a proof of concept, zinc oxane (**6**) was employed as a precursor in the AACVD of ZnO thin films but issues such as non-ideal decomposition and high carbon contamination were observed.

It is likely that through further investigations such as those observed in the literature and those presented in Chapter 4 that a greater understanding of the widely used and commercially important reactions of ZnEt₂ will be realised. The potential application of zinc oxane complexes of this type were only just touched upon as a proof of concept in Chapter 4. The system exhibits significant potential for use as CVD precursors and a much more comprehensive study should be conducted.

Chapter 4 presents the synthesis and use of zinc β -iminoesterate complexes. Four β -iminoester ligands of the type MeC(NHR)CHC(O)OEt where R is ⁱPr (**L**₁), Me (**L**₂), ^tBu (**L**₃) and (CH₂)₂ⁱPr (**L**₄) were synthesised from the reaction between ethyl acetoacetate and the corresponding primary amine using K-10 montmorillonite as a catalyst. Employing these ligands, zinc β -iminoesterates of two structural types were realised. The reaction between ZnEt₂ and 2 equivalence of (**L**₁) – (**L**₄) resulted in the synthesis of homoleptic [Zn(OC(OEt)CHC(Me)NR)₂] monomeric complexes (**9**) – (**12**) respectively in yields of 67 – 85%. The reaction between ZnEt₂ and 1 equivalence of (**L**₁) and (**L**₄) resulted in the synthesis of the heteroleptic dimeric complexes [(Zn(OC(OEt)CHC(Me)NⁱPr)(Et))₂] (**13**) and [(Zn(OC(OEt)CHC(Me)N(CH₂)₂ⁱPr)(Et))₂] (**14**) respectively in a yield of 75 and 67% respectively. Zinc β -iminoesterates (**9**) – (**14**) were successfully characterised with the crystal structures of (**9**), (**10**), (**13**) and (**14**) also determined. As expected, a lower degree of oligomerisation was found with the zinc β -iminoesterate complexes compared to the zinc oxane complexes reported in Chapter 4.

Complexes **(9)** and **(10)** were also used as novel single-source precursors in the AACVD of ZnO thin films. The change of organic ligand on the N moiety from an isopropyl group in **(9)** to a methyl group in **(10)** was found to greatly increase the level of carbon incorporated into the deposited film. This was attributed to the availability of more facile decomposition pathways in **(9)** compared to those available in **(10)**.

Chapter 5 illustrates the suitability of the zinc β -iminoesterate system for the deposition of ZnO thin films with the hexagonal wurtzite structure and high transparency in the visible light region. Chapter 5 also highlights the role of the organic substituents in the decomposition of the zinc β -iminoesterate complex and the subsequent effects observed in the deposited ZnO thin films. Further investigation is required into the effect of the organic substituents in the β -iminoesterate complexes and how these can be optimised for precursor applications. These complexes should also be investigated for use in alternative CVD systems. Further to this and in order to achieve doped ZnO thin films and potentially useful TCO materials, the use of these zinc β -iminoesterate complexes in combination with smaller amounts of other metal β -iminoesterate complexes in CVD applications should be investigated.

Appendix

Table 7.1: Observed and calculated residual mass obtained from TGA at 600 °C for [Zn(OTf)₂], [(Zn(OC(Me)CHC(Me)O)₂Zn(Et)OEt)₂] (6), [Zn(OC(OEt)CHC(Me)NⁱPr)₂] (9) and [Zn(OC(OEt)CHC(Me)NMe)₂] (10).

[Zn(OTf)₂]

Observed Residual Mass	22.7%
Calculated Residual Mass for ZnO	22.4%

[(Zn(OC(Me)CHC(Me)O)₂Zn(Et)OEt)₂] (6)

Observed Residual Mass	51.8%
Calculated Residual Mass for ZnO	40.4%

[Zn(OC(OEt)CHC(Me)NⁱPr)₂] (9)

Observed Residual Mass	19.8%
Calculated Residual Mass	20.1%

[Zn(OC(OEt)CHC(Me)NMe)₂] (10)

Observed Residual Mass	29.6%
Calculated Residual Mass	23.2%

Thermal gravimetric analysis (TGA) patterns for [Zn(OTf)₂], (6) and (9)/(10) are shown in Chapters 3.2.1.2, 4.2.2.1 and 5.2.3.1 respectively.

**Table 7.2: Crystallographic data and structural refinement for
[(Zn(Et)(OC(OMe)CHC(Me))₃)] (1).**

Radiation Wavelength	1.54184 Å	
Temperature	150.05(10) K	
Crystal System	Monoclinic	
Space Group	$P2_1/n$	
Volume	2647.74(3) Å ³	
Unit Cell Dimensions	$a = 14.33392(8)$ Å	$\alpha = 90^\circ$
	$b = 9.09638(5)$ Å	$\beta = 97.3126(6)^\circ$
	$c = 20.47334(14)$ Å	$\gamma = 90^\circ$
Z	4	
Calculated Density	1.577 g/cm ³	
Absorption Coefficient	3.553 mm ⁻¹	
$F(000)$	1296.0	
2θ Data Collection Range	7.122 – 147.316°	
Index Ranges	$-17 \leq h \leq 17, -11 \leq k \leq 11, -23 \leq l \leq 24$	
Reflections Collected	41363	
Independent Reflections	5292 ($R_{int} = 0.0276, R_\sigma = 0.0120$)	
Data / Restraints / Parameters	5292 / 0 / 307	
Goodness-of-fit on F^2	1.074	
Final R Indexes ($I \geq 2\sigma(I)$)	$R_1 = 0.0195, wR_2 = 0.0516$	
Final R Indexes (All Data)	$R_1 = 0.0206, wR_2 = 0.0522$	
Largest Diff. Peak / Hole	0.23 / -0.27 eÅ ⁻³	

Full crystallographic data for (1) is located on the disk attached at the back of this thesis.

Table 7.3: Crystallographic and structural refinement data for
 $[(\text{Zn}(\text{OC}(\text{Me})\text{CHC}(\text{Me})\text{O})_2\text{Zn}(\text{Et})\text{OEt})_2]$ (6).

Radiation Wavelength	0.71073 Å	
Temperature	150.05(10) K	
Crystal System	Triclinic	
Space Group	$P\bar{1}$	
Volume	838.34(11) Å ³	
Unit Cell Dimensions	$a = 9.3721(7)$ Å	$\alpha = 99.361(5)^\circ$
	$b = 9.9549(6)$ Å	$\beta = 113.292(6)^\circ$
	$c = 10.5962(7)$ Å	$\gamma = 104.798(6)^\circ$
Z	2	
Calculated Density	1.5969 g/cm ³	
Absorption Coefficient	2.878 mm ⁻¹	
$F(000)$	417.4	
2θ Data Collection Range	6.32 – 58.3°	
Index Ranges	$-11 \leq h \leq 12, -12 \leq k \leq 12, -14 \leq l \leq 14$	
Reflections Collected	12392	
Independent Reflections	4072 ($R_{\text{int}} = 0.0344, R_\sigma = 0.0392$)	
Data / Restraints / Parameters	4072 / 0 / 195	
Goodness-of-fit on F^2	1.050	
Final R Indexes ($I \geq 2\sigma(I)$)	$R_1 = 0.0328, wR_2 = 0.0706$	
Final R Indexes (All Data)	$R_1 = 0.0433, wR_2 = 0.0775$	
Largest Diff. Peak / Hole	0.58 / -0.57 eÅ ⁻³	

Full crystallographic data for (6) is located on the disk attached at the back of this thesis.

**Table 7.4: Crystallographic and structural refinement data for
[(Zn(OC(O'Bu)CHC(Me)O)₂Zn(Et)OEt)₂] (8).**

Radiation Wavelength	0.71073 Å	
Temperature	150.08(13) K	
Crystal System	Triclinic	
Space Group	<i>P</i> $\bar{1}$	
Volume	2455.44(12) Å ³	
Unit Cell Dimensions	$a = 11.2864(2)$ Å	$\alpha = 110.060(3)^\circ$
	$b = 13.2409(4)$ Å	$\beta = 90.455(2)^\circ$
	$c = 17.7760(5)$ Å	$\gamma = 99.460(2)^\circ$
<i>Z</i>	2	
Calculated Density	1.4046 g/cm ³	
Absorption Coefficient	1.988 mm ⁻¹	
<i>F</i> (000)	1091.0	
2 θ Data Collection Range	5.94 – 58.72°	
Index Ranges	$-15 \leq h \leq 15, -17 \leq k \leq 17, -24 \leq l \leq 24$	
Reflections Collected	36032	
Independent Reflections	11916 ($R_{int} = 0.0415, R_\sigma = 0.0428$)	
Data / Restraints / Parameters	11916 / 0 / 542	
Goodness-of-fit on F^2	1.044	
Final <i>R</i> Indexes ($I \geq 2\sigma(I)$)	$R_1 = 0.0351, wR_2 = 0.0780$	
Final <i>R</i> Indexes (All Data)	$R_1 = 0.0454, wR_2 = 0.0843$	
Largest Diff. Peak / Hole	1.07 / -0.66 eÅ ⁻³	

Full crystallographic data for (8) is located on the disk attached at the back of this thesis.

**Table 7.5: Crystallographic and structural refinement data for
[Zn(OC(OEt)CHC(Me)N^{*i*}Pr)₂] (9).**

Radiation Wavelength	1.54184 Å	
Temperature	150.0(10) K	
Crystal System	Monoclinic	
Space Group	<i>P</i> 2 ₁ / <i>n</i>	
Volume	2128.34(4)	
Unit Cell Dimensions	<i>a</i> = 7.70990(7) Å	<i>α</i> = 90°
	<i>b</i> = 14.23748(16) Å	<i>β</i> = 91.6241(8)°
	<i>c</i> = 19.39700(17) Å	<i>γ</i> = 90°
<i>Z</i>	4	
Calculated Density	1.178 g/cm ³	
Absorption Coefficient	1.820 mm ⁻¹	
<i>F</i> (000)	744.0	
2 θ Data Collection Range	7.704 – 147.282°	
Index Ranges	-9 ≤ <i>h</i> ≤ 9, -16 ≤ <i>k</i> ≤ 17, -24 ≤ <i>l</i> ≤ 24	
Reflections Collected	33021	
Independent Reflections	4250 (<i>R</i> _{int} = 0.0312, <i>R</i> _σ = 0.0158)	
Data / Restraints / Parameters	4250 / 0 / 234	
Goodness-of-fit on <i>F</i> ²	1.046	
Final <i>R</i> Indexes (<i>I</i> ≥ 2σ(<i>I</i>))	<i>R</i> ₁ = 0.0234, <i>wR</i> ₂ = 0.0615	
Final <i>R</i> Indexes (All Data)	<i>R</i> ₁ = 0.0258, <i>wR</i> ₂ = 0.0627	
Largest Diff. Peak / Hole	0.28 / -0.23 eÅ ⁻³	

Full crystallographic data for (9) is located on the disk attached at the back of this thesis.

**Table 7.6: Crystallographic and structural refinement data for
[Zn(OC(OEt)CHC(Me)NMe)₂] (10).**

Radiation Wavelength	0.71073 Å	
Temperature	150.00(10) K	
Crystal System	Monoclinic	
Space Group	<i>P</i> 2 ₁ / <i>c</i>	
Volume	1680.46(16)	
Unit Cell Dimensions	<i>a</i> = 6.8111(4) Å	$\alpha = 90^\circ$
	<i>b</i> = 20.8570(11) Å	$\beta = 101.592(6)^\circ$
	<i>c</i> = 12.0757(7) Å	$\gamma = 90^\circ$
<i>Z</i>	2	
Calculated Density	1.382 g/cm ³	
Absorption Coefficient	1.477 mm ⁻¹	
<i>F</i> (000)	736.0	
2 θ Data Collection Range	6.798 – 58.934°	
Index Ranges	$-7 \leq h \leq 9, -28 \leq k \leq 22, -16 \leq l \leq 15$	
Reflections Collected	7276	
Independent Reflections	3893 (<i>R</i> _{int} = 0.0279, <i>R</i> _{σ} = 0.0507)	
Data / Restraints / Parameters	3893 / 0 / 200	
Goodness-of-fit on <i>F</i> ²	1.054	
Final <i>R</i> Indexes (<i>I</i> ≥ 2 σ (<i>I</i>))	<i>R</i> ₁ = 0.0364, <i>wR</i> ₂ = 0.0691	
Final <i>R</i> Indexes (All Data)	<i>R</i> ₁ = 0.0502, <i>wR</i> ₂ = 0.0739	
Largest Diff. Peak / Hole	0.37 / -0.36 eÅ ⁻³	

Full crystallographic data for (10) is located on the disk attached at the back of this thesis.

Table 7.7: Crystallographic and structural refinement data for
 $[(\text{Zn}(\text{OC}(\text{OEt})\text{CHC}(\text{Me})\text{N}^i\text{Pr})(\text{Et}))_2][(\text{Zn}(\text{L}_1)(\text{Et}))_2]$ (13**).**

Radiation Wavelength	0.71073 Å	
Temperature	153.9(9) K	
Crystal System	Triclinic	
Space Group	$P\bar{1}$	
Volume	648.68(12) Å ³	
Unit Cell Dimensions	$a = 7.9052(6)$ Å	$\alpha = 88.294(9)^\circ$
	$b = 8.2403(10)$ Å	$\beta = 75.054(7)^\circ$
	$c = 11.1073(11)$ Å	$\gamma = 68.489(9)^\circ$
Z	1	
Calculated Density	1.355 g/cm ³	
Absorption Coefficient	2.489 mm ⁻¹	
$F(000)$	280.0	
2θ Data Collection Range	8.26 – 150.932°	
Index Ranges	$-6 \leq h \leq 9, -7 \leq k \leq 10, -13 \leq l \leq 13$	
Reflections Collected	3699	
Independent Reflections	2489 ($R_{\text{int}} = 0.0387, R_\sigma = 0.0504$)	
Data / Restraints / Parameters	2489 / 0 / 141	
Goodness-of-fit on F^2	1.036	
Final R Indexes ($I \geq 2\sigma(I)$)	$R_1 = 0.0472, wR_2 = 0.1197$	
Final R Indexes (All Data)	$R_1 = 0.0528, wR_2 = 0.1268$	
Largest Diff. Peak / Hole	0.83 / -0.70 eÅ ⁻³	

Full crystallographic data for (**13**) is located on the disk attached at the back of this thesis.

Table 7.8: Crystallographic and structural refinement data for
 $[(\text{Zn}(\text{OC}(\text{OEt})\text{CHC}(\text{Me})\text{N}(\text{CH}_2)_2^i\text{Pr})(\text{Et}))_2][(\text{Zn}(\text{L}_4)(\text{Et}))_2]$ (14**).**

Radiation Wavelength	0.71073 Å	
Temperature	150.00(10) K	
Crystal System	Triclinic	
Space Group	$P\bar{1}$	
Volume	759.20(7) Å ³	
Unit Cell Dimensions	$a = 7.6150(4)$ Å	$\alpha = 79.215(4)^\circ$
	$b = 8.0888(4)$ Å	$\beta = 76.682(4)^\circ$
	$c = 13.6777(6)$ Å	$\gamma = 68.774(5)^\circ$
Z	1	
Calculated Density	1.280 g/cm ³	
Absorption Coefficient	1.610 mm ⁻¹	
$F(000)$	312.0	
2θ Data Collection Range	6.162 – 55.714°	
Index Ranges	$-9 \leq h \leq 9, -10 \leq k \leq 10, -17 \leq l \leq 17$	
Reflections Collected	9398	
Independent Reflections	3384 ($R_{\text{int}} = 0.0541, R_\sigma = 0.0562$)	
Data / Restraints / Parameters	3384 / 0 / 159	
Goodness-of-fit on F^2	1.053	
Final R Indexes ($I \geq 2\sigma(I)$)	$R_1 = 0.0350, wR_2 = 0.0811$	
Final R Indexes (All Data)	$R_1 = 0.0407, wR_2 = 0.0864$	
Largest Diff. Peak / Hole	0.43 / -0.47 eÅ ⁻³	

Full crystallographic data for (**14**) is located on the disk attached at the back of this thesis.